HAL
open science

Systèmes transporteurs de principes actifs hydrophobes à base de glycoaminoglycanes thermosensibles : vers une plateforme polyvalente de délivrance

Marlène Rippe

To cite this version:

Marlène Rippe. Systèmes transporteurs de principes actifs hydrophobes à base de glycoaminoglycanes thermosensibles : vers une plateforme polyvalente de délivrance. Polymères. Université Grenoble Alpes, 2018. Français. NNT : 2018GREAV004 . tel-02463460

HAL Id: tel-02463460

https://theses.hal.science/tel-02463460

Submitted on 1 Feb 2020

HAL is a multi-disciplinary open access archive for the deposit and dissemination of scientific research documents, whether they are published or not. The documents may come from teaching and research institutions in France or abroad, or from public or private research centers.

L'archive ouverte pluridisciplinaire **HAL**, est destinée au dépôt et à la diffusion de documents scientifiques de niveau recherche, publiés ou non, émanant des établissements d'enseignement et de recherche français ou étrangers, des laboratoires publics ou privés.

Communauté UNIVERSITÉ Grenoble Alpes

THÈSE

Pour obtenir le grade de

DOCTEUR DE LA COMMUNAUTE UNIVERSITE GRENOBLE ALPES

Spécialité : **Sciences des polymères**

Arrêté ministériel : 25 mai 2016

Présentée par

Marlène RIPPE

Thèse dirigée par **Rachel AUZELY-VELTY et**
co-dirigée par **Anna SZARPAK-JANKOWSKA,**

préparée au sein du **Centre de Recherche sur les Macromolécules Végétales**
dans **l'École Doctorale de Chimie et Sciences du Vivant**

Systèmes transporteurs de principes actifs hydrophobes à base de glycosaminoglycanes thermosensibles : vers une plateforme polyvalente de délivrance.

Thèse soutenue publiquement le **7 février 2018**,
devant le jury composé de :

M. Elias, FATTAL
Professeur, Université Paris Sud, Rapporteur
M. Benoit, FRISCH
Directeur de Recherche, Université de Strasbourg, Rapporteur
M. Jean-Luc, COLL
Directeur de Recherche, Université Grenoble Alpes, Président du jury
Mme Christine, MENAGER
Professeur, Université Pierre et Marie Curie, Paris, Examinateur
M. Bruno, De GEEST
Professeur, Université de Gand, Belgique, Examinateur
Mme Anna, SZARPAK-JANKOWSKA
Maitre de conf., Université Grenoble Alpes, Co-encadrant de thèse
Mme Rachel, AUZELY-VELTY
Professeur, Université Grenoble Alpes, Directeur de thèse

Remerciements

Cette thèse s'est déroulée au sein du Centre de Recherches sur les Macromolécules Végétales (CERMAV). Dans ce cadre je tiens en premier tout d'abord Redouane Borsali et Anne Imberty, ses directeurs successifs, de m'y avoir accueillie.

J'adresse mes plus sincères remerciements à Rachel Auzély-Velty, ma directrice de thèse, et Anna Szarpak-Jankowska, ma co-encadrante, pour la confiance qu'elles m'ont accordée dès mon stage de Master et pour leur soutien lors de ma candidature aux concours de l'école doctorale. Je leur suis reconnaissante de m'avoir confié ce sujet de thèse ainsi que différentes responsabilités grâce auxquelles je me suis enrichie à tout point de vue. Merci pour ces trois années et demie d'aventures à vos côtés.

Je remercie ensuite tous les membres du jury qui ont accepté d'évaluer ces travaux de thèse avec rigueur et bienveillance : Jean-Luc Coll pour avoir endossé le rôle de président du jury, Elias Fattal et Benoît Frisch pour avoir rapporté le manuscrit, Christine Menager et Bruno De Geest en tant qu'examinateurs. Je suis très reconnaissante de l'intérêt et de l'enthousiasme qu'ils ont manifestés pour ces recherches. Ce fût un plaisir de converser avec eux. Je garderai un excellent souvenir de ma soutenance de thèse.

Je remercie également les membres de mon comité de suivi de thèse Isabelle Texier-Nogues et Jean-Luc Coll pour leurs échanges et conseils qui m'ont aidée à avancer.

Je tiens, à présent, à remercier l'ensemble des personnes dont la contribution s'est avérée indispensable pour mener à bien ces travaux de recherche: Vincent Martin (LEPMI) pour les analyses GPC des copolymères thermosensibles ; Francine Roussel-Dherbey (Grenoble INP-CMTC) pour les observations des nanogels par MEB ; Isabelle Jeacomine (CERMAV, plateforme ICMG) pour son aide précieuse en RMN ; Sonia Ortega (CERMAV) pour les analyses thermogravimétriques ; Christine Lancelon-Pin (plateforme ICMG) et Jean-Luc Puteaux (CERMAV) pour l'étude des nanogels en MET et cryo-MET. Ce dernier a joué un rôle bien au-delà des analyses en microscopie, et j'ai été très touchée par son soutien permanent, sa grande disponibilité, ses nombreux conseils et son aide cruciale durant la rédaction de ma thèse ; Claire Boisset (équipe CBO) pour son aide en chromatographie ionique ; Bernard Priem (équipe CBO) pour les discussions scientifiques autour de l'héparosan et sa fabrication ; l'équipe de Nora Dempsey (Institut Néel, Grenoble) pour l'étude des propriétés magnétiques conduite par Gabriel Gomez et Mario Fratzl (merci pour son aide

jusqu'à la dernière minute) ; toute l'équipe brésilienne de Celso Nakamura (Université de Maringá) qui a réalisée l'ensemble des tests in vitro et in vivo.

Ensuite j'ai vécu tout au long de ces trois années de riches expériences humaines et scientifiques grâce à toutes les personnes que j'ai pu rencontrer au CERMAV.

Tout d'abord, je remercie mon équipe « Structure et Modifications des Polysaccharides » pour leur aide scientifique et technique, leurs conseils avisés et leur patience. Je rends un hommage appuyé à mes co-bureaux : Lisa, Tamiris, Dominte et Robin pour tous ces moments mémorables, pour nos discussions, pour nos projets communs, pour avoir été toujours là pour moi et le rester. Je remercie chaleureusement les stagiaires de l'équipe : Fatma, Elena, Laurianne et François pour le dynamisme et la bonne humeur qu'ils ont apportés au sein de l'équipe.

Et ensuite un grand merci à l'ensemble des membres du laboratoire pour l'ambiance conviviale qui y règne et qui font du CERMAV un lieu de travail privilégié. Je tiens à exprimer le plaisir que j'ai eu à travailler à leurs côtés. En particulier, je remercie toute l'équipe des Glycomatériaux, Christelle Breton et William Hebert. J'ajoute une mention spéciale aux « wonder-women » du service gestion et RH : Martine Morales, Sandrine Coindet, Kristina Slavcheva et Isabelle Caldara, aux « MacGyver » du laboratoire, Eric, Pierre et Patrick, ainsi qu'aux sauveurs informaticiens, Alain Rivet et Cyril Bras. Et enfin je remercie Martine Broué, pour l'accueil qu'elle nous réserve tous les jours et son humour contagieux.

Je conclus en remerciant tous mes proches, à commencer par mes copains du CERMAV pour leur soutien moral indéfectible et en particulier : Léa, Harisoa, Clélia, Charlène, Mathilde, Milène, Emilie, Lauric, Agustin, Yotam, Julien, Félix C., Félix P., Yu, Eric, Laurent G., Antoine et Arnaud ; me*s copains de l'association GLOB'ALPS : Carine, Marie, Adèle, Souad, Jérôme et Charles ; mes acolytes de Master : Beaura et Robin, D ; Et mes amis de toujours : Lucie, Marine, Caroline, Agathe, Alexia, Marie-Alix, Linnea, Claire, Arnaud, Jérémy, Samuel, Nicolas et Paul-Hervé.*

Une pensée affectueuse à Guillaume qui m'a permis de me lancer dans cette aventure et m'a initiée aux bienfaits de la technologie et à Kevin qui m'a soutenue dans la toute dernière ligne droite.

Enfin, j'exprime ma reconnaissance éternelle à mes parents et ma famille pour leur soutien indéfectible dans tous ce que j'entreprends, pour leur grain de folie et leur ouverture d'esprit qui ouvrent tous les champs des possibles, et pour la force et le bonheur qu'ils m'apportent.

Table des matières

Introduction général **1**

Chapitre 1 – Glycosaminoglycans based drug delivery systems - Bibliography review 5

I Introduction 5
II Glycoaminoglycans for the design of drug nanocarriers 6
III Self-assembly drug delivery systems based on GAGs 8
III.1 Nanovesicles 9
III.2 Micelles 9
III.3 Nanospheres 10
IV Strategies for the design of GAGs-based drug delivery systems 12
IV.1 Hyaluronic acid-based amphiphilic nanoparticles 12
IV.1.1 Micelles 13
IV.1.2 Polymersomes 16
IV.1.3 Nanogels 18
IV.1.3.1 HA-drug conjugates 18
IV.1.3.2 HA-small hydrophobic molecules conjugates 21
IV.1.3.2.1 Alkylated HA derivatives 21
IV.1.3.2.2 HA-cholesterol conjugates 24
IV.1.3.3 HA-polymer conjugates 28
IV.1.3.3.1 pH-Responsive HA-polymer conjugates 30
IV.1.3.3.2 Thermoresponsive HA-polymer conjugates 33
IV.2 Chondroitine-based amphiphilic nanoparticles 37
IV.3 Heparin and Heparan sulfate-based amphiphilic nanoparticles 41
IV.4 Heparosan-based amphiphilic nanoparticles 43
V Conclusion 46
VI References 48

Chapitre 2 - Synthèse de nouveaux copolymères thermosensibles **65**
I Introduction 65
II Polymérisation radicalaire contrôlée de poly(DEGMA-co-BMA) 67
II.1 Vérification expérimentale du contrôle de la polymérisation RAFT 69
II.2 Caractérisation structurale des copolymères obtenus 73
III Comportement en solution 75
III.1 Etude de l'auto-association par turbidimétrie, détermination de la température de point de trouble 75

III.1.1 Définition de la température de point de trouble 75
III.1.2 Effet de la concentration du copolymère en solution et de la force ionique du milieu 75
III.1.3 Effet de la masse molaire du copolymère poly(DEGMA-co-BMA) sur la transition de phase en fonction de la température 77
III.1.4 Effet du ratio des monomères 79
III.2 Analyse par DLS de la distribution en taille des agrégats formés 80
V Conclusion 81
VI Partie expérimentale 82
V Références 84

Chapitre 3 – Élaboration de nanogels thermosensibles 87
I Introduction 87
II Résultats et discussions 89
II.1 Articles 89
II.2 Résultats et discussions complémentaires 115
II.2.1 Purification des dérivés HA-copolymères synthétisés 115
II.2.1.1. Purification par dialyse 115
II.2.1.2 Purification par chromatographie en batch 116
II.2.1.3 Validation de la purification 118
II.2.2 Détermination du degré de substitution (DS) 121
II.2.3 Etude de la réaction thiol-ène radicalaire 123
II.2.3.1 Mécanisme réactionnel 123
II.2.3.2 Efficacité de la réaction de couplage 124
II.2.3.3 Etude de l'influence de l'agent réducteur (TCEP) sur la réactivité 125
II.2.3.4 Perspective sur la réaction de couplage 128
II.2.4 Etude complémentaire sur les nanogels (non réticulés) 128
II.2.4.1 Etude de l'auto-association en solution 129
II.2.5 Etude complémentaire sur les nanogels réticulés 133
II.2.6 Quantification de la disulfo-cyanine7 amine greffée sur les produits 136
III Conclusions 137
IV Références 139

Chapitre 4 – Design of magnetic nanobeads based on hyaluronic acid 143
I Introduction 143
II Synthesis of hydrophobic iron oxide nanoparticles (IONPs) 147
III Design of magnetic nanobeads based on hyaluronic acid 152

III.1 Preparation of HA-g-copolymer/IONPs nanogels by *in situ* encapsulation 153
III.2 Core/shell nanobeads 158
III.2.1 Preparation of magnetic clusters coated with HA-g-poly(DEGMA-co-BMA) 158
III.2.2 Magnetic attraction.....168
IV Conclusion.....171
V Experimental section 172
VI Supplementary information.....177
VII References 179

Conclusion générale et perspectives **187**

Annexes **191**

Liste des abréviations récurrentes 191
Liste des figures.....192
Liste des tableaux.....201

Résumés **204**

Introduction générale

L'un des principaux problèmes de la chimiothérapie contre le cancer est la sévère toxicité des agents anticancéreux dans l'organisme. De plus, l'administration thérapeutique de principes actifs (PA) est souvent limitée par des problèmes de solubilité et de sensibilité à l'hydrolyse enzymatique. C'est pourquoi, une délivrance sélective de ces médicaments au sein des tissus cancéreux est l'un des points essentiels des recherches effectuées à ce jour.

Parmi les différentes approches issues des nanotechnologies, l'utilisation de nano-vecteurs, cargos de taille nanométrique, s'est imposée comme une des solutions les plus pertinentes pour augmenter l'efficacité des traitements existants, tout en réduisant leur toxicité systémique. Ces vecteurs permettent de contourner les limitations des approches conventionnelles à la fois en thérapie, en imagerie et en diagnostic, tout en améliorant la solubilité en milieu aqueux des PA, leur efficacité thérapeutique (en favorisant leur accumulation au niveau du tissu cible) et leur capacité à évaluer les réponses thérapeutiques.

En effet, leur taille nanométrique peut permettre un « ciblage passif » grâce à l'effet de perméabilité et de rétention tissulaire observé au niveau des zones tumorales (effet « EPR »). Ce phénomène peut varier en fonction de la forme et de la charge globale des nano-systèmes. Par ailleurs, ces vecteurs offrent la possibilité de modifier leur surface à l'aide de ligands spécifiques qui favorisent le ciblage de cellules et confèrent ainsi la propriété de délivrer le PA qu'ils transportent vers des cibles spécifiques.

Dans ce contexte, au cours de ces 20 dernières années, les efforts de recherche dans le domaine des nanovecteurs ont été consacrés à l'élaboration d'une nouvelle génération de nanoparticules intelligentes, à base de polymères amphiphiles synthétiques ou naturels, permettant une délivrance sélective des principes actifs hydrophobes dans les cellules tumorales.

Bien que ce domaine de recherche très actif ait conduit à un grand nombre d'études précliniques et cliniques, qui ont permis de mieux comprendre la validité de cette approche, les nanovecteurs ne remplissent pas toutes les caractéristiques nécessaires pour pouvoir véhiculer un principe actif sélectivement vers des cellules ou tissus cibles et le libérer de manière contrôlée. Ainsi, des défis importants restent à surmonter et passent par la conception de nanoparticules plus sophistiquées, combinant plusieurs fonctions [1-3]. Par ailleurs, la plupart des procédés utilisés pour préparer des nanoparticules impliquent l'utilisation de solvants toxiques et/ou des tensioactifs, ce qui impose des étapes de purification importantes.

Depuis plusieurs années, l'équipe « Structure et Modifications de Polysaccharides » du CERMAV dispose d'une expertise dans la modification chimique de polysaccharides naturels et plus particulièrement dans l'élaboration d'hydrogels innovants à différentes échelles (macrogels, microcapsules, nanogels) pour des applications biomédicales dont la délivrance contrôlée de principes actifs et de cellules (schéma 1.A). Notamment, une partie de l'activité de cette équipe concerne l'expertise dans la caractérisation et la modification chimique de l'acide hyaluronique, activité qui a débutée il y a plus de 15 ans. Ce polysaccharide appartient à la famille des glycosaminoglycanes (GAGs), polysaccharides biocompatibles et biodégradables omniprésents dans le corps, et est un ligand du récepteur protéique CD44 surexprimé par plusieurs cellules cancéreuses (notamment les cellules épithéliales (carcinome) de la glande mammaire et les cellules tumorales ovariennes).

Ainsi des nanogels (réseaux d'hydrogel de taille nanométrique) à base d'acide hyaluronique ont été développés pour la délivrance contrôlée de principes actifs [4-6]. Leur formation repose sur l'auto-association, induite par une élévation de la température, de copolymères thermosensibles greffés sur le squelette polysaccharidique. La déshydratation des chaînes de copolymère par chauffage entraîne un changement de conformation globale du polysaccharide modifié vers la formation de nanogels, capables de piéger sélectivement des PA très peu solubles dans l'eau dans les nanodomaines hydrophobes formés par le copolymère (schéma 1.B) Le potentiel des systèmes élaborés a clairement motivé ce travail.

Dans ce contexte, nous proposons d'étendre cette approche à la formation d'une nouvelle génération de nanogels thermosensibles dans le but, d'une part de mieux contrôler leur pharmacocinétique (stabilité colloïdale) et leur biodistribution (propriétés biologiques) dans l'organisme, et d'autre part d'évaluer leur polyvalence en tant que systèmes plate-formes.

Ce manuscrit décrit les différentes étapes qui ont été suivies pour élaborer et caractériser des nanogels à base d'acide hyaluronique et d'un autre GAG encore peu utilisé pour la conception de nanovecteurs, l'héparosan (Hep). Ce mémoire est divisé en quatre chapitres.

Le premier chapitre consiste en une revue bibliographique qui propose un état de l'art sur les nanovecteurs amphiphiles. Après une description des caractéristiques générales de ces systèmes, nous nous intéresserons en particulier aux potentiels des nanovecteurs amphiphiles élaborés à partir de glycosaminoglycanes.

Le second chapitre présente la synthèse du copolymère thermosensible utilisé pour induire la formation des nanogels.

Le troisième chapitre est dédié à la préparation de nanogels thermosensibles à partir du HA et de l'Hep. La comparaison des nanogels en fonction de leur propriété de surface est présentée. Nous discutons l'impact du choix du GAG ainsi que de la réticulation de ce dernier sur la biodistribution *in vivo* des systèmes synthétisés.

Enfin, le quatrième chapitre est consacré aux perspectives d'utilisation de ces systèmes comme plateformes pour l'encapsulation de différents types de nanoparticules. Il se focalise plus particulièrement sur l'encapsulation de nanoparticules d'oxyde de fer super-paramagnétiques.

Toutes les parties qui feront l'objet de publications ont été rédigées en anglais.

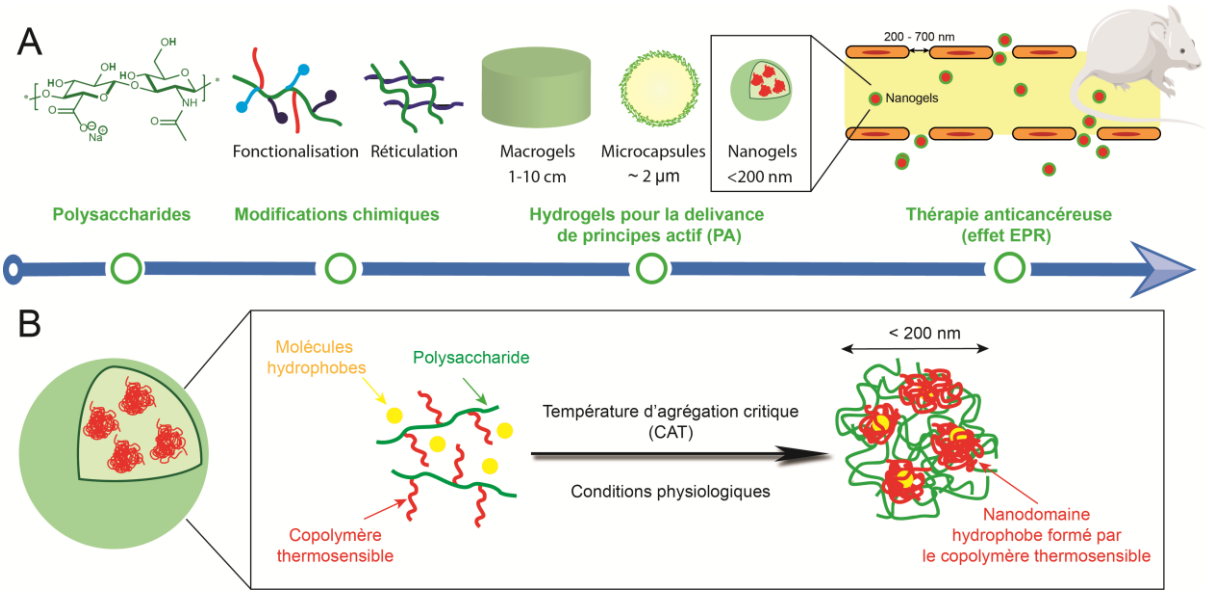

***Schéma 1**. A) Modifications chimiques de polysaccharides pour l'élaboration de systèmes de délivrance contrôlée de principes actifs. B) Elaboration de nanogels thermosensibles à partir de polysaccharides pour la thérapie anti-cancéreuse.*

Références

1. Lammers, T.; Kiessling, F.; Hennink, W.E.; & Storm, G. Drug targeting to tumors: principles, pitfalls and (pre-)clinical progress. *Journal of controlled release*, **2012**, 161, 175-187.
2. Sun, Q.; Ojha, T.; Kiessling, F.; Lammers, T.; & Shi, Y. Enhancing tumor penetration of nanomedicines. *Biomacromolecules*, **2017**, 18, 1449-1459.
3. Shi, Y.; Lammers, T.; Storm, G.; & Hennink, W.E. Physico-chemical strategies to enhance stability and drug retention of polymeric micelles for tumor-targeted drug delivery. *Macromolecular Bioscience*, **2017**, 17, 1600160.
4. Jing, J.; Alaimo, D.; De Vlieghere, E.; Jérôme, C.; De Wever, O.; De Geest, B.G.; & Auzély-Velty, R. Tunable self-assembled nanogels composed of well-defined thermoresponsive hyaluronic acid–polymer conjugates. *Journal of Materials Chemistry B*, **2013**, 1, 3883-3887.
5. Stefanello, T.F.; Szarpak-Jankowska, A.; Appaix, F.; Louage, B.; Hamard, L.; De Geest, B.G.; Van der Sanden, B.; Nakamura, C.V; & Auzély-Velty, R. Thermoresponsive hyaluronic acid nanogels as hydrophobic drug carrier to macrophages. *Acta Biomaterialia,* **2014**, 10, 4750-4758.
6. Stefanello, T.F.; Couturaud, B.; Szarpak-Jankowska, A.; Fournier, D.; Louage, B.; Garcia, F.P.; Nakamura, C.V; De Geest, B.G.; Woisel, P.; Van der Sanden, B.; & Auzély-Velty, R. Coumarin-containing thermoresponsive hyaluronic acid-based nanogels as delivery systems for anticancer chemotherapy. *Nanoscale*, **2017**, 9, 12150-12162.

Chapitre 1 - Glycosaminoglycans based drug delivery systems - Bibliography review

I Introduction

Drugs are substances administered to the body where they are expected to have a beneficial effect regarding disease treatment, disease prevention, discomfort reduction, or injury reparation. However, in chemotherapy, many chemotherapeutic agents can simultaneously improve the survival rate of patients while resulting in adverse effects, owing to a lack of specificity. Development of “smart” carriers allowing controlled release and targeting of drugs to a specific site can overcome this limitation [1-3].

The primary hurdle for the success of any drug delivery system is to overcome innate immunity as a result of blood−NP interaction, which could compromise the potency and efficacy of the drug. The particle size is a factor for controlling the extravation rate of nanoparticles from bloodstream as well as recognition by the reticuloendothelial system (RES). In general, nanoparticles with sizes in the range 30-200 nm are preferred for *in vivo* delivery (size > 30 nm to escape renal clearance and < 200 to prevent sequestration from RES of the spleen and liver). Moreover, their nanoscale dimension enables them to exploit the "passive targeting" thanks to the effect of permeability and tissue retention (EPR) at the level of the tumor zones.

In addition to passive targeting, active targeting can increase drug efficacy. Most tumors are characterized by the overexpression of cancer-specific antigen(s) or receptors(s) on their cell surfaces, which are essential for the growth of tumor cells. Therefore, the use of nanocarrier-based delivery systems to target these receptors is an important modality of treatment. The more targeted a drug is, the lower its chance of triggering drug resistance, a cautionary concern surrounding the use of broad-spectrum antibiotics.

Especially, smart polymeric nanoparticles hold great promise for the selective delivery of hydrophobic active ingredients in tumor cells [4-5]. These systems have typically submicron sizes in the range 20-250 nm and include various architectures such as nanospheres [6], nanovesicles [7-8], micelles [9], and dendrimers [10]. All polymers used to produce nanocarriers, synthetic or natural polymers, have to be carefully chosen for medical applications not only regarding their functional properties but also their biocompatibility and biodegradability. For polymeric materials, the biocompatibility is closely connected to the

biodegradability. Biocompatibility can be defined as the ability of material to exist in contact with tissues of the human body without causing an unacceptable degree of harm [11]. Degradation products and fragments have to be biocompatible. Non-biodegradable material can be used in development too. However, in that case, precaution against polymer accumulation in body has to be taken.

Therefore, biopolymers possess several favourable characteristics in comparison to synthetic polymers used in drug delivery, such as biocompatibility, biodegradability, non-toxicity and abundant renewable sources [12]. Among them, naturally occurring polysaccharides are attractive building blocks for designing drug delivery systems, because they can offer even more advantages over conventional nanocarriers composed of totally chemically synthesized materials i) prevent recognition by the RES ii) intrinsic bioactivity for some polysaccharides such as ability to be recognized by cell-surface protein receptors, mucoadhesive, antimicrobial, and anti-inflammatory properties, and iii) the presence of various functional groups on macromolecular backbone allowing chemical reactions with different kinds of molecules [13-16]. In particular, glycosaminoglycans (GAGs), which are important heteropolysaccharides in the extracellular matrix where they play a unique role in modulating cellular functions, show a great potential in the field of drug delivery. [17]

This review covers recent developments of nanocarriers based on GAGs, highlighting the formation of modular, tunable self-assembled nanoparticles. We will describe the different approaches for chemical modification of GAGs and we will analyze in details their self-assembly, their degradation mechanisms in vivo, their current clinical applications and the possibility to translate some of the recent research achievements into practical clinical application in the near, mid- and long-term future.

II Glycosaminoglycans for the design of drug nanocarriers

Various polysaccharides such as chitosan [18], dextran [19], pullulan [20], galactomannan [21], and alginate [22] have been used for the fabrication of drug delivery nanosystems over the last two decades [23-24]. Among them, glycosaminoglycans have gained increasing interest. They constitute the most abundant hetero-polysaccharides in the body. GAGs are primary components of the cell surface and the extracellular matrix (ECM). Depending on the tissue and cell type, GAGs are structural, adhesion, and/or signalling elements. In the ECM, they interact with numerous proteins and modulate their activity and consequently, govern important biological processes such as cell growth, differentiation, morphogenesis, cell migration and bacterial/viral infections (Figure1.1-B) [25-27]. These

natural polysaccharides have been widely employed as therapeutic agents and targeting moieties, which is typically not seen in their synthetic counterparts [27-31]. Furthermore, unlike the latter, they are free from problems of adverse effects and do not transform into harmful substances upon biodegradation in the body with no risk of bioaccumulation.

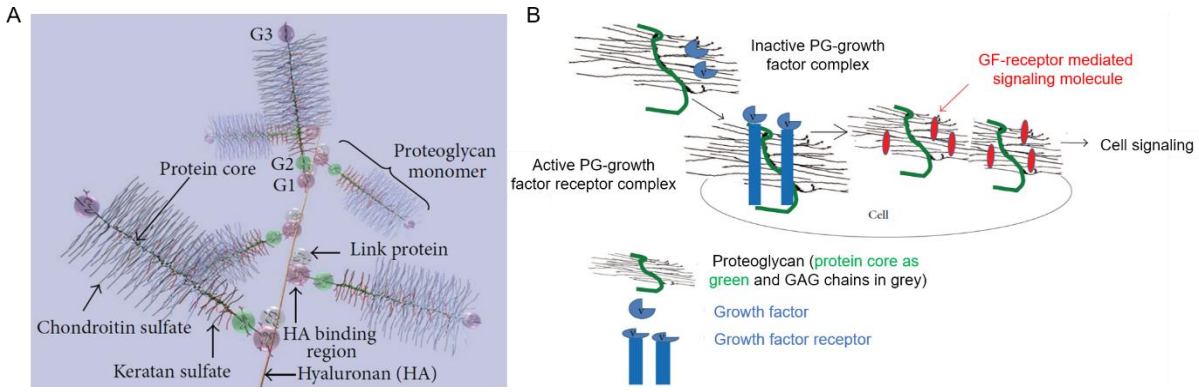

Figure 1.1 *A) Diagram of part of an aggrecan aggregate. G1, G2, and G3 are globular, folded regions of the central core protein. Proteoglycan aggrecan showing the noncovalent binding of proteoglycan to HA with the link proteins B) Proteoglycans act as coreceptors for growth factor receptor (GFR) signaling, thus influencing cell signaling and cell behavior. GAGs present as a part of proteoglycans on the cell surface and in ECM, bind to numerous proteins, and modulate their function. Figure from Misra et al. [17]*

Important types of GAGs that differ in chemical composition, structure and function include hyaluronic acid (HA), heparin (Hp), heparan sulfate (HS), chrondroitin sulfate (CS) dermatan sulfate (DS) and keratan sulfate (KS). The molar masses and sulfation patterns of GAGs vary over a broad range, depending on the organism, tissue type, age and health conditions. With regard to their structure, they are linear anionic heteropolysaccharides composed of repeating disaccharide units of N- acetylated hexosamine linked to hexuronic acid (with the exception of keratan sulfate).

Hyaluronic acid is unique among the GAGs family in that it does not contain any sulfate and is not found covalently attached to the core proteins forming a proteoglycan in the Golgi apparatus (Figure 1.1-A). The enzymes responsible for its production are located in the plasma membrane [32]. Medical grade HA is currently produced by bacterial fermentation by many companies up to several tons per year [33]. It is also available in a wide range of molar masses (from 5 kg/mol to more than 2 million g/mol) to suit various biomedical applications.

In the GAGs family, we can also include another interesting polysaccharide, heparosan, which is the natural precursor of heparin/heparan sulphate. Heparosan has a chemical structure close to that of HA. Indeed, Hep has a repeating disaccharide unit of D-glucuronic

acid (GlcA) and *N*-acetyl-D-glucosamine (GlcNAc) residues such as HA, but the α-1,4 bond between the GlcA and the GlcNAc units replaces the β-1,3 bond found in HA.

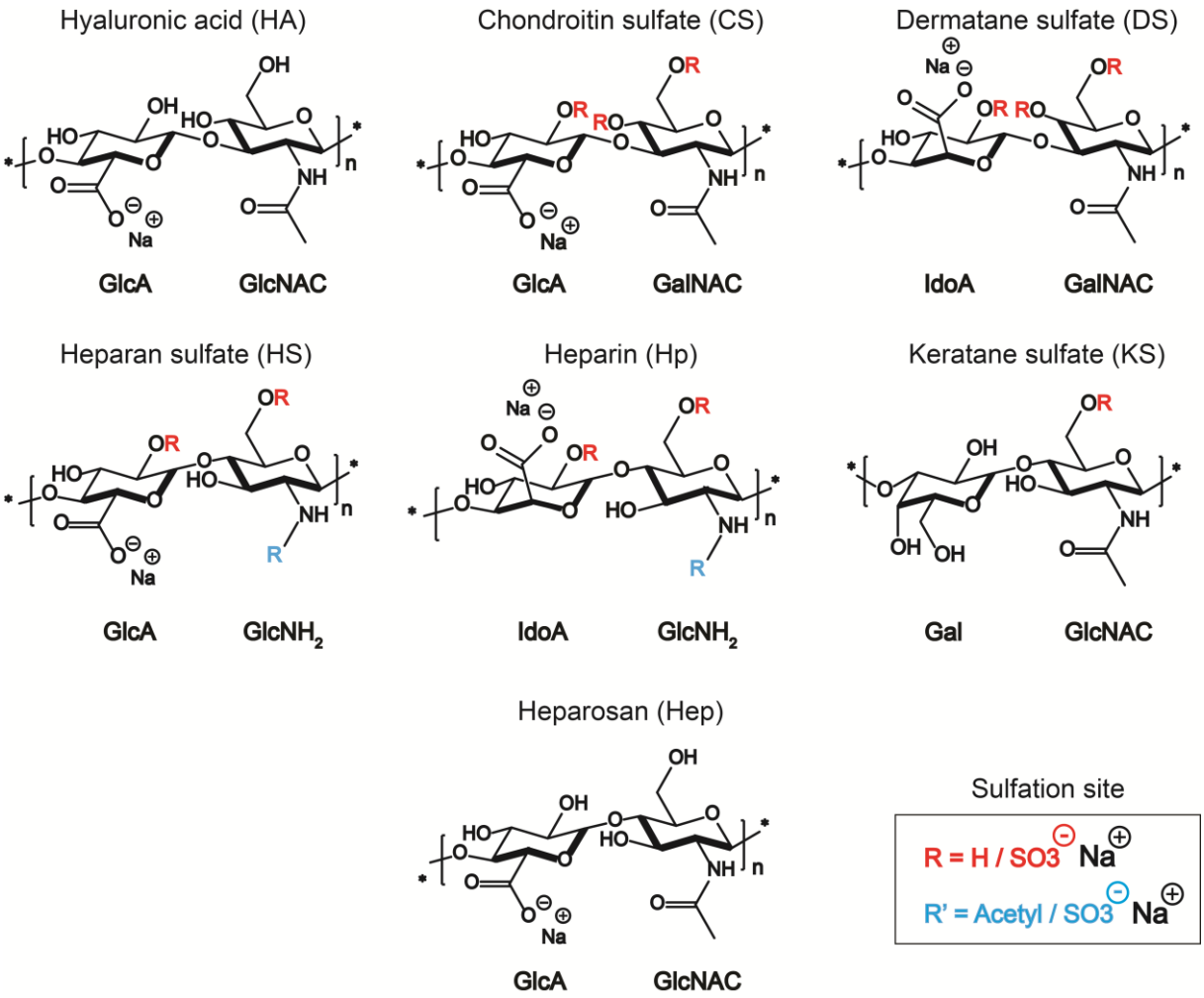

Figure 1.2 *Chemical structures of repeating disaccharides of glycosaminoglycans and Heparosan.*

III Self-assembly drug delivery systems based on GAGs

A wide variety of self-assembled nanosized carriers based on GAGs, with distinct architectures, sizes and surface properties has been developed [17,31]. GAGs NPs can be divided into three groups: micelles, nanovesicles and nanospheres. Herein, GAGs-decorated hydride or composite nanoparticles are not included as polymeric nanoparticles since the polysaccharide is mainly located on the carrier surface and is not the major component. An illustration of the different types of GAGs-based NPs is given in Figure 1.3.

III.1 Nanovesicles

Polymeric nanovesicles are hollow-core systems, acting as drug reservoirs in which the drug can be entrapped in the liquid core and/or in the polymeric shell/wall. Two generations of nanovesicles have been developed.

The first generation are composed of an oily core surrounded by a thin polymer membrane generally prepared by interfacial nano-deposition such as layer-by-layer (LBL) self-assembly of oppositely charged polymer (polyelectrolytes complexes) [34]. The main established methods to control the size of nanocapsules are surfactant assisted inverse water-in-oil emulsion [35-36] and inorganic salt induced mineralization [37-38]. These nanovesicles can be used as reservoirs to encapsulate and protect hydrophobic active species. However, GAGs (CS, HP, HA), due to their high molar mass, do not allow the production of capsules with sizes below 250 nm.

More recently, a second generation of vesicles with an aqueous core commonly referred to as polymersomes, in analogy to the lipid-based vesicles, liposomes, was developed [8, 39]. These latter are hollow spheres consisting of a polymer bilayer in which both hydrophilic and hydrophobic therapeutic molecules can be encapsulated in the aqueous core and in the polymer shell, respectively. The bilayer is made from amphiphilic diblock (A-B) or triblock (A-B-A) copolymer [40]. The size and morphology can be controlled by varying the composition and size of the copolymer, preparation methods and solution properties. Compared to liposomes, polymersomes have a higher membrane thickness, which provides to the bilayer higher stability and robustness against mechanical stresses [8]. Moreover, delivery of two different kind of drugs can work synergistically to enhance the therapeutic effect. So far, however, very few studies have reported on polymersome formation from polysaccharide-based diblock.

III.2 Micelles

Similarly, to polymersomes, nanomicelles are composed of amphiphilic block copolymers. The difference between them lies in the architecture of the self-association. Micelles are characterized by amphiphilic block copolymers adopting in aqueous solution a core-shell structure which can directly entrap the cargo in the hydrophobic core. Thus, only hydrophobic compounds can be encapsulated. The two major advantages of these structures are that i) the synthesis of block copolymer enables the design of well-defined and controlled architectures, ii) they allow to preserve fully or to a large extent the integrity and properties of the GAGs chain.

The transition from polymersomes to micelles and vice-versa is driven by the hydrophilic/hydrophobic balance. The morphology evolves, with the ratio of the hydrophilic part to the total mass of the copolymers, from polymersomes (cylinder form at low hydrophilic content < 40% by weight of the polymer molecule) to spherical micelles (conical form at higher hydrophilic content > 50%) [41].

III.3 Nanospheres

Nanospheres can be described as a solid polymer matrix in which the cargo is dispersed throughout the matrix, grafted to the polymer matrix or adsorbed at the surface. Thus, this architecture offers different possibilities for drug loading.

In the last two decades, nanogels, a new type of nanospheres, were developed. They are described as aqueous dispersion of nanometer-sized (100 to 500 nm) [42] chemically or physically crosslinked networks of hydrophilic polymers [43-47].

The physical crosslinking is based on various physical interactions, including hydrogen bonding, electrostatic interactions and hydrophobic interactions. Self-assembled nanogels can therefore be divided in two main groups: polyelectrolyte nanogels and amphiphilic nanogels. Since GAGs are negatively charged, complexation strategy with oppositely charged polysaccharides, such as chitosan [48-55], has be used for the formation of nanogels. However, the hydrophilic nature of these nanogels make the encapsulation of neutral hydrophobic drugs impossible. On the other hand, amphiphilic soft nanogels are capable of holding small hydrophilic as well as hydrophobic molecular therapeutics, biomacromolecules and inorganic nanoparticles within their crosslinked cores-shell networks.

Compared to other nanoparticles, outlined above, nanogels are able to take up large amounts of water or physiological fluid, while maintaining their internal network structure. Thus, they exhibit the greatest flexibility and deformability, high loading capacities (30 to 50% weight) [47] and the particular feature of efficiently loading drug at any time, i.e. when the nanogels are swollen and equilibrated in water or in biological fluid. Therefore, since their introduction in 1999 by Vinogradov et al. [56] these gel nanoparticles have gained increasing interest and have become the most studied nanovectors among GAGs-based nanoparticles for diverse cancers and other immune disorders [17, 31].

The detailed description for each of the three types of nanocarrier (vesicles, micelles, nanospheres) highlights one common feature which is their ability to self-assemble in water into nanoparticles owing to their amphiphilic nature. This provides a driving force for self-assembly without the need of solvents or surfactants. This property is sought out for the

suitable administration of hydrophobic drugs that constitute a large part of currently available drugs and remains nowadays a great challenge in the field of biomedicine.

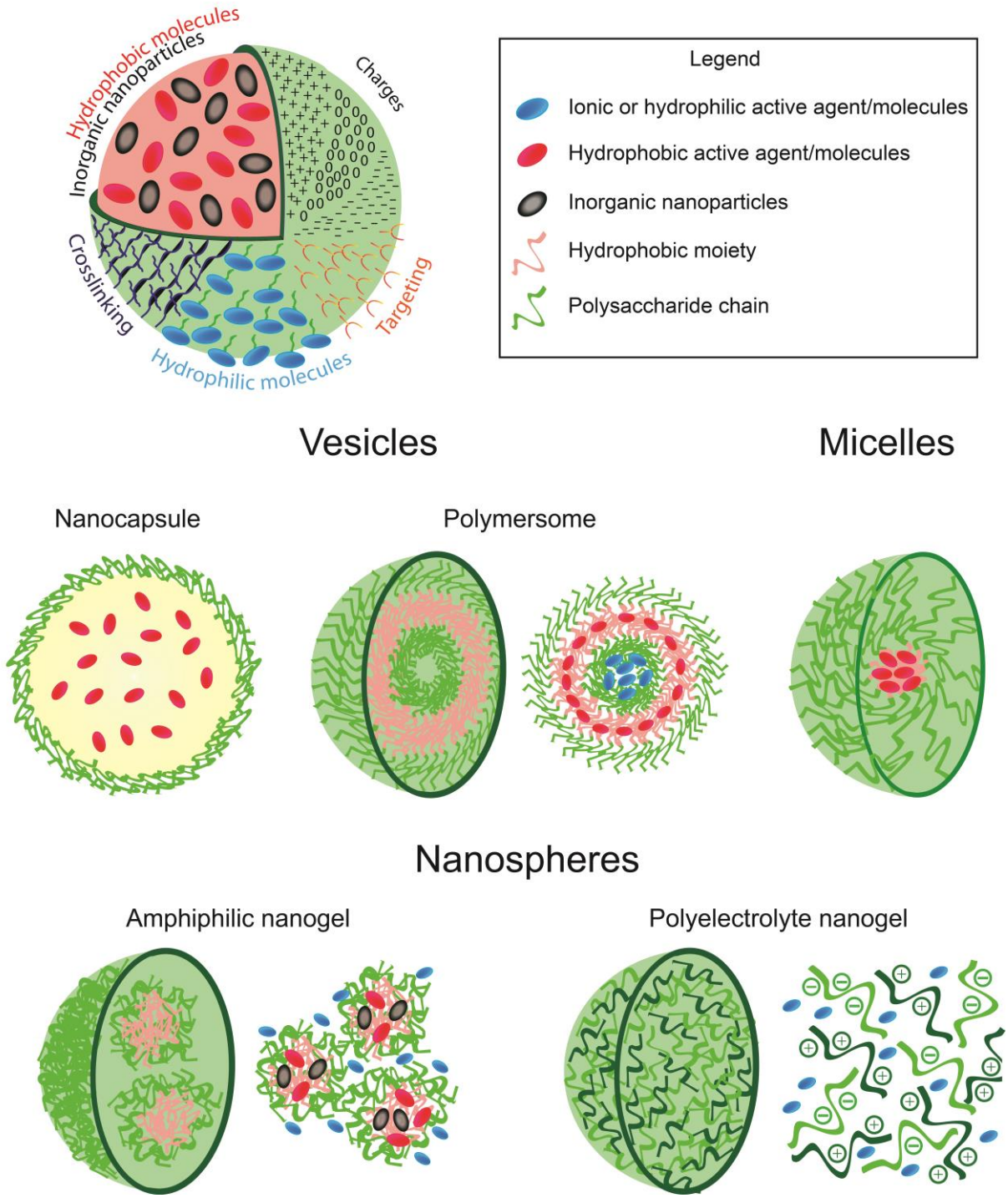

Figure 1.3 *Schematic representation of different GAGs-based nanocarriers.*

IV Strategies for the design of GAGs-based drug delivery systems

Among glycosaminoglycans, hyaluronic acid, heparin, heparan and chondroitin sulfate are the most extensively studied as drug delivery systems owing to their potential as pharmaceuticals and because they are the four most prevalent GAGs in humans. Concerning keratan sulfate (KS) and dermatan sulfate (DS), very few studies have been done. The lack of knowledge regarding the biosynthetic pathway of KS limits its use [57]. DS was principally employed as pharmaceutical (cofactor in variety of therapeutics) especially in cell-mediated tissue repair and wound healing [58]. However, it was noted that DS shares heparin's structure and is able to selectively target the neovascular system, by binding heparin cofactor II, a receptor reported to be upregulated on tumor endothelium, and penetrate into the tumor matrix [59]. Because of that activity, one example of DS based nanogels have been developed by Ranney et al. to encapsulate imaging probe (Fe^{3+}: deferoxamine) and therapeutic agent (doxorubicine) *via* polyelectrolyte complex formation [60].

This section discusses approaches for the synthesis of GAG based amphiphilic nanoparticles.

IV.1 Hyaluronic acid-based amphiphilic nanoparticles

HA is the oldest discovered GAG by Meyer et al in 1950's [61-62]. It consists of repeating disaccharide units of D-glucuronic acid and *N*-acetyl-D-glucosamine, linked together *via* alternating β-1,4 and β-1,3 glycosidic bonds.

In the field of drug-delivery systems, HA is by far the most extensively studied GAG [63-66] not only for its biocompatibility and low immunogenicity but also for its unique opportunity to target various cancer cells that overexpressed HA receptors on their surface (CD44 and RHAMM) [67]. Moreover, HA can be easily degraded after internalization in tumor cells by successive actions of hyaluronidases (HYALs) [68] thus releasing the drug inside the target cells. The level of HYALs is elevated in many cancer cells.

It is noted that successful translocation into cells HA requires binding to multiple receptors. The molar mass of HA is one of the main factors that govern its interaction with the CD44 receptor involved in cellular uptake. Un-modified 6-8 saccharide repeating units are required for selective binding to one CD44 receptor [69]. However, oligosaccharides larger than 20 residues are required for effectively interacting with more than one CD44 receptor [70].

HA with a molar mass below 31 kg/mol binds only one CD44 receptor, while HA with a molar mass above 130 kg/mol binds from 5 to 8 CD44 receptors [71].

IV.1.1 Micelles

Micelles are made from amphiphilic block copolymers (HA-b-polymer). They were synthesized by end-to-end coupling strategies as described in Figure 1.4. The most common ones belong to click chemistry. As shown in Figure 1.4, the terminal reducing end of HA can react as an aldehyde group with amine-functionalized molecules by a reductive amination reaction to produce HA-derivatives that can be coupled with the hydrophobic polymer block *via* a Huisgen cycloaddition or an amine-acid coupling reaction. The other end formed (hydroxymethyl) can also be used to polymerize directly the hydrophobic polymer at the end of the HA chain.

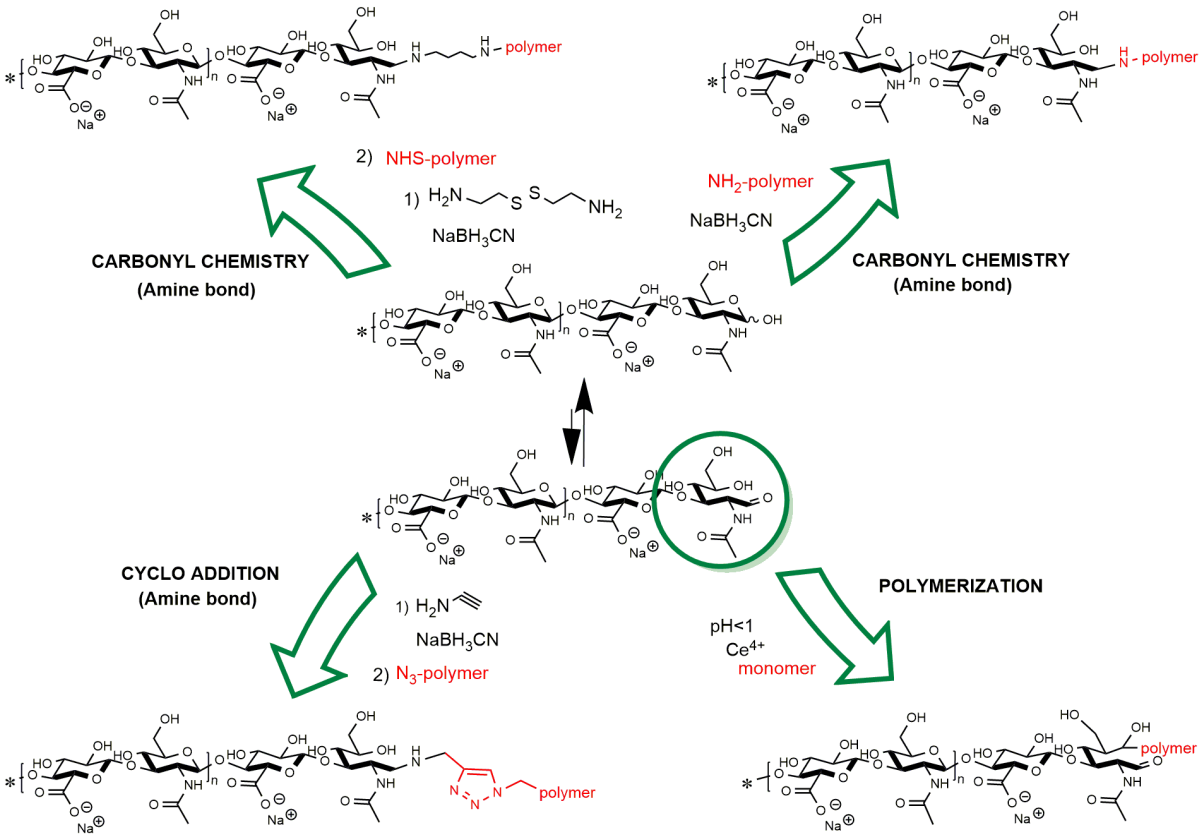

Figure 1.4 *Scheme of main HA conjugation mechanism at the reducing end.*

Table 1.1 summarizes the different synthetic hydrophobic polymers used as the hydrophobic block: poly(ε-caprolactone) (PCL), poly(pyridyl disulphide methacrylate (PDSMA), poly (D,L-lactide-co-glycolide) (PLGA) and poly(*n*-butyl cyanoacrylate) (PBCA). After the coupling reactions, micelles were formulated through, emulsion, dialysis, or nanoprecipitation.

Table 1.1 *HA-b-polymers used for the formation of micelles. Hydrophobic polymer core.*

HA kg/mol	Function at HA extremity	Hydrophobic block structure		Size (nm)	DL (EE) %	Application	Ref
12	Alkyne from propargyl amine	(N_3-) PCL	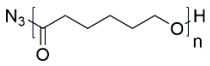	198	9	*In vitro:* Cytotoxicity and intracellular drug release (doxorubicin (DOX)) *In vivo* S-CC7 tumor: biodistribution and antitumor efficacy (DOX)	[72]
7,4	Alkyne from propargyl amine	(N_3-) PDSMA	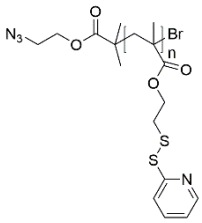	148 - 215	9 (87)	*In vitro:* drug release (DOX) *In vivo* S-CC7 tumor: biodistribution, pharmacokinetics, tumor accumulation profiles and antitumor efficacy (DOX)	[73]
5.7	Amine from cystamine grafted on HA	NHS-PLGA	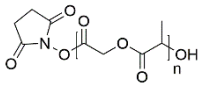	250	8	*In vitro:* hemolytic cytotoxicity *In vivo* Ehrlich ascites tumor: Biodistribution and Antitumor efficacy (DOX)	[74]
5.6, 7.3 and 8.9	Aldehyde	(NHS-) PLGA	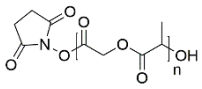	111-192	3	*In vitro*: cellular uptake and cytotoxicity *In vivo MCF-7 and MDA-MB-231 tumors*: tumor targeting and antitumor effect (docetaxel (DTX))	[75]
18,100, 50 and 1000	Hydroxymethyl group	PBCA	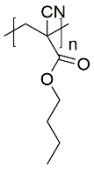	291 - 1000	(90)	*In vitro*: cellular uptake and cytotoxicity *In vivo S-180 tumor:* Antitumor effect (Paclitaxel (PTX))	[76]
10				134 - 170	7	*In vitro*: cellular uptake and cytotoxicity *In vivo S-180 tumor:* Antitumor effect (Morin hydrate and Vitamin E (TPGS))	[77]

He et al. reported micelles with sizes ranging from 291 nm to 1010 nm depending on the molar mass of HA used for the synthesis of the block copolymers (18, 100, 500, 10000 kg/mol) [76]. Thus, small molar masses around 10 kg/mol were preferred for the elaboration of micelles with a size ≤ 200 nm. Furthermore, interesting behaviors were also noted concerning the encapsulation. Abbad et al. found that the combination of the hydrophobic polymer chain with a molecule with a bulky shape and aromatic ring such as vitamin E derivatives (D-alpha-tocopheryl Polyethylene glycol succinate, TPGS) improved the properties of micelles, resulting in a drug loading (DL) increase (from 4,7 % to 7,5 %) and a slightly smaller size (from 170 to 135 nm) [77]. This was explained by the fact that TPGS possesses a bulky shape and has a large surface area which makes it a good emulsifier for hydrophobic drugs, including morin hydrate (MH). Moreover, the aromatic ring of TPGS may cause stronger hydrophobic interactions between drugs and polymers. Concerning *in vivo* antitumor effect, better results were also obtained due to the synergistic effect of the combination of TPGS with MH. Generally, all of the micelles were found to be more potent in suppressing tumor growth after intravenous administration to tumor-bearing mice than free drug injection.

Although physically crosslinked nanoparticles offer several advantages, it is well known that they usually suffer from lack of long-term stability when circulating in the bloodstream. To improve colloidal stability of micelles, Han et al. compared two different reversible crosslinking strategies (shell [72] or core [73]) using the same crosslinker precursor (pyridyldisulphide, PDS), resulting in disulfide crosslinks. These crosslinks are cleavable by cytosolic reductants (glutathione, GSH) in cancer cells. To do so, they synthesized via click chemistry (Huisgen 1,3-dipolar cycloaddition) core-crosslinked micelles (CC-HAM) based on HA-b-PDSMA (poly(pyridyl disulfide methacrylate)) (Figure 1.5-A) and shell-crosslinked micelles (HA-ss-NPs) based on HA-b-PCL (poly(caprolactone)) (Figure 1.5-B). A drug model, the anti-cancer drug doxorubicin (DOX) was encapsulated and micelles with a size around 200 nm were obtained for both systems. Interestingly, these two micelles exhibited different release profiles of drug and biodistributions in SCC7 tumor-bearing mice. The release of DOX for core-crosslinked micelles was more efficient (reaching 100% versus 80%) in the presence of GSH, while it was the same for both systems in the absence of GSH (around 30%). Regarding the biodistribution profiles,the tumor/liver ratio indicated a higher accumulation of HA-ss-NPs in the tumor (tumor/liver ratio > 1) than CC-HAM (tumor/liver ratio < 1). Then, comparison with un-crosslinked micelles showed that the crosslinked micelles exhibited higher structural stability in the presence of serum, sodium dodecyl sulfate or in the blood stream. On the other hand, the tumor/liver ratio between un-crosslinked and crosslinked micelles for each system showed a significant increase (+ 30% and tumor/liver ratio ~ 3) of nanogels accumulation for shell-crosslinked nanogels (HA-ss-NPs).

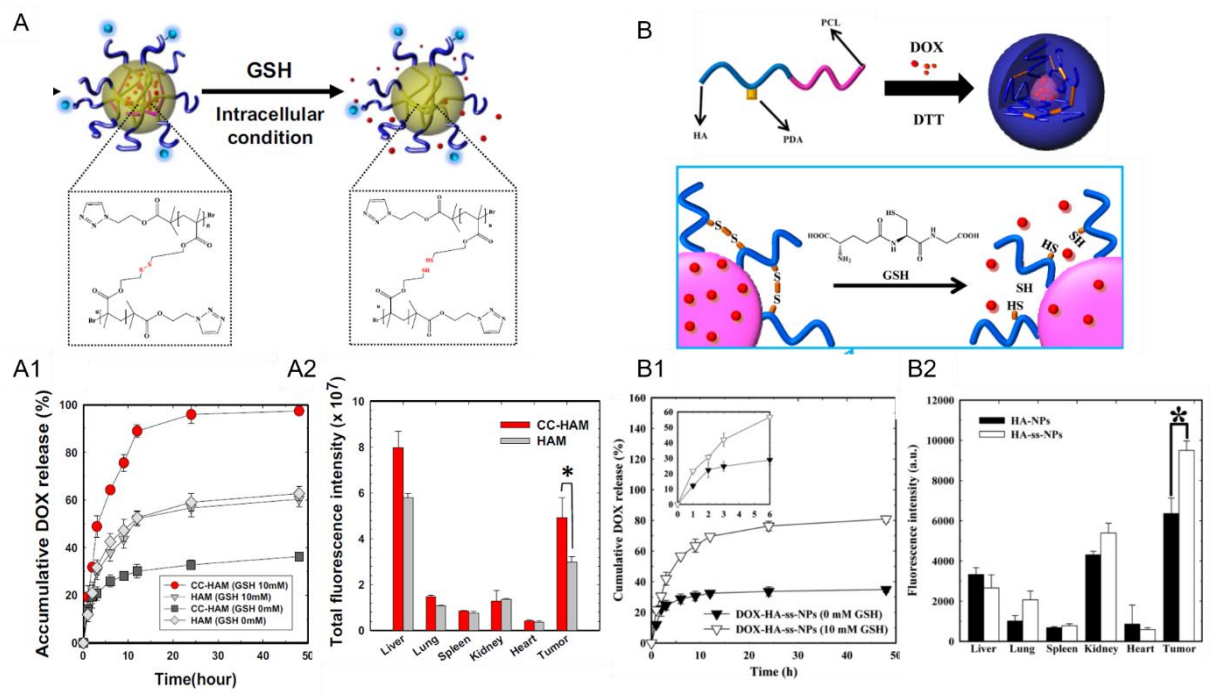

Figure 1.5 *A) Synthetic scheme of core crosslinked HA-b-poly(PDSMA) (CC-HAM) micelles loaded with DOX. A1) Release profiles of DOX from CC-HAMs and HAM in the absence or the presence of GSH. The error bars in the graph represent standard deviations (n=5). A2) Fluorescence intensities of tumors and organs. Asterisks (*) denote statistically significant differences (*p<0,05) calculated by one-way ANOVA test. B) Synthetic scheme of the formation of DOX-loaded crosslinked micelles and their GSH responsive drug release behaviour B1) In vitro release behaviour of DOX from DOX-HA-ss-NPs in the absence or the presence of GSH. The error bars in the graph represent standard deviations (n=3). B2) Quantification of the ex-vivo tumor-targeting characteristics of HA micelles in tumor bearing mice. Error bars in the graph represent the standard deviation for five animals per group. [72-73]*

IV.1.2 Polymersomes

Polymersomes formed from copolymers based on HA have been reported by few team. Such systems were obtained by coupling HA with degradable hydrophobic polymers such as poly(γ-benzyl-L-glutamate) (PBLG) [78-81] and poly(ε-caprolactone) (PCL) [82] (Table 1.2). The synthesis of the HA-block-polymer was carried out using the copper catalysed Huisgen 1,3-dipolar cycloaddition of azide-terminated polymer and alkyne-functionalized HA (as already seen for micelles synthesis in Figure 1.4). The drug was loaded during the formation of polymersomes by the solvent nanoprecipitation method.

Table 1.2 *HA-based polymersomes.*

HA kg/mol	Drug	Hydrophobic block Structure		Size (nm)	DL (EE) %	Application	Ref
5	DOX	PBLG	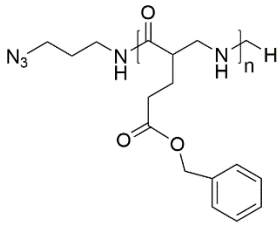	30 and 300	-	*In vitro* and *in vivo* lung tumor cells targeting	[78]
				400	-	*In vivo* antitumor activity in EAT tumor cels	[79]
				440	12 (50)	*In vivo* antitumor efficacy in MCF-7 and U87 cells	[80]
	DOC			260	-	*In vitro* toxicity and release behaviour *In vivo* biodistribution in MCF-7 and U87 cells	[81]
5 - 2100	Hydrophilic antimicrobials and hydrophobic dye Nile red	PCL	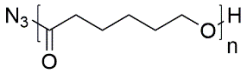	200 - 300	-	Detection of Enzymes of pathogenic bacteria "*Staphylococcus aureus*"	[82]

Lecommandoux et al. described polymersomes based on HA-b-PBLG (Mw_{HA} = 5 kg/mol) with a size around 300-400 nm to convey different chemotherapeutics payloads such as DOX [79-80] and docetaxel (DOC) [81], with a high drug loading capacity (loading capacity of 10 % and encapsulation efficiency of about 50%). These polymersomes accumulated at the tumor site in addition to liver, lungs and spleen. DOC-and DOX-loaded HA-b-$PBLG_{60}$ uptake in tumor was larger at each time (1, 4 and 24h) compared to a solution of free drugs. Lastly, by varying the hydrophilic/hydrophobic balance of the copolymer and the conditions of nanoparticles formation, it was possible to obtain particles with a smaller size of 30 nm [78]. The authors observed that size plays a role in cellular uptake *in vitro*. NPs of 30 nm were bound and internalized by non-small cell lung cancers (NSCLC) cells more efficiently (2-3 times higher) than NPs of 300 nm. However, *in vivo* studies could not confirm these results. After intravenous administration, both systems have the same ability to reach the tumor sites (H322, H358 NSCLC cell lines) except for A549 tumor with a slight preferential uptake of NP 30 nm, but mostly were rapidly taken by the liver after administration.

In contrast, Hass et al. [82] developed polymersomes based on hyaluronic acid and polycaprolactone to encapsulate a dye molecule inside the aqueous core in addition to a hydrophobic dye in the shell. These HA-b-PCL copolymers were assembled using the solvent-shift method with chloroform and water, which yielded assemblies in a size range of 50−400 nm. The authors demonstrated that the size distributions and the hydrodynamic diameter varied considerably depending on the cargo molecule without following a clear trend.

Thus, the capacity to encapsulate either hydrophobic or hydrophilic drugs has been proved. However, the main advantage of this architecture in comparison to micelles to deliver both hydrophilic (in their core) and hydrophobic (inside the bilayer) therapeutics molecules to enhance the therapeutic effect was not shown.

IV.1.3 Nanogels

In contrast to the previous nanocarriers, nanogels are based on grafting hydrophobic molecules along the HA skeleton through its reactive carboxylic acid and hydroxyl groups. When carboxylate or hydroxyl groups are modified, multiple attachments occur and the hydrophobic groups are randomly linked to the polysaccharide chain. Different hydrophobic molecules can be grafted on a HA chain, from very simple HA-drug covalently linked conjugates to complex particulate formulations HA-polymer conjugates based nanogels. These particles have been used to deliver small molecule drugs or proreins that are chemically of physically bound to HA.

IV.1.3.1 HA-drug conjugates

It is believed that polymer-drug conjugates can significantly increase drug loading content compared to traditional polymer carriers in which the drug is physical entrapped, as well as prevent burst release.

Conjugation of drugs to HA was reported as early as 1996 [83]. This approach aimed to convert the drug to an inactive prodrug derivative through a bond that ideally should be sufficiently stable during the blood circulation to increase the prodrug *in vivo*-life and be promptly cleaved at a specific target site. This cleavage should occur without altering the chemical structure of drug, allowing to release it in its active form (Ringsdorf model [84]).

The difference of physiological microenvironment between tumor and normal tissues can be advantageously used to regulate the release of anticancer drugs. In contrast to normal tissues, the physiological features of tumor tissues include weak acidity, overexpressed proteins and enzymes, abnormal temperature gradients. Moreover, the endosomes and lysosomes of tumor tissues are in a reductive state due to the high level of GSH or cysteine. This explains why disulfide bonds have been used extensively for the design of nanocarriers [85].

Based on this finding, in addition to usual amide and ester bonds, different stimuli-labile linkers have been exploited to develop hyaluronic acid nanogels that are sensitive to redox potential, pH, and enzymes, to control drug release at the target site. Thus, HA-drug conjugated can be classified through the kind of stimuli-labile linker. The most common drug model involved in HA-drug conjugates are doxorubicin and paclitaxel (PTX). These anti-cancer agents are among the most effective chemotherapeutics, inducing death of cancer cells in a wide variety of tumors.

The HA (200 kg/mol)-PTX prodrug synthesized via the formation of an ester bond between HA and PTX (renamed as ONCOFID-P by the pharmaceutical company Fidia) achieved a high PTX loading of 20% (w/w) [86]. A significantly increased CD44 dependent cellular uptake of PTX in cancer cells *in vitro* and *in vivo* was observed and PTX was easily release [87]. The same conjugation strategy of ONCOGID-P was successfully applied to other antineoplastic agents, such as docetaxel, doxorubicin and the active metabolite of irinotecan (7-ethyl-10-hydroxycamptothecin). *In vitro* and *in vivo* phase I and II clinical studies were initiated in several CD44-overexpressing cancer cells [88]. In all these studies, these prodrugs reduced tumor cell growth and metastasis, although intravenous injection of ONCOFID-P was followed by a rapid and strong liver uptake (almost 80% of the injected dose) while 6% reached the tumor site [89]. However, no evidence of self-association into nanogel was provided. Actually, only few reports indicated that HA-PTX conjugates can self-assemble into nanoparticles in aqueous solution.

Table 1.3 gives the HA-drug conjugates which demonstrated self-assembly properties by dynamic light scattering and transmission or scanning electron microscopy analyses.

Recently, Xu et al., proved the possibility to form well-defined nanogels based on HA-PTX prodrug [90]. PTX was linked to HA *via* the coupling of two intermediates HA-adipic dihydrazide (HA-ADH) and PTX-hydroxysuccinimide (PTX-NHS) via a carbodiimide coupling between activated ester of PTX and the hydrazide group of HA. Nanogels were then prepared by dispersing HA-PTX prodrug into aqueous solutions followed by ultrasonication. The resulting NPs (size ~ 200 nm) were taken up well by cancer cells, thus enhancing PTX delivery. Importantly, cellular uptake and internalization pathway studies involving receptor inhibitors revealed that HA-PTX NPs obtained cytosolic delivery via by passing lysosomal-endosomal system. It was assumed that cellular entry occurred via direct penetration across the cell membrane. Moreover, HA-PTX nanogels had more than 4-fold decrease in tumor volume on day 14 in contrast to PTX alone, due to their significant accumulation in tumors.

Table 1.3 *Summary of HA-drug conjugates which demonstrated self-assembly properties.*

HA kg/mol	Drug	linkers	Size (nm)	Drug release	Application	Ref
150	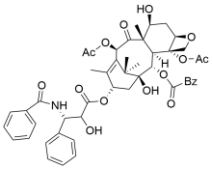 PTX	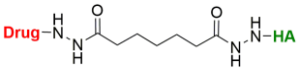 Hydrazone bond	200	-	*In vitro* cellular uptake and internalization pathway H22 cells *In vivo* H22 tumor bearing mice imaging and antitumor activity	[90]
10	PTX	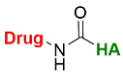 Amino-acid bond (peptide bond)	275 - 285	47-63% 50h	*In vitro* release, and cytotoxicity agents MCF-7	[91]
150	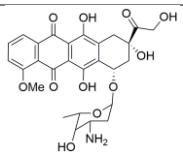	Amide bond	581	0% 72h	In vitro triggered drug and cellular uptake by Human breast cancer HCT116 cells, (MC-7)	[92]
		Hydrazone bond	160 0	31% 72h (pH = 5)		
130	DOX	Legumain-peptide-NH_2 (amino-acid bond)	398 - 474	-	*In vitro* triggered drug and cellular uptake A549, MCF-7, MCF-7/ADR *In vivo* legumain response in A549 cell and anti-tumor ability	[93]

Oommmen et al. [92] compared two HA-DOX prodrugs possessing, respectively, a stable amide linkage (HA-DOX) and a cleavable hydrazone bond (HA=DOX) between DOX and HA. Very large particles with a size of 581 and 1600 nm were obtained for HA-DOX and HA=DOX, respectively. However, HA=DOX with larger size showed better cytoxicity than HA-DOX having a smaller size. Since these particles were sequestered in endosome/lysosome, it was assumed that nanoparticle size was not the only factor governing cellular uptake and cytotoxicity of particles made of HA.

Lin et al. [93] drew the same conclusion looking at the size of a HA-DOX prodrug with a cleavable linker sensitive to the targeted tumor environment. Interestingly, they chose a legumain substrate peptide bridge sensitive to legumain (an asparaginyl endopeptidase) activity that is highly up-regulated in a number of solid tumors, to link HA to DOX. The synthesis was carried out using carbodiimide coupling. The resulting nanogels were further crosslinked in a water/oil solvent system to form large nanogels (~ 400 nm). Despite this size the developed nanogels were uptake in all cell lines (A549, MCF-7 and MCF-7/ADR).

Xin et al. proposed an alternative strategy in which amino acids (aa) were proposed as spacers between HA and PTX [91]. The carboxylic group of aa was first linked to the 2'-hydroxyl group of PTX, and then the amino group of the resulting conjugate to the carboxylic group of HA (Mw = 10 kg/mol). HA-aa-PTX prodrugs with a DL of 10-15% (w/w) spontaneously assembled into nanogels with a size of ~270 nm. Owing to better recognition by the esterase enzymes, the presence of an amino acid spacer resulted in an increase of both the hydrolysis rate and the release of PTX, compared to prodrugs formed by direct ester bond formation between HA and PTX and to the HA–ADH–PTX prodrug.

IV.1.3.2 HA-small hydrophobic molecules conjugates

Various small hydrophobic molecules including linear alkyl chains and cholesteryl derivatives have been conjugated to HA to yield nanoassemblies. More specifically, biologically active molecules such as glycyrrhetinic (hepatic targeting properties) [94-96] and tocopheryl (specific vitamin E with anticancer properties and nontoxic side effects on normal cells) [97] have also been used to prepare self-assembled systems based on HA.

IV.1.3.2.1 Alkylated HA derivatives

HA samples with different molar masses have been modified with short and long alkyl chains (number of carbon atom varying from 8 to 20). Table 1.4 summarizes the main characteristics of nanogels based on alkylated HA derivatives.

The conjugation was performed on the carboxylic acid or hydroxyl groups of HA and with various degrees of substitution. The most common alkylated HA conjugates are ester and amide derivatives. The main difference between these conjugates lies in the stability of covalent bond between HA and the alkyl chain, the ester bond being the easiest to cleave by cellular esterases.

Self-assemblies of the alkylated HA derivatives were prepared by a variety of techniques including ultrasound, dialysis and emulsification depending on the swelling property and solubilization of modified polysaccharide in water.

To further investigate the self-association behavior, the molar feed ratio and the molar mass of HA have been varied. The conclusion is that DS value of alkyl chain affected the diameter of nanogels. The size decrease as the DS increase probably due to the formation of dense hydrophobic inner cores of aggregates nanodomains. Conversely, when focusing on the molar mass of HA, higher sizes were obtained for the higher HA molar masses [98-99].

All self-assembled systems were effective delivery systems for active substances in both *in vitro* and *in vivo* settings. However, the nanogels showed a high distribution in the liver, spleen and lung, possibly owing to their cellular uptake by phagocytic cells of the RES and by liver sinusoidal endothelial cells expressing another HA receptor (hyaluronan receptor for endocytosis, HARE).

Thus, to improve the selective uptake at the tumor site, a dual receptor targeting was proposed by Liu et al. [100-101] with the conjugation of Folic Acid (FA) to HA-octadecylamine *via* an ester bond (FA-HA-octadecylamine). In vitro biological studies revealed enhanced internalization of nanogels in MCF-7 cells compared to HA-octadecylamine via folate-mediated endocytosis. Moreover, the dual targeting of micelles resulted in a better multidrug resistance (MDR)-overcoming performance, and higher PTX tumor accumulation, than HA-octadecylamine or Taxol in MCF-7 tumor-bearing mice. However, nanogels still accumulated substantially in the liver.

Concerning *in vivo* behavior another observation was made by Velebny et al. While the molar mass of HA did not influence the overall performance of nanogels in cellular transport studies, the alkyl chain length and the nature of encapsulated compound affected both the loading capacity and stability of the nanogels [103]. Indeed, alkyl chains can interact with serum albumin in the blood stream which can not only bind to the polymeric drug-delivery systems but also alter their stability and cause release of the payload. Albumin forms part of the most potent binding partners for drugs and drug carriers in blood as immunoglobulins, fibrinogen, apolipoproteins [110-111]. Thus, to further stabilize nanogels based on alkylated HA, Zhong et al. reported on amphiphilic redox-responsive and reversibly crosslinked HA nanogels based on HA-Lys-lipoic acid (LA) [107]. LA is a natural antioxidant containing a disulfure bond. So, the shell of nanogels could be readily crosslinked through disulfide bridges (HA X-NPs) using catalytic amount of a reducing agent (dithiothreitol, DTT) (Figure 1.6). The *in vivo* pharmacokinetics and biodistribution studies in MCF-7/ADR tumor-bearing mice showed that DOX-loaded HA X-NPs exhibited prolonged circulation time and a high accumulation in the tumor (12.71% of injected dose per gram of tissue (ID/g)). DOX-loaded HA X-NPs revealed inhibited DOX release under physiological conditions and fast drug release (89% in 22h) in the presence of GSH (10mM). After reaching the tumor environment, they led to inhibition of tumor growth.

This approach was also considered by Yin et al. [109] to co-deliver a hydrophobic drug (PTX) and hydrophilic gene (aurora kinase A SiRNA, AURKA) for breast cancer treatment. To do so, they designed a redox-responsive and cationic nanogel, HA-ss-(OA-g-bPEI) known as HSOP. In this system, octane dioic acid (OA), the hydrophobic group and branched

polyethyleneimine (bPEI), the hydrophilic cationic group, were linked to HA through cystamine (containing a disulfide bond). The *in vivo* and *in vitro* antitumor efficacy of HSOP in mice was compared to that of single-drug-loaded micelles and non-responsive nanogels (HOP). Due to the synergistic inhibition and the efficient drug release in response to cytoplasmic reducing environment, HSOP nanogels were found to possess the highest antitumor efficacy *in vivo*. The biodistribution profile showed that 2 h after intravenous administration, redox-responsive nanogels (HSOP) and non-responsive nanogels (HOP) accumulated in both liver and tumor, whereas after 24h preferential tumor accumulation was observed.

Finally, Uthaman et al. [102] proposed an alternative to chemotherapy by encapsulating in HA-octadecylamine a photosensitizer (IR 780) which absorbs in the NIR region (HA-IR 780), for photothermal therapy (PTT). The synthesized HA-IR 780 nanogels ($d_{average}$< 200 nm) are non-toxic to tumor cells but promote significant toxicity upon laser irradiation. PTT uses photosensitizers to generate heat upon laser irradiation, leading to cellular necrosis and apoptosis in the tumor (temperature> 49.9°C). Toxicity studies showed that HA-IR 780 does not cause any adverse effects in organs, including heart, liver, lungs, kidney and spleen, although it selectively caused cell damage in the tumor region upon laser irradiation.

Table 1.4 *Alkylated HA conjugates forming nanogels.*

System	Mn HA (kg/mol)	Size (nm)	Drug(s)	Method	DL (EE)%	Tumor model	ref
HA-tetradecylamine	300	200-300	-	sonication	-	_	[98]
HA-decylamine	10, 25	170-300	Budesonide (BDS)	sonication	(18-57)	Caco-2	[99]
FA-HA-octadecylamine	11	176-455	PTX	ultrasonication	18 (77-97)	MCF-7, A549	[100] [101]
HA-octadecylamine	480	150-500	IR780	Dialysis	10	TC-1	[102]
HA-OA (C18)	15	66	PTX	Solvent evaporation	14 (70)	-	[103]
HA-CA (C6)	15	57	PTX	Solvent evaporation	2.2 (44)	-	[103]
HA-OSA	850	400	TA	-	-	-	[105]
HA-SA-CYS-OA	44	290	DTX	Emulsification by sonication	3,56 (75)	MCF-7, A549	[106]
HA-Lys-LA	35	152-237	DOX	Solvent exchange method (dialysis)	15	MCF-7/ADR	[107]
HA-FAs-PEI	20	100-300	SiRNA	sonication	-	A549, B16F10, Hep3B, MDA-MB468	[108]
HA-ss-(OA-g-bPEI)	20	135-220	PTX, AURKA SiRNA	dialysis	13 (PTX)	MDA-MB-231	[109}

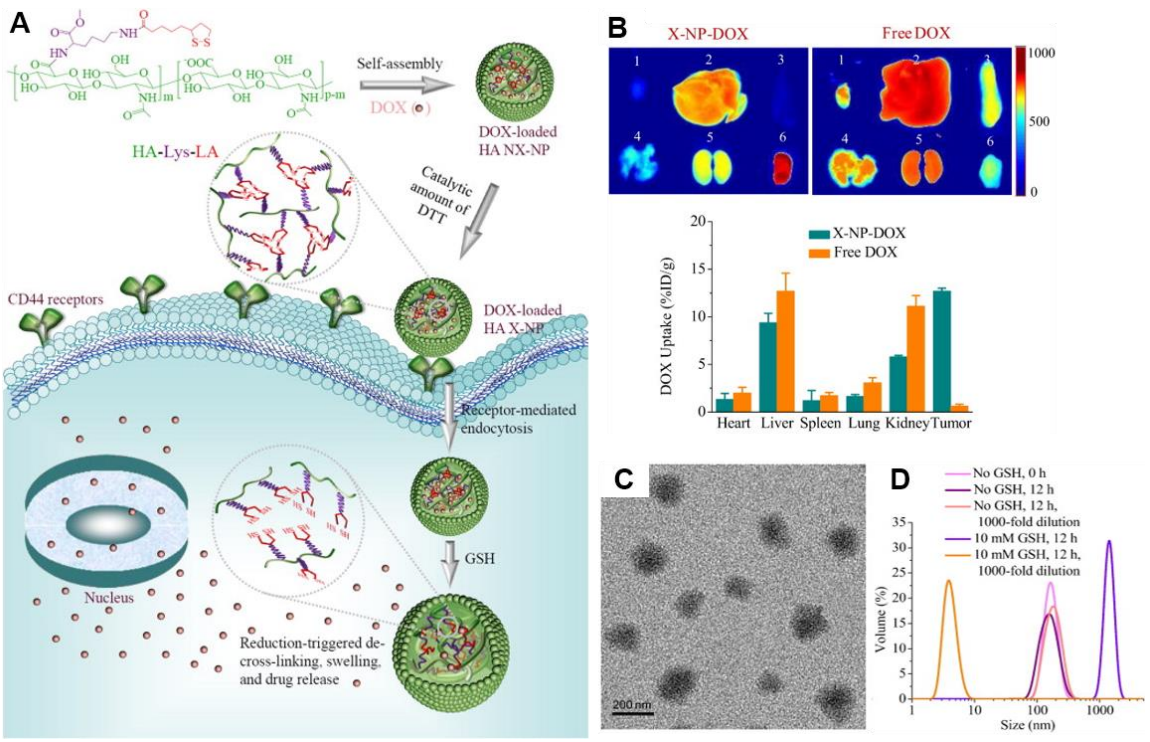

Figure 1.6 *A) Illustration of disulfide-crosslinked HA X-NPs based on HA-Lys-LA conjugates for active CD44-targeting DOX delivery. B) In vivo biodistribution of X-NP-DOX and free DOX in MCF-7/ADR human breast bearing nude mice at 10h post intravenous injection (fluorescence images and quantification of DOX accumulated in different organs and tumors) C) TEM images of HA-Lys-LA X-NPs. D)Change of size distribution in response to 10 mM GSH in PBS [107].*

IV.1.3.2.2 HA-cholesterol conjugates

Cholesterol (CHOL) is a vital component of cell membranes accounting for over 20% of the plasma membrane lipids. Due to their biocompatibility and hydrophobicity, cholesterol derivatives or analogues are often used to design drug delivery nanoparticles. In particular, bile acids which are steroid monocarboxylic acids related to cholesterol are by far the most extensively studied ones. These include 5β-cholanic acid (5β-CHOL) [112-121] and deoxycholic acid (DOCA) [122-124]. Cholesterol and their analogues are distinguished from previous lipid group by their unique structure consisting of several linked hydrocarbon rings forming a bulky steroid structure, which can play a critical role in the encapsulation.

Figure1.7 illustrates several HA derivatives modified with cholesteryl moieties. After sonication in water, HA-5β-Cholanic acid conjugates led to the formation of spherical particles of which the size decreased as the DS increased [112]. Studies by confocal microscopy of the HA-NPs fluorescently labeled with the near-infrared (NIR) dye, cyanine 5.5, incubated with cancer cells (SCC7) over-expressing CD44 demonstrated cellular uptake when were

incubated with cancer cells. When the SCC7 cells were pre-treated with a high dose of free-HA to block CD44 prior to Cy5.5-labeled HA-NPs treatment, cellular uptake of HA-NPs was found to be inhibited. Following systemic administration of Cy5.5-labeled HA-NPs into a tumor-bearing mouse, their biodistribution was monitored as a function of time. Irrespective of the particle size, significant amounts of HA-NPs circulated for two days in the bloodstream and were selectively accumulated into the tumor site. The smaller HA-NPs were able to reach the tumor site more effectively than larger HA-NPs. Interestingly, the concentration of HA-NPs in the tumor site was dramatically reduced when mice were pre-treated with an excess of free-HA. This study thus showed that HA-NPs were effectively accumulated into the tumor site by a combination of passive and active targeting mechanisms. However, a significant portion of HA-NPs was also found in the liver site, possibly owing to their cellular uptake by phagocytic cells of the reticuloendothelial system and by liver sinusoidal endothelial cells expressing another HA receptor (HARE). Therefore, pegylation of HA-NPs was performed by varying the DS of poly(ethylene glycol) (PE in order to control their surface property.) [115-116]. When the PEGylated HA-nanogels (238 nm) were systemically administered into tumor-bearing mice for *in vivo* real-time imaging, they were more effectively accumulated into the tumor tissue, up to 1.6-fold higher than bare HA-nanogels.

In addition to PEGylation, Hans et al. [117] proposed to reinforce the shell of nanoparticles through controlled deposition of inorganic calcium and phosphate ions on the shell *via* a sequential addition method. The resulting mineralized nanoparticles (M-PEG-HA-NPs) had a smaller size (153.7 ± 4.5 nm) than bare PEG-HA-NPs (265.1 ± 9.5nm), implying that mineralization allows the formation of compact nanoparticles. Interestingly, when the mineralized nanoparticles were exposed to acidic buffer conditions (< pH 6.5), their sizes increased rapidly due to dissolution of the inorganic minerals and faster drug (DOX) release was observed. In vivo biodistribution study shows that M-PEG-HA-NPs could reach the tumor site and more effectively than bare PEG-HA-NPs.

In another way, Yoon et al. [120] developed photo-crosslinked HA nanoparticles (c-HA-NPs) to enhance their *in vivo* colloidal stability and reduce unintended burst release of the loaded drug. Nanogels were stabilized by UV-triggered chemical crosslinking of acrylate groups (APMA) grafted on the HA backbone (PEG-HA-CHOL-APMA, Figure 1.7). PTX-c-HA-NPs (230 nm) showed improved stability, which enhanced their *in vivo* tumor-targeted ability. Coupled to a sustained released of drug, the therapeutic efficacy of PTX-loaded c-HA-NPs was better than those of free PTX and un-crosslinked HA-NPs.

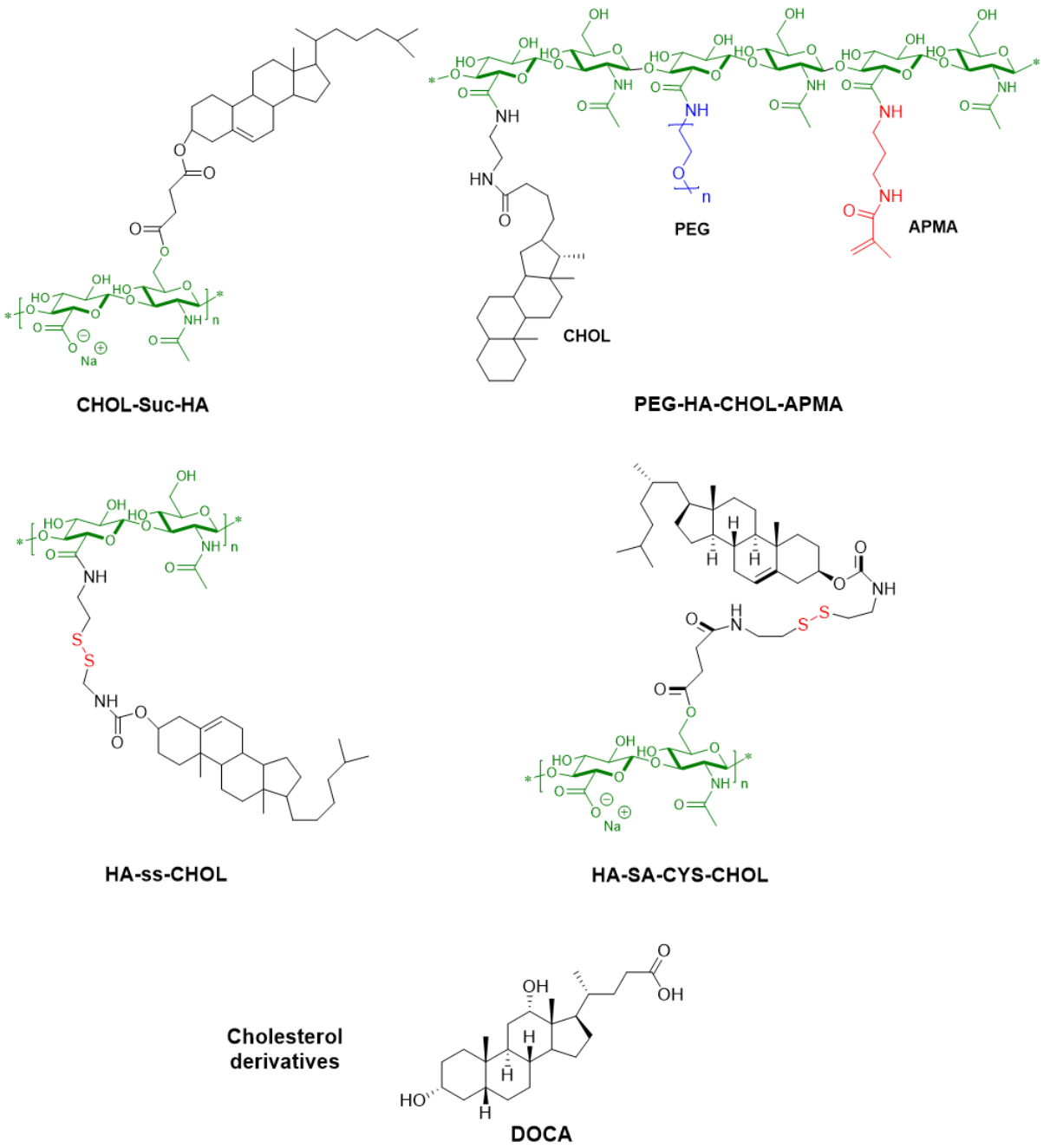

Figure 1.7 *HA derivatives modified by cholesteryl derivatives.*

Sustained release of drug at the target site could also be carried out using a cleavable linker between HA and the cholesterol moiety. Hu et al. [118] designed redox-responsive NPs for the triggered intracellular delivery of DOX for breast cancer. The redox-responsive NPs were based on hyaluronic acid grafted with cholesteryl moiety (HA-ss-Chol) using cystamine as cleavable disulfide linkage. A peptide targeting EGFR (Epidermal growth factor receptor) was further surface-conjugated to HA-ss-Chol (GE11–HA-ss-Chol) to achieve dual active targeting. A novel small peptide GE11 (sequence YHWYGYTPQNVI) was shown to have high affinity toward EGFR-overexpressed cancer cells. In addition, this resulting system exhibited

good properties such as small size (~146 nm) and a high PTX drug loading and encapsulation efficiency of 33% and 91%, respectively.

To highlight the role of the hydrophobic moiety introduced on HA, Zhu et al. [119] compared the effect of modification of HA with a fatty acid (octadecanoic acid, OA) and cholesterol on the properties of nanogels. The latter were obtained from HA-SA-CYS-OA and HA-SA-CYS-CHOL in which cystamine (CYS) is a redox cleavable linkage (Figure 1.8). The authors concluded that: i) the hydrophobic groups affect the distribution, metabolism, excretion and antitumor efficacy of nanogels. ii) the HA-SA-CYS-CHOL-based nanogels exhibit better tumor targeting properties and efficient antitumor effect at very low concentration and with extremely low systemic toxicity compared to HA-SA-CYS-OA. iii) regarding drug encapsulation, it is important to consider the interactions between the hydrophobic group and the drug loaded to select the most appropriate hydrophobic moiety.

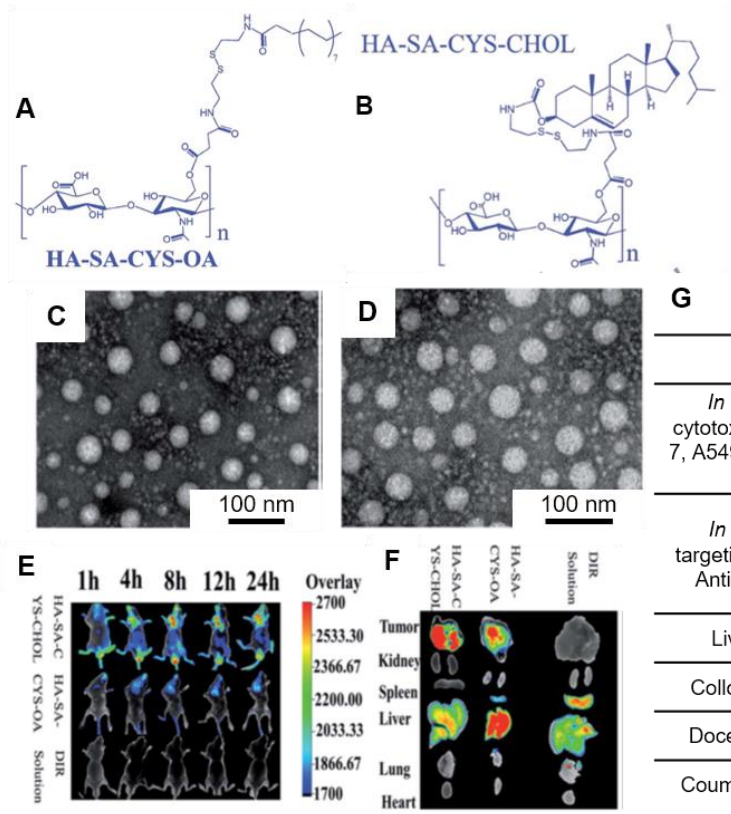

G	HA-SA CYS-OA	HA-SA-CYS-CHOL
Size	+	
In vitro tumor cytotoxicity for MCF-7, A549, S-180 tumor cells	+	
In vivo tumor targeting efficiency / Antitumor effect		+
Liver uptake	+	
Colloidal stability		+
Docetaxel EE/DL		+
Coumarin-6 EE/DL	+	

Figure 1.8 *Synthesis scheme HA-SA-CYS-CHOL (A), HA-SA-CYS-OA (B). Transmission electron micrographs of DTX-loaded HA-SA-CYS-OA (C) and HA-SA-CYS-CHOL (D). In vivo disposition of DIR solution and HA-SA-CYS-CHOL, HA-SA-CYS-OA nanogels at different study intervals (E). Ex vivo fluorescence images of tissue samples collected 24h post-injection (F). Comparison table between HA-SA-CYS-OA and HA-SA-CYS-CHOL nanogels, the cross indicates the higher result, red cross for disadvantageous result and green cross for advantageous one (G). Adapted from Zhu et al. 2017 [119]*

IV.1.3.3 HA-polymer conjugates

Two main strategies have been investigated to design GAG-polymer conjugates: the “grafting from” process and the “grafting onto” process.

The “grafting from” process relies on polymerization methods such as the ring-opening polymerization (ROP), controlled radical polymerization (CRP), or oxidative polymerization [125]. Pendant hydroxyl groups in GAGs are generally used as initiating species for the ROP of cyclic monomers.

The “grafting onto” technique, requires the pre-synthesis of end-functionalized polymer that are subsequently covalently bonded to the polysaccharides. Although this latter strategy usually suffers from low grafting density (due to steric hindrance) and tedious polymerization procedures [126], it is the most used to graft polymers on HA due in particular to the fact that it is possible to perform the reaction in water. HA has been modified *via* either its carboxylic acid or hydroxyl groups. The carboxylic groups are mainly involved in amide-acid coupling and esterification reactions, while the hydroxyl groups are commonly converted into ester or ether derivatives [127]. As can be seen on Figure 1.9, the main strategy is based on amide bond formation using carbodiimide-mediated coupling reactions. Various amine-functionalized polymers have been grafted onto HA through the carboxylic acid group. However, most of the carbodiimides-mediated coupling reactions have been carried out in organic solvent (dimethylsulfoxyde, DMSO). Moreover, when the carboxylate group is selected, it has been found that a degree of substitution (DS, average number of substituting groups per repeating disaccharide unit) above 0.25 decreases the ability of HA to target CD44 receptors [128].

The hydrophobic core is usually derived from the following biodegradable polymers: poly($_{D,L}$-lactide-co-glycolide) (PLGA), poly(lactide) (PLA) and poly-ε-caprolactone (PCL) [129].

In order to prevent recognition by the reticuloendothelial system (RES), PEG chains were introduced to most of these nanogels. The behaviour of nanogels based on polymers above-mentioned (HA-PLGA [131-132], HA-PLA [130],HA-PCL [125]) were compared to their PEG-derivatives (HA-PEG-PLGA [133-135], HA-PEG-PLA [130], HA-PEG-PCL [125]) and each time, the latter exhibited greater stability (prolonged residence in the body) and had a higher drug loading capacity (from DL<10% to DL>80%). Moreover, cytotoxicity tests revealed that the presence of PEG on the carrier’s surface did not interfere with CD44 receptor recognition. However, despite a quite significant concentration of nanogels in tumor tissues, biodistribution studies showed high liver uptake. Although PEG is useful, it presents some drawbacks [137]. The main disadvantage of PEG is its non-biodegradability, resulting in long-term bioaccumulation, especially for pharmaceuticals used at high doses. Moreover, it is

known that immunological reactions can occur with PEGylated liposomes [138]. Therefore, some other hydrophilic polymers have been experimentally employed as an alternative to PEG such as: poly(N-vinyl-2-pyrrolidone) (PVP), poly(vinyl alcohol) or Poly(2-ethyl-2-oxazoline) [139].

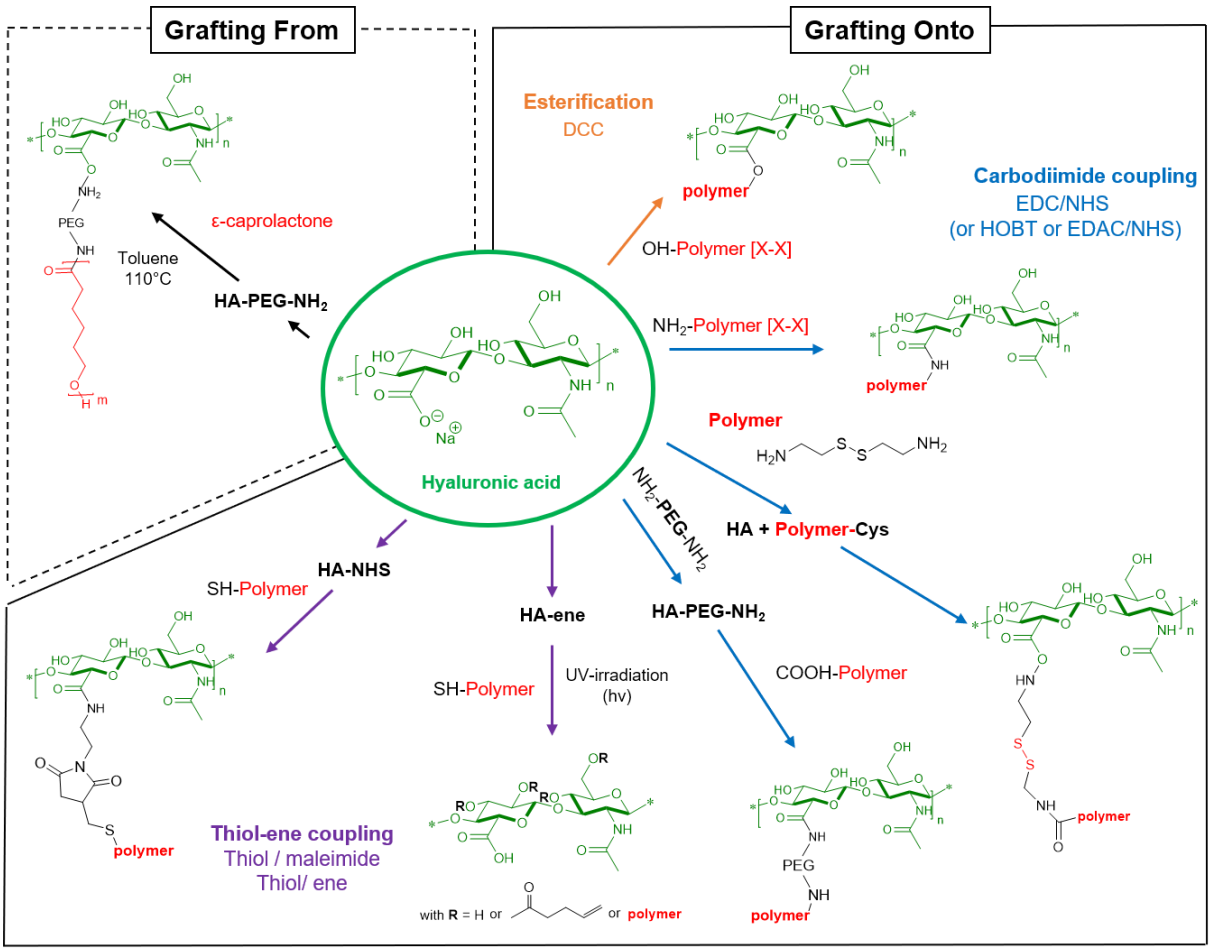

Figure 1.9 *Strategies based on "Grafting from" and "grafting onto" approaches to prepare HA-polymer conjugates.*

As discussed above for nanogels based on alkylated-HA, it is also possible to incorporate redox cleavable bonds to trigger drug release. Hu et al. used this approach to synthesis hyaluronic acid-cystamine polylactic-co-glycolic acid (HA-SS-PLGA), composed of a hydrophobic PLGA chain and a hydrophilic HA chain linked by a bioreducible disulfide bond. With a double emulsion method, a nano delivery system was constructed to deliver doxorubicin (DOX) and cyclopamine (CYC, a primary inhibitor of the hedgehog signaling pathway of Cancer stem cells (CSCs)) to both a CD44-overexpressing breast CSC subpopulation and bulk breast cancer cells and allow an on-demand release [136].

As observe earlier for HA-fatty acid conjugates based nanogels, Wang et al. [131] designed HA-grafted-polyethylenimine-poly(d,l-lactide-co-glycolide) (PEI-PLGA) nanogels

system to target co-delivery of doxorubicin (DOX) and miR-542-3 p for triple negative breast cancer (TNBC) therapy. This association showed again a suitable average size at 131.7 nm and high drug encapsulation efficiency, while prevented miR-542-3p degradation in the serum. HA-PEI-PLGA nanoparticles increased both drug uptake and cytotoxicity in MDA-MB-231 cells compared to MCF-7 cells, which express lower CD44 levels.

In addition to stimuli-labile linkage, the use of a stimuli responsive polymer is attractive for drug delivery due to their ability to change the physical and/or chemical properties of nanogels in response to an external stimulus such as pH, light, temperature.

Table 1.5 *HA-polymer conjugates forming nanogels.*

System	Mn HA (kg/mol)	Size (nm)	Drug(s)	DL (EE)%	Tumor model	ref
HA-PEG-PCL	6	115-196	DOX	(>85)	EAT	[125]
HA-PLA	-	30	DOX	5 (10)	HTC-116	[130]
HA-PLGA-PEI	-	120-195	DOX, miRNAs	Dox: 8 (76) miRNAs: 13 (88)	MCF-7, MDA-MB-231	[131]
HA-PLGA	8.3	49-102	DOX	5-11	HEPG2	[132]
HA-PEG-PLGA	17-64	98	DOX	7.2 (31)	HTC-116	[133]
HA-PEG-PLGA	5.7	100<x<200	DOX	(>88)	EAT	[134]
HA-PEG-PLGA	5.7		5fluoroucacil	(80)	EAT	[135]
HA-PEG-PLA	_	37	DOX	10 (20)	HTC-116	[130]
HA-ss-PLGA	6.4	245	DOX, CYC	Dox:(70) CYC: (58)	MDA-MB-231	[136]

IV.1.3.3.1 pH-Responsive HA-polymer conjugates

It is well known that the physiological pH in cancer cell is lower than that in blood and normal tissues. The pH is about 6.0 and 5.0 in intracellular early lysosomes and late lysosomes respectively [140]. Hence, the acid-triggered rapid release of drugs can be achieved inside tumor cells by using nanogels bearing pH-responsive polymer such as poly(L-histidine) (Phis). In addition to its biocompatibility and biodegradability, poly(L-histidine) shows a natural amphoteric property (deprotonation-protonation (pK_a = 6.5) of its imidazole ring).

Qui et al. demonstrated the possibility to prepare self-assembled nanogels based on HA-PHis (HPHM) and to induce pH-responsive intracellular drug delivery (Figure 1.10-A-B) [141]. They further exploited the potential of this system to overcome multidrug resistance (MDR). To do so, DOX-loaded HPHM nanogels and D-α-tocopheryl poly(ethylene glycol) 2000 (TPGS2k) was combined to co-deliver DOX and TPGS2k into drug-resistant breast cancer

MCF-7 cells (MCF-7/ADR) (Figure 1.10-A1-A2 to -G) [142]. Tocopheryl has been demonstrated to inhibit the efflux pumps (P-gp) leading to the restored sensitivity to anticancer drug [143]. As compared to HPHM, the HPHM/TPGS2k nanogels (size of ~ 100 nm, high DOX loading content of 10% and EE of ~92%), showed higher and comparable cytotoxicity against MCF-7/ADR cells and MCF-7 cells, respectively.

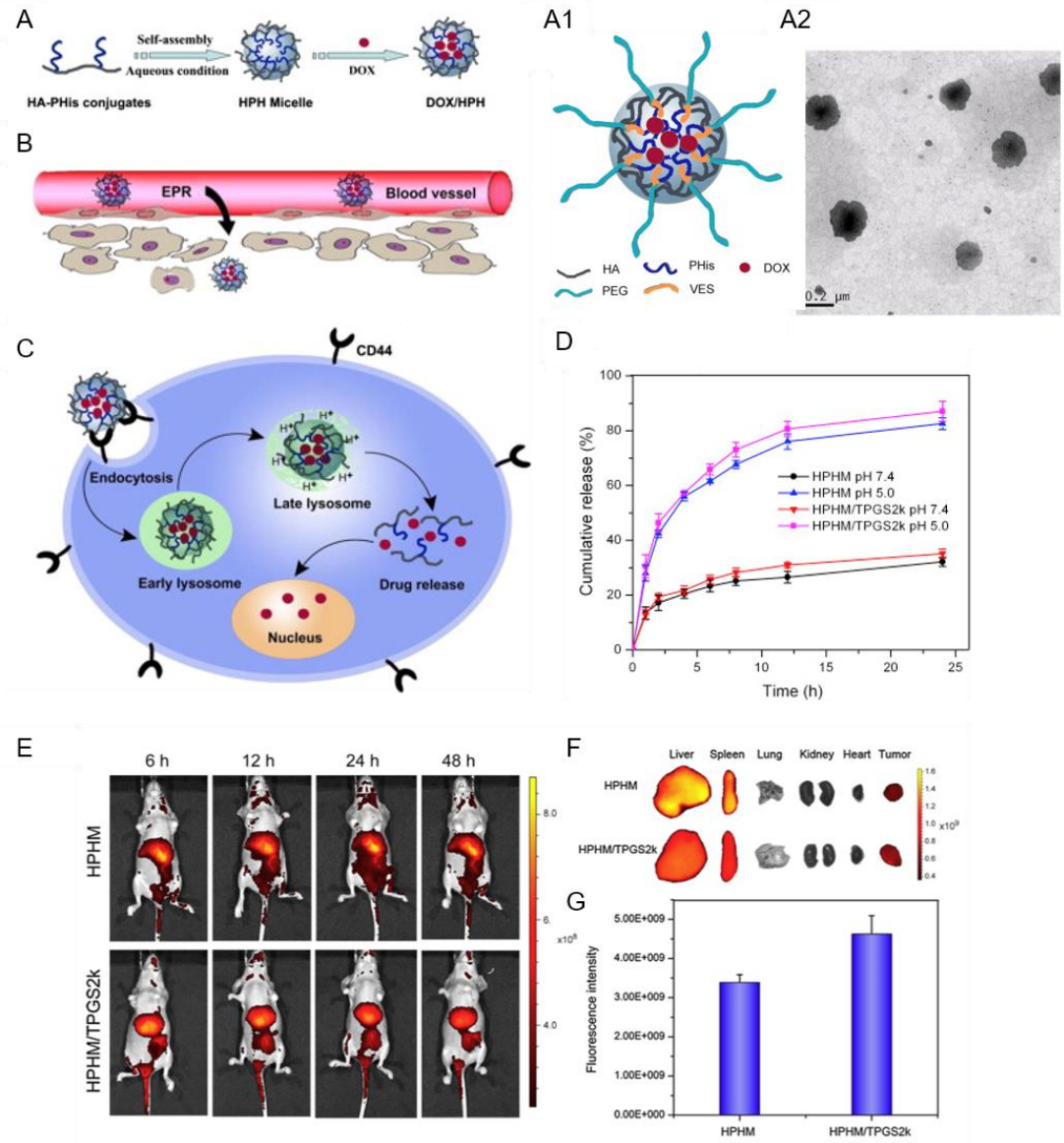

Figure 1.10 *Scheme of self-assembly HA-PHis nanogels and pH-responsive intracellular drug delivery. (A) The DOX-encapsulated micelles based on HA-PHis copolymers are formed in aqueous condition. (A1) (B) Particles of suitable size promote nanocarrier accumulation in tumor tissue by the EPR effect. (C) The micelles are selectively taken up by tumor cells via CD44 receptor-mediated endocytosis and delivered to the lysosomes, triggering the release of DOX into the cytoplasm, improving intracellular drug release and increasing the antitumor efficacy.*

The enhanced MDR reversal effect was attributed to the higher amount of cellular uptake of HPHM/TPGS2k in MCF-7/ADR cells than HPHM. The measurements of P-gp expression level indicated that HPHM/TPGS2k inhibited P-gp activity but without inhibition of

P-gp expression. Moreover, in vivo studies indicated that HPHM/TPGS2k could reach the tumor site more effectively than HPHM. Thus, the pH-sensitive mixed nanogels system was shown to be a promising approach for overcoming the MDR.

Lee et al. proposed to combine pH- and light-responsive properties (Figure 1.11). Light irradiation is safe and easy to use, and lasers have been demonstrated to enhance the intracellular delivery of therapeutic molecules by photo-chemically triggered endolysosomal membrane disruption. [144] To this end, a photochemical agent, chlorin (Ce6) and a pH-responsive polymer, poly(diisopropylaminoethyl)aspartamide (PDIPASP) were attached through a carbodiimide-mediated reaction to acetylated HA (AcHA-g-PDIPASP-g-Ce6). The resulting nanogels, DOX@PHAN (size ~ 200 nm and DOX loading content: 14 %), displayed a pH-response activity due to the hydrophilic-hydrophobic transition of PDISPASP through the protonation of the tertiary amine groups. Moreover, after cellular uptake via receptor-mediated endocytosis, intensity laser irradiation stimulated Ce6 grafted on HA to produce reactive singlet oxygen, which released DOX into the cytosol.

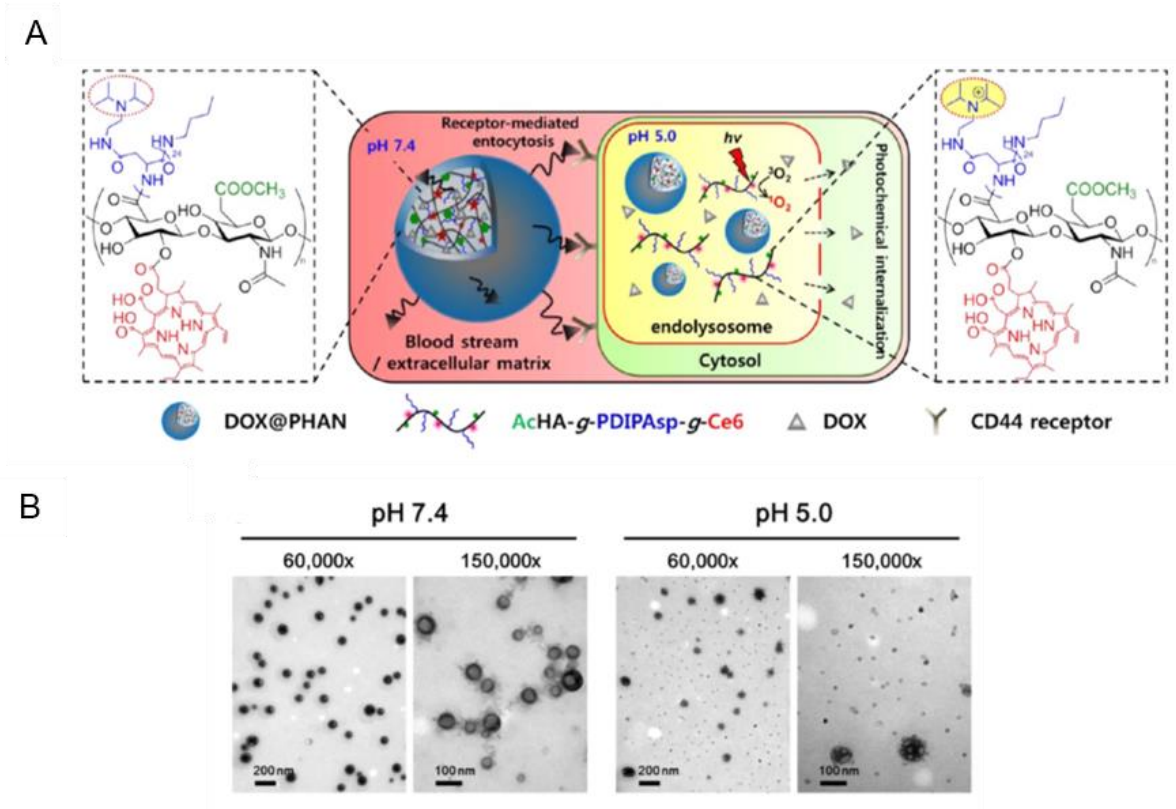

Figure 1.11 *A) Schematic representation of doxorubicin-loaded pH-responsive hyaluronic acid nanonogels (DOX@PHANs). B) TEM photographs of DOX@PHANs at pH 7.4 and 5.0 Magnification is 6000x or 15000x.*

IV.1.3.3.2 Thermoresponsive HA-polymer conjugates

Thermoresponsive polymers have been advantageously used to prepare HA-based nanogels. Auzely-Velty et al. exploited this approach to develop a series of thermoresponsive nanogels based on HA (listed in **table 1.6**).

Table 1.6 *Thermoresponsive HA-polymer conjugates forming nanogels.*

copolymers	Mn HA (kg/mol)	Size (nm)	Drug	responsiveness	CAT (°C)	Tcp (°C)	ref
$DEGMA_{95}$-co-$OEGMA_5$	300 120	95-150	PTX	thermal	34	32	[145]
$DEGMA_{95}$-co-$OEGMA_5$	120 300	150 - 214	PTX	Thermal	34	32	[146]
$DAAM_{95}$-co-DMA_5	40k	200	PTX	Thermal, pH	32	26	[147]
DEGMA-co-CMA	40k	110	PTX	Thermal, Light	27-32	<20	[148]

First, they demonstrated that the grafting of a thermoresponsive copolymer, poly(diethylene glycol methacrylate-co-oligoethylene glycol methacrylate) (poly(DEGMA-co-OEGMA), onto HA allowed temperature-triggered assembly of HA-poly(DEGMA-co-OEGMA) into nanogels (Figure 1.12-A) with a critical aggregation temperature (CAT) of 34°C. This copolymer was coupled with HA via thiol-ene coupling reactions (thiol-maleimide coupling [145] and radical thiol-ene addition reactions [146]). These nanogels exhibited interesting features for drug delivery such as facile formation by simply heating the HA-copolymer solution, tunable size, easy loading of hydrophobic molecules, selectivity for cells expressing the CD44 receptor. *In vivo* biodistribution studies showed that the nanogels circulated freely in the blood but they were rapidly phagocytized within 13 min by circulating macrophage, limiting their therapeutic efficacy.

The authors subsequently focused on the design of more sophisticated nanogels with increased colloidal stability and multiple responsiveness to precisely control their behavior after administration *in vivo*. Thus, they developed core-crosslinked nanogels based on HA modified with a copolymer of diacetone acrylamide (DAAM), *N,N*-dimethylacrylamide (DAAM) (poly(DAAM-co-DMA)) [147]. The selective crosslinking of the core relied on the selective formation of hydrazone crosslinks with bishydrazides within the globular domains of the copolymer chains formed above the cloud point temperature (Figure 1.12-B). The efficiency of the keto-hydrazide ligation allowed tuning the crosslinking density by varying the dihydrazide crosslinker to ketone molar ratio. After core-crosslinking, the nanogel structure became “frozen” and remained stable at low temperature (below the CAT of 30°C) with a size of 200 nm. Their potential of these nanogels to deliver PTX into cancer cells was demonstrated by *in*

vitro cellular uptake studies and cytotoxicity assays. Moreover, to get new insight into the mechanism that determine accumulation of the nanogels in tumor tissues, *in vivo* biodistribution studies were carried out in two different mouse tumor models showing different degrees of EPR-mediated drug targeting as well as CD44 expression levels. These studies showed long circulation of nanogels in blood flow (h) and gave evidence for their EPR effect-based tumor-specific targeting. Importantly, these experiments also demonstrated similar in vivo behaviour of native HA in both tumor models, indicating that the nanogels biodistribution is mainly determined by the nature of the shell-forming polysaccharide.

In another study, the authors developed light- and thermoresponsive HA-based nanogels to trigger drug release “on-demand”. The strategy relied on the incorporation of coumarin moieties within a thermoresponsive ethylene glycol-based copolymer (poly(diethylene glycol methacrylate-co-coumarin methacrylate), poly(DEGMA-co-CMA)) grafting on HA, leading to the formation of nanogels that can undergo disassembly upon-light exposure (Figure 1.12-C) [148]. The nanogel disassembly is due to the hydrolysis of coumarin esters upon UV-light irradiation or near-infrared (NIR) two-photon light excitation (750 nm), resulting in a shift of the CAT from 27°C to a temperature above the body temperature (38°C) of HA-poly(DEGMA-co-CMA) with 5% of CMA (mol%). These nanosystems exhibited efficient internalization by cancer cells overexpressing the CD44 receptor of HA (HeLa cells), ability to circulate for a prolonged period of time in the bloodstream after intravenous injection in mice and considerable detection in tumor tissues.

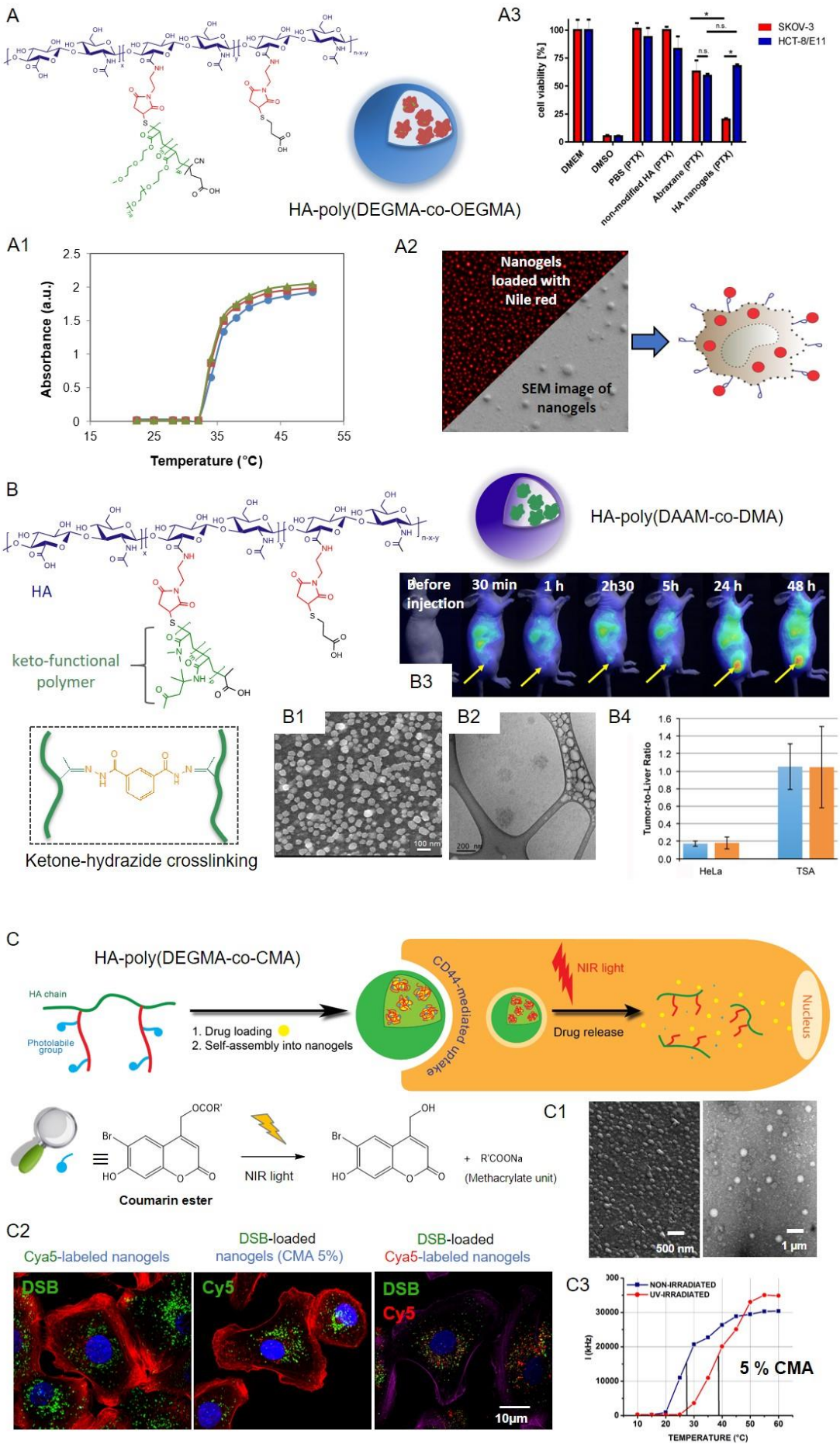
A
HA-poly(DEGMA-co-OEGMA)
A3
cell viability [%]
SKOV-3
HCT-8/E11
DMEM
DMSO
PBS (PTX)
non-modified HA (PTX)
Abraxane (PTX)
HA nanogels (PTX)
A1
Absorbance (a.u.)
Temperature (°C)
A2
Nanogels loaded with Nile red
SEM image of nanogels
B
HA
keto-functional polymer
HA-poly(DAAM-co-DMA)
Before injection
30 min
1 h
2h30
5h
24 h
48 h
B3
B1
B2
B4
Tumor-to-Liver Ratio
HeLa
TSA
Ketone-hydrazide crosslinking
C
HA-poly(DEGMA-co-CMA)
HA chain
Photolabile group
1. Drug loading
2. Self-assembly into nanogels
CD44-mediated uptake
NIR light
Drug release
Nucleus
Coumarin ester
NIR light
+ R'COONa
(Methacrylate unit)
C1
500 nm
1 µm
C2
Cya5-labeled nanogels
DSB-loaded nanogels (CMA 5%)
DSB-loaded Cya5-labeled nanogels
DSB
Cy5
DSB
Cy5
10µm
C3
NON-IRRADIATED
UV-IRRADIATED
I (kHz)
5 % CMA
TEMPERATURE (°C)

Figure 1.12 *A) Synthesis of poly(DEGMA-co-OEGMA) by the RAFT polymerization method. Temperature-responsive behavior of the HA-poly(DEGMA-co-OEGMA) A1) Transmittance plots as a function of temperature with DS respectively 3, 4 and 6 % at a concentration* C_p*= 5 g/L. A2) Fluorescence microscopy image at 40°C (DS: 3 %) loaded with Nile Red and A3) scanning electron microscopy image (Cp = 2 g/L)***.** *B) Formation of hyaluronic acid-based nanogels by temperature-induced self-assembly and their covalent crosslinking by hydrazone bond formation within the hydrophobic domains of the grafted copolymer chains. Morphology of HA-based nanogels crosslinked with an IDH:ketone molar ratio of 0.5 observed at 5 °C by TEM (B1) and by cryo-TEM (B2). (B3) In vivo near-infrared fluorescence (NIRF) images of the time dependent biodistribution of Cy5.5-labeled crosslinked nanogels in breast TS/A-pc and HeLa tumor-bearing mice. The tumor was engrafted subcutaneously on the right flank of the mouse. The fluorescence was measured before injection and at the following time elapse after administration: 30 min, 1h, 2 h 30, 5 h, 24 h, and 48 h. The tumor locations are indicated by the arrows. (B4) Fluorescence intensity ratio of the excised tumor to liver at 24 h (blue) and 48 h (orange) post-injection. The results are expressed as the mean ± SD (n=3). C) Formation of light and thermoresponsive HA-poly(DEGMA-co-CMA) nanogels by temperature increase and disassembly upon light exposure, (C3) shift of the CAT. (C1) Characterisation of HA-poly(DEGMA-co-CMA) nanogels (5% CMA, 0.5 g/L in ultrapure water at 40°C) by Scanning and transmission electron microscopy. Cellular uptake of HA-poly(DEGMA-co-CMA) nanogels by HeLa cells C2) confocal microscopy images of HeLa cells incubated for 16h with nanogels loaded with a fluorescent dye (di-strybenzene derivative, DSB), cyanine5-labelled nanogels and DSB-loaded cyanine5-labelled nanogels (from left to right). C3)*

IV.2 Chondroitin sulfate-based amphiphilic nanoparticles

Chondroitin sulfate is particularly abundant in the extracellular matrix of cartilage and bones. In the biomedical field, CS is used as a type of neutraceuticals for the treatment of osteoarthritis owing to its anti-inflammatory activity [148-149]. Chondroitin sulfate is composed of alternating units of (β-1,3)-glucuronic acid (GlcUA) and (β-1,4) *N*-acetyl galactosamine (GalNAc) with sulfate at either the 4- or 6-position of GalNAc or at 2-position of GlcUA. It structural similarity to hyaluronic acid makes CS an attractive building block for designing drug delivery systems with potential targeting ability to cancer cells via CD44 receptor-mediated endocytosis [150-152]. However, unlike HA, CS is a natural substrate for P-selectin, which is expressed on endothelial cells, platelets, and some cancer cells. Since P-selectin plays a critical role in tumor metastasis, CS based nanoparticles could have dual targeting capabilities, particularly for metastatic cancer [151,153].

Therefore, CS was hydrophobically-modified for the synthesis of drug delivery nanocarriers [154]. Table 1.7 summarizes CS-based amphiphilic nanocarriers obtained in recent years. Most of these nanocarriers have been investigated through *in vitro* studies. From this table, it can be also noticed that the hydrophobic moieties and linkers used are similar to those used for the synthesis of HA-based self-assembled NPs. CS was conjugated through hydrazone, ester, amide linkages to thermoresponsive (pluronic) [164], or pH-responsive (poly(histidine)) [157] polymers, common biodegradable polymers (PLGA, PLA, PCL) [155, 159] or to small hydrophobic molecules such as α-linoleic acid [161], cholesterol [156]. These different conjugates led to the formation of nanogels, micelles and nanocapsules. Based on physico-chemical and *in vitro* studies, CS- and HA- based NPs show very similar characteristics. The lack of *in vivo* studies, does not allow to go further into the conclusions.

Table 1.7 *Amphiphilic derivatives of CS leading to the formation of self-assembled NPs.*

System	Mn HA (kg/mol)	Size (nm)	Drug(s)	DL (EE)%	Application	ref
CS-Lipid conjuagtes						
CS-ss-CHOL	72	124-237	quercetin	23 (30)	*In vitro* triggered release and cytotoxicity against HeLa Cells	[156]
CS-hydrazone-DOCA	10	165	DTX		*In vitro* release and cellular uptake MCF-7	[158]
CS-PEG-DOCA	37	268	DOX	(94)	*In vitro* drug release, cellular uptake SKOV-3 *In vivo* pharmacokinetics	[160]
Linoleic acid	4, 17	78-117	-	-	*In vitro* cytotoxicity in Caco-2 and HT29 cells, transport studies across Caco-2-Cells *In vivo* intragastric absorption efficacy	[161]
CS-drug conjugates						
ChS-drug	97	-	NSAIDs	-	Colon targeting	[162]
CS-small molecule						
CS-acetylated	-	345	DOX Ce6	DOX, 2.5 (91)	*In vitro* triggered release, cellular uptake and cytotoxicity to HeLa cells	[163]
CS-polymer conjugates nanogels						
CS-PCL	85	300	DOX	(>85)	*In vitro* intracellular uptake of KB cells	[158]
CS-PLA	12	92-180	-	-	-	[159]
CS-pluronic	20,50	48-230	DOX	15 (42)	*In vitro* cellular uptake in A549 cells	[164]
pH responsive CS-polymer conjugates based pH responsive nanogels						
CS-polyhistamine pH responsive ester bond	20	133	DOX		*In vitro* cytotoxicity to HepG2 cells	[157]
CS-polymer conjugates micelles						
CS-hydrazone-PLGA	10	255-287	DOX	10	*In vitro* drug release, cellular uptake and anti-tumor effect against MCF-7	[165]
CS-PLA	5	35-54	-	-	-	[166]
CS-polymer conjugates Capsules						
CS-poly(methacrylate)	50	240	Indomethacine (IND)	(90)	*In vitro* release	[167]

Very recently, Ooomen et al. proposed to lift this veil and reported the first direct comparison (under identical conditions) of HA- and CS-based nanogels (Figure 1.13). To facilitate direct comparison, they utilized HA and CS of similar molecular weights (approximately 50 kg/mol). They designed theranostic NPs using fluorescein, a fluorescent aromatic molecule. Thus, self-association was induced by hydrophobically modifying HA and CS with fluorescein moiety. Such a modification fostered self-assembly to form NPs that not only gave an imaging possibility but also improved the binding of aromatic drug molecules using π−π interactions (planar undistorted π-core of fluorescein) with an aromatic hydrophobic drug such as doxorubicin hydrochloride (DOX) resulting in controlled drug release (Figure 1.13) [168].

They examined the drug-loaded nanogels HA-DOX and CS-DOX in two different human cell lines (HCT116 and MCF-7), and cellular uptake, nuclear translocation, dose-dependent cytotoxicity, and dependence of caspase 3/7 for apoptosis were evaluated.

From this first investigation has resulted in the following findings. The FACS and the confocal study showed CD44 mediated cellular uptake and nuclear localization of both nanogels (CS-DOX and HA-DOX). Cytotoxicity studies of these NPs revealed that CS-derived NPs are superior to the HA-derived one in both cell lines tested. Hematological evaluation of HA, CS, and their nanogels show that the chemical modification of biopolymers alters the biological function of the polymers. HA-DOX is less immunogenic compared with CS-DOX. Otherwise, both HA-and CS nanogels could be used for developing targeted drug delivery systems for anticancer therapy. This nanogel formulation and design is straightforward to give a stable GAG based nanoparticles, customizable for a variety of aromatic antineoplastic agents, with a narrow size distribution and efficient drug loading properties without the use of any inactive excipients. The degradation of these NPs using ubiquitous enzymes *in vivo*, particularly at the tumor site (because of increased enzymatic activity) will allow better control of drug release at the tumor site.

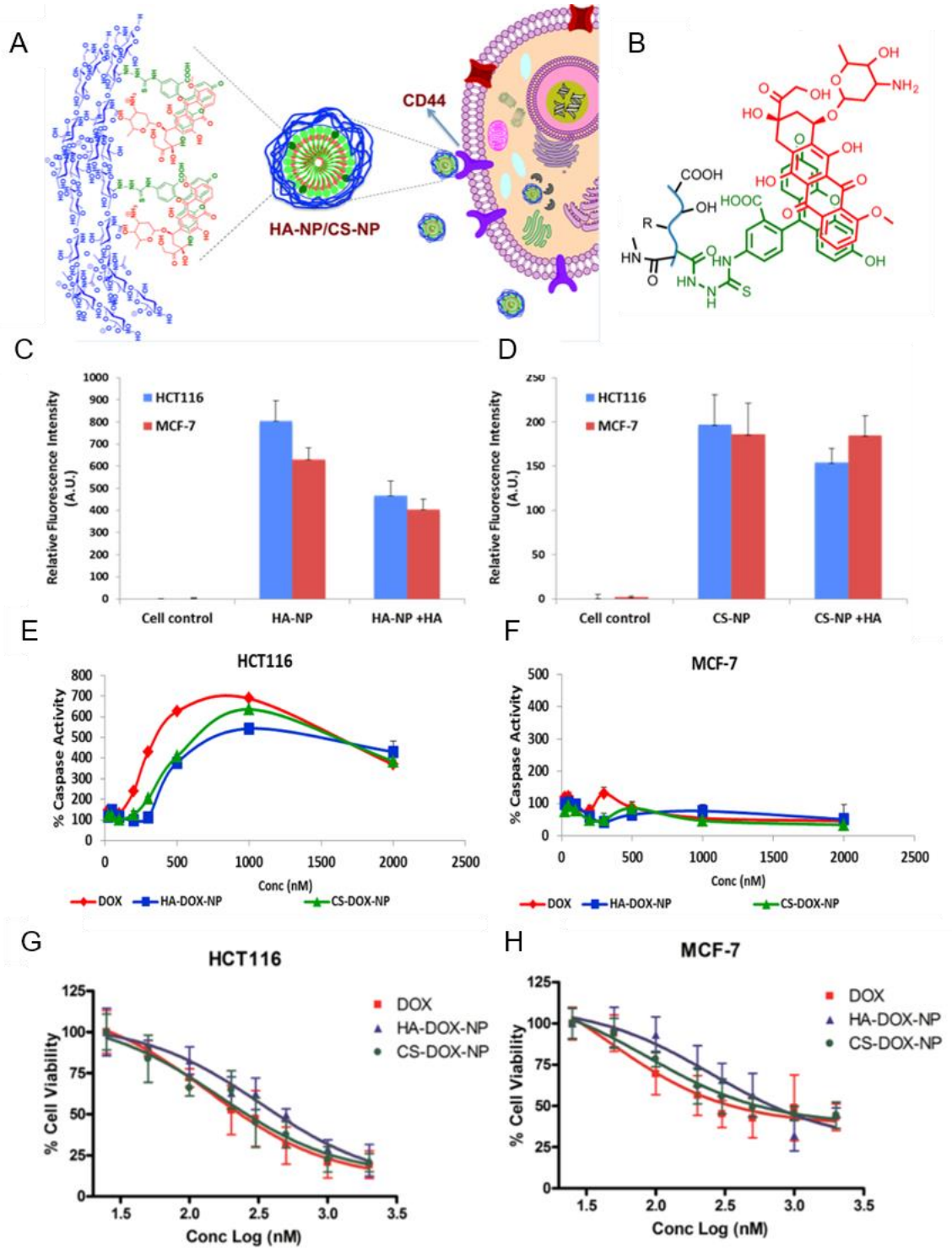

Figure 1.13 *A) and B) Schematic representations of doxorubicin stabilized amphiphilic HA and CS polymers. Flow-cytometric analysis of the uptake of (C) HA NPs and (D) CS NPs by HCT116 and MCF-7 cell lines in the presence and absence of 7.5 kg/mol HA (10 mg/mL). Estimation of caspase 3/7 activities in (E) HCT116 and (F) MCF-7 cell lines, treated with drug- or drug-loaded nanoparticles. The baseline caspase 3/7 levels in each cell line are considered as 100%. E) Dose dependent cytotoxicity of DOX and DOX-loaded nanoparticles in (G) HCT116 and (H) MCF-7 cell lines.*

IV.3 Heparin and heparan sulfate-based amphiphilic nanoparticles

While heparin and heparin sulphate are based on the same repeating disaccharide units, HP and HS show very different compositions with heparin containing a much more higher density of *N*- and *O*-sulfate groups [169-170]**.** This feature, in addition to their blood anticoagulant activity, could inhibit tumor metastasis in different experimental models with the binding of growth factor such as vascular endothelial growth factor (VEGF) and fibroplast growth factor (bFGF). Moreover, HP is involved in the inhibition of heparanase enzymes that are thought to be required by tumor cells for invasion of the vascular basement membrane. Therefore, HP has been more investigated than HS and at first, has been encapsulated and delivered as therapeutic agent [171-172].

Recently, HP based drug delivery systems have been developed as platforms for the delivery of anticancer drugs. Interestingly, due to its inherent properties, it can exhibit a synergistic effect for the prevention and treatment of tumor metastasis through co-delivery with other tumor drugs. To this end, until now, only Heparin based nanogels resulting from the self-association of hydrophobically modified derivatives of HP have been investigated [174].

HP can be hydrophobically modified by the same hydrophobic moieties as the previous GAGs such as cholesterol derivatives [175-178] or drugs [179] conjugate *via* same cleavable linker to trigger drug releasing in tumor environment. The unique difference lies on the synergistic anticancer effect since HP has anticancer property. However, similar to other GAGs, a systemic strong accumulation in liver and RES organs is observed as well as for the two previous GAGs. At least, since strategies followed are the same, comparative studies between GAGs could be performed. Unfortunately, up until now, there is a lack of comparative study between GAGs (or polysaccharides) based drug delivery systems. Such comparison will allow a better understanding and awareness of the strategic challenges/approaches.

Interestingly, the high negative charge density of heparin distinguished it from previous GAGs and has been mainly exploited to form nanogels based on electrostatic interactions. Theoretically any cationic polymers could interact with polysaccharide to form polyelectrolyte nanogels. In practice, these polyelectrolytes are restricted to biocompatible and water-soluble polymers in view of safety purpose. However, combined with hydrophobic feature, a suitable nanogels platform can be obtained.

In this regard, Li et al. [180] combined amphiphilic properties of a heparin-drug conjugate and electrostatic interactions to physically entrap another therapeutic agent to optimize properties for anti-tumor chemotherapy (Figure 1.14). Thus, they designed HP-PTX nanogels via a pH sensitive linkage (cis-acotinic linker). Then a drug, DOX-HCl and a tumor targeting molecule, the cationic folic acid (CFA) were incorporated. The successful preparation of the drug carrier *via* electrostatic adsorption was proved by zeta potential measurements showing a decrease of surface potential due to the incorporation of cationic DOX and CFA. Consequently, following adsorption, an increase of the average nanogel size from 150 nm to a size around 300 nm was observed. Interestingly, HP-PTX provided relatively higher drug loading capacity than previous HP-PCL drug carrier [173] (13% and 9%, respectively). The release was achieved in two times. Most of DOX molecules were released within the first 12h whereas the PTX release continued for the last 12H. Moreover *in vitro* tumor cytotoxicity showed higher cytotoxicity against tumor cells than the HP-polymer conjugate.

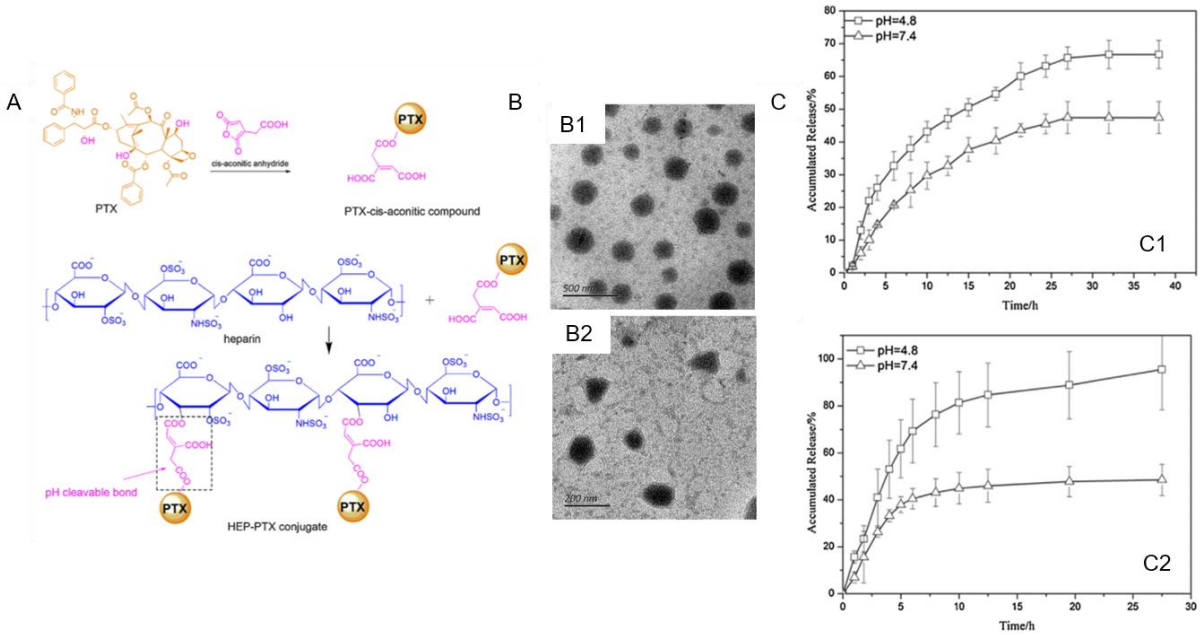

Figure 1.14 *A) The synthetic route for HP-PTX conjugate. B) The TEM observations (B1) HP-PTX polymer carrier before DOX and CFA absorption, and (B2) drug carrier after DOX and CFA absorption. C) The in vitro release profiles of PTX (C1) and DOX (C2) of HP-based drug carrier. [180]*

IV.4 Heparosan-based amphiphilic nanoparticles

Heparosan (Hep), is a particular non-sulfated member of the glycosaminoglycan family. Hep has a chemical structure very similar to HA, in which the β-1,3 bond between the glucuronic acid and the *N*-acetylglucosamine replaces the α-1,4 bond found in Hep. It is found in the capsule of some pathogenic bacteria and it is the natural precursor of the biosynthesis of heparin and heparan sulfate. Therefore, it has been used as a precursor for the synthesis of bio-engineered heparin that is free of contaminants, that can cause adverse reactions in patients. [181-185] Recent studies focused on the development of chemical and biological synthetic strategies for obtaining this important precursor. [186-188] Thus, heparosan is a relatively new polysaccharide used in the biomedical field. [189] Very few investigations have been published on the chemical modification of heparosan for different applications such as nanocarriers.

However, Hep revealed multiple key advantages over the other GAGs for drug delivery systems and implantable biomaterial [190 -192] : i) less substantial biological interactions and degradation in the extracellular space, ii) a longer half-life in the bloodstream of healthy animal, iii) natural biodegradation pathway to prevent accumulation in the tissues after the drug is released and iv) no observed immunogenicity. In contrast to HP and HS, Hep is neither decorated with sulfate groups nor epimerized at glucuronic acid residues, it is thus relatively biologically inactive with respect to: (i) coagulation (i.e., clotting factors not activated), (ii) modulation of proliferation (i.e., growth factors do not bind) and (iii) inflammation (i.e., cytokines do not interact). Moreover, enzymes that degrade (heparanase) or receptors that clear the other GAGs including HA from the bloodstream (hyaluronan receptor for endocytosis or stabilin) do not recognize heparosan because the sulfate groups essential for activity are absent from this polymer [193-197].

In other words, borrowed from DeAngelis [190] “heparosan read as ‘a hole in the sugar code’ that is ignored by the HS recognition systems”. Therefore, heparosan is stable in the extracellular spaces where many therapeutic drugs act. Its degradation through internalization by enzymes called β-glucuronidase, to which Hep is vulnerable, will arrive only once after reached the lysosome space [198]. In conclusion, while most of nanocarriers, seen in this chapter, encountered issues with delivery due to nonoptimal pharmacokinetics and systemic high accumulation in liver, Hep may overcome these limitations.

This hypothesis is also supported by the half-life of native heparosan compared to others GAGs. It is noted that the clearance of HA and CS from circulation depends on its molar mass. The half-life of native high molar mass HA in humans is 2.5−5.5 min [198], whereas CS (M_w = 50 kg/mol) has a half-life of 12−15 min [199]. The chemical modification of HA and CS increases the blood circulation time due to hindered enzymatic recognition [200]. In the case of native heparosan, the half-life in the bloodstream is between 0.5- and 8-day depending on its molar mass and the route of administration.

Therefore, Hep has been recently studied to replace PEG as a coating agent [199-200]. Nevertheless, very few studies have been carried out and to the best of our knowledge, only Chen et al. have reported self-assembled systems based on Heparosan [201-202].

These include Hep-drug (DOX) conjugates and Hep-hydrophobic moieties (DOCA) conjugates. The first one (Figure 1.15) was used as model to investigate the endocytosis pathway of heparosan-based nanocarrier. It should be noted that unusual coupling reactions have been performed. DOX was linked to Hep through aldehyde groups obtained after opening the sugar ring by oxidizing hydroxyl group of the glucuronic acid residue in the presence of sodium periodate. Chen et al. demonstrated that the main endocytosis pathway of Hep-DOX in HeLa cells was clathrin-mediated endocytosis and micropinocytosis. This study also revealed that heparosan could undergo rapid intracellular trafficking of DOX and produced a therapeutic effect in short period. In the case of Hep-DOCA, DOX was effectively encapsulated in nanoparticles based on the amphiphilic Hep derivative (Figure 1.16). Cellular uptake and *in vitro* cytotoxicity assays confirmed that DOX-loaded nanogels could be efficiently internalized by HeLa cells, and showd significant distinction of IC50 between tumor cells and normal cells.

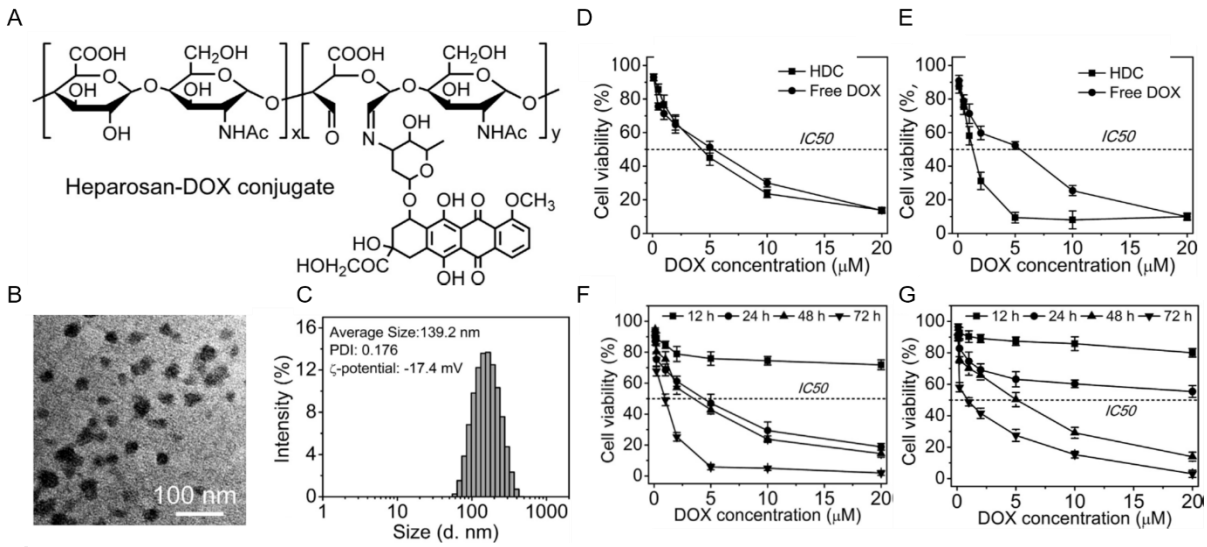

Figure 1.15 *A) Chemical structure of Heparosan-DOX conjugate (HDC). B) TEM image of HDC nanoparticles in PBS (pH 7.4). C) Size distribution and ξ-potential of HDC nanogels. The cytotoxicity of HDC against D) HeLa and E) A549 cells, free DOX with the equivalent amount was used as the control. In vitro cytotoxicity of F) HDC and G) free DOX against HeLa cells within different co-incubation periods.*

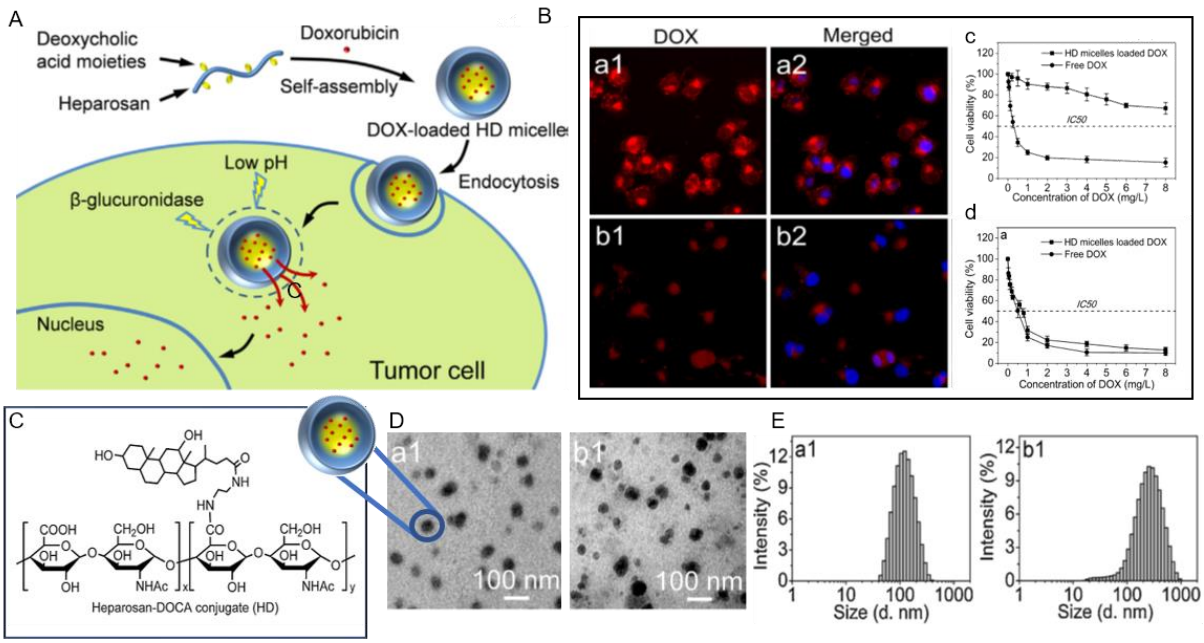

Figure 1.16 *A) Schematic illustration of the formation of self-assembled HD nanogels and intracellular drug delivery. B) In vitro a) fluoreorescent images of HeLa cells and b) COS7-cells co-cultured with DOX-loaded nanogels for 1h. (a1, b1) Red fluorescent showed the DOX has internalized into cells; (a2, b2) blue represented cell nuclei stained by DAPI; In vitro cytotoxicity of DOX-loaded nanogels and DOX against c) HeLa cells and d) COS7 cells. Error bars represent standard deviation of 3 replicates for the test. C) Chemical structure of Heparosan-DOCA conjugate (HD). D) TEM images of a1) HD nanogels b1) DOX-loaded nanogels in PBS solution (1 mg/mL). E) Size distributions of a1) HD nanogels and b1) DOX-loaded nanogels.*

V Conclusion

Glycoaminoglycan-based nanoparticles have a great potential as carriers of different pharmaceutical agents due to their physicochemical and biological properties, which can overcome the limitations upon the administration of conventional anticancer drugs. They are biocompatible, biodegradable, non-toxic and easily tunable. Moreover, the multifaceted functions of GAGs may also have context-dependent therapeutic applications due to their intrinsic biological activities.

A wide variety of self-assembled nanosized carriers has been developed. The introduction of hydrophobic segments into hydrophilic polysaccharide backbones allows forming self-assembled structures with distinct architectures, sizes and surface properties, such as micelles, polymersomes, nanocapsules, and nanogels. The most interesting hydrophobic groups are those that improve interactions with the drug (cholesterol derivatives, aromatic molecules) and possess a dual function such as biological activity (glycyrrhetinic, tocopheryl) or stimuli-responsive properties (pH-, thermo-, photo-responsive) or additional chemical modification (crosslinking).

Each system offers advantages. However, nanogel architectures, which are hydrogels formulated at nanoscale size, have emerged as some of the most promising nanocarriers and are currently the most studied. They are particularly appreciated for their high hydration capacity, which gives them a flexibility that other particles do not have, and the possibility of modifying both the hydrophilic shell and the hydrophobic core, allowing for multiple combinations. Thus, a wide variety of nanogels have been developed and their *in vivo* evaluation raises questions, such as the effect of particle size on biodistribution, their strong or weak stability, or drug burst release, which likely impact on pharmacokinetics, tissues distribution, and drug efficacy.

Among GAGs, hyaluronic acid is the most studied due to its unique ability to target cancer cells overexpressing the HA receptor CD44. By contrast chondroitin, heparin and heparosan are for the moment very little studied and lack further investigations. A thorough comparative study between CS-, HP-, Hep-based nanocarriers and hyaluronic acid-based nanocarriers, under the same conditions, could give us a better understanding of their *in vivo* potential and the biological mechanisms involved during administration. In particular, an important issue is to properly evaluate the advantages of the HA corona in terms of tumor targeting. There is still little evidence that tumor targeting is closely related to the CD44 targeting effect.

Moreover, through this bibliography review, we have seen that most nanogel-based HA systems encountered issues with delivery due to nonoptimal pharmacokinetics and systemic high accumulation in liver. The key to achieve optimal antitumor efficacy is to find a favorable balance between long circulation and targeted cellular uptake exploiting the EPR effect. Thus, most systems have incorporated PEG on their surface to reduce RES uptake and increase the nanoparticle blood half-life. But PEG is also known to be non-biodegradable and able to induce immune reactions after repeated applications. PEGylation does not constitute an appropriate solution. Further studies will be needed to limit off targeting to healthy tissue, in particular to the liver, which is the principal elimination organ of HA. In this regard, heparosan might be a promising alternative to HA since HARE receptors, that clear the other GAGs including HA from the bloodstream (hyaluronan receptor for endocytosis or stabilin) do not recognize heparosan and overcome this current issue. A comparative study between HA- and Hep-based nanogels would allow to gain a better understanding of its in vivo behavior and its potential.

VI References

1. Martín del Valle, E.M.; Galan, M.A.; & Carbonell, R.G. Drug delivery technologies: the way forward in the new decade. *Industrial & Engineering Chemistry Research*, **2009**, 48, 2475-2486.
2. Lammers, T.; Kiessling, F.; Hennink, W.E.; & Storm, G. Drug targeting to tumors: Principles, pitfalls and (pre-) clinical progress. *Journal of Controlled Release*, **2012**, 161, 175-187.
3. Sun, Q.; Radosz, M.; & Shen, Y. Challenges in design of translational nanocarriers. *Journal of Controlled Release*, **2012**, 164, 156-169.
4. El-Say, K.M.; & El-Sawy, H.S. Polymeric nanoparticles: promising platform for drug delivery. *International Journal of Pharmaceutics*, **2017**, 528, 675-691.
5. Shukla, S.K.; Shukla, S.K.; Govender, P.P.; & Giri, N.G. Biodegradable polymeric nanostructures in therapeutic applications: opportunities and challenges. *RSC Advances*, **2016**, 6, 94325-94351.
6. Singh, A.; Garg, G.; & Sharma, P.K. Nanospheres: a novel approach for targeted drug delivery system. *International Journal of Pharmaceutical Sciences Review and Research*, **2010**, 5, 84-88.
7. Kothamasu, P.; Kanumur, H.; Ravur, N.; Maddu, C.; Parasuramrajam, R.; & Thangavel, S. Nanocapsules: The weapons for novel drug delivery systems. *Bioimpacts*, **2012**, 2, 71-81.
8. Anajafi, T.; & Mallik, S. Polymersome-based drug-delivery strategies for cancer therapeutics. *Therapeutic Delivery*, **2015**, 6, 521-534.
9. Kedar, U.; Phutane, P.; Shidhaye, S.; & Kadam, V. Advances in polymeric micelles for drug delivery and tumor targeting. *Nanomedicine*, **2010**, 6, 714-729.
10. Duncan, R.; & Izzo, L. Dendrimer biocompatibility and toxicity. *Advanced Drug Delivery Reviews*, **2005**, 57, 2215-2237.
11. Williams, D.F. On the mechanisms of biocompatibility. *Biomaterials*, **2008**, 29, 2941-2953.
12. Nitta, S.K.; & Numata, K. Biopolymer-based nanoparticles for drug/gene delivery and tissue engineering. *International Journal of Molecular Sciences*, **2013**, 14, 1629-1654.
13. Cardoso, M.J.; Costa, R.R.; & Mano, J.F. Marine origin polysaccharides in drug delivery systems. *Marine Drugs*, **2016**, 14, 34.
14. Wen, Y.; & Oh, J.K. Recent strategies to develop polysaccharide-based nanomaterials for biomedical applications. *Macromolecular Rapid Communications*, **2014**, 35, 1819-1832.

15. Swierczewska, M.; Han, H.S.; Kim, K.; Park, J.H.; & Lee, S. Polysaccharide-based nanoparticles for theranostic nanomedicine. *Advanced Drug Delivery Reviews*, **2016**, 99, 70-84.
16. Zhang, N.; Wardwell, P.; & Bader, R. Polysaccharide-based micelles for drug delivery. *Pharmaceutics*, **2013**, 5, 329-352.
17. Misra, S.; Hascall, V. C.; Atanelishvili, I.; Rodriguez, R.M.; Markwald, R.R.; & Ghatak, S. Utilization of glycosaminoglycans/proteoglycans as carriers for targeted therapy delivery. *International Journal of Cell Biol*ogy, **2015**, 1-25.
18. Ghaz-Jahanian, M.A.; Abbaspour-Aghdam, F.; Anarjan, N.; Berenjian, A.; & Jafarizadeh-Malmiri, H. Application of chitosan-based nanocarriers in tumor-targeted drug delivery. *Molecular Biotechnoly*, **2015**, 57, 201-218.
19. Varshosaz, J. Dextran conjugates in drug delivery. *Expert Opinion on Drug Delivery*, **2012**, 9, 509-23.
20. Singh, R.S.; Kaur, N.; & Kennedy, J.F. Pullulan and pullulan derivatives as promising biomolecules for drug and gene targeting. *Carbohydrate Polymer*s, **2015**, 5, 190-207.
21. De Almeida, R.R.; Magalhaes, H.S.; De Souza, J.R.R.; Trevisan, M.T.S.; Vieira, I.G.P.; Feitosa, J.P.A.; Araujo, T.G.; & Ricardo, N.M.P.S. Exploring the potential of Dimorphandra gardneriana galactomannans as drug delivery systems. *Industrial Crops and Products*, **2015**, 69, 284-289.
22. Jain, D.; & Bar-Shalom, D. Alginate drug delivery systems: application in context of pharmaceutical and biomedical research. *Drug Development and Industrial Pharmacy*, **2014**, 40, 1576-84.
23. Adachi, N.; Maruyama, A.; & Ishihara, T. Cellular distribution of polymer particles bearing various densities of carbohydrate ligands. *Journal of Biomaterials Science, Polymer edition*, **1994**, 6, 463-479
24. Maruyama, A.; Ishihara, T.; Adachi, N.; & Akaike, T. Preparation of nanoparticles bearing high density carbohydrate chains using carbohydrate-carrying polymers as emulsier. *Biomaterials*, **1994**, 103-1042
25. Hardingham, T.E.; & Fosang, A.J. Proteoglycans: many forms and many functions. *The FASEB Journal*, **1992**, 6, 861-870.
26. Sasisekharan, R.; Raman, R.; & Prabhakar, V. Glycomics approach to structure-function relationships of glycosaminoglycans. *Annual Review Biomedical Engineering*, **2006**, 8, 181-231.
27. Lindahl, U.; & Höök, M. Glycosaminoglycans and their binding to biological macromolecules. *Annual Review of Biochemistry,* **1978**, 47, 385–417.

28. Islam, T.; & Linhardt, R.J. Chemistry, biochemistry and pharmaceutical potentials of glycoaminoglycans and related saccharides. *Carbohydrate-based Drug Discovery*, **2006**, Chapter 15, Volume 1, Wiley-VCH, Weinheim.
29. Karamanos, N.K.; & Tzanakakis, G.N. Glycosaminoglycans: from "cellular glue" to novel therapeutical agents. *Current Opinion in Pharmacology*, **2012**, 12, 220-222.
30. Afratis, N.; Gialeli, C.; Nikitovic, D.; Tsegenidis, T.; Karousou, E.; Theocharis, A.D.; Pavao, M.S.; Tzanakakis, G.N.; & Karamanos, N.K. Glycoaminoglycans: Key players in cancer cell biology and treatment. *FEBS Journal*, **2012**, 279, 1177-1197.
31. Freudenberg, U.; Liang, Y.; Kiick, K.L.; & Werner, C. Glycosaminoglycan-based biohybrid hydrogels: a sweet and smart choice for multifunctional biomaterials. *Advanced Materials,* **2016**, 28, 8861-8891.
32. Rilla, K.; Tiihonen, R.; Kultti, A.; Tammi, M.; & Tammi, R. Pericellular hyaluronan coat visualized in live cells with a fluorescent probe is scaffolded by plasma membrane protrusions. *Journal of Histochemistry and Cytochemistry,* **2008**, 56, 901-910.
33. Germershaus, O.; Lühmann, T.; Rybak, J.C.; Ritzer, J.; & Meinel, L. Application of natural and semi-synthetic polymers for the delivery of sensitive drugs. *Internationals Materials Review*, **2015**, 60, 101-131.
34. Almodovar, J.; Place, L.; Gogolski, J.; Erickson, K.; & Kipper, M.J. Layer-by-Layer assembly of polysaccharide-based polyelectrolyte multilayers: a stectroscopic study of hydrophilicity, composition, and Ion pairing. *Biomacromolecules*, **2011**, 12, 2755-2765.
35. Xi, J.; Zhou, L.; & Fei, Y. Preparation of chondroitin sulfate nanocapsules for use as carries by the interfacial polymerization method. *International Journal of Biological Macromolecules*, **2012**, 50, 157-163.
36. Yi, Q.; Ma, J.; Kang, K.; & Gu, Z. Dual cellular stimuli-responsive hydrogel nanocapsules for delivery of anticancer drugs. *Journal of Materials Chemistry B*, **2016**, 4, 4922-4933.
37. Sun, L.; Xiong, X.; Zou, Q.; Ouyang, P.; Burkhardt, C.; & Krastev, R. Design of intelligent chitosan/heparin hollow microcapsules for drug delivery. *Journal of Applied Polymer*, **2017**, 44425,1-10.
38. Szarpak, A.; Pignot-Paintrand, I.; Catherine Picart, C.; & Auzély-Velty. R. Multilayer assembly of hyaluronic acid/poly(allylamine): control of the buildup for the production of hollow capsules. *Langmuir*, **2008**, 24, 9767-9774.
39. Hu, X.; Zhang, Y.; Xie, Z.; Jing, X.; Bellotti, A.; & Gu, Z. Stimuli-responsive polymersomes for biomedical applications. *Biomacromolecules*, **2017**, 18, 649-673.
40. Schatz, C.; & Lecommandoux, S. Polysaccharide-containing block copolymers: synthesis, properties and applications of an emerging family of glycoconjugates. *Macromolecular Rapid Communications*, **2010**, 31, 1664-1684.

41. Zhang, Y.; Wu, F.; Yuan, W.; & Jin, T. Polymersomes of asymmetric bilayer membrane formed by phase-guided assembly. *Journal of Controlled Release*, **2010**, 1, 413-419.
42. Neamtu, I.; Rusu, A.G.; Diaconu, A.; Nita, L.E.; & Chiriac, A.P. Basic concepts and recent advances in nanogels as carriers for medical applications. *Drug Delivery*, **2017**, 24, 539-557.
43. Soni, G.; & Yadav, K.S. Nanogels as potential nanomedicine carrier for treatment of cancer: A mini review of the state of the art. *Saudi Pharmaceutical Journal*, **2016**, 24, 133-139.
44. Soni, K.S.; Desale, S.S.; & Bronich, T.K. Nanogels: an overview of properties, biomedical applications and obstacles to clinical translation. *Journal of Controlled Release*, **2016**, 240, 109-126.
45. Yadav, H.K.S.; Al Halabi, N.A.; & Alsalloum, G.A. Nanogels as novel drug delivery systems - a review. *Journal of Pharmacy and Pharmaceutical Research*, **2017**, 1.
46. Dorwal, D. Nanogels as novel and versatile pharmaceuticals. *International Journal of Pharmacy and Pharmaceutical Sci*ences, **2012**, 4, 67-74.
47. Kabanov, A.V.; & Vinogradov, S.V. Nanogels as pharmaceutical carriers: finite networks of infinite capabilities. *Angewandte Chemie International Edition*, **2009**, 48, 5418-5429.
48. Yeh, M.K.; Cheng, K.M.; Hu, C.S.; Huang, Y.C.; & Young, J.J. Novel protein-loaded chondroitin sulfate-chitosan nanoparticles: Preparation and characterization. *Acta Biomaterialia*, **2011**, 7, 3804-3812.
49. Hu, C.S.; Tang, S.L.; Chaing, C.H.; Hosseinkhani, H.; Hong, P.D.; & Yeh, M.K. Characterization and anti-tumor effects of chondroitin sulfate-chitosan nanoparticles delivery system. *Journal of Nanoparticle Research*, **2014**, 16, 2672.
50. Santo, V. E.; Gomes, M.E.; Mano, J.F.; & Reis, R.L. Chitosan-chondroitin sulfate nanoparticles for controlled delivery of platelet lysates in boneregenerative medicine. *Journal of Tissue Engineering and Regenerative Medicine*, **2012**, 6, 47-59.
51. Umerska, A.; Corrigan, O.; & Tajber, L. Design of chondroitin sulfate-based polyelectrolyte nanocomplexes: formation of nanocarriers with chitosan and a case study of salmon. *Carbohydrate Polymers*, **2017**, 156, 276-284.
52. Place, L.W.; Sekyi, M.; & Kipper, M.J. Aggrecan-mimetic: glycosaminoglycan-containing nanoparticles for growth factor stabilization and delivery. *Biomacromolecules*, **2014**, 15, 680-689.
53. Hagiwara, K.; Nakata, M.; Koyama, Y.; & Sato, T. The effects of coating DNA/chitosan complexes with chondroitin sulfate on physicochemical characteristics and cell transfection. *Biomaterials*, **2012**, 33, 7251-7260.
54. Tsai, H.Y.; Chiu, C.C.; Lin, P.C.; Chen, S.H.; Huang, S.J.; & Wang, L.F. Antitumor efficacy of doxorubicin released from crosslinked nanoparticulate chondroitin

sulfate/chitosan polyelectrolyte complexes. *Macromolecular Bioscience*, **2011**, 11, 680-688.

55. Boddohi, S.; Killingsworth, C.E.; Kipper, M.J. Polyelectrolyte multilayer assembly as a function of pH and ionic strength using the polysaccharides chitosan and heparin. *Biomacromolecules*. **2008**, 9, 2021-2028.
56. Vinigradov, S.; Batrakova, E.; & Kabanov, A. Poly(ethylene glycol)-polyethyleneimine NanoGek™ particles: novel drug delivery systems for antisense oligonucleotides. *Colloids and Surfaces B: Biointerfaces*, **1999**, 16, 291-304.
57. Funderburgh, J. L. Keratan sulfate biosynthesis. *International Union of Biochemistry and Molecular Biology: Life*, **2002**, 54, 187-194.
58. Wen, Y.; Grondahl, L.; Gallego, M.R.; Jorgensen, L.; Moller, E.H.; & Nielsen, H.M. Delivery of dermatan sulfate from polyelectrolyte complex-containing alginate composite microspheres for tissue regeneration. *Biomacromolecules*, **2012**, 13, 905-917.
59. Yamada, S.; & Sugahara, K. Potential therapeutic application of chondroitin sulfate/dermatan sulfate. *Current Drug Discovery Technologies*, **2008**, 5, 289-301.
60. Ranney, D.; Antich, P.; Dadey, E.; Mason, R.; Kulkarni, P.; Singh, O.; Chen, H.; Constantanescu, A.; & Parke, R. Dermatan carriers for neovascular transport targeting, deep tumor penetration and improved therapy. *Journal of Controlled Release*, **2005**, 109, 222-235.
61. Rapport, M.M.; Weissmann, B.; Linker, A.; & Meyer, K. Isolation of a crystalline disaccharide, hyalobiuronic acid, from hyaluronic acid. *Nature*, **1951**, 168, 996-997.
62. Weissmann, B.; & Meyer, K. The structure of hyalobiuronic acid and of hyaluronic acid from umbilical cord. *Journal of the American Chemical Society*, **1954**, 76, 1753-1757.
63. Dosio, F.; Arpicco, S.; Stella, B.; & Fattal, E. Hyaluronic acid for anticancer drug and nucleic acid delivery. *Advanced Drug Delivery Reviews*, **2016**, 204-236.
64. Rao, N.V.; Yoon, H.Y.; Han, H.S.; Ko, H.; Son, S.; Lee, M.; Lee, H.; Jo, D.G.; Kang, Y.M.; & Park, J.H. Recent developments in hyaluronic acid-based nanomedicine for targeted cancer treatment. *Expert Opinion on Drug Delivery*, **2016**, 13, 239-252.
65. Choi, K.Y.; Saravanakumar, G.; Park, J.H.; & Park, K. Hyaluronic acid-based nanocarriers for intracellular targeting: interfacial interactions with proteins in cancer. *Colloids and Surfaces B: Biointerfaces*, **2012**, 99, 82-94.
66. Ossipov, D.A. Nanostructured hyaluronic acid-based materials for active delivery to cancer. *Expert Opinion on Drug Delivery*, **2010**, 76, 681-703.
67. Kong, M.; Park, H.; Feng, C.; Hou, L.; Cheng, X.; & Chen, X. Construction of hyaluronic acid noisome as functional transdermal nanocarrier for tumor therapy. *Carbohydrate Polymers*, **2013**, 94, 634-641.

68. Tan, J.X.; Wang, X.Y.; Su, X.L.; Li, H.Y.; Shi, Y.; Wang, L.; & Ren, G.S. Upregulation of HYAL1 expression in breast cancer promoted tumor cell proliferation, migration, invasion and angiogenesis. *PLoS One*, **2011**, 6, 22836.
69. Platt, V.M.; & Szoka Jr, F.C. Anticancer therapeutics: targeting macromolecules and nanocarriers to hyaluronan or CD44, a hyaluronan receptor. *Molecular Pharmaceutics*, **2008**, 5, 474-486.
70. Ponta, H.; Sherman, L.; & Herrlich, P.A. CD44: from adhesion molecules to signalling regulators. *Nature Reviews Molecular Cell Biology*, **2003**, 4, 33-45.
71. Mizrahy, S.; Raz, S.R.; Hasqaard, M.; Liu, H.; Soffer-Tsur, N.; Cohen, K.; Dvash, R.; Landsman-Milo, D.; Bremer, M.G.; Moghimi, S.M.; & Peer, D. Hyaluronan-coated nanoparticles: the influence of the molecular weight on CD44-hyaluronan interactions and on the immune response. *Journal of Controlled Release*, **2011**, 156, 231-238.
72. Han, H.S.; Thambi, T.; Choi, K.Y.; Son, S.; Ko, H.; Lee, M.C.; Jo, D.G.; Hae, Y.S.; Kang, Y.M.; Lee, J.Y.; & Park, J.H. Bioreducible shell-cross-linked hyaluronic acid nanoparticles for tumor-targeted drug delivery. *Biomacromolecules*, **2015**, 16, 447-456.
73. Han, H.S.; Choi, K.Y.; Ko, H.; Jeon, J.; Saravanakumar, G.; Suh, Y.D.; Lee, D.S.; & Park, J.H. Bioreducible core-crosslinked hyaluronic acid micelle for targeted cancer therapy. J*ournal of Controlled Release*, **2015**, 200, 158-166.
74. Park, H.K.; Lee, S.J.; Oh, J.S.; Lee, S.G.; Jeong, Y.I.; & Lee, H.C. Smart nanoparticles based on hyaluronic acid for redox-responsive and CD44 receptor-mediated targeting of tumor. *Nanoscale Research Letters*, **2015**, 10, 288.
75. Huang, W.Ch.; Chen, S.H.; Chiang, W.H.; Huang, C.W.; Lo, C.L.; Chern, C.S.; & Chiu, H.C. Tumor microenvironment-responsive nanoparticle delivery of chemotherapy for enhanced selective cellular uptake and transportation within tumor. *Biomacromolecules*, **2016**, 17, 3883-3892.
76. He, M.; Zhao, Z.; Yin, L.; Tang, C.; & Yin, C. Hyaluronic acid coated poly(butylcyanoacrylate) nanoparticles as anticancer drug carriers. *International Journal of Pharmaceutics*, **2009**, 373, 165-173.
77. Abbad, S.; Wang, C.; Waddad, A.Y.; Lv, H.; & Zhou, J. Preparation, in vitro and in vivo evaluation of polymeric nanoparticles based on hyaluronic acid-poly(butyl cyanoacrylate) and D-alpha-tocopheryl polyethylene glycol 1000 succinate for tumor-targeted delivery of morin hydrate. *International Journal of Nanomedicine*, **2015**, 10, 305-320.
78. Jeannot, V.; Mazzaferro, S.; Lavaud, J.; Vanwonterghem, L.; Henry, M.; Arboléas, M.; Vollaire, J.; Josserand, V.; Coll, J.L.; & Lecommandoux, S. Targeting CD44 receptor-positive lung tumors using polysaccharide-based nanocarriers: influence of nanoparticle size and administration route. *Nanomedicine: Nanotechnology, Biology and Medicine*, **2016**, 12, 920-932.

79. Upadhyay, K.K.; Mishra, A.K.; Chuttani, K.; Kaul, A.; Schatz, C.; Le Meins, J.-F.; Mistra, A.; & Lecommandoux, S. The in vivo behaviour and antitumor activity of doxorubicin-loaded poly(ɣ-benzyl L-glutamate)-block-hyaluronan polymersome in Ehrlich ascites tumor-bearing BalB/c mice. *Nanomedicine: Nanotechnology, Biology, and Medicine*, **2012**, 8, 71-80.
80. Upadhyay, K.K.; Bhatt, A.N.; Castro, E.; Mishra, A.K.; Dwarakanath, B.S.; Jain, S.; Schatz, C.; Le Meins, J.F.; Farooque, A.; Chandraiah, G.; Jain, A.K.; Mistra, A.; & Lecommandoux, S. The intracellular drug delivery and anti-tumor activity of doxorubicin loaded poly([gamma]-benzyl-glutamate)-b-hyaluronan polymersomes. *Biomaterials*, **2010**, 31, 2882-2892.
81. Upadhyay, K.K.; Bhatt, A.N.; Castro, E.; Mishra, A.K.; Chuttani, K.; Dwarakanath, B.S.; Schatz, C.; Le Meins, J.-F.; Mistra, A.; & Lecommandoux, S. In vitro and in vivo evaluation of docetaxel loaded biodegradable polymersomes. *Macromolecular Bioscience*, **2010**, 10, 503-512.
82. Haas, S.; Hain, N.; Raoufi, M.; Handschuh-Wang, S.; Wang, T.; Jiang, X.; & Schönherr, H. Enzyme degradable polymersomes from hyaluronic acid-block-poly(ε-Caprolactone) copolymers for the detection of enzymes of pathogenic bacteria. *Biomacromolecules*, **2015**, 16, 832-841.
83. Akima, K.; Ito, H.: Iwata, Y.; Matsuo, K.; Watari, N.; Yanagi, M.; Hagi, H.; Oshima, K.; Yagita, A.; Atomi, Y.; & Tatekawa, I. Evaluation of antitumor activities of hyaluronate binding antitumor drugs: Synthesis, characterization and antitumor activity, *Journal of Drug Targeting*, **1996,** 4, 1-8.
84. Ringsdorf, H. Structure and properties of pharmacologically active polymers. *Journal of Polymer Science: Polymer Symposia*, **1975**, 51, 135-153.
85. Ge, Z.; & Liu, S. Functional block copolymer assemblies responsive to tumor and intracellular microenvironments for site-specific drug delivery and enhanced imaging performance. *Chemical Society Reviews*, **2013**, 42, 7289-7325.
86. Leonelli, F.; La Bella, A.; Francescangeli, A.; Joudioux, R.; Capodilupo, A.; Quagliariello, M.; Migneco, L.M.; Bettolo, R.M.; Crescenzi, V.; & De Luca, G. A new and simply available class of hydrosoluble bioconjugates by coupling paclitaxel to hyaluronic acid through a 4-hydroxybutanoic acid derived linker. Helvetica Chimica Acta, **2005**, 88, 154-159.
87. Montagner, I.M.; Banzato, A.; Zuccolotto, G.; Renier, D.; Campisi, M.; Bassi, P.; Zanovello, P.; Rosato, A. Paclitaxel–hyaluronan hydrosoluble bioconjugate: Mechanism of action in human bladder cancer cell lines. *Urologic Oncologic Seminars and Original Investigations*, **2003**, 31, 1261-1269.

88. Renier, D.; & Bettella, F. Antitumoral bioconjugates of hyaluronic acid or its derivatives obtained by indirect chemical conjugation, and their use in the pharmaceutical field. WIPO Patent No. 2007014784. 9 February **2007**.
89. Campisi, M.; Renier, D.; Pierimarchi, P.; & Serafino, A. Therapeutic use of new pharmaceutical preparations containing antitumoral drugs bound to hyaluronic acid in the treatment of neoplasias. EP2279006, 30 October **2009**.
90. Xu, C.; He, W.; Lv, Y.; Qin, C.; Shen, L.; & Yin, L. Self-assembled nanoparticles from hyaluronic acid-paclitaxel prodrugs fro direct cytosolic delivery and enhanced antitumor activity. *International Journal of Pharmaceutics*, **2015**, 483, 172-181.
91. Xin, D.; Wang, Y.; & Xiang, J. The use of amino acid linkers in the conjugation of paclitaxel with hyaluronic acid as drug delivery system: synthesis, self-assembled property, drug release, and *in vitro* efficiency. *Pharmaceutical Research*, **2010**, 47, 380-388.
92. Oommen, O.P.; Garousi, J.; Sloff, M.; & Varghese, O.P. Tailored doxorubicin-hyaruronan conjugate as a potent anticancer glycol-drug: an alternative to prodrug approach. *Macromolecular Bioscience*, **2014**, 14, 327-333.
93. Lin, S.; Li, T.; Xie, P.; Li, Q.; Wang, B.; Wang, B.; Wang, L.; Li, L.; Wang, Y.; Chen, H.; & Nan, K. Targeted delivery of doxorubicin to tumour tissues by a novel legumain sensitive polygonal nanogel. *Nanoscale*, **2016**, 8, 18400-18411.
94. Zhang, L.; Yao, J. ; Zhou, J.; Wang, T.; & Zhang, Q. Glycyrrhetinic acid-graft-hyaluronic acid conjugate as a carrier for synergistic targeted delivery of antitumor drugs. Int J Pharm. **2013**, 441, 654-664.
95. Han, X.; Wang, Z.; Wang, M.; Li, J.; Xu, Y.; He, R.; Guan, H.; Yue, Z.; & Gong, M. Liver-targeting self-assembled hyaluronic acid-glycyrrhetinic acid micelles enhance hepato-protective effect of silybin after oral administration. *Drug Delivery*, **2016**, 23, 1818-1229.
96. Wang, X.; Gu, X.; Wang, H.; Sun, Y.; Wu, H.; & Mao, S. Synthesis, characterization and liver targeting evaluation of self-assembled hyaluronic acid nanoparticles functionalized with glycyrrhetinic acid. *European Journal of Pharmaceutical Sciences*, **2017**, 96, 255-262.
97. Liang, D.; Wang, A.T.; Yang, Z.Z.; Liu, Y.J.; & Qi, X.R. Enhance cancer cell recognition and overcome drug resistance using hyaluronic acid and α-tocopheryl succinate based multifunctional nanoparticles. *Molecular Pharmaceutics*, **2015**, 12, 2189-2202.
98. Choi, K.Y.; Lee, S.; Park, K.; Kim, K.; Park, J.H; Kwon, I.C.; & Jeong, S.Y. Preparation and characterization of hyaluronic acid-based hydrogel nanoparticles. *Journal of Physics and Chemistry of Solids*, **2008**, 69, 1591-1595.

99. Vafaei, S.Y.; Esmaeili, M.; Amini, M.; Atyabi, F.; Ostad, S.N.; & Dinarvand, R. Self-assembled hyaluronic acid nanoparticles as a potential carrier for targeting the inflamed intestinal mucosa. *Carbohydrate Polymers*, **2016**, 144, 371-381.

100. **Liu**, Y.; Sun, J.; Cao, W.; Yang, J.; Lian, H.; Li, X.; Sun, Y.; Wang, Y.; Wang, S.; & He, Z. Dual targeting folate-conjugated hyaluronic acid polymeric micelles for paclitaxel delivery. *International Journal of Pharmaceutics*, **2011**, 421, 160-169.

101. **Liu**, Y.; Sun, J.; Lian, H.; Cao, W.; Wang, Y.; & He, Z. Folate and CD44 receptors dual-targeting hydrophobized hyaluronic acid paclitaxel-loaded polymeric micelles for overcoming multidrug resistance and improving tumor distribution. *Journal of Pharmaceutical Sciences*, **2014**, 103, 1538-1547.

102. **Uthaman**, S.; Mathew, A.P.; Park, H.J.; Lee, B.; Kim, H.S.; Huh, K.M.; & Park. I.K. IR 780-loaded hyaluronic acid micelles for enhanced tumor-targeted photothermal therapy. carbohydrate polymers, **2018**, 181, 1-9.

103. Šmejkalová, D.; Nešporová, K.; Hermannová, M.; Huerta-Angeles, G.; Čožíková, D.; Vištejnová, L.; Šafránková, B.; Novotný, J.; Kučerík, J.; & Velebný, V. Paclitaxel isomerisation in polymeric micelles based on hydrophobized hyaluronic acid. *International Journal of Pharmaceutics*, **2014**, 466, 147-55.

104. Nešporová, K.; Šógorková, J.; Šmejkalová, D.; Kulhánek, J.; Huerta-Angeles, G.; Kubala, L.; & Velebný, V. Influence of serum albumin on intracellular delivery of drug-loaded hyaluronan polymeric micelles. *International Journal of Pharmaceutics*, **2016**, 511, 638-664.

105. Mayol, L.; Biondi, M.; Russo, L.; Malle, B.M.; Schwach-Abdellaoui, K.; & Borzacchiello, A. Amphiphilic hyaluronic acid derivatives toward the design of micelles for the sustained delivery of hydrophobic drugs. *Carbohydrate Polymers*, **2014,** 102, 110-116.

106. Zhu, Z.; Li, D.; Li, Y.; Yang, X.; & Pan, W. In vitro–in vivo evaluation of hyaluronic acid-based amphiphilic copolymers for tumour targeted delivery: the role of hydrophobic groups. *RSC Advances,* **2017**, 7, 23942-23953.

107. Zhong, Y.; Zhang, J.; Cheng, R.; Deng, C.; Meng, F.; Xie, F.; & Zhong, Z.; Reversibly crosslinked hyaluronic acid nanoparticles for active targeting and intelligent delivery of doxorubicin to drug resistant CD44+ human breast tumor xenografts. *Journal of Controlled Release*, **2015**, 205, 144-154.

108. Ganesh S, Iyer, A.K.; Morrissey, D.V.; & Amiji M.M. Hyaluronic acid based self-assembling nanosystems for CD44 target mediated siRNA delivery to solid tumors. *Biomaterials,* **2013**, 34, 3489-3502.

109. Yin, T.; Wang, L.; Yin, L.; Zhou, J.; & Huo, M. Co-delivery of hydrophobic paclitaxel and hydrophilic AURKA specific siRNA by redox-sensitive micelles for effective treatment of breast cancer. *Biomaterials*, **2015**, 61, 10-25.

110. Dobrovolskaia, M.A.; Aggarwal, P.; Hall, J.B.; & McNeil, S.E. Preclinical studies to understand nanoparticle interaction with immune system and its potential effects on nanoparticle biodistribution. *Molecular Pharmaceutics*, **2008**, 5, 487-495.

111. Lynch, I.; & Dawson, K.A. Protein-nanoparticle interactions. *Nanotoday*, **2008**, 3.

112. Choi, K.Y.; Min, K.H.; Na, J.H.; Choi, K.; Kim, K.; Park, J.H.; Kwona, I.C.; & Jeong, S.Y. Self-assembled hyaluronic acid nanoparticles as a potential drug carrier for cancer therapy: synthesis, characterization, and *in vivo* biodistribution. *Journals of Materials Chemistry*, **2009**, 19, 4102-4107.

113. Montanari, E.; Capece, S.; Di Meo, C.; Meringolo, M.; Coviello, T.; Agostinelli, E.; & Matricardi, P. Hyaluronic acid nanohydrogels as a useful tool for BSAO immobilization in the treatment of melanoma cancer cells. Macromolecular Bioscience, **2013**, 13, 1185-1194.

114. Song, S.; Qi, X.; Xu, J.; Guo, P.; Chen, F.; Li, F.; Yang, X.; Sheng, N.; Wu, Y.; & Pan, W. Hyaluronan-based nanocarriers with CD44-overexpressed cancer cell targeting. *Pharmaceutical Research*, **2014**, 31, 2988-3005.

115. Choi, K.Y.; Yoon, H.Y.; Kim, J.H.; Bae, S.M.; Park, R.W.; Kang, Y.M.; Kim, I.S.; Kwon, I.C.; Choi, K.; Jeong, S.Y.; Kim, K.; & Park, J.H. Smart nanocarrier based on PEGylated hyaluronic acid for cancer therapy. *ACS Nano,* **2011**, 5, 8591-8599.

116. Choi, K.Y.; Jeong, E.J.; Yoon, H.Y.; Lee, B.S.; Na, J.H.; Min, K.H.; Kim, S.Y.; Myung, S.J.; Lee, S.; Chen, X.; Kwon, I.C.; Choi, K.; Jeong, S.Y.; Kim, K.; & Park, J.H. Theranostic nanoparticles based on PEGylated hyaluronic acid for the diagnosis, therapy and monitoring of colon cancer. *Biomaterials*, **2012**, 33, 6186-6193.

117. Han, H.S.; Lee, J.; Kim, H.R.; Chae, S.Y.; Kim, M.; Saravanakumar, G.; Yoon, H.Y.; You, D.G.; Ko, H.; Kim, K.; Kwon, I.C.; Park, J.C.; & Park, J.H. Robust PEGylated hyaluronic acid nanoparticles as the carrier of doxorubicin: mineralization and its effect on tumor targetability in vivo. *Journal of Controlled Release*, **2013**, 168, 105-114.

118. Hu, D.; Mezghrani, O.; Zhang, L.; Chen, Y.; Ke, X.; & Ci, T. GE11 peptide modified and reduction-responsive hyaluronic acid-Based nanoparticles induced higher efficacy of doxorubicin for breast carcinoma therapy. *International Journal of Nanomedicine*, **2016**, 11, 5125-5147.

119. Zhu, Z.; Li, D.; Li, Y.; Yang, X.; & Pan, W. In vitro–in vivo evaluation of hyaluronic acid-based amphiphilic copolymers for tumour targeted delivery: the role of hydrophobic groups. *RSC Advances,* **2017**, 7, 23942-23953.

120. Yoon, H.Y.; Koo, H.; Choi, K.Y.; Kwon, I.C.; Choi, K.; Park, J.H.; & Kim, K. Photo-crosslinked hyaluronic acid nanoparticles with improved stability for in vivo tumor-targeted drug delivery. *Biomaterials,* **2013**, 34, 5273-5280.

121. Yoon, H.Y.; Koo, H.; Choi, K.Y.; Lee, S.J.; Kim, K.; Kwon, I.C.; Leary, J.F.; Park, K.; Yuk, S.H.; Park, J.H.; & Choi, K. Tumor-targeting hyaluronic acid nanoparticles for photodynamic imaging and therapy, *Biomaterials*, **2012**, 33, 3980-3989.
122. Dong, X.; & Liu, C. Preparation and characterization of self-assembled nanoparticles of hyaluronic acid-deoxycholic acid conjugates. *Journal of Nanomaterials*, **2010**, 1-9.
123. Li, J.; Huo, M.; Wang, J.; hou, J.; Mohammad, J.M.; Zhang, Y.; Zhu, Q.; Waddad, A.Y.; & Zhang, Q. Redox-sensitive micelles self-assembled from amphiphilic hyaluronic acid-deoxycholic acid conjugates for targeted intracellular delivery of paclitaxel, Biomaterials, **2012**, 33, 2310-2320.
124. Li, J.; Yin, T.; Wang, L., Yin, L.; Zhou, J.; Huo, M.; Biological evaluation of redox-sensitive micelles based on hyaluronic acid-deoxycholic acid conjugates for tumor-specific delivery of paclitaxel. *International Journal of Pharmaceutics*, **2015,** 483, 38-48.
125. Yadav, A.K.; Mishra, P.; Jain, S.; Mishra, A.K.; & Agrawal, G.P. Preparation and characterization of HA-PEG-PCL intelligent core corona nanoparticles for delivery of doxorubicin, Journal of Drug Targeting 16, **2008**, 464-478.
126. Tizzotti, M.; Charlot, A.; Fleury, E.; Stenzel, M.; & Bernard, J. Modification of polysaccharides through controlled/living radical polymerization grafting-towards the generation of high performance hybrids. *Macromolecular Rapid Communications*, **2010**, 31, 1751-1772.
127. Schanté, C.E.; Zuber, G.; Herlin, C.; & Vandamme, T.F. Chemical modifications of hyaluronic acid for the synthesis of derivatives for a broad range of biomedical applications. *Carbohydrate Polymers*, **2011**, 85, 469-489.
128. Oh, E.J.; Park, K.; Kim, K.S.; Kim, J.; Yang, J.A.; Kong, J.H.; Lee, M.Y.; Hoffman, A.S.; Hahn, S.K. Target specific and long-acting delivery of protein, peptide, and nucleotide therapeutics using hyaluronic acid derivatives. *Journal of Controlled Release*, **2010**, 141, 2-12.
129. FDA/Center for rug evaluation and research, inactive ingredient search for approved drug products. available from URL http://www. Accessdata.fda.goc/scripts/cder/iig/inex.Cfm
130. Pitarresi, G.; Palumbo, F.S.; Albanese, A.; Fiorica,C.; Picone, P.; & Giammona, G. Self-assembled amphiphilic hyaluronic acid graft copolymers for targeted release of antitumoral drug. *Journal of Drug Targeting*, **2010**, 18, 264-276.
131. Wang, S.; Zhang, J.; Wang, Y.; & Chen, M. Hyaluronic acid-coated PEI-PLGA nanoparticles mediated co-delivery of doxorubicin and miR-542-3p for triple negative breast cancer therapy. *Nanomedicine: Nanotechnology, Biology and Medicine*, **2016**, 12, 411-420.

132. Son, G.; Kim, H.; Ryu, J.; Chu, C.; Kang, D.; Park, S.; & Jeong, Y.I. Self-assembled polymeric micelles based on hyaluronic acid-G-Poly(d,l-Lactide-Co-Glycolide) copolymer for tumor targeting. *International Journal of Molecular Sciences*, **2014**, 15, 16057-16068.
133. Lee, C.S.; & Na, K. Photochemically triggered cytosolic drug delivery using pH-responsive hyaluronic acid nanoparticles for light-induced cancer therapy. *Biomacromolecules,* **2014**, 15, 4228-4238.
134. Yadav, A.K.; Mishra, P.; Mishra, A.K.; Mishra, P.; Jain, S.; & Agrawal, G.P. Development and characterization of hyaluronic acid–anchored PLGA nanoparticulate carriers of doxorubicin. *Nanomedicine: Nanotechnology, Biology and Medicine,* **2007**, 3, 246-257.
135. Yadav, A.K.; Agarwal, A.; Rai, G.; Mishra, P.; Jain, S.; Mishra, A.K.; Agrawal, H.; & Agrawal, G.P. Development and characterization of hyaluronic acid decorated PLGA nanoparticles for delivery of 5-Fluorouracil. *Drug Delivery*, **2010**, 17, 561-572.
136. Hu, K.; Zhou, H.; Liu, Y.; Liu, Z.; Liu, J.; Tang, J.; Li, J.; Zhang, J.; Sheng, W.; Zhao, Y.; Wu, Y.; & Chen, C. Hyaluronic acid functional amphipathic and redox-responsive polymer particles for the co-delivery of doxorubicin and cyclopamine to eradicate breast cancer cells and cancers stem cells. *Nanoscale*, **2015**, 7, 8607-8618.
137. Knop, K.; Hoogenboom, R.; Fischer, D.; & Schubert, U.S. Poly(ethylene Glycol) in drug delivery: pros and cons as well as potential alternatives. *Angewandte Chemie International Edition*, **2010**, 49, 6288-6308.
138. Jevsevar, S.; Kunstelj, M.; & Porekar, V.G. PEGylation of therapeutic proteins, *Biotechnology Journal*, **2010**, 5, 113-128.
139. Bauer, M.; Lautenschlaeger, C.; Kempe, K.; Tauhardt, L.; Schubert, U.S.; & Fischer, D. Poly(2-Ethyl-2-Oxazoline) as alternative for the stealth polymer poly(ethylene Glycol): comparison of in vitro cytotoxicity and hemocompatibility. *Macromolecular Bioscience*, **2012**, 12, 986-998.
140. Gu, Z. Bioinspired and biomimetic polymer systems for drug and gene delivery. **2015**, Wiley-VCH.
141. Qiu, L.; Li, Z.; Qiao, M.; Long, M.; Wang, M.; Zhang, X.; Tian, C.; & Chen, D. Self-Assembled pH-Responsive Hyaluronic Acid–g-Poly(l-Histidine) Copolymer Micelles for Targeted Intracellular Delivery of Doxorubicin. *Acta Biomaterialia*, **2014**, 10, 2024-2035.
142. Qiu, L.; Qiao, M.; Chen, Q.; Tian, C.; Long, M.; Wang, M.; Li, Z.; Hu, W.; Li, G.; Cheng, L.; Cheng, L.; Hu, H.; Zhao, X.; & Chen, D. Enhanced effect of pH-sensitive mixed copolymer micelles for overcoming multidrug resistance of doxorubicin. *Biomaterials*, **2014**, 35, 9877-9887.
143. Hong, W.; Chen, D.; Zhang, X.; Zeng, J.; Hu, H.; Zhao, X.; & Qiao, M. Reversing multidrug resistance by intracellular delivery of Pluronic® P85 unimers. *Biomaterials*, **2013**, 34, 9602-9614.

144. Lee, C.S.; & Na, K. Photochemically triggered cytosolic drug delivery using pH-responsive hyaluronic acid nanoparticles for light-induced cancer therapy. *Biomacromolecules*, **2014**, 15, 4228-4238.
145. Jing, J.; Alaimo, D.; De Vlieghere, E.; Jerôme, C.; De Wever, O.; De Geest, B.G.; & Auzely-Velty, R. Tunable self-assembled nanogels composed of well-defined thermoresonsive hyaluronic acid-polymer conjugates. Journal of Materials Chemistry B, 2013, 1, 3883-3887.
146. Garcia, F.; Rippe, M.; Companhoni, M.; Stefanello, T.; Louage, B.; Van Herck, S.; Sancey, L.; Coll, J.L.; De Geest, B.; & Nakamuea, C.V. Hyauronic acid-based nanogels with tunable stability using ketone-hydrazide cross-linking for anticancer therapy. *ACS Applied Materials & Interfaces* (under publication)
147. Stefanello, T.F.; Couturaud, B.; Szarpak-Jankowska, A.; Fournier, D.; Louage, B.; Garca, F.P.; Nakamura, C.V.; De Geest, B.; Woisel, P.; Van der Sanden, B.; & Auzely-Velty. R. Coumarin-containing thermoresponsive hyaluronic acid-based nanogels as delivery systems for anticancer chemotherapy. *Nanoscale*, **2017**, 9, 12150-12162.
148. Iovu, M.; Dumais, G.; & Du Souich, P. Anti-inflammatory activity of chondroitin sulfate. *Osteoarthritis Cartilage*, **2008**, 16, 14-18.
149. Volpi, N. Analytical aspects of pharmaceutical grade chondroitin sulfates. *Journal of Pharmaceutical Sciences*, **2007**, 96, 3168-3180.
150. Li, F., & Na, K. Self-assembled chlorin e6 conjugated chondroitin sulfate nanodrug for photodynamic therapy. *Biomacromolecules*, **2011**, 12, 1724-1730.
151. Lo, Y.L.; Sung, K.H.; Chiu, C.C.; & Wang, L.F. Chemically conjugating polyetlenimine with chondroitin sulfate to promote CD44 mediated endocytosis gene delivery. *Molecular Pharmaceutics*, **2013**, 10, 664-676.
152. Mucci, A.; Schenetti, L.; & Volpi, N. ^{1}H and ^{13}C nuclear magnetic resonance identification and characterization of components of chondroitin sulfates of various origin. *Carbohydrate Polymers*, **2000**, 41, 37-45.
153. Wang, C.; Li, M.; Yang, T.; Ding, X.; Bao, X.; Ding, Y.; Xiong, H.; Wu, Y.; Wang, W.; & Zhou, J. A self-assembled system for tumor-targeted co-delivery of drug and gene. *Materials Science and Engineering: C*, **2015**, 56, 280-285.
154. Zhao, L.; Liu, M.; Wang, J.; & Zhai, G. Chondroitin sulfate-based nanocarriers for drug/gene delivery. *Carbohydrate Polymers*, **2015**, 133, 391-399.
155. Chen, A.L.; Ni, H.C.; Wang, L.F.; & Chen, J.S. Biodegradable amphiphilic copolymers based on polycaprolactone graft chondroitin sulfate as drug carriers. Biomacromolecules, **2008**, 9, 2447-2457**.**

156. Yu, C.; Gao, C.; Lü, S.; Chen, C.; Huang, Y.; & Liu, M. Redox-responsive shell-sheddable micelles self-assembled from amphiphilic chondroitin sulfate-cholesterol conjugates for triggered intracellular drug release. *Chemical Engineering Journal*, **2013**, 228, 290-299.
157. Yu, C.; Gao, C.; Lü, S.; Chen, Yang, J.; Di, X.; & Liu, M. Facile preparation of pH-sensitive micelles self-assembled from amphiphilic chondroitin sulfate-histamine conjugate for triggered intracellular drug release. *Colloids and Surfaces B: Biointerfaces,* **2014**, 115, 331-339.
158. Liu, M.; Du, H.; & Zhai, G. Self-assembled nanoparticles based on chondroitin sulfate-deoxycholic acid conjugates for docetaxel delivery: effect of degree of substitution of deoxycholic acid. *Colloids and Surfaces B: Biointerfaces*, **2016**, 146, 235-244.
159. Lee, C.T.; Huang, C.P.; & Lee, Y.D. Preparation of amphiphilic poly(L-Lactide)-graft-chondroitin sulfate copolymer self-aggregates and its aggregation behavior. *Biomacromolecules,* **2006**, 7, 1179-1186.
160. Lee, J.Y.; Park, J.H.; Lee, J.J.; Lee, S.Y.; Chung, S.J.; Cho, H.J.; & Kim, D.D. Polyethylene glycol-conjugated chondroitin sulfate A derivative nanoparticles for tumor-targeted delivery of anticancer drugs. *Carbohydrate Polymers*, **2016**, 151, 68-77.
161. Xiao, Y.; Li, P.; Cheng, Y.; Zhang, X.; Sheng, J.; Wang, D.; Li, J.; Zhanga, Q.; Zhonga, C.; Caoa, R.; & Wanga, F. Enhancing the intestinal absorption of low molecular weight chondroitin sulfate by conjugation with α-linolenic acid and the transport mechanism of the conjugates. *International Journal of Pharmaceutics*, **2014**, 465, 143-158.
162. Peng, Y.S.; Lin, S.C.; Huang, S.J.; Wang, Y.M.; Lin, Y.J.; Wang, L.F. Lin, Y.J.; Wang, L.F.; & Chen, J.S. Chondroitin sulfate-based anti-inflammatory macromolecular prodrugs. *European Journal of Pharmaceutical Sciences*, **2006**, 29, 60-69.
163. Park, W.; Park, S.J.; & Na, K. Potential of self-organizing nanogel with acetylated chondroitin sulfate as an anti-cancer drug carrier. *Colloids and Surfaces B: Biointerfaces*, **2010**, 79, 501-508.
164. Lü, S.; Gao, N.; Cao, Z.; Gao, C.; Xu, X.; Bai, X.; Feng, C.; & Liu, M. Pluronic F127–chondroitin sulfate micelles prepared through a facile method for passive and active tumor targeting. *RSC Advances*, **2016**, 6, 49263-49271.
165. Zhang, H.; Xu, J.; Xing, L.; Ji, J.; Yu, A.; & Zhai, G. Self-Assembled micelles based on chondroitin sulfate/poly (D,L-lactideco-glycolide) block copolymers for doxorubicin delivery. *Journal of Colloid and Interface Science*, **2017**, 492, 101-111.
166. Fajardo, A.R.; Guerry, A.; Britta, E.A.; Nakamura, C.V.; Muniz, E.C.; Borsali, R.; & Halila, S. Sulfated glycosaminoglycan-based block copolymer: preparation of biocompatible chondroitin sulfate- b -poly(lactic acid) micelles. *Biomacromolecules*, **2014**, 15, 2691-2700.

167. Xi, J.; Zhou, L.; & Fei, Y. Preparation of chondroitin sulfate nanocapsules for use as carries by the interfacial polymerization method. *International Journal of Biological Macromolecules*, **2012**, 50, 157-163.
168. Oommen, O.P.; Duehrkop, C.; Nilsson, B.; Hilborn, J.; & Varghese, O.P. Multifunctional hyaluronic acid and chondroitin sulfate nanoparticles: impact of glycosaminoglycan presentation on receptor mediated cellular uptake and immune activation. *ACS Applied Materials & Interfaces,* **2016**, 8, 20614-20624.
169. Zacharski, L.R.; & Ornstein, D.L. Heparin and Cancer. *Thrombosis and Haemostasis*, **1998**, 80, 10-23.
170. Laremore, T.N.; Zhang, F.; Dordick, J.S.; Liu, J.; & Lindardt, R.J. Recent progress and applications in glycoaminoglycan and heparin research. *Current Opinion in Chemical Biology*, **2009**, 13, 633-640.
171. Arbit, E.; Goldberg, M.; Gomez-Orellana, I.; & Majuru, S. Oral heparin: status review. *Thrombosis Journal*, **2006**, 4, 6.
172. Fan, B.; Xing, Y.; Zheng, Y.; Sun, C.; & Liang, G. pH-responsive thiolated chitosan nanoparticles for oral low-molecular weight heparin delivery: in vitro and in vivo evaluation. *Drug Delivery*, **2016**, 23, 238-247.
173. Ye, L.; Gao, Z.; Zhou, Y.; Yin, X.; Zhang, X.; Zhang, A.; & Feng, Z.A. pH-sensitive binary drug delivery system based on poly(caprolactone)-heparin conjugates: a pH-sensitive binary drug delivery system. *Journal of Biomedical Materials Research Part A*, **2014**, 102, 880-889.
174. Jee, K.S.; Park, H.D.; Park, K.D.; Kim, Y.H.; & Shin, J.W. Heparin conjugated polylactide as a blood compatible material. *Biomacromolecules,* **2004**, 5, 1877-1881.
175. Khatun, Z.; Nurunnabi, M.; Cho, K.J.; & Lee, Y.K. Imaging of the GI tract by QDs loaded heparin-deoxycholic acid (DOCA) nanoparticles. *Carbohydrate Polymers*, **2012**, 90, 1461-1468.
176. Mei, L.; Liu, Y.; Zhang, H.J.; Zhang, Z.; Gao, H.; & He, Q. Antitumor and antimetastasis activities of heparin-based micelle served as both carrier and drug. *ACS Applied Materials & Interfaces*, **2016**, 8, 9577-9589.
177. Park, K.; Kim, K.; Kwon, I.C.; Kim, S.K.; Lee, S.; Lee, D.Y.; & Byun, Y. Preparation and characterization of self-assembled nanoparticles of heparin-deoxycholic acid conjugates. *Langmuir*, **2004**, 20, 11726-11731.
178. Debele, T.A.; Mekuria, S.L.; & Tsai, H.C. Synthesis and characterization of redox-sensitive heparin-β-Sitosterol micelles: their Application as carriers for the pharmaceutical agent, doxorubicin, and investigation of their antimetastatic activities in vitro. *Materials Science and Engineering: C*, **2017**, 75, 1326-1338.

179. Yan, X.; Yang, Y.; He, L.; Peng, D.; & Yin, D. Gambogic acid grafted low molecular weight heparin micelles for targeted treatment in a hepatocellular carcinoma model with an enhanced anti-angiogenesis effect. *International Journal of Pharmaceutics*, **2017**, 522, 110-118.
180. Li, Q.; Gan, L.; Tao, H.; Wang, Q.; Ye, L.; Zhang, A.; & Feng, Z. The synthesis and application of heparin-based smart drug carrier. *Carbohydrate Polymers*, **2016**, 140, 260-268. ht.
181. Bera, S.; & Linhardt, R.J. Design and synthesis of unnatural heparosan and chondroitin building blocks. *The Journal of Organic Chemistry*, **2011**, 76, 3181-3193.
182. Lidholt, K. Biosynthesis of glycosaminoglycans in mammalian cells and in bacteria. *Biochemical Society Transactions*, **1997**, 25, 866-870.
183. Esko, J.D.; & Lindahl, U. Molecular diversity of heparan sulfate. *Journal of Clinical Investigation*, **2001**,108, 169-173.
184. Laremore, T.N.; Zhang, F.; Dordick, J.S.; Liu, J.; & Linhardt, R.J. Recent progress and applications in glycosaminoglycan and heparin research. *Current Opinion in Chemical Biology*, **2009**, 13, 633-640.
185. Linhardt, R.; Dordick, J.; Deangelis, P.; & Liu, J. Enzymatic synthesis of glycosaminoglycan heparin. *Seminars in Thrombosis and Hemostasis*, **2007**, 33, 453-465.
186. Chavaroche, A.; Lambertus, A.E.; Van den Broek, A.M.; & Eggink, G. Production methods for heparosan, a precursor of heparin and heparan sulfate. *Carbohydrate Polymers*, **2013**, 93, 38-47.
187. Kuberan, B.; Beeler, D.L.; Lawrence, R.; Lech, M.; & Rosenberg, R.D. Rapid two-step synthesis of mitrin from heparosan: a replacement for heparin. *Journal of the American Chemical Society*, **2003**, 125, 12424-12425.
188. Wang, Z.; Ly, M.; Zhang, F.; Zhong, W.; Suen, A.; Hickey, A.M.; Dordick, J.S.; & Linhardt, J.R. E. Coli K5 Fermentation and the preparation of heparosan, a bioengineered heparin precursor. *Biotechnology and Bioengineering*, **2010**,107, 964-973.
189. Raman, K.; Kuberan, B.; & Arungundram, S. Chemical modification of heparin and heparosan. *In Glycosaminoglycans*, **2015**, edited by Kuberan Balagurunathan, Hiroshi Nakato, and Umesh R. Desai, 31-36. Methods in Molecular Biology 1229. Springer New York.
190. DeAngelis, P.L. Heparosan, a promising 'naturally good' polymeric conjugating vehicle for delivery of injectable therapeutics. *Expert Opinion on Drug Delivery*. **2015**, 12, 340-352.

191. Li, P.; Sheng, J.; Liu, Y.; Li, J.; Liu, J; & Wang, F. Heparosan-derived heparan sulfate/heparin-like compounds: one kind of potential therapeutic agents. *Medicinal Research Reviews*, **2013**, 33, 665-692.
192. Grinda, M.; Clarhaut, J.; Renoux, B.; Tranoy-Opalinski, I.; & Papot. S. A Self-immolative dendritic glucuronide prodrug of doxorubicin. *MedChemComm*, **2012**, 3, 68-70.
193. Raman, K., Mencio, C., Desai, U.R., & Kuberan, B. Sulfation patterns determine cellular internalization of heparin-like polysaccharides. *Molecular Pharmaceutics*, **2013**, 10, 1442-1449.
194. Harris, E.N.; & Weigel, P.H. The ligand-binding profile of HARE: hyaluronan and chondroitin sulfates A, C, and D bind to overlapping sites distinct from the sites for heparin, acetylated low-density lipoprotein and dermatan sulfate. *Glycobiology*, **2008**, 18, 638-648.
195. Jordan, S.W.; & Chaikof, E.L. Novel thromboresistant materials. *Journal of Vascular Surgery*, **2007**, 45, 104-115.
196. Pikas**,** D.S.; Li, J.P.; Vlodavsky, I.; & Lindahl, U. Substrate specificity of heparanases from human hepatoma and platelets. *Journal of Biological Chemistry*, **1998**, 273, 18770-18777.
197. Capila, I.; & Lindhart, R.J. Heparin-protein interactions. *Angewandte Chemie International Edition*, **2002**, 41, 391-412.
198. Barzu, T.; Van Rijn, J.L.; Petitou, M.; Tobelem, G.; & Caen, J.P. Heparin degradation in the endothelial cells. *Thrombosis Research*, 1987, 47, 601-609.
199. DeAngelis, P.L. Heparosan-based biomaterials and coatings and methods of production and use thereof. Google Patents, **2013**, US 8580290 B2.
200. DeAngelis, P. L. Heparosan-multimolecular assembly drug delivery compositions and methods of making and using same. Google Patents, **2015**, US 20150140073 A1.
201. Chen, J.X.; Liu, W.; Zhang, M.; & Chen, J.H. Heparosan based negatively charged nanocarrier for rapid intracellular drug delivery. *International Journal of Pharmaceutics*, **2014**, 473, 493-500.
202. Chen, J.X.; Zhang, M.; Liu, W.; Lu, G.Z.; & Chen, J.H. Construction of serum resistant micelles based on heparosan for targeted cancer therapy. *Carbohydrate Polymers*, **2014**, 110, 135-141.

Chapitre 2 - Synthèse de nouveaux copolymères thermosensibles

I Introduction

Les copolymères thermosensibles ciblés dans cette thèse ont été conçus de façon à induire l'auto-association en milieu aqueux de polysaccharides en nanoparticules (nanogels), après greffage le long de la chaîne polysaccharidique. Afin d'améliorer les propriétés de ces nanogels en termes de stabilité et de capacité à transporter des molécules hydrophobes, il s'est avéré nécessaire de développer une nouvelle famille de copolymères permettant la formation de nanogels à température ambiante. Comme nous l'avons souligné dans la partie bibliographique, il est important de tenir compte de l'augmentation de la température d'auto-association du copolymère, résultant de sa déshydratation, une fois greffé sur le polysaccharide hydrophile, chargé négativement.

Ainsi, les travaux présentés dans ce chapitre portent sur la mise au point d'un copolymère thermosensible possédant une température de point de trouble (T_{cp}) inférieure à la température ambiante. Cette condition est nécessaire pour conférer au polysaccharide modifié par ce copolymère une température d'agrégation critique (CAT) inférieure à la température ambiante (~ 25 °C).

Roy et al. ont répertorié l'ensemble des systèmes de polymères thermosensibles à LCST (Lower Critical Solution Temperature) [1]. Il en existe une dizaine dont le plus étudié est le système reposant sur les poly(*N*-alkyl(meth)acrylamide)s, dans lequel le poly(*N*-isopropylacrylamide) (PNIPAM) fait figure de référence comme polymère thermosensible, depuis la publication en 1967 par Scarpa et al. de sa transition de phase [2]. Cependant, la température critique inférieure de démixtion de ce polymère est supérieure à la température ambiante (LCST ~ 32°C) et sa toxicité potentielle n'autorise pas son utilisation *in vivo*. Une autre catégorie de polymères thermosensibles, des copolymères à base de (méth)acrylate d'oligo(éthylène glycol) (OEGMA), a été rapportée plus récemment. Plusieurs études ont montré l'excellente biocompatibilité *in vitro* ou *in vivo* de ces copolymères, comme observé avec le poly(éthylène glycol) [3], autorisé par l'agence américaine du médicament (Food and Drug Administration - FDA). Ainsi, plusieurs nanosystèmes incluant des copolymères à base d'OEGMA, biocompatibles et thermosensibles, ont été élaborés au cours de ces quinze dernières années [4-9].

Dans ce contexte, un copolymère de méthacrylate de di(éthylène glycol) et d'OEGMA (poly(DEGMA-co-OEGMA), avec un ratio DEGMA/OEGMA de 95:5) avait été synthétisé au sein de l'équipe et utilisé pour la conception de nanogels à base d'acide hyaluronique (HA) [10-11]. Cependant, la T_{cp} de ce copolymère, supérieure à la température ambiante et proche de la température corporelle (T_{cp} ~ 34°C à 3 g/L dans le PBS), ne permet pas de garantir une bonne stabilité des nanogels lors des manipulations et des tests *in vivo*. Compte tenu de ces observations, nous nous sommes proposés de remplacer le monomère OEGMA par un monomère hydrophobe, le méthacrylate de *n*-butyle (BMA), afin d'obtenir un copolymère présentant une T_{cp} inférieure à 25°C (Figure 2.1). Afin de comparer ce copolymère, poly(DEGMA-co-BMA), avec le poly(DEGMA-co-OEGMA) utilisé pour réaliser des nanogels de HA « de première génération », le ratio DEGMA/BMA a été fixé à 95/5.

La stratégie de synthèse retenue pour élaborer ces copolymères est la polymérisation par transfert de chaîne réversible par addition-fragmentation (RAFT, Reversible-Addition Fragmentation Chain Tranfer). Cette méthode de polymérisation radicalaire contrôlée permet non seulement d'obtenir des (co)polymères avec des masses molaires prédéfinies et homogènes (polydispersité (*Đ*) ~ 1), mais aussi de les fonctionnaliser sélectivement à une extrémité [12]. Par ailleurs, il a été montré que des polymères synthétisés par polymérisation radicalaire contrôlée, possèdent des transitions de phase plus étroites que des polymères obtenus par polymérisation radicalaire classique, caractérisés par des polydispersités plus élevées (*Đ* ~ 2) [13].

Ce chapitre décrit dans une première partie la synthèse de copolymères thermosensibles poly(DEGMA-co-BMA) par la polymérisation RAFT. La seconde partie est consacrée à l'étude des propriétés des copolymères obtenus.

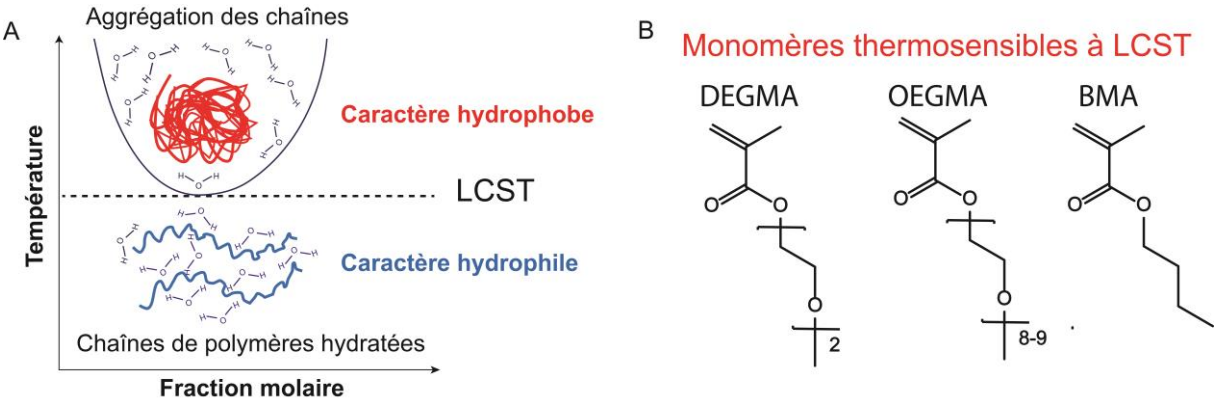

Figure 2.1 *A) Illustration du diagramme de phase d'un polymère thermosensible en solution en fonction de la température et de la fraction molaire. B) Monomères thermosensibles présentés dans l'introduction.*

II Polymérisation radicalaire contrôlée de poly(DEGMA-co-BMA)

Des poly(DEGMA-co-BMA) possédant différentes masses molaires moyennes en nombre (M_n) allant de 5 à 16 kg/mol ont été synthétisés par polymérisation RAFT afin d'évaluer l'influence de ce paramètre sur leur comportement en solution (Figure 2.2 et Tableau 2.2).

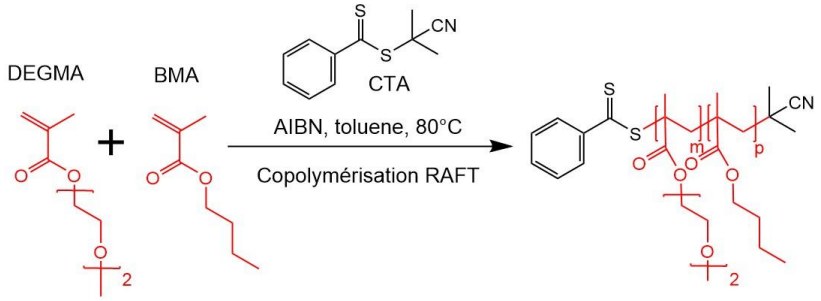

Figure 2.2 *Synthèse de la polymérisation de type RAFT du poly(DEGMA-co-BMA).*

La méthode de polymérisation RAFT, introduite en 1998, repose sur la polymérisation radicalaire d'un monomère en présence d'un agent de transfert de chaîne (Agent RAFT ou CTA), qui régule la concentration en radicaux, dans le milieu, tout au long de la réaction [14]. En effet, cet agent RAFT permet de terminer de manière réversible les macro-radicaux en croissance pour les transformer en « espèces dormantes », momentanément inactives. La Figure 2.3 illustre le mécanisme d'activation/désactivation de la chaîne en croissance par l'agent RAFT. Ainsi, le processus global de polymérisation donne lieu à une durée d'amorçage des chaînes courtes par rapport à celle de la propagation, et des réactions de terminaison et de transfert fortement minimisées. Les chaînes sont encore sous forme dormante dans leur grande majorité en fin de polymérisation.

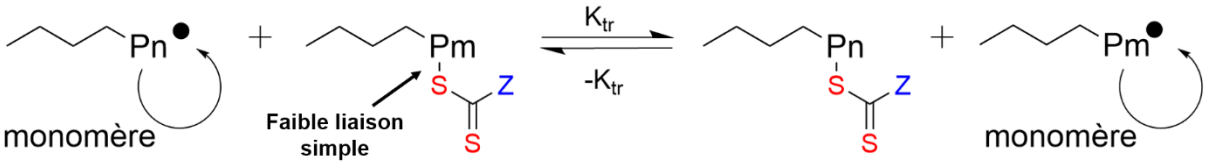

Figure 2.3 *Mécanisme de transfert de chaîne par addition-fragmentation réversible lors de la polymérisation de type RAFT. Rôle de l'agent de transfert de chaîne (CTA) avec P_n et P_m, les chaînes de polymères en croissance, K_{tr}, la constante de transfert de chaîne de l'agent RAFT et Z, le groupement qui détermine le taux d'addition-fragmentation.*

L'utilisation d'un agent RAFT approprié permet de synthétiser des polymères à architectures contrôlées, possédant des polydispersités proches de 1 et fonctionnalisés sélectivement à une extrémité (Figure 2.4). Le choix de l'agent de transfert est donc déterminant [15]. Concernant la copolymérisation des méthacrylates, les agents RAFT les plus utilisés comprennent des composés thiocarbonylthio comme les dithiobenzoates [16-17].

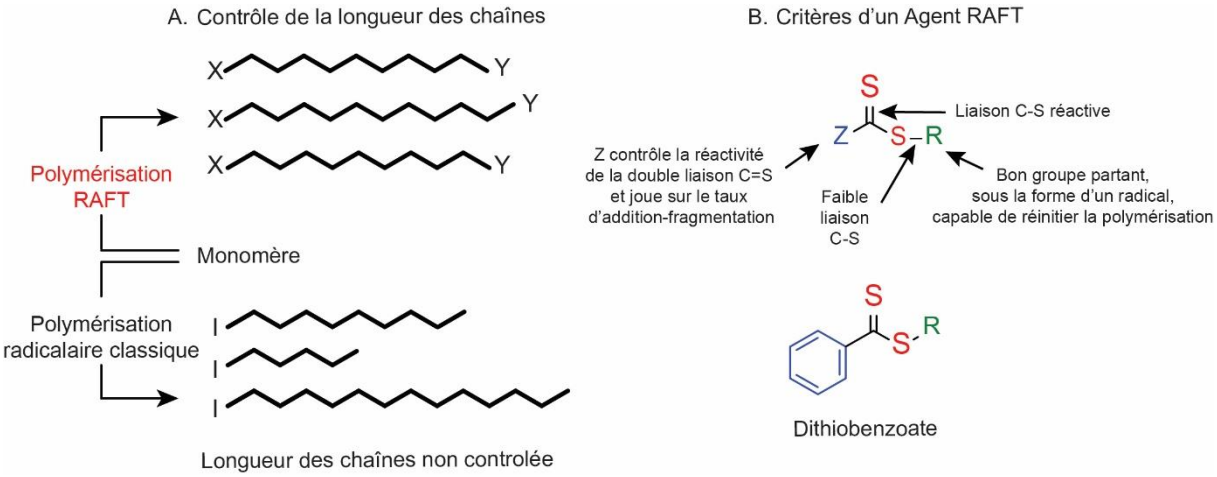

Figure 2.4 *A) Comparaison schématique de polymères synthétisés par polymérisation radicalaire classique et par la méthode RAFT. B) Représentation de la structure d'un agent RAFT, où les groupements R et Z influencent la cinétique de polymérisation, la solubilité de l'agent RAFT et donc le degré de contrôle de la longueur des chaînes. Le choix de l'agent RAFT est crucial pour obtenir des polymères de faible polydispersité et d'architecture contrôlée. Adapté de Moad et al. [18].*

Par ailleurs, ce type d'agent RAFT permet, après aminolyse du dithioester, l'introduction d'une fonction thiol à une extrémité du polymère, pouvant être utilisée pour réaliser des réactions de couplage « thiol-ène » (Figure 2.5).

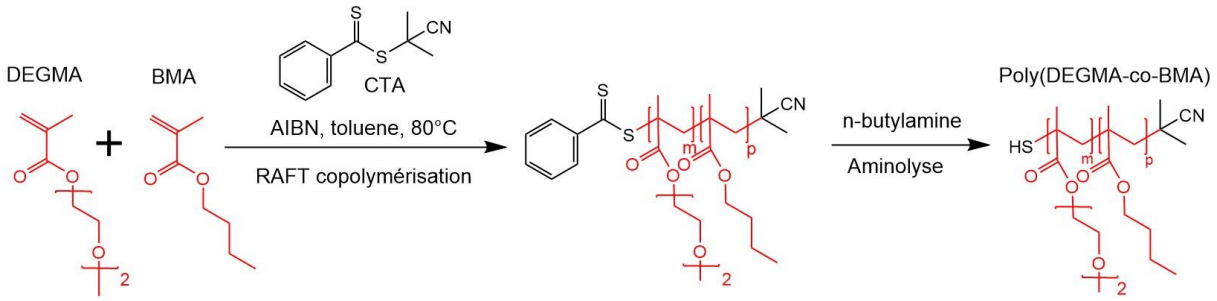

Figure 2.5 *Réaction de polymérisation RAFT du poly(DEGMA-co-BMA) suivie d'une étape d'aminolyse.*

II.1 Vérification expérimentale du contrôle de la polymérisation RAFT

Un suivi cinétique des réactions de copolymérisation a été réalisé par RMN ^{1}H afin de s'assurer du caractère contrôlé de la polymérisation par RAFT (Figure 2.6). Concrètement, l'avancement de la réaction a été suivi à partir de :

- la disparition progressive des signaux i) des protons éthyléniques du DEGMA (Hb et Hb') à 6,2 et 5,6 ppm et du BMA (Hc et Hc') à 6,1 et 5,5 ppm et ii) des protons méthyléniques (Hd) du monomère DEGMA à 4,4 ppm. Le monomère BMA étant présent en faible quantité il est plus difficile d'observer ses signaux caractéristiques.
- l'apparition progressive des signaux i) des protons du groupe méthyle (Hg) du poly(DEGMA-co-BMA) à 4,2 ppm ainsi que celle des signaux des protons CH_3 du groupe butyle du poly(DEGMA) et du poly(BMA) centrés sur 1 ppm.

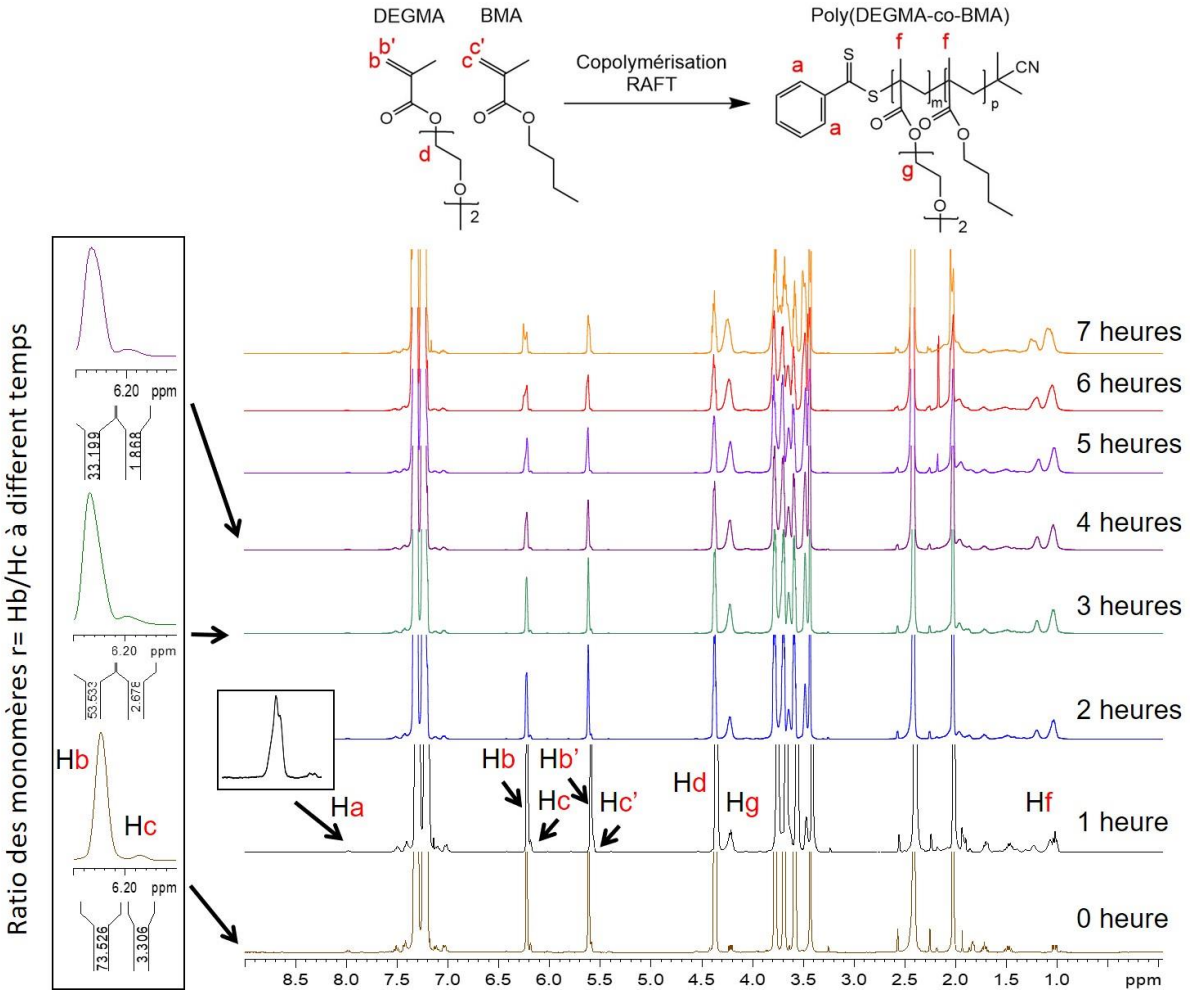

Figure 2.6 *Suivi cinétique par analyse des spectres RMN ^{1}H (400 MHz, $CDCl_3$, 25°C) au cours de la polymérisation du poly(DEGMA-co-BMA) à t= 0h,1h, 2h, 3h, 4h, 5h, 6h et 7h pour un ratio en monomères DEGMA/BMA de 95/5 soit r~19.*

La comparaison de ces spectres avec ceux des réactifs en présence : CTA, BMA et DEGMA respectivement (Figure 2.7), permet d'identifier plus clairement l'attribution des signaux et comprendre leur évolution au cours de la polymérisation.

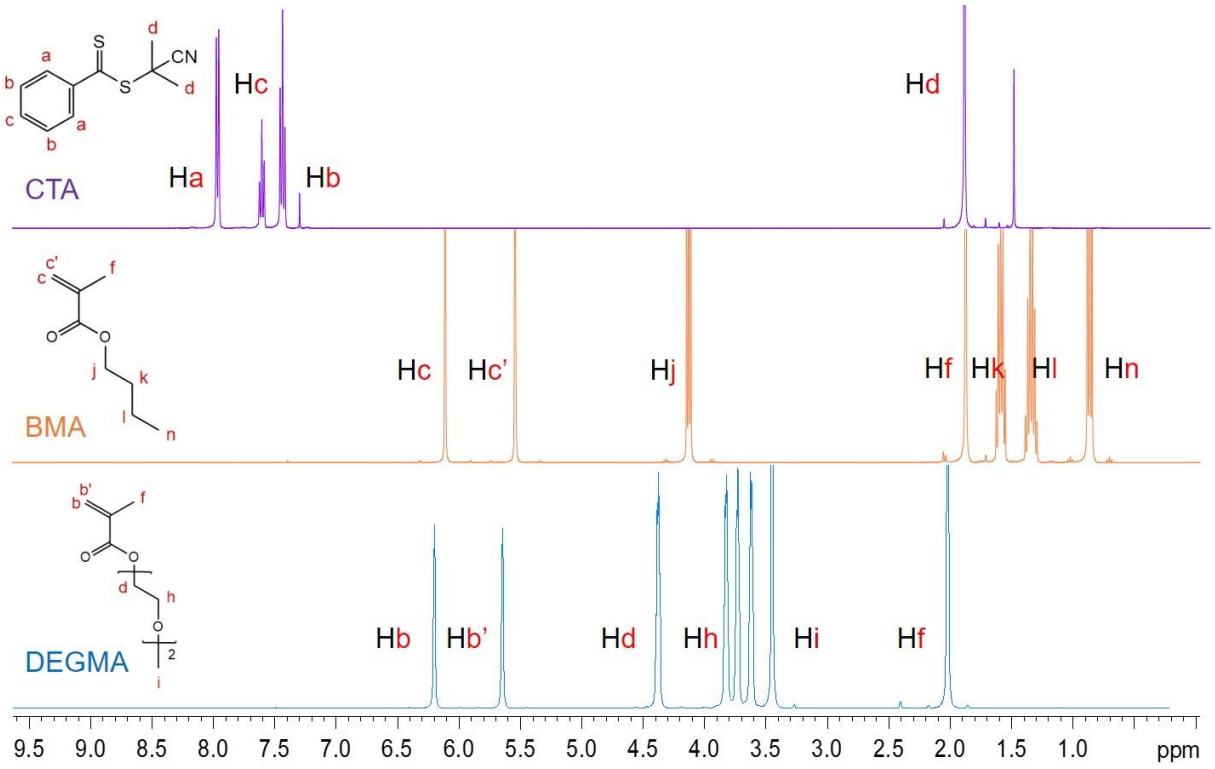

Figure 2.7 *Spectres RMN ^{1}H (400 MHz, $CDCl_3$, 25°C) des monomères DEGMA et BMA (après purification) ainsi que du CTA.*

L'intégration des signaux des différents protons mentionnés dans la Figure 2.6, nous a permis de calculer la masse molaire moyenne en nombre du copolymère (M_n), le taux de conversion (ρ) et le rapport de réactivité des monomères (r) en fonction du temps (t) en utilisant les équations appliquées à l'analyse RMN ^{1}H regroupées dans le Tableau 2.1.

La réactivité des monomères se calcule théoriquement par le rapport des constantes de réactivité ($r_{théo}$) cela se traduit expérimentalement lors de l'analyse RMN ^{1}H par le ratio des intégrales des monomères (r). Les deux monomères ayant des structures similaires, présentent la même réactivité au début de la réaction (temps<4h), la valeur du ratio en monomères DEGMA/BMA (r) reste aux alentours de 19. Le calcul du ratio, r, nous donne le résultat suivant : $r = \frac{I_{DEGMA}}{I_{BMA}} = \frac{I_{Hb}}{I_{Hc}} \cong \frac{95}{5} \cong 19$ (voir encadré Figure 2.6) lors des 4 premières heures de réaction. Le ratio de départ entre les monomères est conservé, ce qui signifie que les monomères sont consommés à la même vitesse. Au-delà de 4 heures de réaction, du fait de la proximité des déplacements chimiques des protons éthyléniques des deux monomères Hb (DEGMA) et Hc (BMA) (Figure 2.7), la bonne discrimination de ces derniers devient difficile

avec la diminution de l'intensité des signaux au fur et à mesure de l'avancement de la réaction. Ainsi, nous avons vérifié le maintien du ratio DEGMA/BMA pour la suite de la réaction par le calcul du ratio final en poly(DEGMA) et poly(BMA) dans les poly(DEGMA-co-BMA) synthétisés après purification. Le calcul du ratio, ($r = \frac{I_{poly(DEGMA)}}{I_{poly(BMA)}} = \frac{I_{Hg}}{I_{Hj}}$) réalisé à partir des spectres RMN ^{1}H des différents polymères synthétisés (Figure 2.9) confirme la réactivité observée au cours de la polymérisation, avec un ratio final aux alentours de 19. Cette observation, nous permet donc de fixer le ratio des momères à l'instant t à 19 et de s'affranchir du problème de superposition des signaux Hb et Hc, lors de la détermination du DP_n et de la masse molaire expérimentale (M_n exp).

Tableau 2.1 *Récapitulatif des équations permettant de déterminer le ratio des monomères (r), le taux de conversion (ρ), le degré de polymérisation (DP_n), la masse molaire théorique (Mn théo) et expérimentale (Mn exp) ainsi que la cinétique de croissance des chaînes (ln[M0]/[Mt]), appliquées à l'analyse par spectroscopie RMN ^{1}H.*

Equation	En théorie	En RMN ^{1}H
Rapport de réactivité des monomères	$r_{théo} = \text{rapport de réactivité} = \frac{K_{DEGMA}}{K_{polymère}} = \frac{\ln([M_{DEGMA}]_0/[M_{DEGMA}]_t)}{\ln([M_{BMA}]_0/[M_{DEGMA}]_t)}$	$\text{r} = \text{ratio des monomères à } t$ $\text{r} = \frac{I_{Hb}}{I_{Hc}}$
Taux de conversion	$\rho = \frac{[M0] - [Mt]}{[M0]}$	$\rho = \frac{I_{Hg}}{(2 \times I_{Hb}) + I_{Hb}}$
Degré de polymérisation	$DP_n = \frac{[M0] \times \rho}{[CTA]} = \frac{[Mt]}{[CTA]}$	$DP_n = \frac{I_{Hg}}{I_{Ha}} \times 0{,}95 + \frac{I_{Hg}}{I_{Ha}} \times 0{,}05$
Masse molaire théorique	$M_n\ théo = \frac{\Sigma\ masse\ des\ monomères \text{ à } t0 \times \rho}{\text{nombre de mole de l'agent RAFT à t0}} + M_{RAFT}$	$M_n\ théo$ avec $\rho = \frac{I_{Hg}}{(2 \times I_{Hb}) + I_{Hg}}$
Masse molaire expérimentale	$M_n\ exp = \text{DPn} \times [\frac{r}{r+1} \times \text{Mdegma} + \frac{\text{Mbma}}{r+1}] + \text{MCTA}$	$M_n\ exp = I_{Ha} \times I_{Hg} \times [0{,}95 \times \text{Mdegma} + 0{,}05 \times \text{Mbma}] + \text{MCTA}$
Cinétique	$\text{Ln}\ (\frac{[M0]}{[Mt]}) = \frac{[M0]}{[M0] - ([M0] \times \rho)}$	$\text{Ln}\ (\frac{[M0]}{[Mt]}) = \frac{(I_{Hb} + I_{Hg})/2}{I_{Hb}}$

Où [M0] correspond à la concentration initiale en monomères, [Mt] à la concentration en monomère à l'instant t et K, la constante de réactivité. Dans ce système de polymérisation, le nombre de chaînes étant déterminé par le nombre de molécules de CTA, nous pouvons également prévoir le DP_n du système en fonction du taux de conversion (ρ) du monomère M dont la concentration initiale est [M0] et la concentration [CTA] et en déduire la masse molaire attendue.

La Figure 2.8-A montre que la copolymérisation du DEGMA et du BMA visant à obtenir un copolymère de masse M_n ~ 16 kg/mol nécessite un temps de réaction d'environ 7 heures. La réaction a été effectuée en utilisant un ratio $[DEGMA]_0/[BMA]_0/[CTA]_0/[AIBN]_0$ de 95/5/0,77/0,038. Le taux de conversion a été fixé à 70% afin d'éviter d'atteindre un plateau synonyme d'un fort ralentissement ou d'un arrêt de la réaction en faveur de réactions secondaires ou de terminaisons. L'évolution linéaire de ln $[M_0]/[M_t]$ en fonction du temps jusqu'à un taux de conversion de ~ 70 % illustre le caractère contrôlé de la copolymérisation. Ceci est confirmé par la variation linéaire de M_n avec le taux de conversion [19-21]. L'évolution de M_n avec la conversion obtenue met par ailleurs en avant une bonne corrélation entre les valeurs théoriques et expérimentales.

La cinétique de polymérisation est également montrée pour le poly(DEGMA-co-BMA) de masse 4 kg/mol (Figure 2.8-B), en utilisant un ratio DEGMA/BMA de 95/5. Comme attendu le caractère contrôlé de la polymérisation a été observé.

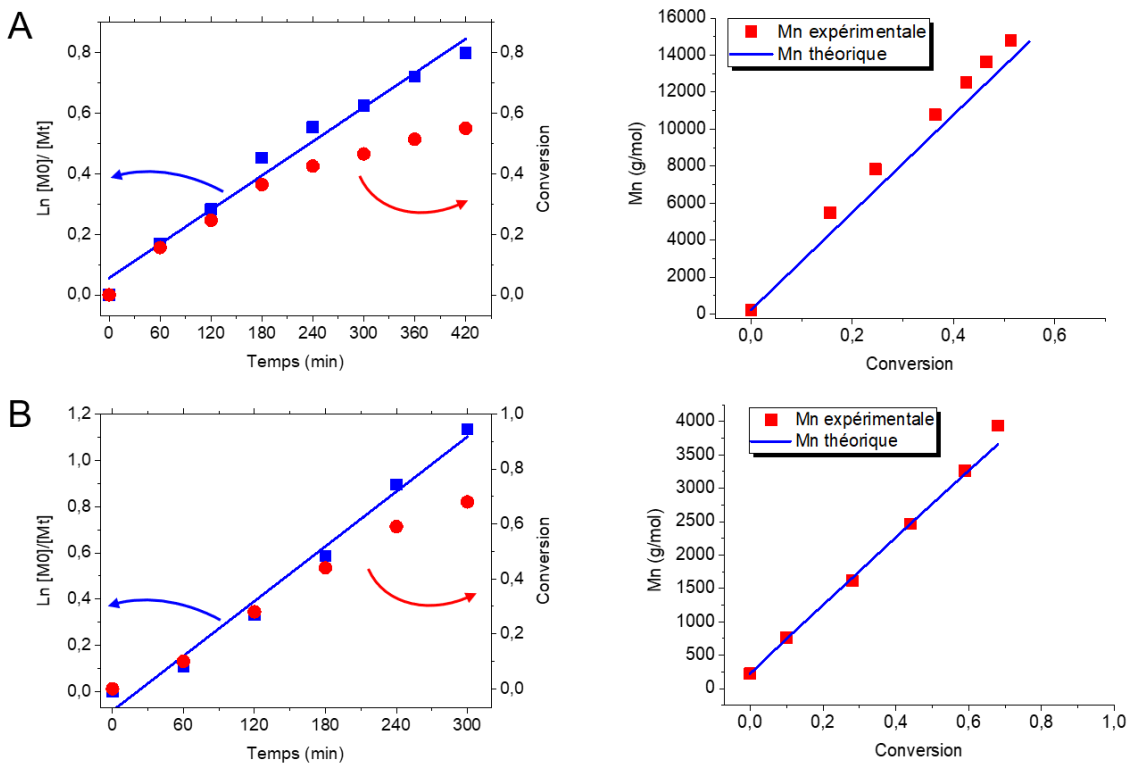

Figure 2.8 *Evolution de Ln ([M0]/[Mt]) en fonction du temps (min) et de la masse molaire (M_n* en g/mol*) en fonction du taux de conversion pour la synthèse du poly(DEGMA-co-BMA) avec une masse molaire (M_n théo) visée de A) 16 kg/mol (Tableau 2.2, Entrée 1) et (B) 4 kg/mol (Tableau 2.2, Entrée 5).*

Le copolymère isolé après précipitation dans le cyclohexane a été analysé par chromatographie d'exclusion stérique équipée d'un détecteur de diffusion de la lumière multi-angle (SEC-MALLS). Cette analyse a permis de confirmer la masse molaire du copolymère ($M_{n,SEC}$ = 15,5 kg/mol et $M_{n,RMN}$ = 15,7 kg/mol) et sa polydispersité proche de 1 (***Đ*** = 1,12).

Ces résultats montrent donc que la synthèse par polymérisation RAFT de copolymères poly(DEGMA-co-BMA) répond aux critères d'une polymérisation radicalaire contrôlée et permet de réaliser avec succès des poly(DEGMA-co-BMA) de masses molaires prédéfinies avec des distributions de masses molaires étroites.

II.2 Caractérisation structurale des copolymères obtenus

Suite à ces résultats, plusieurs réactions de copolymérisation du DEGMA et du BMA ont été réalisées en faisant varier le ratio DEGMA/BMA (DEGMA/BMA = 95/5 ou 99/1) et le ratio monomères (DEGMA et BMA)/CTA de façon à obtenir des copolymères ayant des masses molaires (M_n) comprises entre 5 et 16 kg/mol (Tableau 2.2). Les copolymères obtenus à la fin des synthèses ont été analysés par RMN ^{1}H (Figure 2.9) et par SEC-MALLS afin de déterminer leur masse molaire ainsi que leur polydispersité (***Đ***).

Tableau 2.2 *Récapitulatif des synthèses des poly(DEGMA-co-BMA) par polymérisation RAFT. M_n théo : masse molaire en nombre théorique ; M_n exp : masse molaire en nombre expérimentale : Đ : indice de polydispersité ; Rdt : rendement de la réaction. [a] Analyse RMN ^{1}H dans le $CDCl_3$; [b] analyse SEC-MALLS dans le DMF.*

Entrée	Ratio[a] [DEGMA]/ [BMA]	Ratio final [poly(DEGMA)/ poly(BMA)]	$M_n$théo en g/mol	$M_n$exp[a] (RMN) en g/mol	$M_n$exp[b] (SEC) en g/mol	*Đ*	Rdt (%)
1	95/5	95/5	16950	15740	15500	1,12	92
2	99/1	99/1	16000	16500	15916	1,2	91
3	95/5	95/5	12700	13000	12600	1,17	94
4	95/5	95/5	8000	9000	9095	1,2	90
5	95/5	95/5	4000	5000	5600	1,17	94

[a] M_n exp déterminée en injectant dans l'équation (Figure 2.9) les intégrations des pic correspondant aux poly(DEGMA) (Hg) et au poly(BMA) (Hj) en fonction du CTA (intégrale de Ha fixée à 1).

[b] M_n exp analyse par SEC–MALLS dans le DMF contenant 50 mM de $NaNO_3$.

La superposition des spectres RMN ^{1}H (Figure 2.9) permet d'apprécier l'augmentation de la masse molaire en fonction de l'intensité des signaux caractéristiques du poly(DEGMA-co-BMA) (Hg, Hj, He, Hn, Hf) par rapport à celui de l'agent RAFT (Ha) en extrémité de chaînes.

$$M_n(\mathrm{RMN}) = H_a \times H_g \times M_{DEGMA} \times 0{,}95 + \mathrm{H_a} \times Hj \times M_{BMA} \times 0{,}05 + M_{CTA}$$

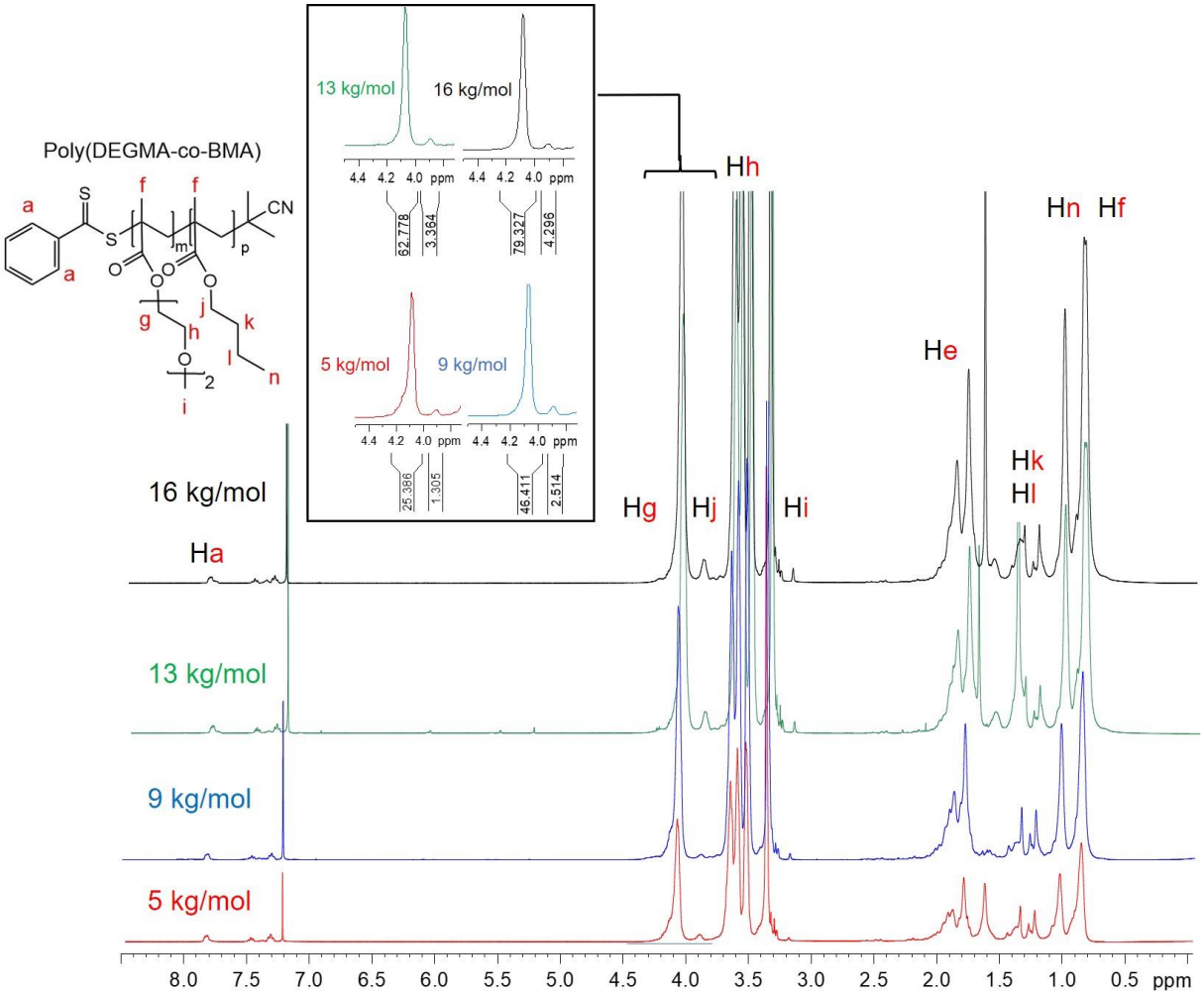

Figure 2.4 *Spectres RMN ^{1}H (400 MHz, $CDCl_3$, 25 ºC) de copolymères poly(DEGMA-co-BMA) possédant des masses molaires comprises entre 5 kg/mol et 16 kg/mol. Détermination de la masse molaire du polymère final à partir des intégrales des pics Hg (poly(DEGMA)) et Hj (poly(BMA)) par rapport au pic Ha (CTA), en utilisant l'équation ci-dessus.*

III Comportement en solution

III.1 Etude de l'auto-association par turbidimétrie, détermination de la température de point de trouble

La turbidité nous renseigne sur la diminution de l'intensité du rayon lumineux incident traversant l'échantillon à une longueur d'onde donnée, causée par la diffusion de la lumière des particules en suspension. Cette température de transition est appelée température de point de trouble (T_{cp}).

III.1.1 Définition de la température de point de trouble

Ce phénomène de température d'agrégation critique est dirigé par l'équation thermodynamique de Gibbs, où la force motrice pour tous les processus se produisant dans un système non spécifique est la minimisation de l'énergie libre (ΔG) :

$$\Delta G = \Delta H - T\Delta S$$

Les (co)polymères à LCST sont solubles en dessous d'une certaine température par la formation de liaisons hydrogène entre les molécules d'eau proches des chaînes polymères et ces dernières, créant ainsi une coque d'hydratation. Cette dernière se rompt lorsque la température augmente au-dessus de la température de point de trouble (T_{cp}). Les chaînes polymères précipitent en faveur d'interactions plus stables entre elles. Le terme entropique ΔS devient alors prédominant, du fait de la libération de molécules d'eau dans le milieu, conduisant à une énergie libre négative.

III.1.2 Effet de la concentration du copolymère en solution et de la force ionique du milieu

Une étude de la T_{cp} des copolymères par mesure de l'intensité lumineuse (transmission) des solutions de copolymère dans une solution tampon phosphate salin (PBS 10 mM, pH 7,4)) et en solution aqueuse (eau ultrapure) a été réalisée par spectrométrie UV, à une longueur d'onde λ = 500 nm, aux concentrations de 0,05, 0,1, 0,5 et 3 g/L. La valeur se mesure au point d'inflexion de la courbe, comme représenté pour le poly(DEGMA-co-BMA) de M_n 15,5 kg/mol à 3 g/L dans le PBS (Figure 2.10-A).

Les résultats montrent que le comportement du poly(DEGMA-co-BMA) en solution varie en fonction de sa concentration et du milieu salin. Les valeurs des T_{cp} augmentent avec la dilution des solutions (+12°C), tandis qu'elles diminuent en milieu salin (-2 ou 3°C) (Figure 2.10-B).

La diminution de la T_{cp} avec l'augmentation de la concentration est principalement due au fait que pour des concentrations élevées, les chaînes polymères sont plus susceptibles de s'agréger en raison d'un plus grand nombre de chaîne de polymères dans le même volume de solution.

La diminution de la T_{cp} en fonction de la concentration en sel est bien connue et a été étudiée en détail pour le poly(NIPAM) [22-24]. Elle est également décrite pour les polymères dérivés de poly(DEGMA) [25-26]. La présence d''ions en solution déstabilise la coque de solvatation du polymère et modifie l'état d'hydratation des chaînes de polymère. L'effet obtenu est d'autant plus important que la concentration en sel ajouté est élevée mais il dépend également de la nature du sel employé (série de Hofmeister).

A

[poly(DEGMA-co-BMA] (g/L)	Tcp (PBS) (°C)	Tcp (Eau) (°C)
3	12	14,5
0,5	17,5	20
0,1	22	25
0,05	24	28

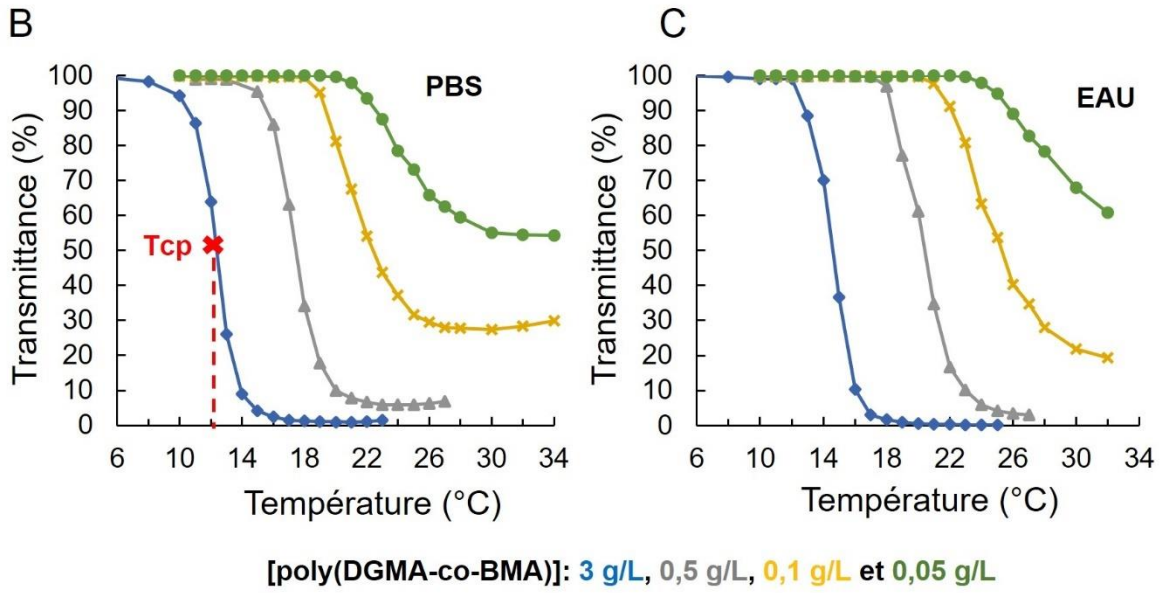

Figure 2.10 *A) Tableau récapitulatif des T_{cp} en fonction du milieu aqueux et de la concentration. Graphe récapitulatif de l'intensité lumineuse des solutions du poly(DEGMA-co-BMA) (M_n = 16 kg/mol) en fonction de la concentration B) dans le PBS et C) dans l'eau.*

III.1.3 Effet de la masse molaire du copolymère poly(DEGMA-co-BMA) sur la transition de phase en fonction de la température

Une comparaison des valeurs de T_{cp} pour les copolymères poly(DEGMA-co-BMA) possédant des masses molaires comprises entre 5 et 16 kg/mol a également été réalisée afin de sélectionner la masse molaire la plus appropriée pour le greffage du copolymère sur l'acide hyaluronique et l'héparosan.

Ces résultats montrent que le comportement varie également en fonction de la masse molaire (Figure 2.11). La valeur de la T_{cp} des polymères augmente en fonction de leur masse molaire et, donc, de la longueur des chaînes. En particulier, la Figure 2.12 montre une nette différence entre 8 kg/mol et 12 kg/moL.

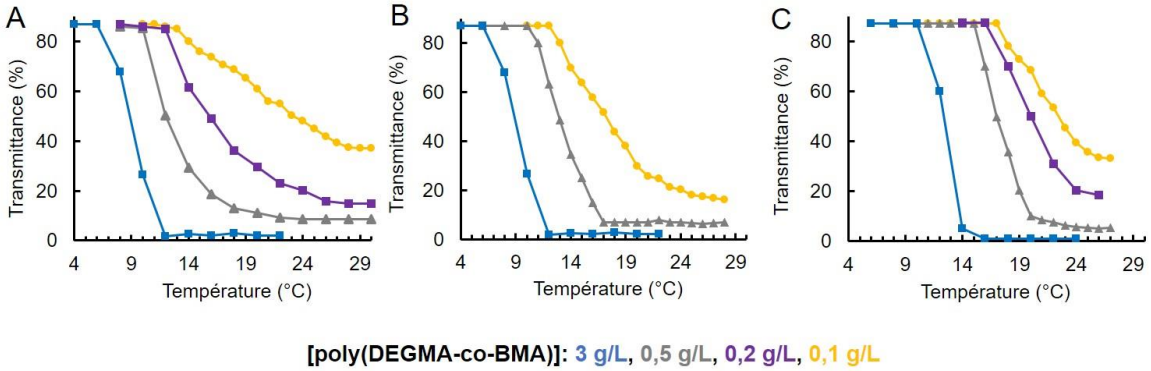

Figure 2.11 *Influence de la température sur la transmission optique (T_{cp}) de la lumière à 500 nm du poly(DEGMA-co-BMA) de masse molaire A) 4 kg/mol, B) 8 kg/mol et C) 12 kg/mol, dans le PBS sur la gamme de concentration : 3 g/L, 0,5 g/L, 0,2 g/L et 0,1 g/L avec une rampe de température de 0,1°C/min.*

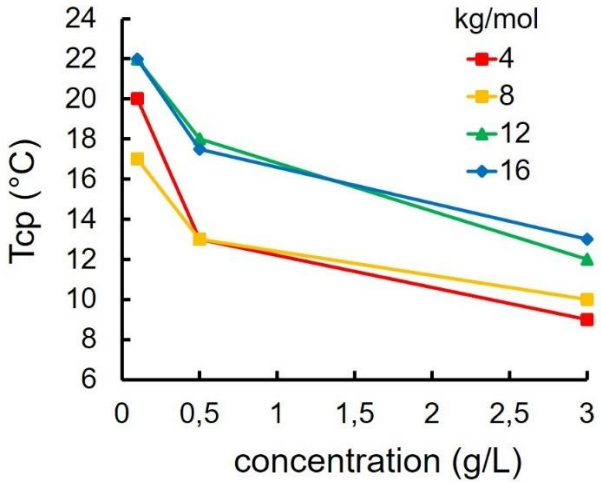

Figure 2.12 *Evolution de la température sur la transmission optique (T_{cp}) en fonction de la concentration en solution des copolymères de masse molaire 4, 8, 12 et 16 kg/mol, d'après les données extraites de la Figure 2.11.*

Une possible explication de ces résultats peut être associée au caractère hydrophobe intensifié des poly(DEGMA-co-BMA) synthétisés, apporté par l'agent RAFT en bout de chaîne (cycle aromatique). Avec la diminution de la longueur des chaînes, ces dernières deviennent plus sensibles à la nature des groupements à leur extrémité. Nous avons vu précédemment lors de la superposition des spectres RMN ^{1}H (Figure 2.9) que le ratio CTA/polymère (Ha/Hg) augmente avec la diminution de la masse molaire. Ainsi, le caractère hydrophobe des polymères serait amplifié pour les polymères de faibles masses molaires, ce qui explique la faible valeur de la T_{cp} du poly(DEGMA-co-BMA) de M_n = 5 kg/mol et 9 kg/moL par rapport aux autres échantillons de 13 kg/moL et 16 kg/moL.

Ce phénomène a déjà été décrit dans la littérature. Li et al. ont mis en avant la forte dépendance des groupes terminaux (agent RAFT) sur la T_{cp} du poly(NIPAM) dans le cas de faibles masse molaires (4 kg/moL) [27]. Ils montrent un effet significatif des groupements terminaux de la chaîne sur la solubilité du polymère. La T_{cp} avant élimination de l'agent RAFT en bout de chaîne (PNIPAM-CTA) est de 25, 29 et 33°C pour des masses molaires respectives de 4, 6 et 9 kg/mol. Après élimination(PNIPAM-SH) la T_{cp} augmentent, pour atteindre 32, 34 et 34°C. A présent la T_{cp} en fonction de la masse molaire ne varie que très légèrement (2°C) voire plus du tout.

Par ailleurs, Qiao et al. [28] ainsi que Luz et al. [5] ont étudié l'influence de la masse molaire sur la T_{cp} du poly(DEGMA-co-OEGMA) et le poly(MEO$_2$MA-co-OEGMA), (poly((2-(2methoxyethoxy)ethylmethacrylate-co-oligo(ethylene glycol)), synthétisé par ARTP (Atom Transfer Radical Polymerization), une autre polymérisation radicalaire contrôlée. Cette dernière n'entraîne pas la présence de groupements particuliers en bout de chaîne in fine. Dans ce cas-là, la variation de la masse molaire de 6 kg/mol à 30 kg/mol n'entraine pas une modification de la T_{cp} mais seulement un élargissement de la transition en température.

Afin de vérifier cette hypothèse, nous avons étudié la T_{cp} des poly(DEGMA-co-BMA) de masse molaire 4 kg/mol et 16 kg/mol après aminolyse afin d'apprécier l'influence de l'agent RAFT en extrémité de chaînes. Les résultats regroupés Figure 2.13 confirment notre hypothèse. Le graphe 2.13-A met en évidence un décalage de la T_{cp} vers de plus hautes valeurs de température pour le polymère de plus faible masse molaire (4 kg/mol), tandis que la T_{cp} reste constante aux alentours de 13°C pour la plus haute masse molaire (16 kg/mol). Si l'on compare à présent en fonction de la concentration en solution (graphe 2.13-B) le comportement de ces copolymères, nous constatons peu de différence. Nous observons ainsi le même comportement décrit par Li et al. [29].

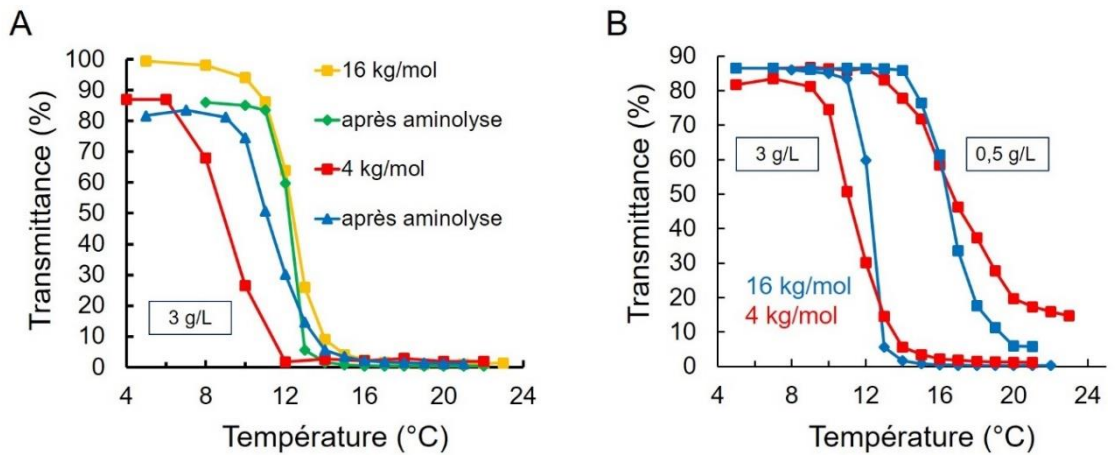

Figure 2.13 *A) Influence de l'agent RAFT en bout de chaîne sur la transition optique (T_{cp}) des copolymères de M_n 4 kg/mol et 16 kg/mol. Comparaison des T_{cp} avant et après aminolyse, à 3 g/L et B) Comparaison de la T_{cp} du poly(DEGMA-co-BMA) après aminolyse pour deux masses molaires : 4 kg/mol et 16 kg/mol dans le PBS à 3 g/L et 0,5 g/L. Transmission optique (T_{cp}) de la lumière mesurée à 500 nm, avec une rampe de température de 0,1°C/min dans le PBS.*

III.1.4 Effet du ratio en BMA : 99/1 passage de 13°C à 20°C

Des études réalisées sur les copolymères poly(DEGMA-co-OEGMA) ont montré la possibilité de moduler la T_{cp} des copolymères en fonction du ratio des monomères méthacrylates par polymérisation contrôlée [30-31]. Ainsi il est possible d'ajuster avec précision la T_{cp} sur une large gamme de températures allant de 28°C à 90°C par variation des méthacrylates utilisés et de leurs ratios. Nous avons cherché à étudier ce phénomène en comparant les ratios DEGMA/BMA suivant : 95/5 et 99/1 (Figure 2.14). Un écart de 7°C est observé entre les deux ratios, la T_{cp} passant de 12°C à 19°C avec la diminution du nombre d'unités butyle méthacrylate. Ce résultat confirme la pertinence du ratio DEGMA/BMA de 95/5 dans l'objectif d'obtenir des nanogels présentant une température d'agrégation critique proche de l'ambiante,

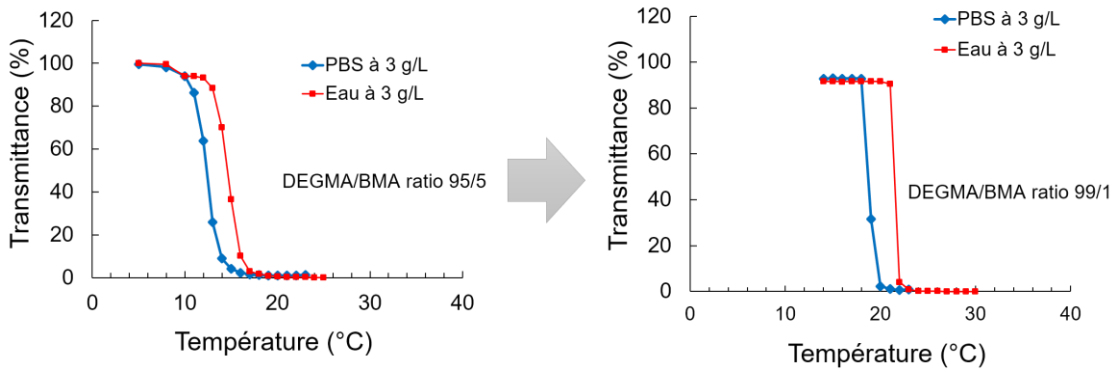

Figure 2.14 *Influence de la température sur la transmission optique (T_{cp}) de la lumière à 500 nm du poly(DEGMA-co-BMA) pour une masse molaire de 16 kg/mol et un ratio en monomères DEGMA/BMA de A) 95/5 B) 99/1 à 3 g/L avec une rampe de température de 0,1°C/min*

III.2 Analyse par DLS de la distribution en taille des agrégats formés

Nos investigations sur ce phénomène d'agrégation à haute température ont été poursuivies en essayant de déduire la morphologie des agrégats formés. La distribution en taille des copolymères à 37°C dans l'eau et dans le PBS a été analysée pour une concentration de 0,1 g/mol (Figure 2.15). En revanche, pour les solutions concentrées (>0,5 g/mol), nous observons une précipitation macroscopique du système. Les objets observés présentent des tailles élevées, supérieures à 350 nm dans l'eau et de l'ordre du micron dans le PBS. Ainsi, le copolymère thermosensible hydrophobe poly(DEGMA-co-BMA) ne s'agrège pas sous la forme de nanoparticules (~ 100 nm) et est instable en milieu aqueux et salin. Ce comportement pourra être comparé par la suite avec celui obtenu pour les dérivés HA- et Hep-poly(DEGMA-co-BMA) à 37°C.

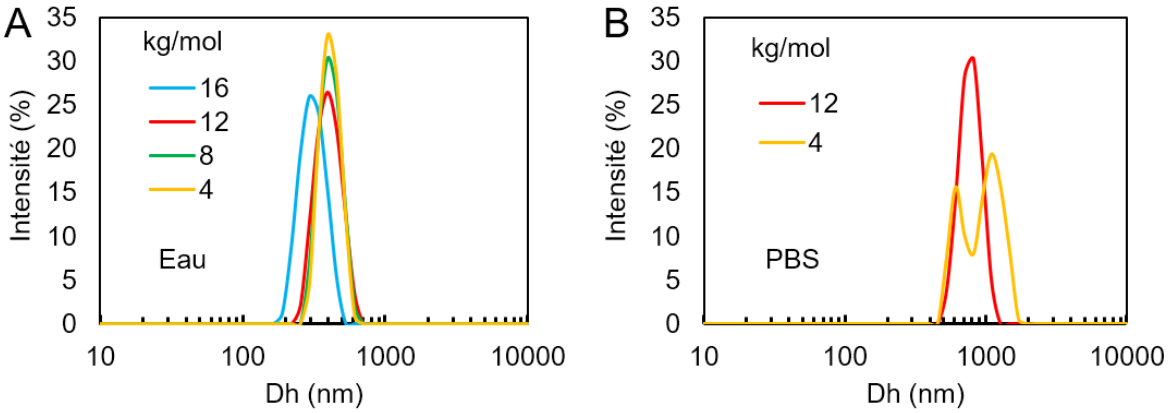

Figure 2.15 *Evolution du diamètre hydrodynamique par DLS des copolymères en fonction de la masse molaire, en solution A) eau ultrapure, B) PBS au-dessus de la T_{cp} à 37°C, à une concentration de 0,1 g/L.*

IV Conclusion

La copolymérisation du poly(DEGMA-co-BMA) a été réalisée par la méthode RAFT qui repose sur un mécanisme de transfert de chaîne réversible par addition-fragmentation. L'intérêt de cette polymérisation réside dans l'utilisation d'un agent de transfert de chaîne (CTA) qui régule la concentration en radicaux dans le milieu réactionnel tout au long de la réaction. De cette façon, il est possible de synthétiser des polymères d'architectures contrôlées, de faible polydispersité et de haute fonctionnalité.

L'étude du comportement en solution en fonction de la masse molaire et du ratio en monomère montre que l'association des monomères sélectionnés présente un fort caractère hydrophobe. Elle permet ainsi d'obtenir des copolymères avec une T_{cp} inférieure à la température ambiante. Les poly(DEGMA-co-BMA) répondent ainsi au premier critère visé.

Les quatre masses molaires synthétisés, 4, 8, 12 et 16 kg/mol présentent une T_{cp} proche après élimination de l'agent de transfert en bout de chaîne. Par conséquent, nous retenons la masse molaire la plus élevée, en vue de l'élaboration de dérivés HA-g-copolymère afin de créer plus facilement des domaines hydrophobes. En effet, celle-ci permet de réticuler physiquement les nanogels tout en présentant une bonne capacité d'encapsulation.

V Partie expérimentale

Produits chimiques

Les différents monomères DEGMA et BMA proviennent de la société Sigma Aldrich. Une purification des monomères par une colonne d'oxyde d'aluminium a été effectuée avant la polymérisation, afin d'éliminer les inhibiteurs empêchant leur auto-polymérisation. L'agent RAFT, le 2-Cyano-2-propyl benzodithioate, ainsi que le n-butylamine également fournis par la société Sigma-Aldrich et l'azobisisobutyronitrile (AIBN) fourni par Acros ont été utilisés dans l'état de réception. Les différents solvants ont été fournis par la société Carlo Erba, excepté le toluène anhydre fourni par Acros et le tampon phosphate fourni par Sigma-Aldrich. Le chloroforme deutéré ($CDCl_3$) provient de chez SDS. L'eau ultrapure (milli-Q) utilisée dans toutes les expériences a été purifiée par le système de purification Elga Purelab avec une résistivité de 18.2 MΩ.cm.

Synthèse des copolymères poly(DEGMA-co-BMA)

Dans un ballon de 100mL, l'AIBN, l'agent RAFT puis les monomères DEGMA et BMA sont successivement pesés. La quantité d'agent RAFT à introduire est donnée par l'équation suivante :

$$M_n \text{ théorique} = \frac{\sum([M0] \times Mmono) \times \rho}{[RAFT]_{t=0}} + \mathrm{M_{RAFT}}$$

Avec M_n théorique, M_{RAFT}, ρ, $[M_0]$ et $[RAFT]_{t=0}$ qui sont respectivement la masse molaire théorique du copolymère, la masse molaire de l'agent RAFT, le taux de conversion de monomères, la concentration initiale en monomères, et la concentration initiale en agent RAFT. Le nombre de moles d'amorceur nécessaire correspondre à 5% du nombre de mole d'agent RAFT. Le toluène anhydre est ensuite ajouté et la solution est placée sous agitation en milieu inerte (N_2), à 80°C jusqu'à la fin de la réaction. La durée de la réaction est déterminée par un suivi cinétique par RMN ^{1}H. Une fois la polymérisation terminée, le milieu réactionnel est refroidi à température ambiante puis le copolymère est précipité dans du cyclohexane (10/1 v/v) sous vive agitation. Le précipité est laissé pour la nuit à 4°C. Après cette première précipitation, le copolymère est solubilisé dans un minimum de dichlorométhane, puis précipité à nouveau selon le même protocole afin d'éliminer les traces d'impuretés. Le lendemain le précipité est séparé du surnageant et placé à l'étude sous vide pendant 4 heures à 40°C, puis pesé afin de déterminer le rendement.

Analyse RMN

Les spectres RMN ^1H ont été enregistrés à 25°C en utilisant un spectromètre Bruker AVANCE III HD fonctionnant à 400 MHz. Le chloroforme deutéré ($CDCl_3$) a été obtenu auprès de SDS (Vitry, France). Tous les spectres ont été enregistrés en appliquant une impulsion d'excitation de 45° et un retard de cycle de 10 s. Les déplacements chimiques (δ en ppm) sont donnés par rapport au tétraméthylsilane (TMS = 0 ppm) comme référence externe et l'étalonnage a été effectué en utilisant le signal des protons résiduels du solvant comme référence interne.

Analyse GPC

La masse molaire moyenne en nombre (M_n), la masse molaire moyenne en poids (M_w) et la polydispersité (*Đ*) du poly(DEGMA-co-BMA) ont été déterminées par chromatographie d'exclusion stérique (SEC, Size Exclusion Chromatography) dans du diméthylformamide contenant 50 mM de $NaNO_3$. Les mesures ont été effectuées sur un système SEC équipé d'une pompe Waters modèle 515, d'un détecteur d'indice de réfraction RI 2000 de Schambeck SFD GmbH et d'un détecteur de diffusion de lumière (MALLS) de Wyatt (USA). Les échantillons ont été analysés en utilisant une colonne 161123-Agilent-10 à 30°C et à un débit de 1 L/min.

Analyse par spectroscopie UV-Visible

La température du point de trouble (T_{cp}) du poly(DEGMA-co-BMA) a été déterminée par des mesures de turbidité UV-vis (λ = 500 nm) effectuées sur un scanner Varian Cary 50. Les échantillons ont été préparés à température ambiante dans du PBS (de 0,1 à 3 g/L), après quoi l'échantillon a été placé dans l'instrument. La transmittance de la lumière a été mesurée par une élévation contrôlée de la température, de 8°C à 40°C, en utilisant un intervalle de 1°C /10 min. La T_{cp} a été considérée comme la température à laquelle le facteur de transmission de la lumière était de 50% de celui obtenu pour le même échantillon à 8°C.

Analyse par diffusion dynamique de la lumière

La diffusion dynamique de la lumière (DLS, Dynamic Light Scattering) est une technique d'analyse non invasive permettant de mesurer la distribution en taille des particules de copolymère en suspension dans une solution. Les mesures ont été effectuées sur l'appareil Zetasizer NanoZS (Malvern Instruments) équipé d'un laser hélium-néon à lumière monochromatique (633 nm, 173°) et d'un contrôleur de température.

VI Références

1. Roy, D.; Brooks, W.L.A.; & Sumerlin, B.S. New directions in thermoresponsive polymers. *Chemical Society Reviews*, **2013**, 42, 7214-7243.
2. Scarpa, J.S.; Mueller, D.D.; & Klotz, I.M. Slow hydrogen-deuterium exchange in a non-.alpha.-helical polyamide. *Journal of American Chemical Society*, **1967**, 89, 6024-6030.
3. Lutz, J.-F.; Andrieu, J.; Üzgün, S.; Rudolph, C.; & Agarwal, S. Biocompatible, thermoresponsive, and biodegradable: simple preparation of “all-in-one” biorelevant polymers. *Macromolecules*, **2007**, 40, 8540-8543.
4. Cai, T.; Marquez, M.; & Hu, Z. Monodisperse thermoresponsive microgels of poly(ethylene glycol) analogue-based biopolymers. *Langmuir*, **2007**, 23, 8663-8666.
5. Lutz, J.-F. Polymerization of oligo(ethylene glycol) (meth)acrylates: toward new generations of smart biocompatible materials. *Journal of Polymer Science Part A: Polymer Chemistry,* **2008**, 46, 3459-3470.
6. Hu, Z.; Cai, T.; & Chi, C. Thermoresponsive oligo(ethylene glycol)-methacrylate-based polymers and microgels. *Soft Matter***, 2010**, 6, 2115-2123.
7. Lutz, J.-F. Thermo-switchable materials prepared using the OEGMA-platform. *Advanced Materials,* **2011**, 23, 2237-2243.
8. Yang, H.; Wang, Q.; Chen, W.; Zhao, Y.; Yong, T.; Gan, L.; Xu, H.; & Yang, X. Hydrophilicity/hydrophobicity reversible and redox-sensitive nanogels for anticancer drug delivery. *Molecular Pharmaceutics,* **2015**, 12, 1636-1640.
9. Cazares-Cortes, E.; Espinosa, A.; Guigner, J.-M.; Michel, A.; Griffete, N.; Wilhelm, C.; & Ménager, C. Doxorubicin intracellular remote release from biocompatible oligo(ethylene glycol) methyl ether methacrylate-based magnetic nanogels triggered by magnetic hyperthermia. *ACS Applied Maerials & Interfaces*, **2017**, 9, 25775-25788.
10. Jing, J.; Alaimo, D.; De Vlieghere, E.; Jérôme, C.; De Wever, O.; De Geest, B.G.; & Auzély-Velty, R. Tunable self-assembled nanogels composed of well-defined thermoresponsive hyaluronic acid–polymer conjugates. *Journal of Materials Chemistry B*, **2013**, 1, 3883-3887.
11. Stefanello, T.F.; Szarpak-Jankowska, A.; Appaix, F.; Louage, B.; Hamard, L.; De Geest, B.G.; Van der Sanden, B.; Nakamura, C.V; & Auzély-Velty, R. Thermoresponsive hyaluronic acid nanogels as hydrophobic drug carrier to macrophages. *Acta Biomaterialia,* **2014**, 10, 4750-4758.
12. Tizzotti, M.; Charlot, A.; Fleury, E.; Stenzel, M.; & Bernard, J. Modification of polysaccharides through controlled/living radical polymerization grafting-towards the generation of high performance hybrids. *Macromolecular Rapid Communications*, **2010**, 18, 1751-1772.

13. Mori, H.; Iwaya, H.; Nagai, A.; & Endo, T. Controlled synthesis of thermoresponsive polymers derived from L-proline via RAFT polymerization. *Chemical Communications*, **2005**, 38, 4872-4874.
14. Chiefari, J.; Chong Y.K.; Ercole, F.; Krstina, J.; Jeffery, J.; Le, T.P.T.; Mayadunne, R.T. A.; Meijs, G.F; Moad, C.L.; Moad, G.; Rizzardo, E.; & Thang, S.H. Living free-radical polymerization by reversible addition-fragmentation chain transfer: the RAFT process. *Macromolecules*, **1998**, 31, 5559-5562.
15. Destarac, M. On the critical role of RAFT agent design in reversible addition-fragmentation chain transfert (RAFT) polymerization. *Polymer Reviews*, **2011**, 51, 163-187.
16. Pietsch, C.; Fijten M.W.M.; Lambermont-Thijs, H.M.L.; Hoogenboom, R.; & Schubert, U.S. Unexpected reactivity for the RAFT copolymerization of oligo(ethylene glycol) methacrylates. *Journal of Polymer Science Part A: Polymer Chemistry,* **2009**, 47, 2811-2820.
17. Fijten M.W.M.; Paulus R.M.; & Schubert, U.S. Systematic parallel investigation of RAFT polymerizations for eight different (meth)acrylates: A basis for the designed synthesis of block and random copolymers. *Journal of Polymer Science Part A: Polymer Chemistry*. **2005,** 43, 3831-3839.
18. Moad, G.; Riccardo, E.; & Thang, S.H. A micro review of reversible/addition fragmentation chain transfert RAFT polymerization. *Aldrich Materials Science*.
19. Moad, G.; Riccardo, E.; & Thang, S.H. Radical addition-fragmentation chemistry in polymer synthesis. *Polymer*, **2008**, 49, 1079-1131.
20. Semsarilar, M.; & Perrier, S. “Green” reversible addition-fragmentation chain-transfert (RAFT) polymerization. *Nature Chemistry*, **2010**, 2, 811-820.
21. Chernikova, E.V.; Golubev, V.B.; Filippov, A.N.; & Garina, E.S. The role of termination reactions of radical intermediates in reversible addition fragmentation chain-transfer polymerization. *Polymer Science Series C*, **2015**, 57, 94-109.
22. Zhang, Y; Furyk, S.; Bergbreiter, D.E.; & Cremer, P.S. Specific ion effects on the water solubility of macromolecules: PNIPAM and the Hofmeister series. *Journal of American Chemical Society*, **2005**, 127, 14505-14510.
23. Zhang, Y; & Cremer, P.S.; Interactions between macromolecules and ions: The Hofmeister series. *Current Opinion in Chemical Biology*, **2006**, 10, 658-663.
24. Zhang, Y.; Furyk, S.; Sagle, L.B.; Cho, Y.; Bergbreiter, D.E.; & Cremer, P.S. Effects of Hofmeister Anions on the LCST of PNIPAM as a Function of Molecular Weight. *Journal of Physical Chemistry C*, **2007**, 111, 8916-8924.
25. Han, S.; Hagiwara, M.; & Ishizone, T. Synthesis of thermally sensitive water-soluble polymethacrylates by living anionic polymerizations of oligo(ethylene glycol) methyl ether methacrylates. *Macromolecules*, **2003**, 26, 8312-8319.

26. Luzon, M.; Boyer, C.; Peinado, C.; Corrales, T.; Whittaker, M.; Tao, L.; & Davis, T.P. Water-soluble, thermoresponsive, hyperbranched copolymers based on PEG-methacrylates: synthesis, characterization, and LCST behavior. *Journal of Polymer Science Part A: Polymer Chemistry*, **2010**, 48, 2783-2792.
27. Weaver, L.G., Stockmann, R.; Postma, A.; & Thang, S.H. Multi-responsive (diethylene glycol) methyl ether methacrylate (DEGMA)-based copolymer systems. *RSC Advance,* **2016**, 6, 90923-90933
28. Qiao, Z.Y.; Du, F.S.; Zhang, R.; Liang, D.H.; & Li, Z.C. Biocompatible thermoresponsive polymers with pendent oligo(ethyleneglycol) chains and cyclic ortho ester groups. *Macromolecules*, **2010**, 43, 6485-6494.
29. Li, X.; ShamsiJazeyi, H.; Pesek, S.L.; Agrawal, A.; Hammouda, B.; & Verduzco, R.; Thermoresponsive PNIPAAM bottlebrush polymers with tailored side-chain length and end-group structure. *Soft Matter*, **2014**, 10, 2008-2015.
30. Lutz, J.F.; & Hoth, A. Preparation of ideal PEG analogues with a tunable thermosensitivity by controlled radical copolymerization of 2-(2-methoxyethoxy) ethyl methacrylate and Oligo(ethylene glycol) methacrylate. *Macromolecules*, **2006**, 39, 893-896.
31. Porsch, C.; Hansson, S.; Nordgren, N.; & Malmström, E.; Thermo-responsive cellulose-based architectures: tailoring LCST using poly(ethylene glycol) methacrylates. *Polymer Chemistry*, **2011**, 2, 1114-1123.

.

Chapitre 3 - Élaboration de nanogels thermosensibles

I Introduction

Les principes actifs (PA) pour être efficaces doivent atteindre spécifiquement le site tumoral. Par conséquent pour assurer leur succès il est nécessaire de contrôler leur libération dans le temps et l'espace, à l'aide de nano-vecteurs.

Au cours des trois dernières décennies, tout une gamme de systèmes transporteurs de principes actifs a été développée, notamment de nombreuses nanoparticules polymériques (NPs) [1-2]. Avec le développement croissant des PA hydrophobes, les systèmes formés à partir de polymères amphiphiles capables de s'auto-associer en « cœur-coquille » s'avèrent aujourd'hui les plus prometteurs. Ainsi, le cœur hydrophobe permet l'encapsulation du PA, tandis que la coquille hydrophile assure la stabilité colloïdale des systèmes. L'auto-association des polymères amphiphiles conduit à la formation de différentes architectures sous la forme de nanocapsules, polymersomes, micelles ou encore de nanosphères. Parmi cette dernière catégorie, les nanogels constitués de réseaux physiquement ou chimiquement réticulés de polymères amphiphiles ont suscité un vif intérêt pour la vectorisation. En effet, ils sont particulièrement appréciés pour leur grande capacité d'hydratation (gonflement/rétractation) qui leur confère une flexibilité que les autres particules n'ont pas. De plus, ils présentent des atouts tels que : une taille ajustable, une faible toxicité et une bonne stabilité en solution. Enfin et surtout, la possibilité de modifier aussi bien la couronne hydrophile que le coeur hydrophobe permet d'envisager de multiples combinaisons de PA pour le traitement de différents cancers ainsi que différents mécanismes de libération [3].

Les nanogels peuvent être élaborés à partir de polymères synthétiques, de polymères naturels ou d'une combinaison des deux. Comparés aux polymères synthétiques majoritairement utilisés, les polysaccharides naturels offrent de nombreux avantages : ils sont en général biodégradables, biocompatibles et peuvent présenter des propriétés biologiques particulières [4]. C'est le cas notamment des glycosaminoglycanes (GAGs), une famille de polysaccharides omniprésents dans le corps [5]. Comme nous l'avons relevé au cours de l'étude bibliographique, deux polysaccharides se distinguent au sein de cette famille : l'acide hyaluronique (HA) et l'héparosan (Hep). De structures similaires (seule la liaison β-1,3 entre l'unité GlcA et l'unité GlcNAc du HA est remplacée par une liaison α-1,4 dans le cas de Hep), ils se différencient l'un de l'autre par leurs propriétés biologiques. Le premier (HA) est réputé

pour être reconnu par de nombreux récepteurs notamment les récepteurs CD44, surexprimés à la surface des cellules cancéreuses ainsi que par d'autres récepteurs présents à la surface de nombreux organes. Cela fait de lui un agent de ciblage intéressant. A contrario le second (Hep) en tant que précurseur de l'héparine et de l'héparane sulfate, n'est pas reconnu par les récepteurs cités précédemment. De par leurs propriétés biologiques antagonistes, la comparaison de ces deux GAGs comme matrice hydrophile, offre l'opportunité de mieux comprendre les mécanismes d'accumulation des nanogels au sein des tissus cancéreux après injection.

Récemment, nous avons montré au sein de notre équipe la possibilité d'obtenir des nanogels stables en milieu aqueux à base d'acide hyaluronique (HA) par simple élévation de la température grâce à l'incorporation d'un polymère thermosensible sur le squelette du polysaccharide. L'avantage majeur de cette approche réside dans la simplicité du procédé de fabrication qui ne nécessite pas l'utilisation de solvants organiques, ni de tensioactifs. Trois générations de nanogels thermosensibles ont alors été développés à partir de dérivés HA : i) HA-poly(DEGMA-co-OEGMA) avec une CAT proche de la température du corps humain (T=34°C) induisant une faible stabilité *in vivo* ii) HA-poly(DAAM-co-DMA) dont le cœur hydrophobe est réticulé afin d'améliorer la stabilité des nanogels et iii) HA-poly(DEGMA-co-CMA) avec un groupement photolabile conduisant à une libération contrôlée du PA dans l'espace et dans le temps. Ces deux derniers systèmes sont très prometteurs et montrent une accumulation dans la tumeur après administration par voie intraveineuse chez la souris. Cependant, une part importante des nanogels est détectée dans le foie, ce qui s'explique par leur capture par des cellules phagocytaires du système réticulo-endothélial et probablement aussi par des cellules exprimant le récepteur HARE (hyaluronan receptor for endocytosis) du HA, abondant dans les sites hépatiques.

Il ressort du Chapitre I que les propriétés physico-chimiques des nanoparticules, telles que la taille, la forme, la rigidité, la structure et la chimie de surface, sont cruciales pour guider et comprendre les interactions entre l'environnement biologique et les nanoparticules pour des applications biomédicales [6].

C'est pourquoi, au regard des systèmes préalablement étudiés, nous souhaitons, dans le cadre de ce travail, étendre à présent cette approche à l'élaboration d'une nouvelle classe de nanogels thermosensibles présentant cette fois :

- une CAT plus basse, inférieure ou proche de la température ambiante (>25°C)
- la possibilité de réticuler leur couronne (chaînes de polysaccharides entre elles)
- différentes propriétés biologiques en fonction du polysaccharide choisi comme matrice hydrophile (à partir de HA ou de Hep)

Pour atteindre cet objectif, un polymère thermosensible a été conçu « sur mesure » dans le chapitre précédent (poly(DEGMA-co-BMA)) et une voie de synthèse reposant sur la chimie thiol-ène radicalaire permettant à la fois de greffer le polymère thermosensible et de réticuler la surface des nanogels a été développée.

Ce chapitre se divise en deux parties. Dans un premier temps, un article décrit la synthèse et la caractérisation de nanogels élaborés à partir de HA et de Hep ainsi que leur biodistribution après administration par voie intraveineuse chez des souris porteuses d'une tumeur. Enfin, une partie complémentaire apporte une vision sur les enjeux d'élaboration de ces systèmes.

II Résultats et discussions

II.1 Article

Can Heparosan be a glycosaminglycan alternative to Hyaluronic acid for the design of nanovectors in anticancer therapy ?

Marlène Rippe,[‡] Talitha F. Stefanello,[§] Vanessa Kaplum,[§] Elizandra A. Britta,[§] Francielle P. Garcia,[§] Robin Poirot,[‡] Mychelle V. P. Companhoni,[§] Celso V. Nakamura,[§] Anna Szarpak-Jankowska,[‡] Rachel Auzély-Velty[‡]*

[‡]Univ. Grenoble Alpes, CNRS, Centre de Recherches sur les Macromolécules Végétales (CERMAV), 38000 Grenoble, France

[§]Laboratory of technological innovation in the development of pharmaceuticals and cosmetics, State University of Maringa, Maringa, Brazil

Key words: thermoresponsive nanogels, heparosan, hyaluronic acid, shell crosslinking

Introduction

Self-assembled nanogels, nanometer-sized hydrogels obtained by physical self-assembly of interactive hydrophilic polymers, have attracted growing interest for drug delivery as these systems combine the advantages of hydrogels with nanoscale formulations. [1-2] Such systems can be designed to facilitate the encapsulation of diverse classes of bioactive compounds, and their hydrophilic shell can be exploited to control their biological behavior and targeting ability. In this regard, nanogels made of amphiphilic polysaccharides hold promise as versatile nanocarriers due to the presence of various functional groups on shell-forming polysaccharides in addition to their unique physicochemical properties, including biocompatibility and biodegradability.[3-4] Among polysaccharides, hyaluronic acid (HA), a natural glycosaminoglycan ubiquitous in the body, has been widely explored to design self-assembled nanogels for anticancer drug delivery because this polysaccharide can be specifically recognized by cell surface CD44 receptors that are over-expressed by several cancer cells.[5-8] Several studies thus showed that when systemically administered into tumor-bearing mice, HA-based nanogels (HA-NGs) were effectively accumulated into the tumor site. However, a significant portion of HA-NGs was also found in the liver site, possibly owing to their cellular uptake by phagocytic cells of the reticuloendothelial system (RES) and by liver sinusoidal endothelial cells expressing another HA receptor (hyaluronan receptor for endocytosis, HARE).[9] In an attempt to reduce the accumulation of self-assembled HA-NGs into the liver site, Choi et al. modified the HA-gel particles with poly(ethylene glycol) (PEG).[10] When the PEGylated HA-nanogels were systemically administered into tumor-bearing mice for *in vivo* real-time imaging, they were more effectively accumulated into the tumor tissue, up to

1.6-fold higher than bare HA-nanogels. However, though adding PEG to a therapeutic cargo is a FDA approved process, the synthetic nature of this polymer presents some drawbacks especially for pharmaceuticals used at high doses.[11-14]

In this study, we explored the possibility of using heparosan (Hep) as an alternative to HA for designing nanogels as drug carriers for tumor targeted drug delivery. This was motivated by the fact that the HARE receptor does not recognize heparosan,[15-16] although its chemical structure is very similar to HA. Indeed, Hep has a repeating disaccharide unit of D-glucuronic acid (GlcA) and *N*-acetyl-D-glucosamine (GlcNAc) residues such as HA, but the α-1,4 bond between the GlcA and the GlcNAc units replaces the β-1,3 bond found in HA. Moreover, since Hep is the natural precursor in the heparin/heparan sulfate biosynthetic pathway, it should be biocompatible in the human body.[15] It can also be noted that this polysaccharide is stable in the extracellular environment but degraded by lysosomal enzymes following entry into the cell. In this work, Hep-based nanogels (Hep-NGs) were prepared by temperature-induced self-assembly of Hep suitably modified with a thermoresponsive ethylene glycol-based copolymer (Scheme 1). Such temperature-triggered approach allows spontaneous nanogel formation due to the dehydration of the grafted copolymer chains when heated above the cloud point temperature (T_{cp}). Herein, we synthesized a copolymer of di(ethylene glycol) methacrylate and butylmethacrylate (poly(DEGMA-co-BMA)) exhibiting a T_{cp} well below the room temperature by judiciously adjusting the comonomer ratio. This allowed obtaining stable nanogels at room temperature as required for good handling and biological application. As such carrier systems may disassemble in the bloodstream because of the large dilution volume and/or interactions with biomolecules, shell-crosslinked (SCL) nanogels were also designed to increase their colloidal stability (Scheme 1). The synthetic route to the nanogels relied on thiol-ene chemistry[17-18] allowing the coupling of the thiol-end functionalized copolymer with the polysaccharide modified with alkene groups, and the subsequent crosslinking of the shell-forming polysaccharide using a bi-functional thiol reagent. For comparison, nanogels based on HA were also synthesized. These different nanogels were then carefully characterized in terms of size, morphology and cytotoxicity. Biodistribution studies demonstrated a more pronounced accumulation of Hep-NGs in the tumor tissue after systemic administration into tumor-bearing mice, compared to HA-NGs. To our knowledge, this study provides the first evaluation of the *in vivo* potential of a Hep-based nanogels as tumor-targeting nanocarriers.

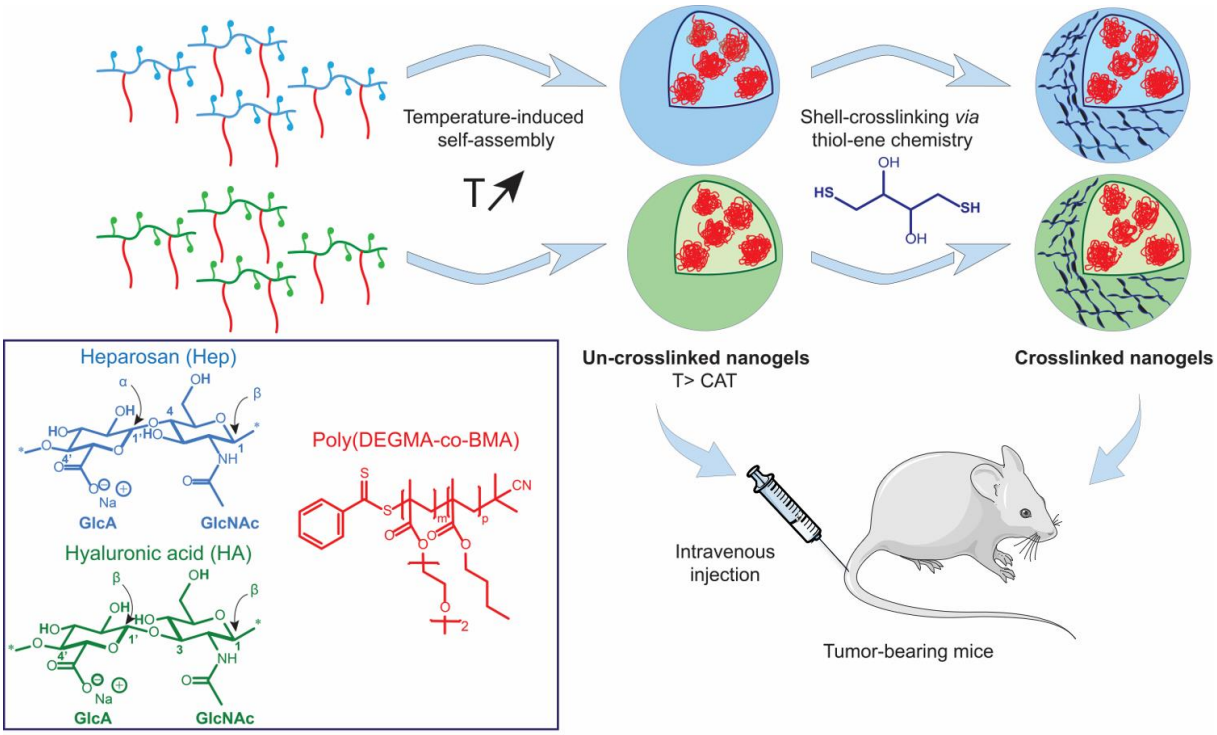

Scheme 1. *Strategy for the synthesis of un-crosslinked and shell-crosslinked nanogels based on heparosan and hyaluronic acid modified with poly(DEGMA-co-BMA) (Hep- poly(DEGMA-co-BMA) and HA-poly(DEGMA-co-BMA)).*

Results and discussion

Synthesis of poly(DEGMA-co-BMA)

The copolymer poly(DEGMA-co-BMA) was prepared *via* the reversible addition–fragmentation chain transfer (RAFT) process from di(ethylene glycol) methacrylate (DEGMA) and butylmethacrylate (BMA) monomers using 2,2-azobis(2-methylpropionitrile) (AIBN) as an initiator and 2-cyano-2-propyl benzodithioate (CPB) as a chain transfer agent (CTA) (Scheme 2A). A DEGMA/BMA ratio of 95:5 was selected to obtain a copolymer exhibiting a T_{cp} well below the room temperature and thereby, allow formation of nanogels at room temperature (i.e. ~ 25 °C). ^{1}H NMR analysis was conducted to monitor the copolymerization kinetics. The kinetic plots proved that, in these reaction conditions, CPB allowed a good control over the RAFT copolymerization of DEGMA and BMA (Figure S1). ^{1}H NMR and size exclusion chromatography (SEC) analysis of the final copolymer revealed a final copolymer composition DEGMA/BMA of 95:5, a low dispersity (*Đ* = 1.12), and a number average molar mass M_n of ~ 16 kg/mol ($M_{n,NMR}$ = 15500 g/mol, $M_{n,SEC}$ = 15740 g/mol, Figure S2)**.** The copolymer exhibited a T_{cp} of 18 °C at 0.5 g/L in phosphate buffer saline (PBS), pH 7.4 (Figure S3).

Synthesis of HA and Hep-based nanogels

In order to couple poly(DEGMA-co-BMA) to HA and Hep, the polysaccharides were first esterified with pentenoic anhydride to produce ene-functional derivatives that were previously shown to react efficiently with various thiol-containing molecules via thiol−ene photochemistry.[17 -18] The pentenoate-modified HA and Hep (HA-p and Hep-p, respectively), possessing a degree of substitution (DS, average number of substituents per repeating unit) of 0.5, were subsequently reacted with poly(DEGMA-co-BMA) on which the RAFT end-group was converted to a thiol by aminolysis using *n*-butylamine. The thiol-ene coupling reaction was conducted under UV-light irradiation (λ = 365 nm) in water, in the presence of Irgacure 2959 as a photoiniator (Scheme 2B). The HA- and Hep-poly(DEGMA-co-BMA) conjugates were then purified *via* a batch ion exchange process performed at low temperature (< 10 °C) to ensure effective removal of the non-grafted copolymer during washes with water, followed by a rapid dialysis to remove salt. This purification process, completed in less than four days, afforded the final products in 50 % yield. This avoided difficulties encountered when using dialysis to remove the free copolymer (low purification yield (< 50 %) and purification for a period of more than 7 days).

Successful grafting of the copolymer was confirmed by ^{1}H-NMR analysis. In the ^{1}H-NMR spectrum, the proton signals at 4.25 ppm, 3.76 ppm, 3.39 ppm and in the region of 0.99-1.2 ppm arising from poly(DEGMA-co-BMA) can easily be observed (Figure 1). The DS of the conjugates, determined by the carbazole assay, were found to be 0.02 ± 0.01 for the HA- and Hep-poly(DEGMA-co-BMA) conjugates.

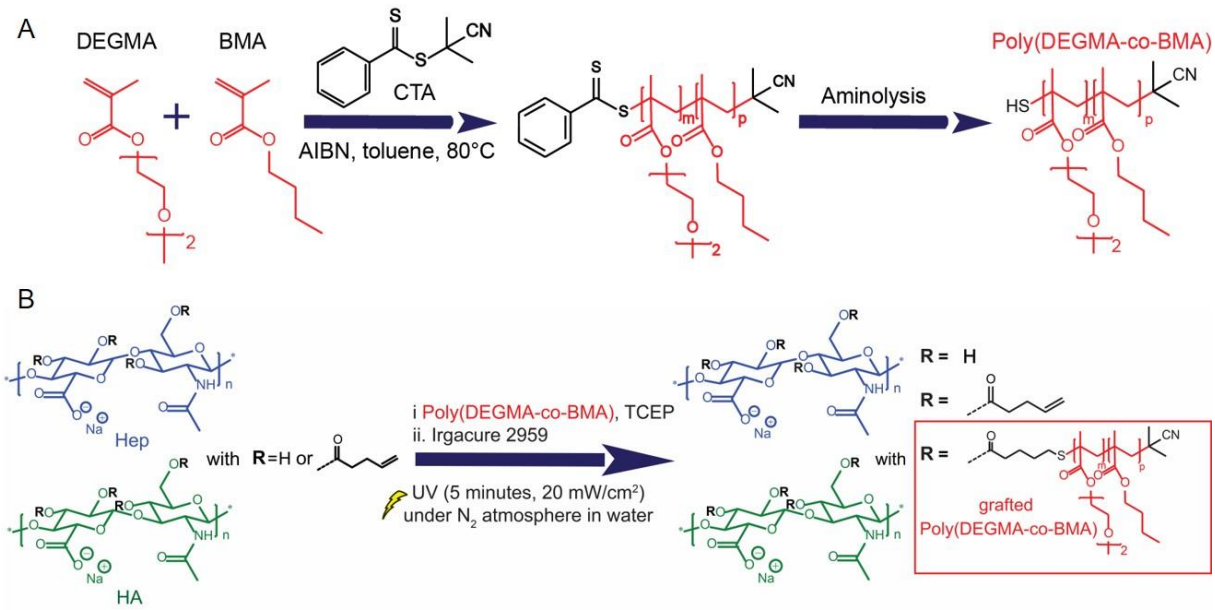

Scheme 2. *Synthetic pathway to HA- and Hep-poly(DEGMA-co-BMA). A) Synthesis of poly(DEGMA-co-BMA) via the RAFT process; B) Grafting of the thermoresponsive copolymer on HA and Hep using radical thiol-ene chemistry.*

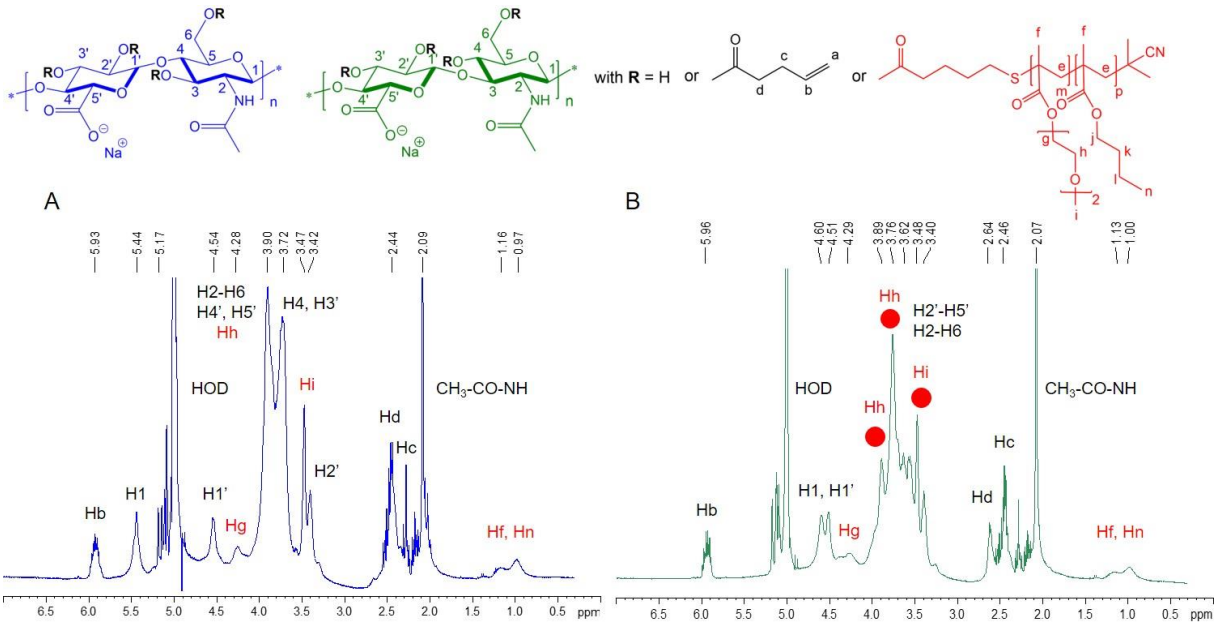

Figure 1. *^{1}H NMR spectra (400 MHz, 6 mg/mL in D_2O) of HA-poly(DEGMA-co-BMA) (A) and Hep-poly(DEGMA-co-BMA) (B) at 5°C.*

Temperature responsiveness of Hep- and HA-poly(DEGMA-co-BMA)

Dynamic light scattering analysis of solutions of Hep- and HA-poly(DEGMA-co-BMA) in PBS at 37 °C revealed a monomodal size distribution for both derivatives, indicating their self-assembly into nanogels at the body temperature (Figure 2A). The Hep and HA-based nanogels exhibited a similar average size (mean diameter derived from the intensity distribution (D_h) ~115 nm and Z-Ave ~ 110 nm). Self-assembly into nanogels was confirmed by transmission electron microscopy (TEM) analysis, performed by drying at 40 °C droplets of suspensions of poly(DEGMA-co-BMA)-modified Hep and HA in pure water (Fig. 2B).

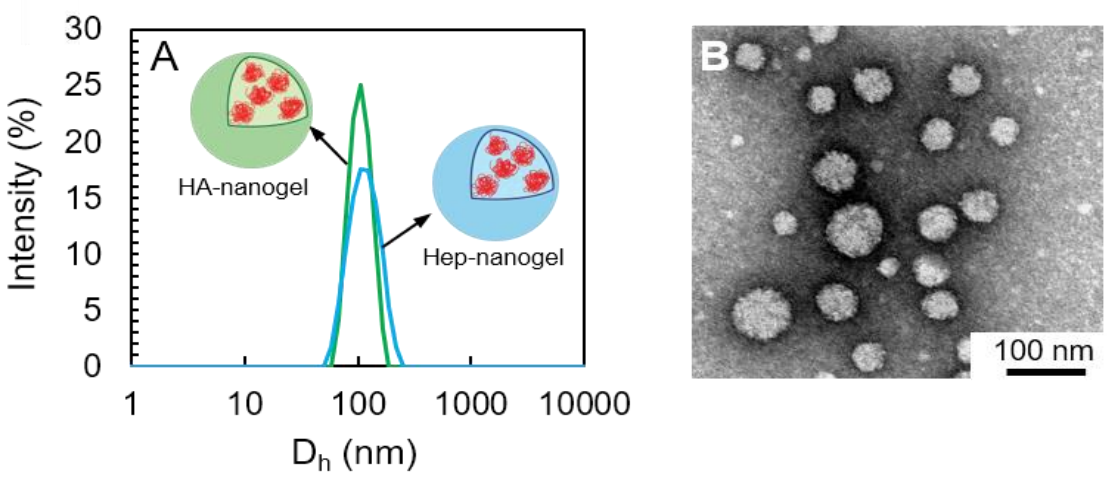

Figure 2. *Temperature responsiveness of Hep- and HA-poly(DEGMA-co-BMA). A) Dynamic light scattering analysis of Hep and HA-poly(DEGMA-co-BMA) solutions in PBS (C_p = 0.5 g/L) at 37 °C. B) TEM image of Hep-NGs in water at 40 °C (C_p = 0.5 g/L).*

The CAT of the HA- and Hep-poly(DEGMA-co-BMA) conjugates was determined by measuring the light scattering intensity of aqueous solutions of the derivatives as a function of temperature (Figure 3). The CAT, defined as the temperature at the intersection between the lower horizontal portion of the plotted curve and the tangent line, was found to be 20 °C and 22 °C for HA- and Hep-poly(DEGMA-co-BMA), respectively. Both HA and Hep derivatives are thus able to self-assemble into nanogels at room temperature. Self-assembly into well-defined nanostructures is also reflected in the sharp decrease of the PdI above the CAT as well as in the values of mean diameter in different distributions (intensity and number distribution) and of Z-average size, which are similar. In contrast, strong discrepancies between the mean size values are observed below the CAT.

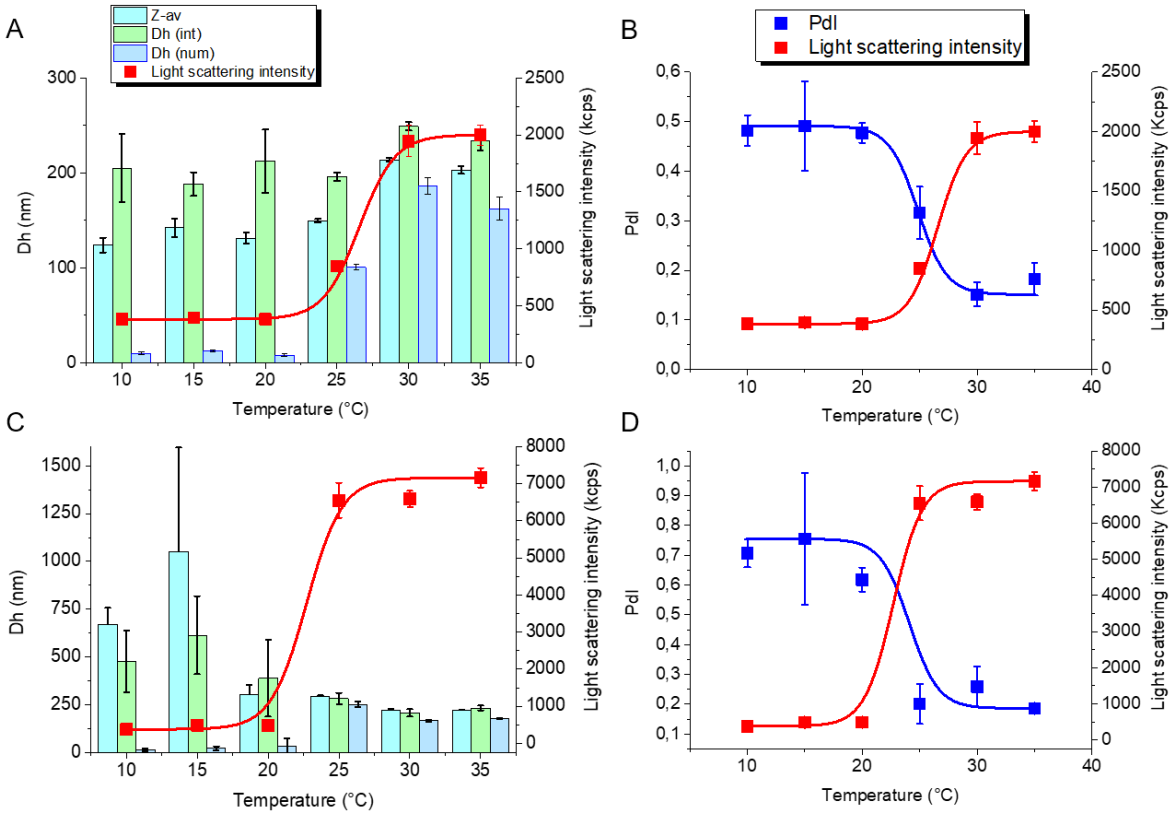

Figure 3. *Analysis by DLS of the temperature sensitivity of Hep-poly(DEGMA-co-BMA) (A, B) and HA-poly(DEGMA-co-BMA) (C, D) in PBS (pH 7.4, C_p = 0.5 g/L). A and C) Variation of the D_h, Z-Ave and LSI values upon cooling from 35 °C to 10 °C (0.5 °C/min). B and D) Variation of the LSI and PdI upon cooling from 35 °C to 10 °C.*

Synthesis and characterization of shell-crosslinked nanogels

Aiming at capturing the nanogel structure, the polysaccharide shell of Hep- and HA-NGs was crosslinked using thiol-ene chemistry by reaction of the remaining pentenoate groups with dithiothreitol (DTT) as a bis-thiol crosslinker (Figure 4A). This crosslinking step was performed under relatively dilute conditions (C_p = 0.5 g/L) to avoid internanogel coupling, and by varying the [SH]/[=] ratio from 1 to 2 to ensure that all nanogels were sufficiently crosslinked to be stable at low temperature. Comparison of ^{1}H NMR spectra before and after the thiol-ene reaction with DTT provided evidence of successful shell-crosslinking (Figure 4B), A decrease of the alkene proton signal at 5.9 ppm can be clearly observed after reaction with DTT, and the proton signals arising from the polysaccharide backbone and the copolymer are significantly broadened as a result of the extension of relaxation time after shell crosslinking. Successful crosslinking was further confirmed by FT-IR spectroscopy (Figure S4). In the IR spectra of the crosslinked nanogels, additional bands at 839 cm^{-1} and 911 cm^{-1} are observed after reaction with DTT, which can be attributed to C-S bend, C-S stretching and H-C-S bend, respectively. The new band observed at 1253 cm^{-1} (CH_2 vibrations) also suggests incorporation of DTT.[19-20]

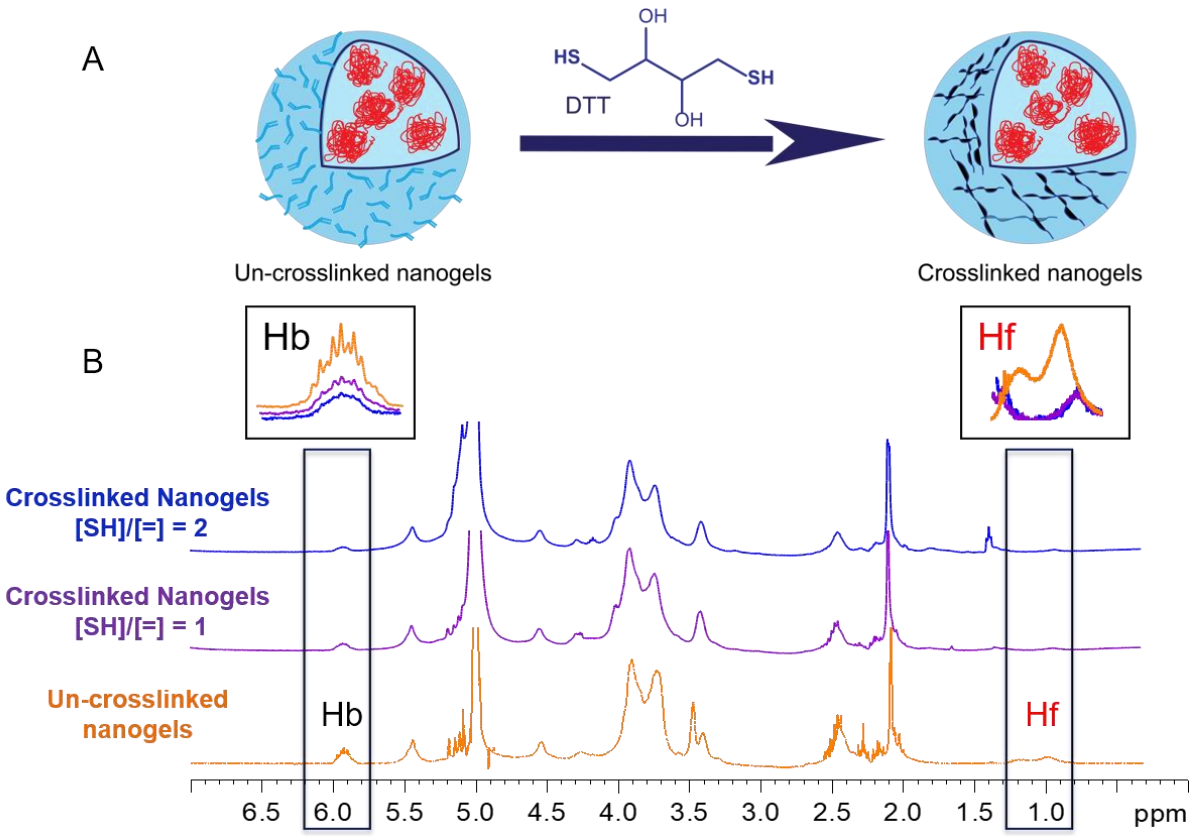

Figure 4. Shell crosslinking of NGs by reaction between DTT and alkene groups of the shell-forming polysaccharide. A) Reaction conditions: Irgacure 2959, UV-light (λ = 365 nm) exposure for 15 min, C_p = 0.5 g/L in PBS. B) Comparison of ^{1}H NMR spectra of un-crosslinked Hep-NGs and crosslinked Hep-NGs by varying the [SH]/[=] ratio from 1 to 2.

Temperature responsiveness of crosslinked nanogels

While the un-crosslinked nanogels of Hep-p-poly(DEGMA-co-BMA) and HA-p-poly(DEGMA-co-BMA) disassemble below the CAT (~ 22 °C), their counterparts crosslinked with excess DTT ([SH]/[=] of 2) were found to be stable below the CAT. This was clearly demonstrated by DLS measurements at temperatures varying from 30 to 10 °C with a cooling rate of 0.3 °C/min (Figure 5). The LSI and PdI of the nanogels were constant upon cooling, demonstrating efficient nanogel crosslinking. Furthermore, scanning electron microscopy (SEM) images revealed the presence of nanogels at 5 °C (Figure 5C and 5F). It should be noted that a ratio of [SH]/[=] of 2 is required to ensure complete stability of nanogels. Indeed, the LSI of the nanogels crosslinked with a [SH]/[=] ratio of 1 slightly decreased upon cooling, suggesting dissociation of some nanogels (Figure S5).

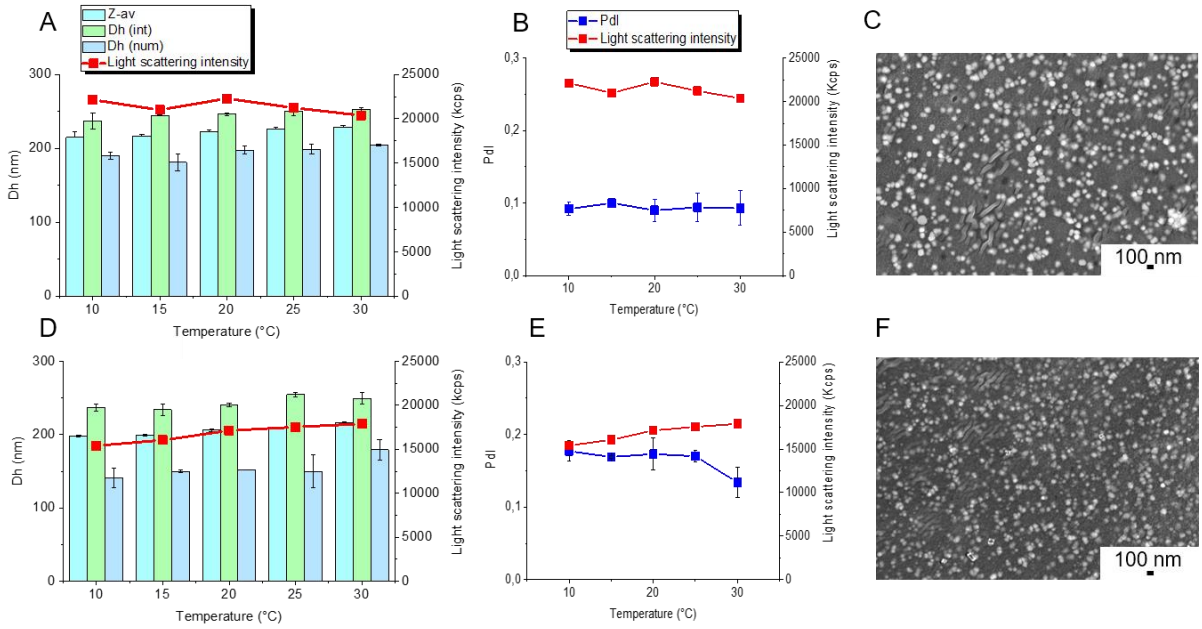

Figure 5. Analysis by DLS and SEM of crosslinked Hep-NGs (A, B, C) and HA-NGs (D, E, F) in PBS (pH 7.4, Cp = 0.5 g/L). A and D) Variation of the D_h, Z-Ave and LSI values upon cooling from 35 °C to 10 °C (0.5 °C/min). B and E) Variation of the LSI and PdI upon cooling from 35 °C to 10 °C. C and F) SEM observation at 5 °C.

Interestingly, the SCL nanogels showed temperature-dependent swelling/deswelling transitions between 15 and 40 °C. The swelling-deswelling transition was fully reversible over multiple heating/cooling cycles.

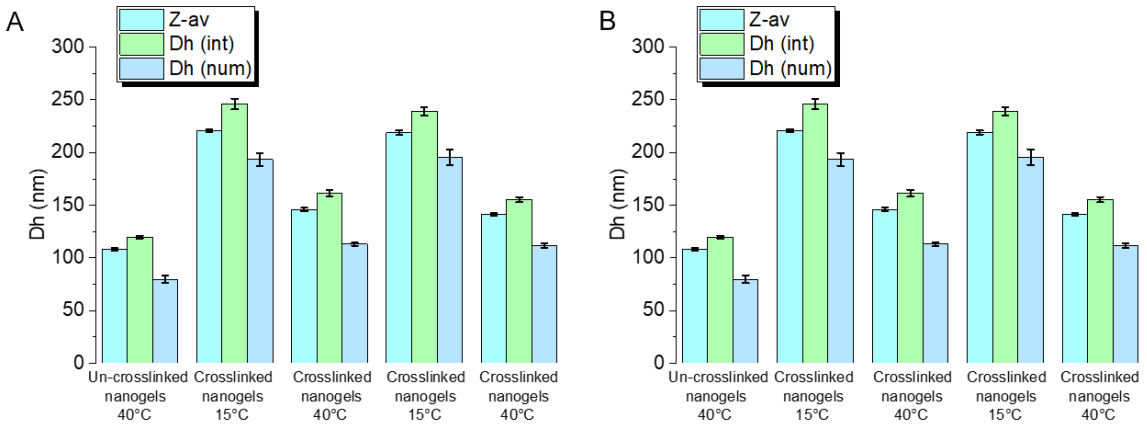

Figure 6. Analysis by DLS of the swelling-deswelling transition of crosslinked Hep-NGs (A) and HA-NGs (B) over multiple heating/cooling cycles (C_p = 0.5 g/L in PBS).

Cytotoxicity of crosslinked and un-crosslinked Hep-NGs and HA-NGs

The cytotoxicity of un-crosslinked and shell-crosslinked Hep-NGs and HA-NGs, as well as of native HA and Hep, was evaluated in Vero cells after 72 h of incubation by MTT assay. For all the samples, the toxic concentration for 50% of the cells was higher than 1000 µg/mL, the maximum assessed concentration, demonstrating the very low cytotoxicity and biocompatibility of our HA and Hep derivatives (Figure S6).

***In vivo* biodistribution and tumor targeting of crosslinked and uncrosslinked Hep-NGs and HA-NGs**

The *in vivo* biodistribution and tumor targeting of Hep- and HA-based nanogels were evaluated in Ehrlich solid tumor (EST)-bearing mice[12] by a non-invasive fluorescence imaging system. The main characteristics of the nanogels in terms of mean size and PdI are summarized in Table 1. Importantly, the similar size of both HA- and Hep-based un-crosslinked nanogels as well as of both crosslinked ones together with their similar chemical composition, except the hydrophilic shell structure, allowed a proper comparison of the biodistribution of HA- and Hep-NGs. The nanogels and the native polysaccharides, HA (Mw = 20 and 40 kg/mol) and Hep (Mw = 30 kg/mol), were labeled with the NIR dye Sulfo-Cyanine7 (Cy7) to visualize their biodistribution. Briefly, the samples were chemically modified with Cy7-amine using 4-(4,6-dimethoxy-1,3,5-triazin-2-yl)-4-methylmorpholinium chloride as an amine-acid coupling agent.[21] The content of Cy7 molecules in the polysaccharide derivatives (DS) was 0.002, as determined by UV/Vis spectroscopy at 680 nm. After Cy7 labeling, the nanogels maintained their size as shown by nanoparticle tracking analysis (NTA),[22] which enables the visualization and recording of nanoparticles in solution (Figure S7). Particle size distribution obtained by NTA ranged from 60 to 250 with an average of 150 ± 40 nm and from 60 to 300 with an average of 190 ± 43 nm for the SCL NGs based on HA and Hep, respectively (Figure S7).

Table 1. Size and polydispersity of nanogels based on Hep-poly(DEGMA-co-BMA) and HA-poly(DEGMA-co-BMA) determined by dynamic light scattering at 40 °C (0.5 g/L in PBS).

	Nanogels	Z-Average size (nm)	PdI
HA	Un-crosslinked nanogel	108 ± 1	0.174 ± 0.03
	Crosslinked nanogels (1 eq DTT)	151± 2	0.176 ± 0.01
Hep	Un-crosslinked nanogel	119 ± 1	0.095 ± 0.006
	Crosslinked nanogel (1 eq DTT)	146 ± 2	0.095 ± 0.013

Time-dependent biodistribution of Cy7-labeled native Hep, HA and nanogels on EST-bearing mice was observed after intravenous administration. *Ex-vivo* fluorescence images of excised organs and tumors showed a higher accumulation of Hep-NGs in the tumor than HA-NGs. As shown in Figure 7A, the intensity ratio of tumor-to-liver between 1 h and 24 h was in the order un-crosslinked Hep-NGs > crosslinked Hep-NGs > un-crosslinked HA-NGs ≈ crosslinked HA-NG, suggesting lower liver uptake and higher tumor accumulation for the nanogels based on Hep. These results were consistent with those obtained from native polysaccharides (Figure 7B). Indeed, as can be seen from Figure 7B, the intensity ratio of tumor to liver is much higher for Hep (M_w = 30 kg/mol) than HA, whatever the molar mass of HA (20 or 40 kg/mol). Interestingly, the intensity ratio of tumor-to-liver for the Hep-NGs and linear Hep progressively increased during the whole period of time studied (24 h). This shows their preferential accumulation at the tumor site.

The higher liver uptake of HA-NGs and linear HA may be related to the HARE-mediated endocytosis.[6] This assumption is supported by the fact that the un-crosslinked Hep- and HA-NGs have similar average diameters (D_h ~ 113-120 nm) as well as the crosslinked ones (D_h ~ 161-183 nm). Regarding the effect of shell-crosslinking on the biodistribution, no conclusion could be drawn from the comparison between uncrosslinked and crosslinked nanogels. The biodistribution of both HA-NGs appeared to be relatively similar, despite the slightly higher size and decreased deformability of the crosslinked nanogels. With regard to the Hep NGs, the fluorescence of the crosslinked ones was detected with higher levels in most organs, including tumor and liver. This resulted in a lower value of tumor-to-liver intensity ratio compared to the uncrosslinked NGs.

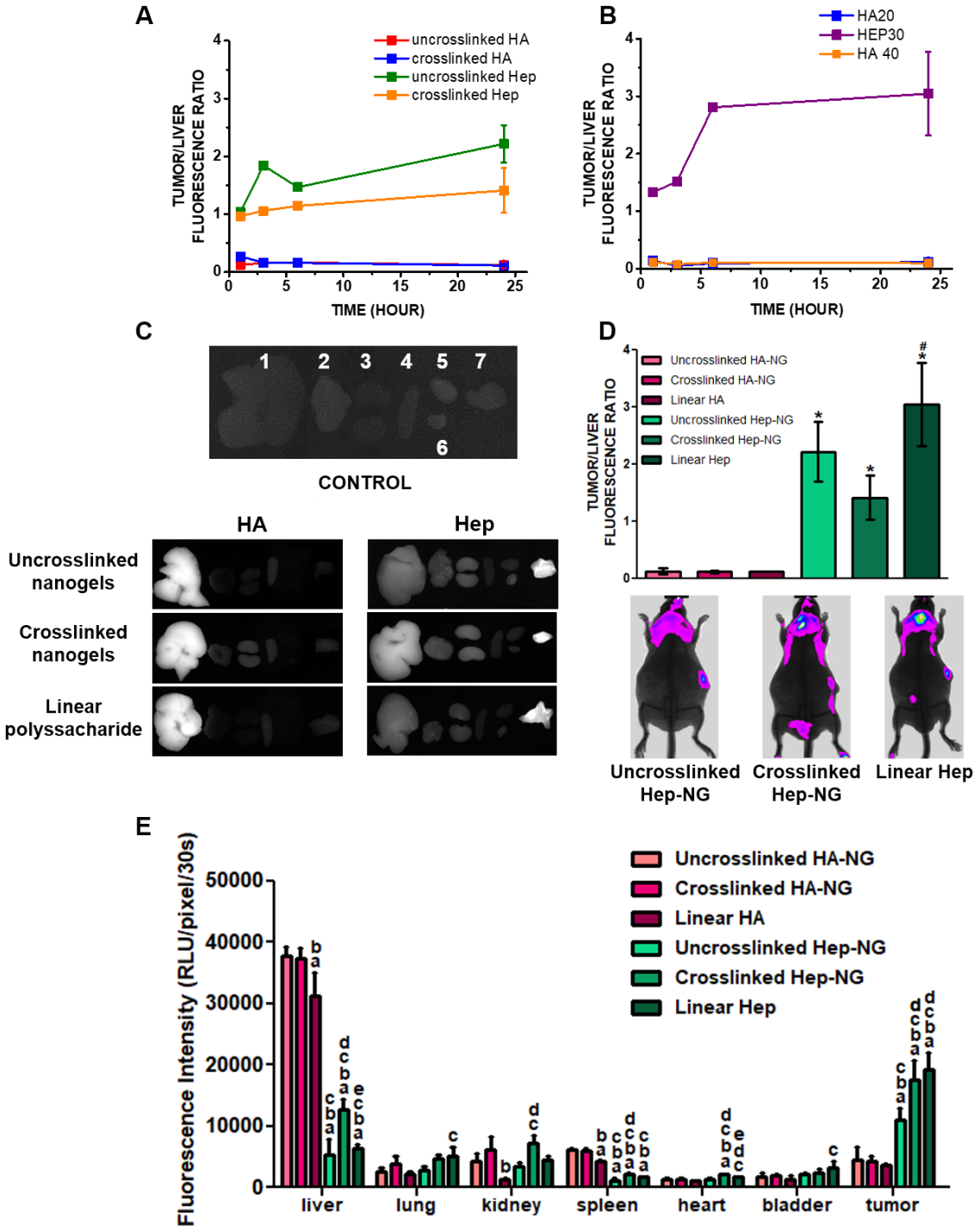

Figure 7. *In vivo biodistribution of Hep- and HA-NGs in EST tumor-bearing mice. Fluorescence intensity ratio of the excised tumor to liver at 1 h, 3 h, 6 h (n= 1) and 24 h (n = 3) post-injection of Hep- and HA-NGs (A), and of native Hep and HA (B). C) Ex vivo fluorescence images of organs and tumors retrieved from the tumor-bearing mice at 24 h post-injection of NGs and of the native polysaccharides: (1) liver; (2) lung; (3;3') kidney; (4) spleen; (5) heart; (6) bladder; (7) tumor. D) Top: fluorescence intensity ratio of the excised tumor to liver at 24 h post-injection of Hep- and HA-NGs as well as of native Hep and HA (n = 3); bottom: representative images of in vivo fluorescence images of the tumor-bearing mice after intravenous injection Hep-NGs and of native Hep. Error bars represent standard deviations (SD). One-way ANOVA followed by Tukey post hoc test. *# P < 0.05. *Compared to HA (native polysaccharide and nanogels).*

[#]Compared to crosslinked Hep-NG. E) Ex vivo fluorescence intensity of main organs at 24 h post-administration of uncrosslinked and crosslinked HA- and Hep-NGs and native polyssacharides (HA and Hep) (n = 3). The results were expressed as mean ± SD. One-way ANOVA followed by Tukey post hoc test: [a]Compared to uncrosslinked HA-NG; [b]compared to crosslinked HA-NG; ccompared to linear HA; [d]compared to uncrosslinked Hep-NG; [e]compared to crosslinked Hep-NG.

Conclusion

In this study, novel biocompatible and biodegradable nanogels based on heparosan were developed by modification of the polysaccharide backbone with a thermoresponsive copolymer, poly(DEGMA-co-BMA), properly designed to obtain stable nanogels at room temperature. The versatile synthetic route to nanogels also allowed their further shell-crosslinking to capture the nanogel structure at low temperature. Following intravenous administration in tumor-bearing mice, both un-crosslinked and crosslinked Hep-NGs were able to accumulate in the tumor at a much higher level than their counterparts based on HA. Importantly, the well-defined properties of both Hep- and HA-NGs families in terms of chemical structure (except the hydrophilic outer-shell), size and morphology allowed to reliably assess the effect of the outer-shell forming glycosaminoglycan on their *in vivo* biodistribution. These results thus showed that Hep-NGs provide an exciting new class of drug delivery platform for cancer therapy. To the best of our knowledge, our study provides the first analysis of the *in vivo* behavior of self-assembled nanoparticles based on Hep, demonstrating significant differences compared to HA-based self-assembled nanoparticles. Regarding the effect of shell-crosslinking on *in vivo* biodistribution, higher accumulation levels in most of organs, especially in liver and tumor, were observed for the crosslinked Hep-NGs compared to the un-crosslinked ones, 24 h after administration. At this stage, it is difficult to explain these results as the uncrosslinked and crosslinked NGs are different not only in size but also in shell stiffness/deformability. So far, the impact of nanoparticles flexibility/stiffness on their function has been very little explored, and the potential benefits of tuning nanoparticle elasticity are not clear.[23-25] Based on these considerations, these Hep-NGs represent an attractive platform to investigate the impact of design parameters such as shell crosslinking, incorporation of combination regimens as well as inorganic nanoparticles (magnetic nanoparticles, gold nanoparticles) in order to more optimally exploit the biocompatibility and the beneficial distribution of these novel nanocarriers.

Experimental section – Materials and Methods

Materials. Hyaluronic acid samples (M_w = 20 and 40 kg/mol) were purchased from Lifecore (USA). Heparosan (M_w = 30 kg/mol) was kindly provided by HTL (Javené, France). (Diethylene glycol) methyl ether methacrylate, butyl methacrylate, 2-cyano-2-propyl benzodithioate, 2,2-azobis(2-methylpropionitrile), phosphate buffer saline (PBS, pH 7.4), sodium chloride, aluminum oxide, tris-(2-carboxyethyl) phosphine hydrochloride (TCEP), *n*-butylamine, 4-pentenoic anhydride, thiazolyl blue tetrazolium bromide, 1,4-dithiothreitol and 4-(4,6-dimethoxy-1,3,5-triazin-2-yl)-4-methylmorpholinium chloride were purchased from Sigma-Aldrich-Fluka (France). 2-Hydroxy-1-[4-(2-hydroxy-ethoxy)phenyl]-2-methyl-1-propanone (Irgacure 2959) was kindly provided by Ciba Speciality Chemicals (Basel, Switzerland). Sulfo-Cyanine7 amine (Cy7-amine) was purchased from Lumiprobe. Dulbecco's Modified Eagle's Medium (DMEM), L-glutamine and fetal bovine serum (FBS) were provided by Gibco. All chemicals, except DEGMA and BMA which were purified by running them through a column packed with aluminum oxide, were used without any further purification. The positively charged resin, diethylaminoethyl cellulose (DEAE Sepharose CL-6B) was purchased from GE Healthcare Life Science. Spectra/Por 1 (MWCO 6-8000 g/mol) membrane used for dialysis was obtained from Fisher Scientific (Rancho Domingez, CA). The water used in all experiments was purified by a Elga Purelab purification system, with a resistivity of 18.2 MΩ cm. Deuterium oxide (D_2O) and deuterated dichloromethane ($CDCl_3$) were obtained from SDS (Vitry, France). The pentenoate-modified HA20 and Hep30 derivatives with a degree of substitution of 0.5 were synthesized as previously described. [17]

Analytical Techniques. ^{1}H NMR spectra were recorded at 10, 25 or 80 °C using a Bruker AVANCE III HD spectrometer operating at 400 MHz. All spectra were recorded by applying a 45° tip angle for the excitation pulse, and a 10 s recycle delay. Chemical shifts (δ in ppm) are given relative to external tetramethylsilane (TMS = 0 ppm) and calibration was performed using the signal of the residual protons of the solvent as a secondary reference. Fourier transform infrared spectroscopy (FTIR) measurements were performed on a RX1 spectrometer (Perkin Elmer, UK) with horizontal ATR accessory. For each sample, 32 scans were recorded between 4000 and 400 cm^{-1} with a resolution of 2 cm^{-1} using the Spectrum software V 5.0.0. The spectra was then analyzed using the Origin 7.0 software. The number-average molar mass (M_n), the weight-average molar mass (M_w) and the dispersity (*Đ*) of poly(DEGMA-co-BMA) were determined by size exclusion chromatography (SEC) in dimethylformamide containing 50 mM $NaNO_3$. Measurements were done on a GPC system equipped with a Waters model 515 pump, a refractive Index Detector RI 2000 from Schambeck SFD GmbH and a light scattering detector (MALLS) from Wyatt (USA). The samples were analysed using a 161123-Agilent-10 column

at 30 °C and at a flow rate of 1 mL/min. The cloud point temperature (T_{cp}) of poly(DEGMA-co-BMA) was determined by UV-vis turbidity measurements (λ = 500 nm) performed on a Varian Cary 50 Scan. The samples were prepared at room temperature in PBS (from 0.1 to 3 g/L), after which the sample was placed in the instrument. The light transmittance was measured during at least two controlled cooling/heating cycles from 10 °C to 40 °C using a 1°C/10 min interval. T_{cp} was considered to be the temperature at which the light transmittance was 50 % of that obtained for the same sample at 10 °C. The critical aggregation temperature (CAT) of HA-poly(DEGMA-co-BMA) or Hep-poly(DEGMA-co-BMA) in aqueous solution was assessed using a Zetasizer NanoZS Malvern Instruments apparatus equipped with a HeNe laser at 173° and a temperature controller. A solution of HA-poly(DEGMA-co-BMA) or Hep-poly(DEGMA-co-BMA) in PBS at a concentration of 0.5 mg/mL was filtered through a 0.45 µm polycarbonate filter and heated from 10 to 40 °C using a 5 °C interval. The CAT was considered to be the temperature at the intersection between the lower horizontal portion of the plotted curve (average scattered intensity versus temperature dependence) and the tangent line of the curve. The size and size distribution of nanogels were simultaneously measured with the CAT by dynamic light scattering (DLS) using a Zetasizer NanoZS Malvern Instruments apparatus operating with a HeNe laser at 173°. The hydrodynamic diameters were calculated from diffusion coefficients using the Stokes-Einstein equation. All correlogram analyses were performed with software supplied by the manufacturer. All the measurements were performed in PBS (pH 7.4, [NaCl] = 0.15 M).

Synthesis of copolymer poly(DEGMA-co-BMA). DEGMA (10 g, 50 mmol) and BMA (0.398 g, 2.79 mmol), the RAFT agent 2-Cyano-2-propyl benzodithioate (0.082 g, 0.372 mmol) and AIBN (3 mg, 0.0186 mmol) in anhydrous toluene (25 mL) were placed in a round bottom Schlenk flask and oxygen was removed via bubbling the mixture under nitrogen atmosphere for 30 min. Then, the flask was sealed and placed in a thermostatic oil bath pre-heated at 80 °C. The reaction was quenched by cooling and exposure to oxygen. The resulting copolymer was precipitated in cyclohexane. The precipitate was dissolved in dichloromethane and the copolymer was precipitated again in cyclohexane. The resulting precipitate was finally dried under high vacuum to give 6 g of pure poly(DEGMA-co-BMA). Samples taken before and during the polymerization were analyzed by ^{1}H NMR to determine monomers conversion. The M_n, M_w and $Đ$ values of the copolymer were determined by size exclusion chromatography in DMF.

Synthesis of HA-poly(DEGMA-co-BMA) and Hep-poly(DEGMA-co-BMA). Prior to the coupling reaction with HA-pentenoate, or Hep-pentenoate, the poly(DEGMA-co-BMA) copolymer was subjected to aminolysis using *n*-butylamine, to convert the RAFT end-group to

a thiol. Briefly, the copolymer (600 mg, 0.375 mmol) was solubilized in dichloromethane (9 mL) and *n*-butylamine (6.5 mL, 66 mmol) was added. After 5 min under stirring at room temperature, the reaction mixture was concentrated under reduced pressure, resulting in a waxy liquid that was solubilized in dichloromethane. The copolymer was recovered by precipitation in cyclohexane and dried under vacuum at 45 °C during 4 hours to remove residual solvent. Next, the thiol-end-functionalized copolymer (550 mg, 0.0312 mmol) was solubilized in 14 mL of pure water and TCEP (10 mg, 0.0350 mmol) was added. After 30 min of stirring at 4 °C under nitrogen atmosphere, the copolymer solution was added to an aqueous solution of HA-pentenoate or Hep-pentenoate (50 mg, 0.116 mmol) in pure water (4 mL), followed by a solution of Irgacure 2959 (2 mL) in water (10 g/L) in order to obtain a final photoiniator concentration of 0.1 % (w/v) in the reaction media. The reaction mixture cooled in a ice bath, was exposed to UV light (λ = 365 nm) with an intensity of 20 mW/cm^2 for 5 min under stirring and nitrogen atmosphere. The resulting HA-poly(DEGMA-co-BMA) and Hep-poly(DEGMA-co-BMA) derivatives were purified via a batch ion exchange process using DEAE Sepharose CL-6B as a weak-anion exchanger. Briefly, DEAE resin (20 mL), stored in a solution of ethanol 30 %, was washed three times with ultrapure water at 4 °C (3 × 20 mL, contact times of 10 min). Excess liquid was removed by centrifugation (10000 rpm, 10 min) at 4° C. Then, the resin was activated by successive washes with a 0.5 M NaCl aqueous solution (20 mL), a 1 M NaCl aqueous solution (20 mL) and finally, four times with ultrapure water (4 × 20 mL). The HA-poly(DEGMA-co-BMA) or Hep-poly(DEGMA-co-BMA) derivative was then added to the resin in a conical tube and allowed to interact with the resin overnight at 4°C under stirring with an orbital shaker. Then, the HA or Hep derivative bound to the resin was subjected to seven washes with ultrapure water (7 × 20 mL) to remove un-grafted copolymer. Finally, the HA or Hep derivative was eluted with a 1 M NaCl aqueous solution (4 × 10 mL). After filtration of the solutions of the HA or Hep derivative through a Buchner funnel with a porous glass filter plate (porosity 4), the solution was dialyzed against deionized water (membrane with cut-off 6-8 Da MW, 72 h). The product was recovered by freeze-drying as a white powder.

Synthesis of crosslinked nanogels. To a solution of HA-poly(DEGMA-co-BMA) or Hep-poly(DEGMA-co-BMA) (0.015 g, 0.022 mmol) with a DS of 0.03 at a concentration of 0.5 g/L in PBS (pH 7.4) at 4°C under nitrogen atmosphere in an ice bath, 564 µL (1.41 mg, 0.009 mmol) of a solution of DTT in PBS (2.5 g/L) was added under stirring. Next, the temperature of the solution was increased to 40°C well above the CAT. After stirring at 40°C for 45 min, 3.3 mL of an aqueous solution of Irgacure 2959 (10 mg/mL) was then added to the nanogels suspension to obtain a final photoiniator concentration of 10 % (w/v). The mixture was exposed to UV light (λ = 365 nm) with an intensity of 20 mW/cm^2 for 15 min under stirring and nitrogen atmosphere. The nanogels suspension was transferred into a dialysis bag (MWCO = 6-8000

g/mol) and dialyzed against deionized water for 72 h. The shell cross-linked nanogels were recovered by freeze-drying. The volume of the DTT solution (218 μL, 652 μL) was varied to obtain [SH]/[=] ratios of 0.5 and 1.0, respectively. Next, the temperature of the solution was increased to 40 °C.

Determination of the degree of substitution of HA-poly(DEGMA-co-BMA) and Hep-poly(DEGMA-co-BMA) samples by the carbazole reaction. The DS was indirectly determined by reaction of D-glucuronic acid units of HA with carbazole [26] Briefly, 800 µL of 25 mM sodium tetraborate solution in sulfuric acid was added to an aqueous solution of HA-poly(DEGMA-co-BMA) or Hep-poly(DEGMA-co-BMA) (200 µL) at a concentration of 0.1 g/L. After heating at 100 °C for 10 min, the solution was cooled at room temperature for 15 min, and then a solution of carbazole (200 µL) in absolute ethanol 0.125 % (m/v) was added. The sample was heated again at 100 °C for 10 min and its absorbance was determined by spectrophotometry at 530 nm. The polysaccharide concentration was calculated from a calibration curve (0.050 to 0.200 g/L), which allowed the indirect determination of copolymer amount in the HA- and Hep-poly(DEGMA-co-BMA) samples.

Scanning electron microscopy and transmission electron microscopy. For SEM analysis, drops of un-crosslinked and crosslinked nanogels solutions (0.5 mg/mL) in ultrapure water at both 5 and 40 °C were deposited onto mica-coated copper stubs (also precooled/heated at 5 or 40 °C, respectively) and allowed to air drying at 4 or 40 °C. The samples were then coated by approximately 2 nm of sputtered Au-Pd and observed in secondary electron imaging mode with a ZEISS Ultra 55 FEG-SEM (Grenoble INP - CMTC). Images were acquired at low voltage of 3 kV using an in-lens detector. For TEM analysis, all samples were dispersed in ultrapure water, stained with 5 % uranyl acetate and observed with a JEOL JEM 1400 (Jeol, USA) transmission electron microscope operating at 120 kV acceleration voltage.

Labeling of nanogels based on HA-poly(DEGMA-co-BMA) and Hep-poly(DEGMA-co-BMA) with sulfo-cyanine7. Fluorescent nanogels were prepared by grafting the dye Cy7-amine on un-crosslinked and crosslinked nanogels based on HA-poly(DEGMA-co-BMA) and Hep-poly(DEGMA-co-BMA) (DS= 0.01) by an amine-acid coupling reaction using DMTMM as a coupling agent[29]. To this end, crosslinked nanogels (0.008g, 0.0135 mmol) were solubilized in water/DMF (1:1 v/v; 4 mL) and DMTMM (3.7 mg, 0.0135 mmol) was added to the solution, followed by adjusting the pH to 6.5. After 30 min of stirring, Cy7-amine (0.5 mg, 0.000676 mmol) solubilized in water/DMF (1:1 v/v) at a concentration of 5 g/L was added to the reaction mixture. After stirring at room temperature for **72 h**, the nanogels were purified by dialysis using a membrane MWCO 6-8 kg/mol against a mixture of water/ethanol (2/1 v/v) then, against deionized water for 48 h and finally, they were recovered by freeze-drying.

Cytotoxicity assay. Vero cells (ATCC, Maryland) were maintained in DMEM supplemented with 2 mM L-glutamine and 10% heat-inactivated FBS at 37 °C in a 5% CO_2 atmosphere. In order to investigate a possible toxicity of Hep and HA nanogels towards mammalian cells, Vero cells obtained from confluent cultures were plated (5 x 10^5 cells/mL) in 96-well plates and incubated for 24 h at 37 °C in a 5% CO_2 atmosphere. Next, the cells were treated with different concentrations (10 – 1000 µg/mL) of HA- and Hep-NGs as well as the native polysaccharides solutions in DMEM. After 72 h of incubation, the cultures were evaluated by MTT assay, as previously described[30]. After treatment, the medium was removed, and the cellular monolayer was washed with 0.01 M PBS (pH 7.4), and 50 µL of MTT solution at 2 mg/mL were added to each well. After incubation for 4 h at 37 °C protected from light, MTT solution was removed and 150 µL of DMSO was added to each well. Absorbance was read in a microplate reader (BIO-TEK Power Wave XS) at 570 nm. The percentage of viable cells was calculated compared with controls (not treated cells). The concentration that decreased 50% of the absorbance compared with the control cells was considered the toxic concentration for 50% of cells (CC_{50}).

***In vivo* biodistribution**. All *in vivo* procedures were carried out in accordance with the Brazilian legislation issued by the National Council for Control of Animal Experimentation (CONCEA) and was approved by the Ethic Committee on Animal Use of State University of Maringá (CEUA/UEM), protocol number CEUA 6160200416. Male hairless mice (3 weeks old, 20-30 g, Londrina, Brazil) were housed under controlled conditions of temperature (22 ± 1°C) and humidity, 12:12 h light/dark cycle and *ad libitum* access to food and water. Xenografted tumors were obtained by subcutaneously injectinga suspension of 5 × 10^5 Ehrlich cells in PBS (50 µL), obtained from Ehrlich tumor ascitic fluid, on the right flanks of mice. After tumor grown period (≈10 days), animals were anesthetized with isoflurane 2% in an air/O_2 mixture, and 100 µL of suspensions of Cy7-labeled uncrosslinked and crosslinked HA- and Hep-NGs (3 g/L in PBS) were administered in the tail vein. For comparison, Cy7-labeled HA (M_w = 20 and 40 kg/mol) and Hep (M_w = 30, 3 g/L in PBS) were also injected. Immediately after injection, mice were evaluated using an In-vivo MS FX PRO (Carestream Molecular Imaging, Carestream Health, United States). Fluorescent images (λexc = 750 nm; λem = 790 nm) were obtained with a CCD camera (Kodak Image Station) at 0, 1, 3 and 24 h post-injection. Mice were then sacrificed and the main organs (liver, spleen, lung, kidney, heart, bladder and tumor) were removed for *ex-vivo* imaging. Images acquisition and semi-quantification of relative fluorescence intensity in regions of interest (ROI) were performed using Carestream Molecular Imaging 5.0 software (Carestream Molecular Imaging, Carestream Health, United States).

ASSOCIATED CONTENT

Supporting Information. The Supporting Information is available free of charge on the ACS Publications website.

Kinetics of copolymerization of DEGMA and BMA, detailed characterization of poly(DEGMA-co-BMA), analysis of nanogel shell-crosslinking by FT-IR and DLS, *in vitro* cytotoxicity data of NGs and NTA analysis of Cy7-labeled NGs (PDF).

AUTHOR INFORMATION

Corresponding Author

* E-mail: rachel.auzely@cermav.cnrs.fr

Notes

The authors declare no competing financial interest.

ACKNOWLEDGMENT

The authors thank the Conselho Nacional de Desenvolvimento Científico e Tecnológico-Conselho Nacional de Desenvolvimento Científico e Tecnológico (CNPq) and Financiadora de Estudos e Projetos (FINEP) for financial support to this work. MR gratefully acknowledges the MESR for a PhD fellowship. The authors thank Vincent Martin at LEPMI for the GPC analysis of thermoresponsive copolymer; Francine Roussel-Dherbey at Grenoble INP-CMTC for her help with SEM observations; Isabelle Jeacomine for her assistance in NMR spectroscopy analysis at the platform of ICMG (FR2607); Rubia Casagrande and Waldiceu Aparecido Verri Junior (Londrina - Brazil), for kindly providing Hairless mice and Erlich ascites tumor cells.

Supporting information

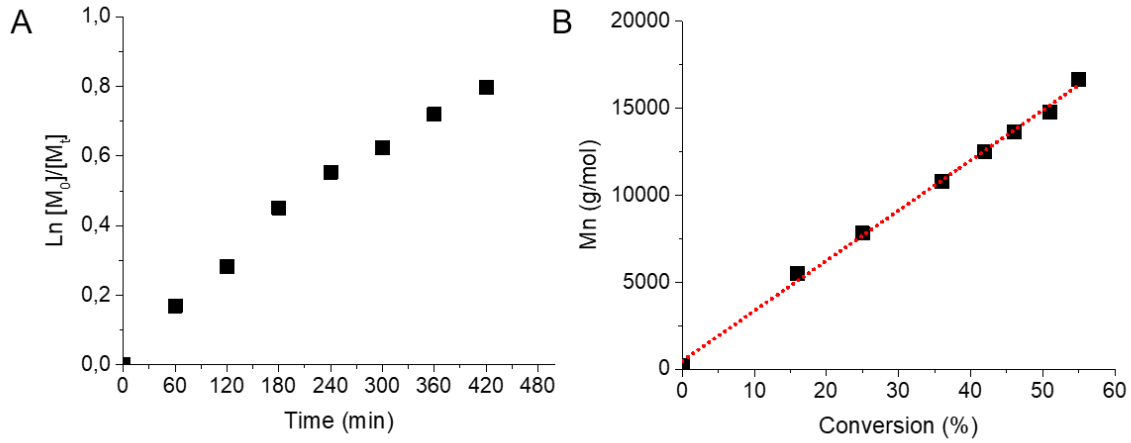

Figure S1. (A) Kinetic plots and (B) dependence of the number-average molar masses (M_n) on monomer conversion for the RAFT copolymerization of DEGMA and BMA. Reaction conditions: $[DEGMA]_0/[BMA]_0/[CTA]_0/[AIBN]_0$ = 95/5/0.77/0.038 at 80°C in toluene.

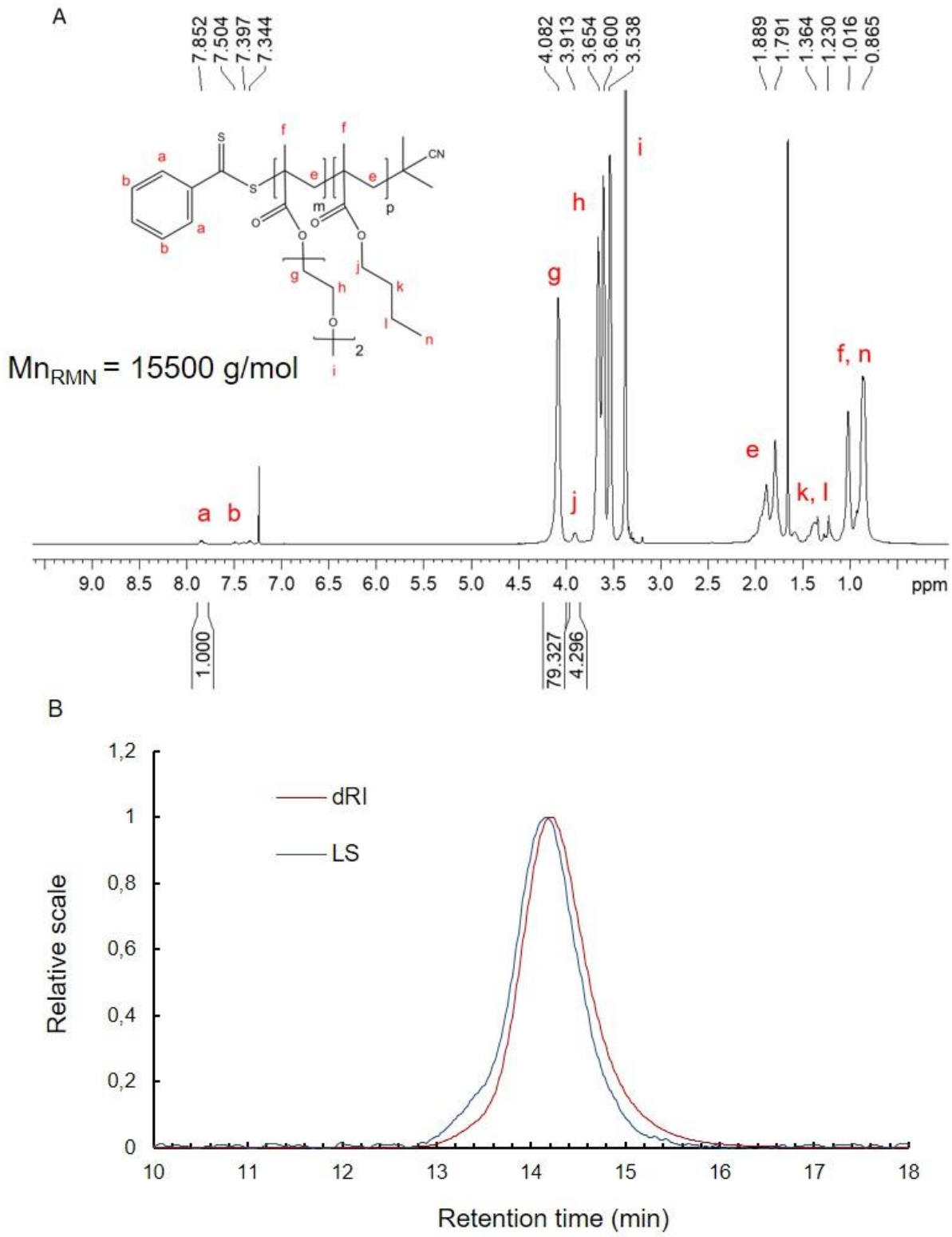

Figure S2. Characterisation of poly(DEGMA-co-BMA) by A) ^{1}H NMR spectroscopy (300 MHz, 10 mg/mL in $CDCl_3$, 25 °C) and, B) size exclusion chromatography (30 °C, flow rate of 1 mL/min; eluent: dimethylformamide containing 50 mM $NaNO_3$).

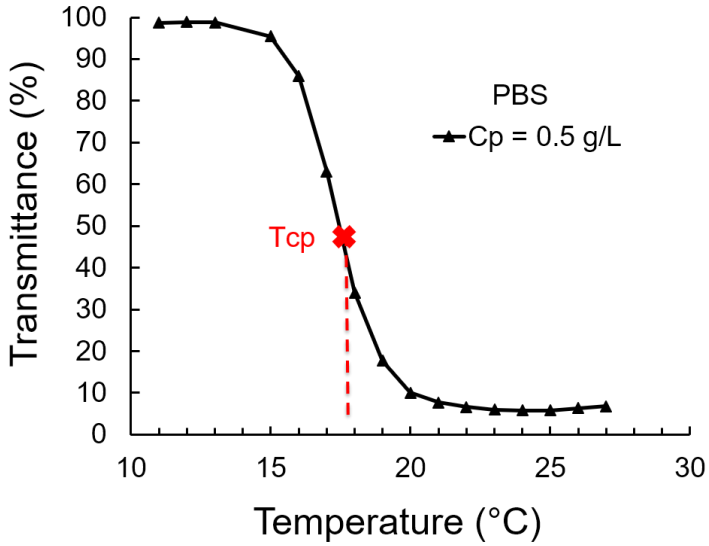

Figure S3. Turbidity measurement of a solution of poly(DEGMA-co-BMA) in PBS (0.5 g/L) as measured by UV/Vis spectroscopy at 500 nm.

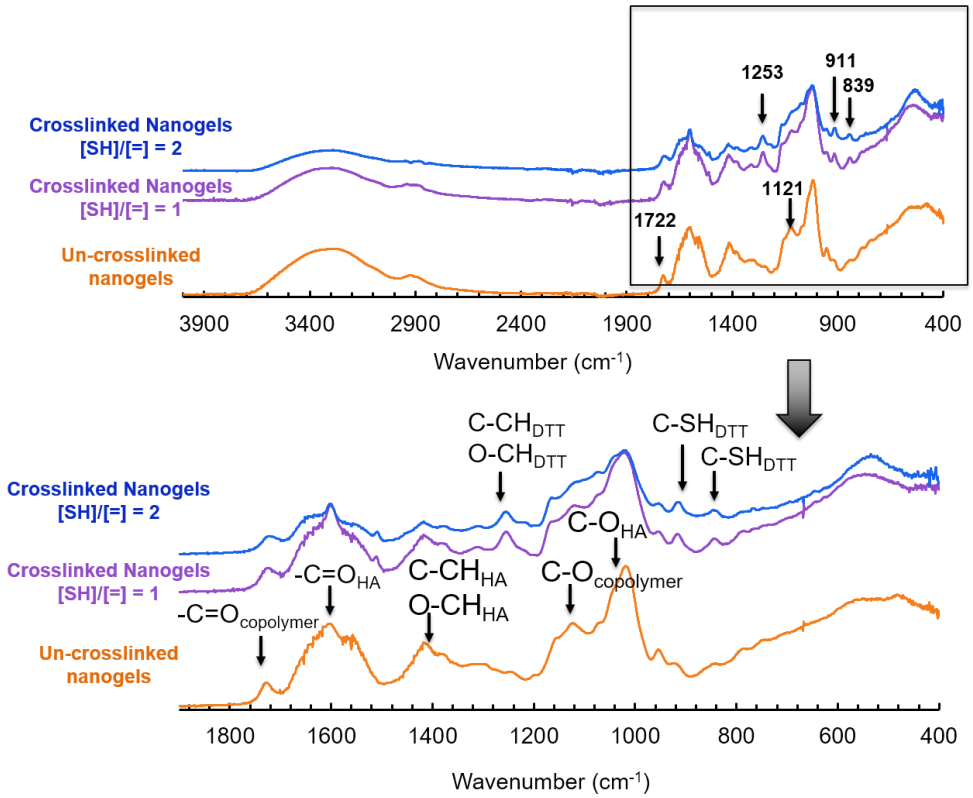

Figure S4. FT-IR spectra of crosslinked Hep-NGs with [SH]/[=] = 2 (blue) and [SH]/[=] = 1 (purple), and of uncrosslinked Hep-NGs (orange). Focus on the 1800-400 cm^{-1} region includes characteristic bands of DTT on the Heparosan backbone.

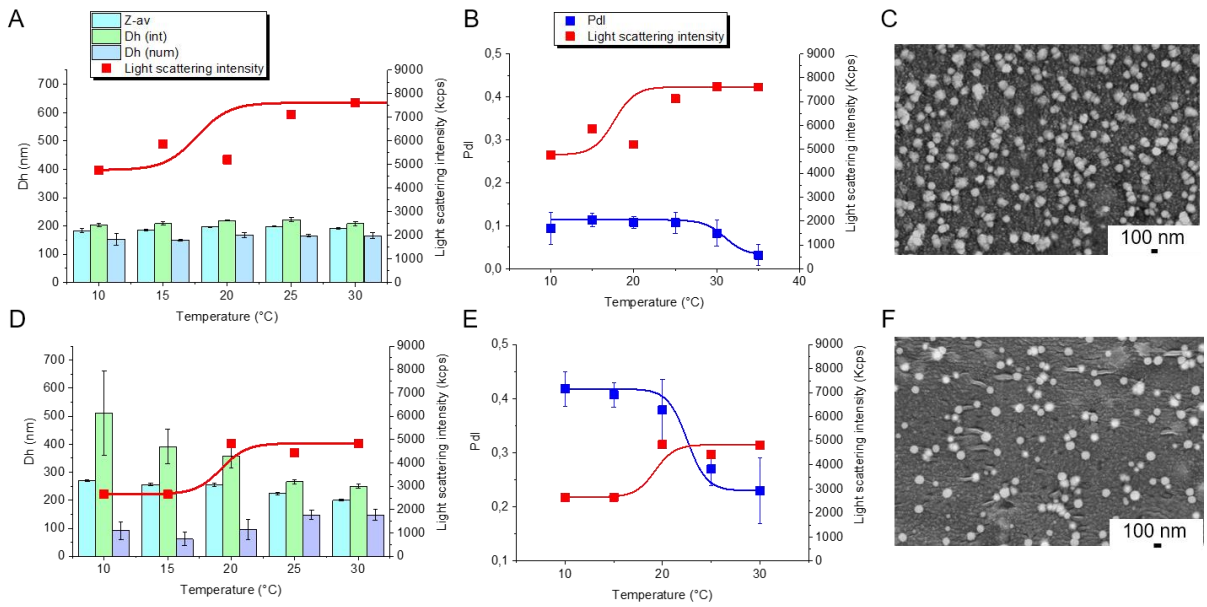

Figure S5. Behavior of crosslinked nanogels (CAT) based on Hep-poly(DEGMA-co-BMA) and HA-poly(DEGMA-co-BMA) with a [SH]/[=] ratio of 1. Analysis by DLS (C_p = 0.5 g/L in PBS) and by SEM of Hep-NGs (A, B, C) and of HA-NGs (D, E, F).

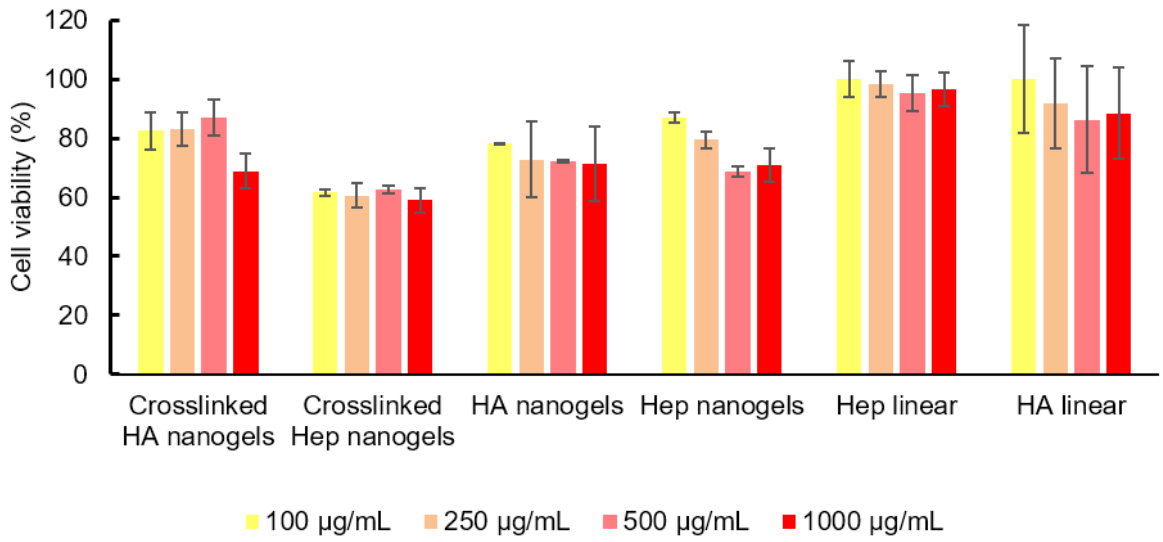

Figure S6. *In vitro* cytotoxicity of un-crosslinked and crosslinked HA- and Hep-NGs as well as of native HA and Hep in Vero cells after 72 h of incubation, evaluated by the MTT method. Data are expressed as mean ± SD of three independent experiments.

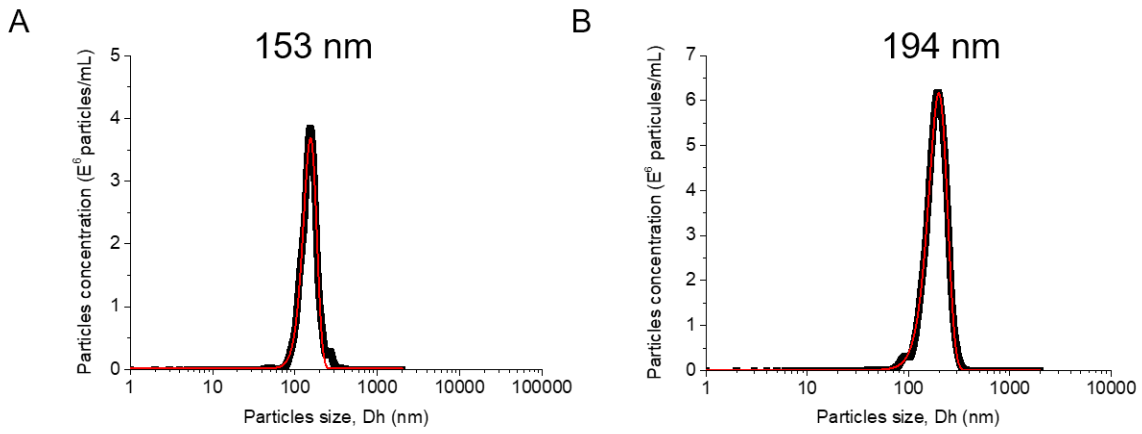

Figure S7. Size distribution of shell-crosslinked HA-NGs (A) and Hep-NGs (B) in PBS (C_p = 5×10^{-4} g/L) determined by nanoparticle tracking analysis at 25 °C. The experimental results (black curve) were fitted by a Gaussian curve (red curve).

References

1. Soni, K.S.; Desale, S.S.; & Bronich, T.K. Nanogels: an overview of properties, biomedical applications and obstacles to clinical translation. *Journal of Controlled Release*. **2016**, 240, 109-126.
2. Neamtu, I.; Rusu, A.G.; Diaconu, A.; Nita, L.E.; & Chiriac, A.P. Basic concepts and recent advances in nanogels as carriers for medical applications. *Drug Delivery*, **2017**, 24, 539-557.
3. Debele, T.A.; Mekuria Shewaye, L.; & Tsai, H.C. Polysaccharide based nanogels in the drug delivery system: Application as the carrier of pharmaceutical agents. *Materials Sciences and Engeneering. C Materials for Biological Appl*ications, **2016**, 68, 964-981.
4. Swierczewska, M.; Han, H. S.; Kim, K.; Park, J.H.; & Lee, S. Polysaccharide-based nanoparticles for theranostic nanomedicine, **2016**, 1, 70-84.
5. Rao, N.V.; Yoon, H.Y.; Han, H.S.; Ko, H.; Son, S.; Lee, M.; Lee, H.; Jo, D.-G.; Kang Y.M.; & Park, J. H. Recent developments in hyaluronic acid-based nanomedicine for targeted cancer treatment *Expert Opininion on Drug Delivery*, **2016,** 13, 239-252.
6. Dosio, F.; Arpicco, S.; Stella, B.; & Fattal, E.; Hyaluronic acid for anticancer drug and nucleic acid delivery. *Adv. Drug Deliv. Rev*. **2016**, 97, 204-36.
7. Cadete, A.; & Alonso, M.J. Targeting cancer with hyaluronic acid-based nanocarriers: recent advances and translational perspectives. *Nanomedicine*, **2016**, 11, 2341-2357.
8. Jing, J.; Alaimo, D.; De Vlieghere, E.; Jérôme, C.; De Wever, O.; De Geest, B.G.; & Auzély-Velty, R. Tunable self-assembled nanogels composed of well-defined thermoresponsive hyaluronic acid–polymer conjugates. *Journal of Materials Chemistry B*, **2013**, 1, 3883-3887.
9. Zhou, B.; Weigel, J.A.; Fauss, L.; & Weigel, P.H. Identification of the hyaluronan receptor for endocytosis (HARE). *Journal of Bioligal Chemistry*, **2000**, 275, 37733-37741.
10. Choi, K.Y.; Min, K.H.; Yoon, H.Y.; Kim, K.; Park, J.H.; Kwon, I.C.; Choi, K.; & Jeong, S.Y. PEGylation of hyaluronic acid nanoparticles improves tumor targetability in vivo. *Biomaterials*, **2011**, 32, 1880-1889.
11. Veronese, F. M. Peptide and protein PEGylation: a review of problems and solutions. *Biomaterials*, **2001**, 22, 405-417.
12. Caliceti, P.; & Veronese, F. M. Pharmacokinetic and biodistribution properties of poly(ethylene glycol)-protein conjugates. *Advanced Drug Delivery Rev*iews, **2003**, 55, 1261-1277.
13. Gaberc-Porekar, V.; Zore, I.; Podobnik, B.; & Menart, V. Obstacles and pitfalls in the PEGylation of therapeutic proteins. *Current Opinion in Drug Discover*y & Development, **2008**, 11, 242-250.
14. Knop, K.; Hoogenboom, R.; Fischer, D.; & Schubert, U.S. Poly(ethylene Glycol) in drug delivery: pros and cons as well as potential alternatives. *Angewandte Chemie International,* **2010**, 49, 6288-6308.
15. DeAngelis, P.L. Heparosan, a promising 'naturally good' polymeric conjugating vehicle for delivery of injectable therapeutics. *Expert Opinion on Drug Deliv*ery, **2015**, 12, 349-352.
16. Harris, E.N.; & Weigel, P.H. The ligand-binding profile of HARE: hyaluronan and chondroitin sulfates A, C, and D bind to overlapping sites distinct from the sites for heparin, acetylated low-density lipoprotein, dermatan sulfate, and CS-E 2008. *Glycobiology*, **2008**, 18, 638-648.

17. Mergy, J.; Fournier, A.; Hachet, E.; & Auzély-Velty, R. Modification of polysaccharides via thiol-ene chemistry: a versatile route to functional biomaterials. *Journal of Polymer Science Part A: Polymer Chemistry*. **2012**, 50, 4019-4028.
18. Jing, J.; Fournier, A.; Szarpak-Jankowska, A.; Block, M.R.; Auzély-Velty, R. Type, density, and presentation of grafted adhesion peptides on polysaccharide-based hydrogels control preosteoblast behavior and differentiation. *Biomacromolecules*, **2015**, 16, 715-22.
19. Acosta Ortiz, R.; Martinez, A.Y.R.; García Valdez, A.E.; Berlanga Duarte, M.L. Preparation of a crosslinked sucrose polymer by thiol–ene photopolymerization using dithiothreitol as comonomer. *Carbohydrate Polym*ers, **2010**, 82, 822-828.
20. Nicolas, J.; Jaafar, M.; Sepetdjian, E.; Saad, W.; Sioutas, C.; Shihadeh, A.; Saliba, N.A. Redox activity and chemical interactions of metal oxide nano- and micro-particles with dithiothreitol (DTT). *Environmental Science: Processes Impacts*. **2015,** 17, 1952–1958.
21. Stefanello, T. F.; Couturaud, B.; Szarpak-Jankowska, A.; Fournier, D.; Louage, B.; Garcia, F. P.; Nakamura, C. V.; De Geest, B. G.; Woisel, P.; Van der Sanden, B.; & Auzely-Velty, R. Coumarin-containing thermoresponsive hyaluronic acid-based nanogels as delivery systems for anticancer chemotherapy. *Nanoscale*, **2017**, 9, 12150-12162.
22. Filipe, V.; Hawe, A.; & Jiskoot, W. Critical evaluation of nanoparticle tracking analysis (NTA) by nanoSight for the measurement of nanoparticles and protein aggregates. *Pharmaceutical Research*, **2010**, 27, 796–810.
23. Anselmo, A.C.; Zhang, M.; Kumar, S.; Vogus, D.R.; Menegatti, S.; Helgeson, M.E.; & Mitragotri, S. Elasticity of nanoparticles influences their blood circulation, phagocytosis, and targeting. *ACS NANO*, **2015**, 9, 3169-3177.
24. Sun, H.; Björnmalm, M.; Cui, J.; Wong, E.H.H.; Dai, Y.; Dai, Q.; Qiao, G.G.; & Caruso, F. Structure governs the deformability of polymer particles in a microfluidic blood capllary model. *ACS Macro Letters*, **2015**, 4, 1205-1209.
25. Zhang, L.; Cao, Z.; Li, Y.; Ella-Menye, J.R.: Bai, T.; & Jiang, S. Softer zwitterionic nanogels for longer circulation and lower splenic accumulation. *ACS Nano*, **2012**, 6, 6681-6686.
26. Cesaretti, M.; Luppi, E.; Maccari, F.; & Volpi, N. A 96-well assay for uronic acid carbazole reaction. *Carbohydrate Polymers*, **2003**, 54, 59-61.

II.2 Résultats et discussions complémentaires

Certaines études n'ont pas été décrites dans l'article et sont présentées dans la partie qui suit. Ces dernières mettent en avant les enjeux rencontrés lors de l'élaboration des nanogels thermosensibles.

Nous montrerons tout d'abord en section II.2.1 et II.2.2 respectivement, les démarches qui ont permis d'obtenir de façon reproductible des nanogels de taille contrôlée. En particulier, nous décrivons la mise au point de la purification par chromatographie ionique et celle des conditions de la réaction de couplage par chimie radicalaire thiol-ène.

Les propriétés de thermo-association en solution des dérivés HA- et Hep-poly(DEGMA-co-BMA) sont présentées plus en détail afin de mieux comprendre la formation de nos systèmes. La dernière partie est consacrée à l'optimisation de la réticulation.

II.2.1 Purification des dérivés HA-copolymères synthétisés

II.2.1.1 Purification par dialyse

La dialyse est la purification la plus utilisée pour les polysaccharides conjugués. Elle repose sur la séparation d'espèces chimiques en fonction de leur masse molaire par une membrane poreuse qui joue le rôle de tamis. Une des difficultés rencontrées lors de la synthèse des dérivés HA-copolymère est leur purification par cette technique après greffage du copolymère par chimie thiol-ène sur le squelette du HA. La purification implique en effet d'éliminer complètement le copolymère non greffé du dérivé HA-copolymère. Or, dans notre cas, les masses molaires du HA (Mn ~ 20 g/mol) et du copolymère (Mn ~ 16 kg/mol) sont très proches et peuvent ainsi limiter leur bonne discrimination.

C'est pourquoi dans un premier temps, nous avons identifié le seuil de coupure minimum afin d'éliminer le copolymère puis étudié le comportement du HA linéaire non modifié et des dérivés HA-copolymère synthétisés à travers cette dernière. L'ensemble des purifications est réalisé à une température inférieure à la T_{cp} du copolymère (T<12°C), à 4°C, afin que ce dernier soit soluble dans l'eau et puisse passer à travers la membrane.

Le Tableau 3.1 regroupe la masse récupérée et le rendement de la purification en fonction du seuil de coupure de la membrane utilisée (50 kDa ou 100 kDa). L'élimination par dialyse du copolymère de masse molaire (M_n) ~16 kg/mol nécessite une membrane avec un seuil de coupure minimal de 100 kDa (Entrées 1 et 2). Or, celui-ci entraîne également une perte des dérivés HA-copolymère synthétisés (Entrée 4). Ainsi, avec ce protocole de purification, la dialyse s'étale sur 8 jours (3 lavages/jour) et présente un rendement aux

alentours de 20%. A titre comparatif, le HA natif (M_n ~ 20 kg/mol, PdI =1,45), non modifié, est éliminé à plus de 50% par dialyse sur cette taille de membrane (Entrée 3).

Par ailleurs, après purification sur la membrane avec le seuil de coupure de 100 kDa, nous observons après lyophilisation la présence de traces de poly(DEGMA-co-BMA) résiduel (masse ± 1 mg). Le remplacement de l'eau par un mélange plus apolaire eau/éthanol (2/1) dans la solution de lavage a été envisagé mais n'améliore pas la purification. Ainsi, la dialyse n'est pas adaptée à la purification des dérivés synthétisés.

Tableau 3.1 *Conditions expérimentales de la purification par dialyse.*

Entrée	Produit	Masse molaire (kg/mol)	Masse de départ HA (mg)	Membrane Seuil de coupure (kDa)	Nombre de lavage	Masse récupérée (mg)	Rende-ment (%)[a]
1	Copolymère	15	50	50	9	50	
2	Copolymère	15	50	100	9	>1	
3	HA	20	50	100	9	15-20	30-40
4	HA-copo (DS 2%)	--	50	100	9	20-25	17-21

[a] calculé en divisant le nombre de mole d'unité de répétition du dérivé HA-copolymère (M = 740 g/mol) par le nombre de mol d'unité de répétition du HA (M = 401 g/mol)

II.2.1.2 Purification par chromatographie ionique en batch

La technique de chromatographie ionique en batch (Figure 1.1), consiste à séparer les molécules présentes en solution en fonction de leur charge. Cette technique, aussi appelée chromatographie sur échangeur d'ions, porte sur l'interaction entre l'acide hyaluronique chargé négativement et une résine chargée positivement. Le copolymère thermosensible étant non chargé, il peut ainsi être éliminé facilement. Dans cette étude, nous avons utilisé, la résine DEAE Sepharose CL-6B, qui a pour ion échangeur le groupement diéthylaminoéthyle, dont la charge reste stable sur la gamme de pH 3-9.

Dans la littérature, cette technique est fréquemment utilisée pour séparer et purifier des protéines, des polysaccharides et de manière générale des biomolécules chargées [6-7]. Nous avons envisagé d'explorer cette technique de purification en batch qui nous permet de réaliser l'ensemble des étapes à 4°C (au réfrigérateur).

Le protocole final, décrit dans la publication, a été mis au point au fil des optimisations. En particulier, la concentration en sel aux différentes étapes constitue un paramètre clé. Il est nécessaire de commencer par une élimination de l'éthanol présent dans la solution de stockage et de terminer par une étape de rinçage pour éliminer le sel présent en forte concentration après l'élution. Deuxièmement, la complexation des dérivés chargés négativement avec la résine est optimale pour une conductivité de ~ 1-2 mS/cm^2. En dessous de cette valeur, la complexation électrostatique est moins efficace [8-9].

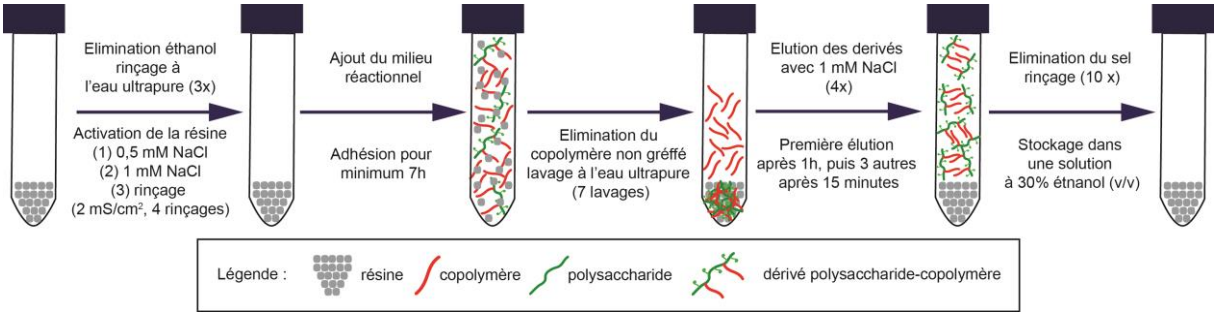

Figure 3.1 *Schéma représentatif de la méthode expérimentale mise au point pour réaliser la purification par chromatographie ionique en batch des dérivés de polysaccharides.*

L'une des étapes nécessaires au bon déroulement de la purification est celle qui permet d'éliminer le copolymère non greffé : le lavage de la résine à l'eau froide. Le nombre de lavages a été validé d'une part visuellement, par observation de la turbidité des eaux de lavage avec la montée en température (Figure 3.2-C), et d'autre part, par analyse UV/Vis de la turbidité à 37°C (Figure 3.2-B). Il est important de noter ici que la longueur d'onde d'absorbance du copolymère varie avec la présence ou non de l'agent RAFT en bout de chaîne. En effet, les dérivés thiocarbonylthio sont des chromophores qui absorbent fortement dans l'UV aux alentours de 300-310 nm. L'absorbance relative à l'agent RAFT disparaît après son élimination par aminolyse [10]. Ainsi, seule l'absorbance des esters d'alkyle aux alentours de 290-300 nm est observée pour le copolymère à purifier (Figure 3.2-A). Nous observons au fur et à mesure des lavages une diminution progressive des esters d'alkyle par analyse UV/Vis des eaux de lavage jusqu'à une disparition totale après 7 lavages (Figure 3.2-B) qui se traduit visuellement par une diminution progressive de la turbidité (Figure 3.2-C).

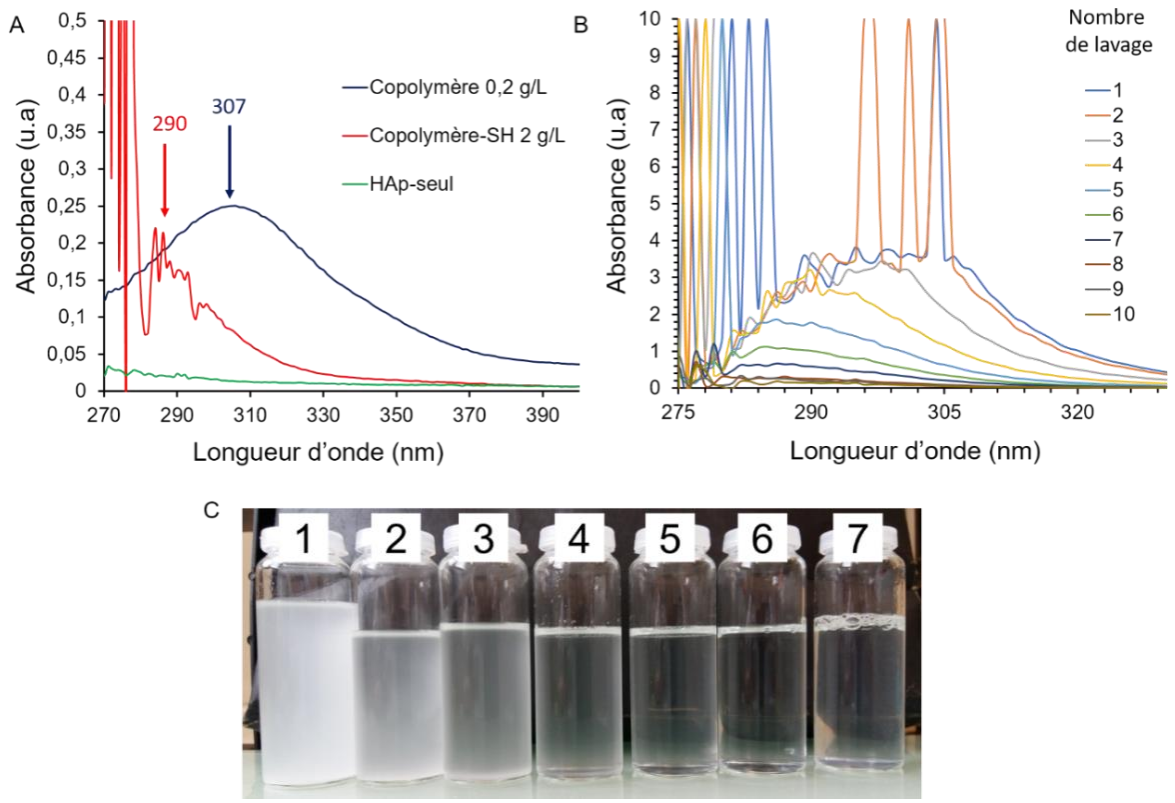

Figure 3.2 *Analyse des eaux de lavage A) Spectres UV/Vis du copolymère avant et après aminolyse ainsi que du dérivé HA-pentènoate à 20°C B) Spectres UV/Vis des eaux de lavage (n=10) à 20°C, C) Eaux de lavage à température ambiante (n=7).*

II.2.1.3 Validation de la purification

Pour vérifier la fiabilité de ce protocole de purification, nous avons dans un premier temps confronté les deux techniques, la chromatographie ionique et la purification par dialyse. Dans un deuxième temps, nous avons analysé et comparé les propriétés des dérivés ainsi obtenus.

Comparaison des techniques de purification

Le tableau 3.2 résume les caractéristiques : temps et rendement, des deux purifications. Il apparaît que la chromatographie ionique permet de diviser le temps de purification par deux (passage de 8 à 4 jours) et d'augmenter le rendement par deux. L'échantillon 3 joue le rôle de contrôle et met en évidence une perte de HA pendant la purification aux alentours de 10%.

Tableau 3.2 *Comparaison des purifications par dialyse et chromatographie ionique pour les dérivés de HA-copolymère et le HA.*

Entrée	Produit	Masse de HA de départ (mg)	Purification	Temps (jour)	Masse récupérée (mg)	Rendement (%)[b]
1	HA-copolymère	50	Dialyse	8	20-25	17-21 [a]
2	HA-copolymère	50	Chro. Ion	3-4	50-60	42-51 [a]
3	HA	50	Chro-Ion	3-4	42-45	84-90 [a]

[a] observé pour 3 réplicas; [b] calculé en divisant le nombre de mole d'unités de répétition du dérivé HA-copolymère par le nombre de mol d'unité de répétition du HA.

Afin de vérifier l'efficacité de la complexation du HA avec la résine, une étude par analyse FTIR de la composition des eaux de lavage en chromatographie ionique et en dialyse a été menée (Figure 3.3). La comparaison des spectres avec ceux correspondant au copolymère et au HA confirme la complexation efficace du polysaccharide avec la résine. En effet, seule la présence du copolymère (2850, 1750, 1450, 1250, 850 cm^{-1}) est observée dans les eaux de lavage issues de la chromatographie ionique tandis qu'un mélange HA/copolymère est observé dans les eaux de lavage provenant de la dialyse.

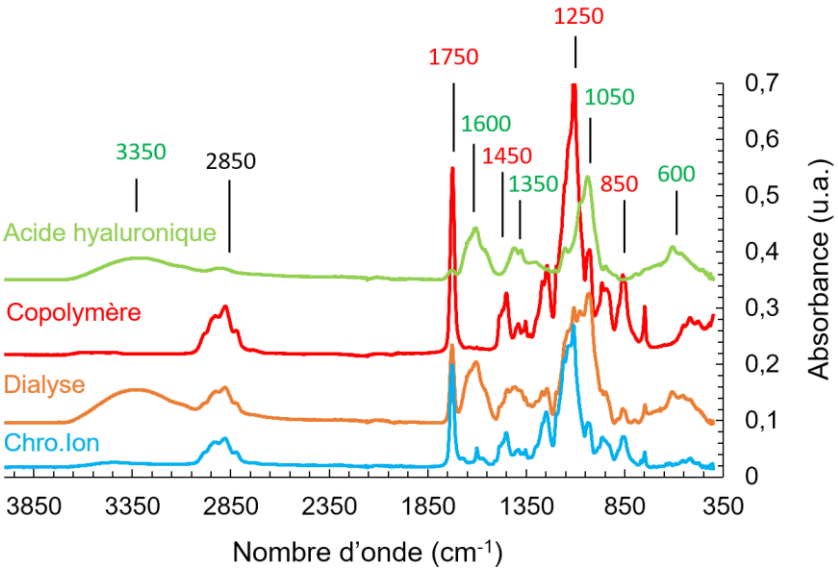

Figure 3.3 *Comparaison des spectres infra-rouge de l'acide hyaluronique, du copolymère, des eaux de lavage lyophilisées obtenues en dialyse et issues de la chromatographie ionique en batch. Attribution des bandes d'absorption (cm^{-1}) des spectres FTIR (32 scans, résolution de 2s) : 3350 (-OH), 2850 (-CH, $-CH_2$, CH_3), 1750 (-C=O copolymère), 1600 (-C=O AH), 1450 et 1350 (-C-CH, O-CH), 1250 (C-O des esters aliphatiques), 1200-900 (-C-O, -C-CH élongation, -CO et -C-O-C flexion du cycle glycosidique) 850 (H-C-S flexion), 600 (allomorphe), 500 (-C-S-S-C coude dièdral) [11-12].*

Une fois les dérivés purifiés, des nanogels ont été formés à partir de ces derniers par simple élévation de la température. Etant donné la présence de traces de copolymère dans les dérivés obtenus après dialyse, nous avons voulu évaluer leur impact sur le comportement des nanogels en solution. Pour cela, le milieu réactionnel après couplage par chimie thiol-ène a été séparé en deux. Une moitié a été purifiée par dialyse et l'autre par chromatographie ionique. Le tableau 3.3 récapitule l'ensemble des propriétés des nanogels en solution analysées par DLS (polydispersité (PdI) et tailles).

Nous constatons une différence de comportement entre les lots de nanogels en fonction de la purification pour les dérivés de plus faible DS (DS 2 %). Dans le cas des nanogels obtenus après dialyse, le PdI chute et leur taille augmente d'un facteur 2 (Entrée 1). Cela peut être dû à deux effets : 1) le copolymère résiduel (~1mg) est encapsulé lors de la montée en température au sein des nanogels, 2) seul reste après purification, les dérivés les plus substitués. A titre comparatif, nous avons analysé les propriétés des nanogels obtenus dans le cas où l'élimination du copolymère est impossible (Entrée 3, membrane de dialyse avec seuil de coupure 50 kDa) et le même comportement est observé. La présence de chaînes de copolymère libres en solution auto-associées au-dessus de la T_{cp} entraîne une forte augmentation de la taille des particules.

Tableau 3.3 *Analyse DLS des propriétés en solution des nanogels AH-copolymère obtenue après purification par chromatographie ionique ou par dialyse.*

Entrée	Purification	DS copo	PdI	Diamètre (Z-av)	Diamètre (int)	Diamètre (nb)
1	Chro. Ion	2±1 %	0,250 (±0,065)	103 (±5,0)	109 (±1,42)	65 (±4,54)
	Dialyse (100 kg/mol)	-	0,053 (±0,010)	204 (±0,010)	230 (±0,010)	181 (±0,010)
2	Chro. Ion.	7±0.5%	0,165 (±0,065)	86 (±5,0)	88 (±1,42)	64 (±4,54)
	Dialyse (100 kg/mol)	-	0,025 (±0,010)	111 (±1,81)	117 (±0,2,58)	89 (±0,010)
3	Dialyse (50 kg/mol)	-	0,153 (±0,025)	252 (±0,025)	291 (±0,025)	217 (±0,025)

En revanche, pour des dérivés HA-copolymère de DS 7% (Entrée 2), la purification par dialyse n'entraîne pas une perte importante des dérivés HA-copo lors de l'élimination du copolymère (rendement compris entre 40-50%). Ceci peut s'expliquer par leur masse molaire

plus importante du fait de leur DS plus élevé. La taille des nanogels obtenus à partir des dérivés purifiés par dialyse est là encore plus élevée que celle des nanogels résultant des dérivés purifiés par chromatographie ionique.

L'ensemble des résultats obtenus au cours de cette étude nous permet de valider la pertinence de la purification par chromatographie ionique en batch mise au point. Ce protocole reproductible surmonte les difficultés techniques et peut être étendu à la purification d'autres dérivés de polysaccharides comprenant des molécules hydrophobes ou thermosensibles.

II.2.2 Détermination du Degré de Substitution (DS)

Le degré de substitution définit le nombre de chaînes de copolymères greffées en moyenne toutes les 100 unités disaccharides de répétition du HA (ou de l'héparosan). Il est ensuite possible de remonter au nombre de chaînes de copolymères greffées par chaîne de HA (ou d'héparosan) (Tableau 3.4). La superposition des signaux des protons du copolymère et du HA/Hep rendant impossible la détermination du DS par intégration des spectres RMN ^{1}H, le DS a été évalué en effectuant un dosage au carbazole.

Tableau 3.4 *Nombre de chaîne de copolymère par chaîne de HA en fonction du degré de substitution.*

DS (%)	**1**	**2**	**4**	**6**	**8**	**10**
Copolymère chaine/HA chaîne (20 kg/mol)	0,5	1	2	3	4	5

II.2.2.1.1 Quantification par la méthode au carbazole

La détermination du DS selon la méthode au carbazole repose sur le dosage des unités glucuroniques par le carbazole. Cette méthode de quantification du HA est souvent rapportée dans la littérature [13-14] et reste la méthode de référence. Le dosage au carbazole est considéré comme aussi fiable que le dosage par HPLC pour la quantification des GAG contenant de l'acide uronique [15]. Cependant les produits doivent être exempts de sels et de tout autre sucre tel que le glucose [16-17].

Le principe repose sur l'obtention d'une coloration pouvant être quantifiée après réaction du carbazole avec les acides uroniques (Figure 3.4). Cette coloration est due à la formation d'un dérivé du furfural obtenu par chauffage en milieu acide sulfurique et condensation avec le carbazole. La quantité d'acide uronique est estimée en comparaison à une gamme étalon réalisée, à partir de l'acide hyaluronique de départ (non modifié) à chaque nouvelle quantification.

Dans ce travail, la quantité d'unité D-glucuronique a été déterminée par spectroscopie UV-visible (λ = 530 nm) à l'aide d'une courbe de calibration obtenue à partir d'une gamme étalon établie en utilisant le polysaccharide concerné (HA ou Hep) dégradé dans les mêmes conditions.

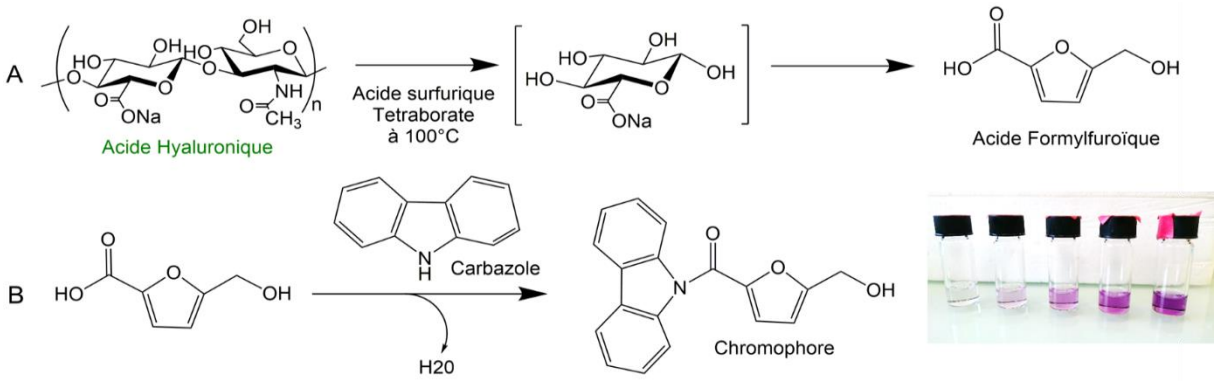

Figure 3.4 *Schéma réactionnel du dosage des unités glucuronique de HA par le carbazole A) formation du dérivé furfural B) formation du chromophore (λ = 530 nm).*

La figure 3.5 regroupe les DS déterminés par cette technique pour plusieurs dérivés préparés dans les mêmes conditions et purifiés par chromatographie ionique (DS visé 30%, en présence de TCEP). Sur huit synthèses nous constatons une disparité des DS obtenus, deux valeurs se distinguent 1,5% et 4%, soit un DS moyen de 2±1 %.

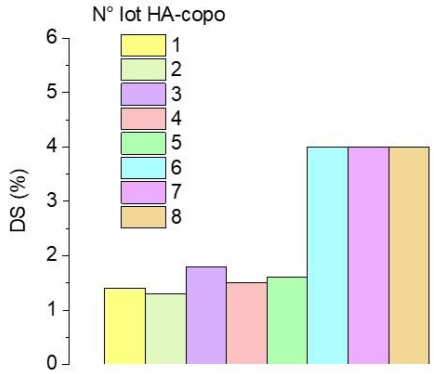

Figure 3.5 *Détermination du DS par dosage au carbazole de dérivés HA-poly(DEGMA-co-BMA) synthétisés dans les mêmes conditions réactionnelles.*

Au regard de cette constatation, l'objectif est de comprendre à présent l'origine des faibles DS obtenus. Nous avons alors étudié l'efficacité de la réaction thiol-ène radicalaire, en particulier l'influence des paramètres, tels que la quantité de copolymère initiale et la présence d'un agent réducteur, sur le taux de greffage et la reproductibilité des synthèses.

II.2.3 Etude de la réaction thiol-ène radicalaire

Comme décrit dans le chapitre précédent, plusieurs approches permettent de greffer des molécules sur des glycosaminoglycanes et en particulier le HA. Dans ce travail, notre choix s'est porté sur la réaction de couplage thiol-ène amorcée par des radicaux pour plusieurs raisons.

Premièrement, cette réaction permet d'effectuer, dans des conditions simples et de manière séquentielle, le greffage du copolymère sur le polysaccharide et sa réticulation en partant d'un dérivé polysaccharidique modifié par des groupements alcène (pentènoate). Le choix de la fonction réactive (acide carboxylique ou hydroxyle) sur le squelette de HA peut avoir son importance. Selon Wang et al, il est préférable de préserver la fonction carboxylique car cette dernière semble impliquée dans la reconnaissance du HA par les récepteurs CD44 [18]. Dans le cas du dérivés HA-pentènoate, la modification porte sur les hydroxyles (estérification avec l'anhydride pentènoïque). Deuxièmement, l'utilisation de la lumière UV pour amorcer la réaction thiol-ène par voie radicalaire permet le contrôle temporel et spatial de la réaction, ce qui est particulièrement intéressant pour la synthèse d'hydrogels chimiques microstructurés. Soulignons également que le couplage thiol-ène par voie radicalaire est plus rapide et efficace que l'addition de Michael (addition d'un thiol sur un acrylate en l'absence de radicaux) [19]. De plus, contrairement au couplage thiol-maléimide, également utilisé au sein de l'équipe, les dérivés HA-pentènoate sont stables au stockage à sec et peuvent ainsi être conservés et utilisés à façon. Enfin, cette réaction est fréquemment utilisée pour former des hydrogels à visée thérapeutique [20-24] ainsi que pour la fonctionnalisation de leur surface par des molécules biologiques d'intérêts [25].

II.2.3.1 Mécanisme réactionnel

La réaction s'effectue en milieu aqueux et nécessite la présence d'un amorceur pour générer le premier radical thiyl. Cet amorceur peut être activé par une source de lumière, une source de chaleur ou bien une réaction d'oxydo-réduction. Le radical thiyl formé réagit à son tour avec la double liaison de l'alcène pour former une liaison thioéther (Figure 3.6). Le radical thiyl est ensuite régénéré.

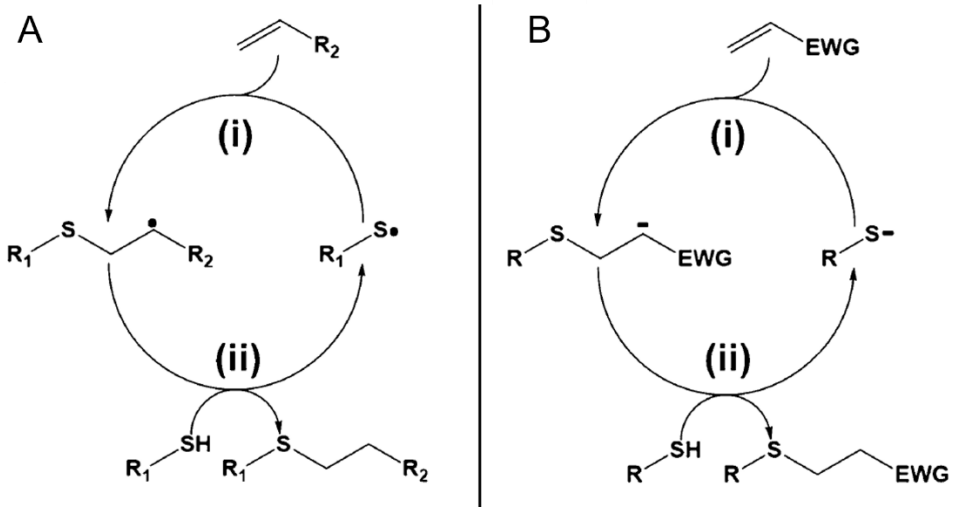

Figure 3.6 *Mécanismes réactionnels proposés pour la chimie thiol-ène suivant une suite cyclique dans le cas A) de la réaction d'addition radicalaire B) de la réaction d'addition de Michael où (i) représente une étape de propagation et (ii) représente une étape de transfert de chaîne. R_1 et R_2 sont des groupes de substituants, et EWG représente un groupe électroattracteur [26].*

II.2.3.2 Efficacité de la réaction de couplage

Dans ce travail, la réaction de couplage thiol-ène a été effectuée en milieu aqueux à une température de 5°C (bain de glace), c'est-à-dire à une température bien inférieure à la température de point trouble du copolymère (T_{cp} = 12 °C à 3 g/L), afin de garantir la bonne solubilité du copolymère dans le milieu réactionnel. Les degrés de substitution des dérivés HA- et Hep-copolymère obtenus après réaction (DS ~ 2 %, Tableau 3.5) sont faibles comparés à la quantité de copolymère utilisée pour le couplage (0.3 équivalent molaire de copolymère/unité de répétition du HA ou de Hep). Ce faible rendement de couplage (~ 8-7%) est vraisemblablement lié à des encombrements stériques.

Tableau 3.5 *Taux de greffage du copolymère thermosensible sur les chaînes de HA obtenus par dosage au carbazole après purification par chromatographie ionique.*

Entrée	Produit	DS moyen (carbazole) (%)	DS visé (couplage 100%) (%)
1	HA-copo	2 ± 1 (n=8)	30
2	Hep-copo	2 ± 1 (n=3)	30

La présence des groupements DEGMA et la masse molaire du copolymère relativement élevée, similaire à celle du polysaccharide (HA ou Hep), ne sont en effet pas favorables au couplage de plusieurs chaînes copolymère. On sait peu de choses de l'impact des paramètres structuraux sur le contrôle de l'efficacité du couplage thiol-ène en milieu

aqueux. Cette chimie a particulièrement été étudiée pour la synthèse ou la fonctionnalisation des polymères en milieu organique [19]. Seul Colak et al. ont étudié la chimie thiol-ène radicalaire dans le PBS afin de former des systèmes hydrogel-peptide capables d'encapsuler des cellules [27]. Ils observent une dépendance du couplage en fonction de l'encombrement stérique associé à la taille de la molécule à greffer. Ils présument également que cela entraînerait dans le cas du greffage de molécules plus volumineuses, des taux de greffage nettement plus faibles. Les auteurs attribuent ce phénomène à des problèmes de diffusion des radicaux.

Cette conclusion fait écho aux travaux antérieurs réalisés par Koo et al. qui ont comparé la fonctionnalisation de polymères par réaction thiol-ène radicalaire par des petites molécules et par un autre polymère dans des solvants organiques [28]. L'influence des paramètres clés de la réaction, à savoir le ratio [SH]/[=], le temps d'irradiation, la puissance de la lampe, la concentration ont été explorés par Koo et al [28]. La réaction thiol-ène s'est révélée infructueuse pour tous les couplages polymère-polymère ne comprenant pas un large excès (facteur 5) de thiol ou de groupement alcène (efficacité du couplage ≈ 25%) et a uniquement conduit à un rendement satisfaisant lorsque le polymère est fonctionnalisé avec de petites molécules. Selon ces auteurs, ce phénomène s'expliquerait par la présence de réactions de terminaison dues à des réactions de recombinaison et à l'addition de radicaux.

Une importante différence de couplages entre polymère-petite molécule et polymère-polymère a également été mise en évidence par Derboven et al [29]. Cependant, ces auteurs proposent une tout autre explication et remettent en cause celle communément admise jusqu'à présent. En complétant les travaux précédents de Koo et al. par l'analyse en modélisation de la cinétique de couplage, ils concluent que l'efficacité limitée du couplage polymère-polymère et la formation de produits secondaires pouvaient être attribuées d'une part à la solubilité limitée du polymère et d'autre part à des concentrations inférieures en groupement terminal (SH) par rapport au cas des petites molécules.

Cette dernière hypothèse permet difficilement d'expliquer nos résultats dans la mesure où la réaction est effectuée dans des conditions pour lesquelles le copolymère est soluble dans le milieu réactionnel, qui reste limpide tout au long de la réaction.

II.2.3.3 Etude de l'influence de l'agent réducteur (TCEP) sur la réactivité

Lors de cette réaction, il est important de prendre en compte la présence d'un agent réducteur, le TCEP, une phosphine hydrosoluble introduite afin d'éviter l'oxydation des

fonctions thiol et la formation de ponts disulfures [31]. En effet, cet agent pourrait également jouer un rôle secondaire défavorable.

Nous trouvons dans la chimie des peptides l'utilisation de l'irradiation UV en présence de TCEP dans le but de réaliser une désulfurisation à l'extrémité de certains acides aminés (cystéine) [32-33]. Par exemple, Wang et al., ont observé, lors de la mise en présence de la cystéine avec le TCEP, à des températures supérieures à l'ambiante, une modification correspondant à la perte de 32 g/mol suggérant la conversion de la cystéine en alanine par désulfurisation [34]. Une autre étude met en lumière la responsabilité des catalyseurs à base de phosphine et donc du TCEP, dans la création de nombreuses réactions secondaires lors de la réaction d'addition de Michael [35].

Afin de vérifier cette possibilité, nous avons étudié l'influence de la présence du TCEP lors de la réaction thiol-ène radicalaire sur le taux de greffage. Pour ce faire, une étape d'élimination du TCEP en milieu inerte a été ajoutée au protocole en amont de la réaction. Nous avons procédé de la façon suivante : après solubilisation en présence de TCEP du copolymère-SH obtenu par aminolyse, une étape de purification par dialyse (membrane 6-8 KDa) en condition inerte au réfrigérateur (eau dégazée sous azote) du TCEP est réalisée (deux lavages, 4h).

D'après les résultats obtenus (Tableau 3.6), il semblerait que l'absence de TCEP permettrait d'augmenter le taux de greffage. Nous observons une multiplication d'un facteur deux du DS moyen obtenu à partir de dérivés synthétisés en l'absence de TCEP pour l'ensemble des dérivés HA- et Hep (entrée 1, passage d'un DS de 2 à 4,5). Cette tendance se confirme avec l'augmentation du DS de 4,5 à 9 % après une augmentation par deux de la quantité de copolymère introduite en début de réaction, en l'absence de TCEP (Entrée 3, Figure 3.7).

Tableau 3.6 Taux de greffage obtenu en présence et en absence de TCEP lors de la réaction thiol-ène radicalaire. n : nombre de lot de dérivés synthétisés dans les mêmes conditions.

Entrée	Produit	DS (%) pentenoate	DS (%) Avec TCEP	DS (%) Sans TCEP	DS visé (%) (couplage 100%)
1	HA-copo	50	2 ± 1 (n=8)	4,5 ± 0,5 (n=6)	30
2	Hep-copo	50	2 ± 1 (n=3)	4,5 ± 0,5 (n=3)	30
3	HA-copo	50	3 ± 1 (n=3)	9 ± 0,5 (n=2)	60

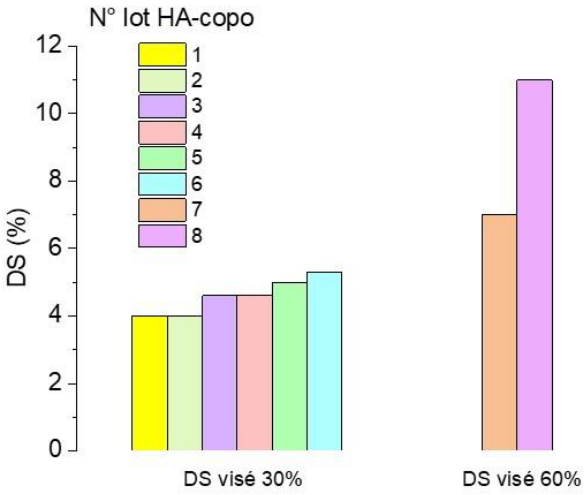

Figure 3.7 *Taux de greffage (DS%) obtenus en absence de TCEP lors de la réaction thiolène radicalaire pour deux DS visé 30% (n=6) et 60% (n=2).*

Les spectres RMN ^{1}H des dérivés synthétisés dans les mêmes conditions, en absence (DS = 7% et 11%) et en présence (DS = 2% et 4%) de TCEP sont respectivement superposés en Figure 3.8.

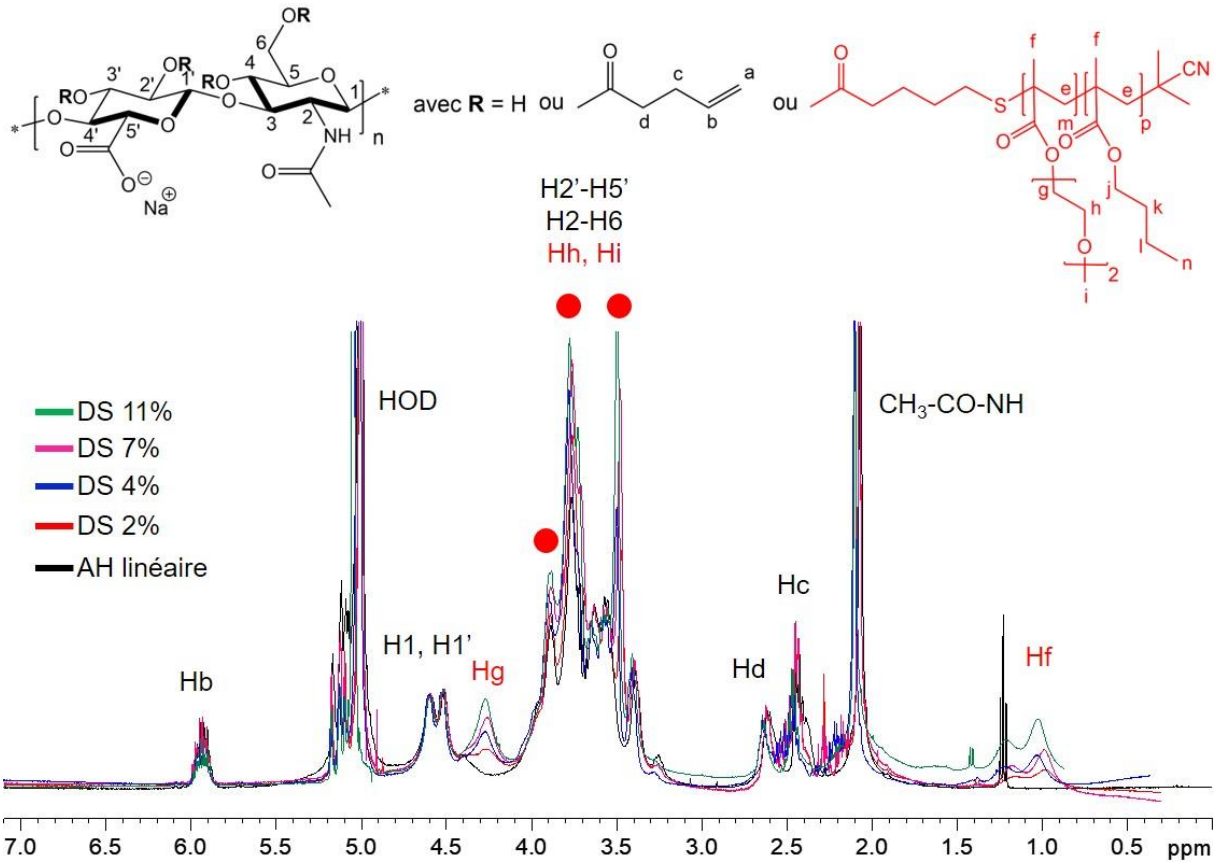

Figure 3.8 *Spectres RMN ^{1}H des dérivés de HA présentant différents DS en copolymère.*

II.2.3.4 Perspectives sur la réaction de couplage

La synthèse des dérivés par chimie radicalaire thiol-ène s'est avérée plus délicate que prévu. Dans notre cas, il est nécessaire d'ajouter un large excès de copolymère (DS obtenu 2% pour 30% de copolymère introduit par rapport aux groupement pentenoate), ce qui implique une étape importante de purification pour éliminer le copolymère libre en solution.

Dans ce contexte, la chimie radicalaire thiol-ène ne présente pas comme attendu les critères d'une « chimie *clic* ». Suivant la définition d'origine donnée par Sharpless [36], une réaction *clic* doit, parmi d'autres exigences, permettre des rendements élevés pour un temps de réaction raisonnable, sans générer la formation de produits secondaires et doit se conclure par une étape de purification des produits peu fastidieuse.

Il faut ajouter à cela l'effet indésirable apporté par l'agent réducteur. Bien que préliminaire, notre étude semble montrer une implication du TCEP sur le faible taux de greffage. Une autre piste, que celle que nous proposons ici, a été explorée dans la littérature afin d'éviter l'ajout d'un agent réducteur tout en préservant la stabilité des fonctions thiols. Elle consiste à réaliser en simultané l'aminolyse et le couplage [10, 37]. Cependant cette réaction « en un seul pot » nécessite l'utilisation de solvant organique. Dans cette démarche, des expériences complémentaires seraient nécessaires pour mieux comprendre la cinétique de formation des liaisons disulfures. Il est possible que cette dernière soit suffisamment lente pour ne pas s'inquiéter de l'oxydation des thiols dans la mesure où le couplage est entièrement réalisé en milieu inerte et dans un court délai après l'aminolyse.

II.2.4 Etude complémentaire sur les nanogels (non réticulés)

La suite de ce travail a consisté à étudier les propriétés de thermo-association en solution des nanogels.

En effet, les propriétés thermosensibles des nanogels peuvent être ajustables en jouant sur les caractéristiques macromoléculaires des dérivés HA- et Hep-poly(DEGMA-co-BMA) : DS, masse molaire du polysaccharide et composition du copolymère thermosensible (ratio des comonomères) [38].

Pour identifier précisément l'influence de ces paramètres sur l'auto-association, la structure et les propriétés des nanogels, nous avons conduit une étude systématique par RMN ^{1}H et DLS sur les différents lots de nanogels obtenus. Cette étude a été réalisée sur les dérivés HA-poly(DEGMA-co-BMA) après lyophilisation et redispersion des dérivés dans les solutions adéquates (eau deutérée, eau, PBS).

II.2.4.1 Etude de l'auto-association en solution

Pour commencer, nous complétons l'étude de la formation des nanogels présentée dans la publication par une présentation de leur morphologie par microscopie électronique en transmission (MET) et à balayage (MEB).

Rappelons que la CAT des nanogels de HA pour un $DS_{copolymère}$ de 2 % se situe aux alentours de 20-22°C. Les dérivés de HA ont été observés en-dessous (5°C) et au-dessus (37°C) de cette valeur par DLS et microscopie (MEB et TEM). Les résultats montrent clairement l'association des dérivés de HA en nanogels (Figure 1.11).

A 5°C, en dessous de la CAT, les dérivés HA-poly(DEGMA-co-BMA) sont solubles en milieu aqueux. Par conséquent, les données DLS ne sont pas acceptables et n'ont pas de signification réelle (PDI élevé > 0,7 et non reproductibles). Seule une couche de polymère est observée après séchage des échantillons par microscopie (Figure 3.9-B-C).

A 40°C, au-dessus de la CAT les dérivés forment des nanogels par auto-association du copolymère thermosensible en nanodomaines hydrophobes. Les clichés obtenus par TEM (Figure 3.9-F) montrent des nanogels présentant une structure sphérique avec un contour relativement diffus.

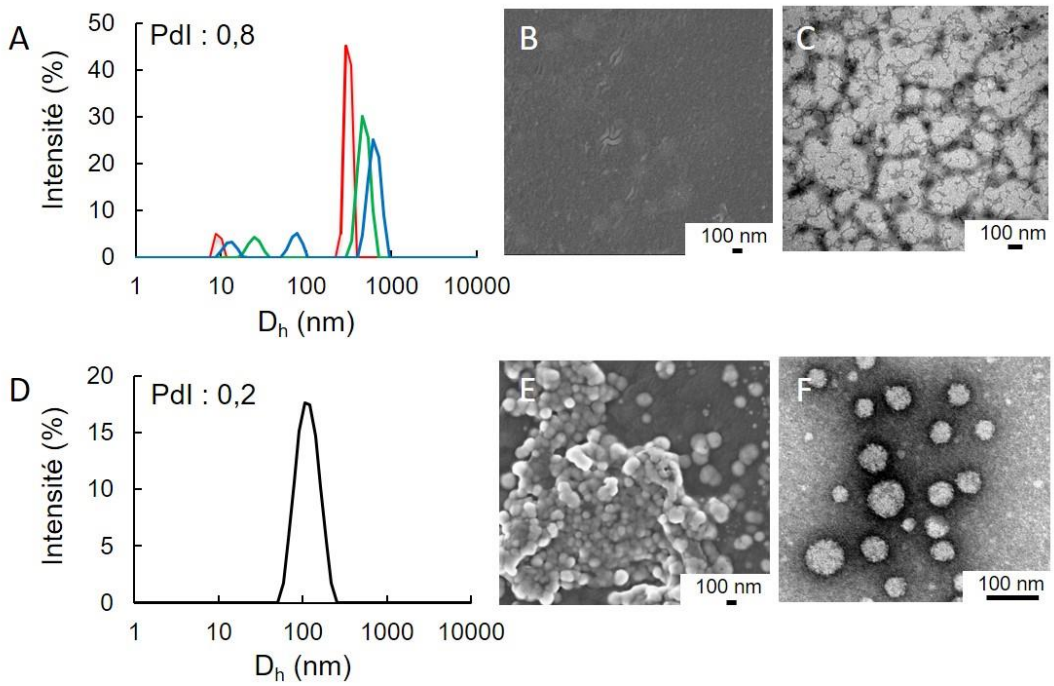

Figure 3.9 *Caractérisation des dérivés HA-copolymère en-dessous de la CAT, à 5°C A) en solution par DLS ([HA-copolymère] = 0,5 g/L, PBS) et par analyses microscopiques en B) MEB et C) TEM. Caractérisation des dérivés HA-copolymère au-dessus de la CAT, à 37° D) en solution par DLS ([HA-copolymère] = 0,5 g/L, PBS) et par analyses microscopiques en E) MEB et F) TEM.*

Par la suite, différentes séries de nanogels ont été préparées à partir des dérivés de HA en faisant varier les paramètres physico-chimiques suivant :

- la concentration en dérivé (3 g/L, 0,5 g/L)
- la masse molaire du HA (Mw = 20 kg/mol ou 120 kg/mol)
- le degré de substitution $DS_{copolymère}$ (2%, 4% et 7%)

Afin de visualiser l'étude globale, les caractéristiques de chaque lot sont résumées dans le Tableau 3.7. L'influence de chacun de ces paramètres sera discutée dans cette partie, dédiée à analyser le comportement en milieu aqueux des nanogels préparés afin de le relier aux conditions d'auto-associaton.

Tableau 3.7 *Récapitulatif de l'ensemble des nanogels préparés en fonction de la masse molaire et du DS en copolymère des dérivés HAp-copolymère obtenus après purification par chromatographie ionique.*

Entrée	Nom	Mn (Kg/mol)	DS (%)[a] pentenoate	DS (%)[b]	Copo/chaîne de HA
1	HA-20	20	50	2	1
2	HA-120	120	50	4	6
3	HA-20	20	50	4	2
4	HA-20	20	50	7	3,5

[a]déterminé par RMN ^{1}H, [b]déterminé par dosage au carbazole

(i) ***Influence de la masse molaire de l'acide hyaluronique (20 et 120 kg/mol) sur les propriétés d'auto-association***

Nous avons observé la turbidité des solutions de HA-poly(DEGMA-co-BMA) en solution à 3 g/L et 0,5 g/L, pour deux différentes masses molaires de HA (20 et 120 kg/mol) par spectrométrie UV-Vis, à 500 nm, afin d'étudier à la fois l'influence de la concentration en copolymère et de la masse molaire du polysaccharide sur la température d'agrégation critique (CAT) des dérivés (Figure 3.10-A). Notons que ces valeurs de concentration n'ont pas été fixées au hasard. Elles correspondent aux deux concentrations considérées dans ce projet : 0,5 g/L, concentration de travail choisie pour réaliser l'ensemble des caractérisations et 3 g/L, concentration d'injection des nanogels pour les études *in vivo*.

Suivant le même mécanisme d'auto-association que le copolymère thermosensible décrit au chapitre précédent, la transmission de la lumière incidente est perturbée par l'apparition de nanogels en solution. Cependant, elle ne se mesure pas au même endroit que la T_{cp}. A l'instar de la CAC (concentration micellaire critique) la CAT correspond à la

température à partir de laquelle se forment les nanogels et se mesure au point d'intersection des deux droites. On observe donc la formation de nanogels à différentes températures, comprises entre 21°C et 28°C, en fonction de la masse molaire du polysaccharide et de la concentration en dérivé introduit.

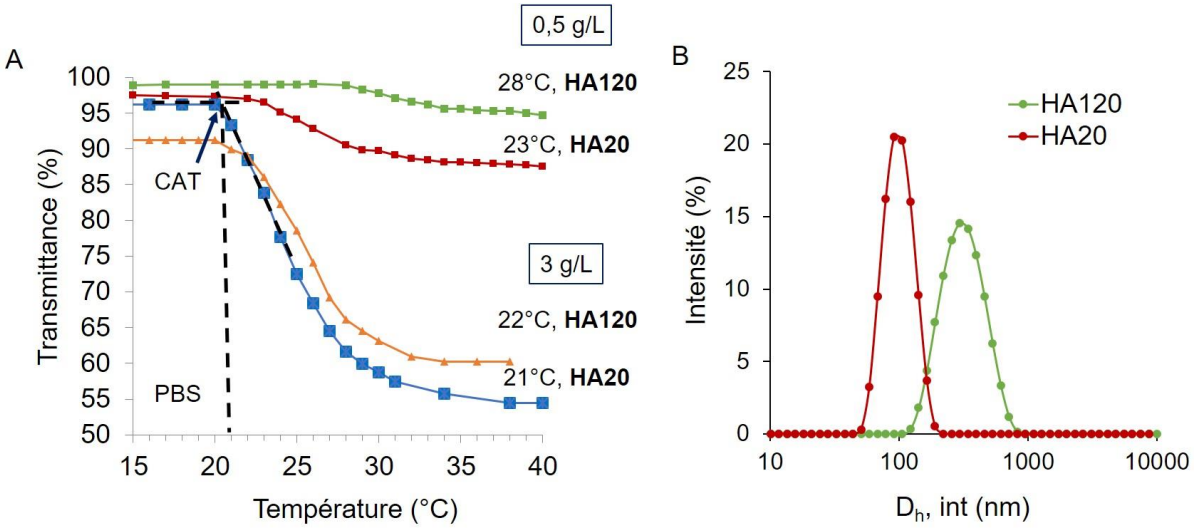

C

Entrée	Produit	Purification	DS copo (%)	[HA-copo] (g/L)	PdI	Diamètre (Z-av, nm)	Diamètre (int, nm)	Diamètre (nb, nm)
1	HA120	Chro. Ion	4	0,5	0,210 (±0,030)	172 (±0,87)	213 (±1,38)	137 (±9,38)
2	HA20	Chro. Ion	4	0,5	0,216 (±0,030)	128 (±3,56)	113 (±2,55)	89 (±1,53)
3	HA20	Chro. Ion	4	3	0,319 (±0,063)	185 (±15,54)	159 (±5,00)	126 (±2,11)

Figure 3.10 *A) DS fixé à 4% (RMN) B) DLS réalisée à 40°C dans le PBS (0,01 M) C) Diamètre hydrodynamique (Z-ave, int, nb) et PdI déterminés par DLS pour des dispersions de HA-copolymère à 0,5 ou 3 g/L.*

Comme attendu, phénomène longuement décrit dans la littérature et déjà constaté auparavant dans le cas du copolymère seul en solution, il y a une importante variation de la CAT en fonction de la concentration en HA-copolymère (Figure 3.10-C, Tableau 3.7). Par ailleurs, lorsque la masse molaire du HA augmente, la CAT du HA-poly(DEGMA-co-BMA), solubilisé dans le PBS à une concentration de 0.5 g/L, passe de 22 à 28°C. Cependant, cet écart important entre les valeurs de CAT n'est pas observé pour une concentration en HA-poly(DEGMA-co-BMA) de 3 g/L. Ces résultats ont été couplés à une analyse DLS, à 0,5 g/L dans le PBS à 40 °C (Figure 3.10-B). On constate une augmentation du diamètre des nanogels lorsque la masse molaire du HA augmente.

Notre objectif étant d'élaborer des nanogels à température ambiante dès 0,5 g/L, les nanogels synthétisés à partir du HA de masse molaire 20 kg/mol ont été sélectionnés pour la suite du projet.

Tableau 3.8 *Récapitulatif des résultats obtenus pour des nanogels élaborés à partir de dérivés de HA obtenus après purification par chromatographie ionique, présentant une masse molaire et un DS en copolymère différent.*

Entrée	Nom	Mn (Kg/mol)	DS (%)	Copo/HA*	[HA-copo] g/L	CAT (°C)	Dh (Z-av, nm)	PDI
1	HA120	120	4	6	0,5	28	172	0,210
2	HA20	20	4	2	0,5	23	128	0,216

(ii) ***Comparaison des CAT de dérivés HA-poly(DEGMA-co-BMA) possédant des DS différents***

Ainsi, à partir du HA de masse molaire 20 kg/mol, l'auto-association en nanogels de dérivés présentant cette fois deux $DS_{copolymère}$ différents (4 % et 7 %) a été étudiée (Figure 3.11-A). Une étude par DLS complète cette démarche en comparant les propriétés en solutions de nanogels préparés à partir de trois DS différents. Nous pouvons observer une légère variation du diamètre en intensité des nanogels, de 110 à 90 nm et une diminution du PdI, de 0,250 à 0,165, avec l'augmentation du DS (Figure 3.11-B).

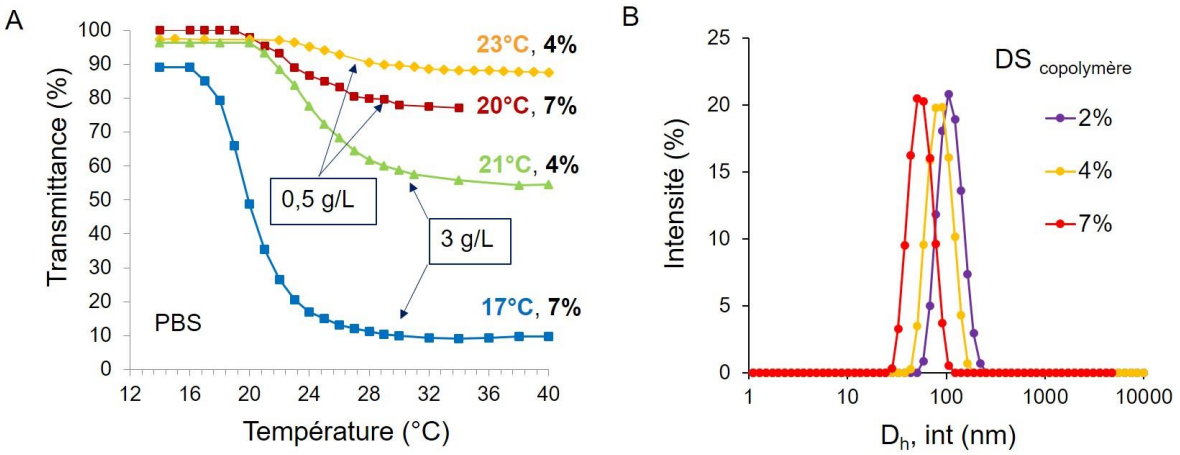

C

Entrée	Produit	Purification	DS copo (%)	[HA-copo] (g/L)	PdI	Diamètre (Z-av, nm)	Diamètre (int, nm)	Diamètre (nb, nm)
1	HA20	Chro. Ion	2	0,5	0,250 (±0,065)	103 (±5,0)	109 (±1,42)	65 (±4,54)
2	HA20	Chro. Ion	4	0,5	0,216 (±0,030)	87 (±1,63)	98 (±6,31)	54 (±7,67)
3	HA20	Chro. Ion	7	0,5	0,165 (±0,003)	87 (±2,476)	89 (±0,77)	64 (±2,22)

Figure 3.11 *A) CAT en fonction du $DS_{copolymère}$ (4 % et 7%) et de la concentration des dérivés en solution (3 g/L et 0,5 g/L) B) DLS réalisée à 40°C dans le PBS (0,01 Mol) à 0,5 g/L C) Diamètre hydrodynamique (Z-ave, int, nb) et PdI obtenus par DLS pour une dispersion de HA-copolymère à 0,5 ou 3 g/L.*

(iii) ***Comparaison PBS et eau***

Après l'observation, au chapitre précédent, de l'importance de la force ionique sur l'agrégation du copolymère, l'étude a été poursuivie sur les nanogels.

Concernant la CAT, celle-ci est toujours plus faible en milieu salin avec une différence généralement observée de 3°C (même écart constaté dans le cas du copolymère seul en solution).

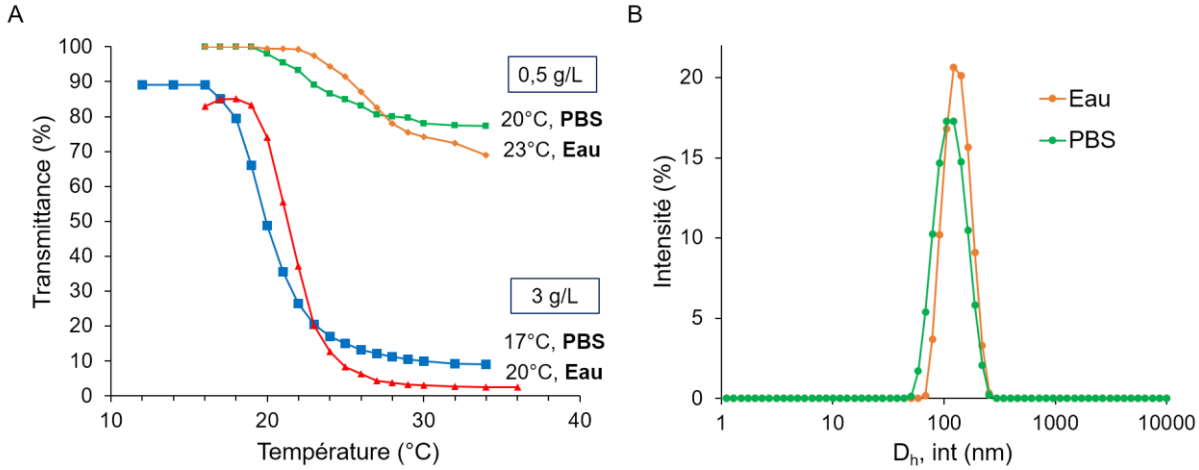

Figure 3.12 *A) CAT des dérivés présentant un* $DS_{copolymère}$ *de 7% en fonction de la concentration (3g/L et 0,5 g/L) et du milieu (eau ou PBS) B) DLS réalisée à 40°C dans le PBS (0,01 Mol) ou dans l'eau à 0,5 g/L C), diamètre hydrodynamique donné en intensité.*

Comme attendu, une diminution du diamètre des nanogels est observée en milieu salin ([NaCl] = 0,15M) du fait de l'écrantage des répulsions électrostatiques entre les chaînes de HA (Figure 3.12-B).

II.2.5 Etude complémentaire sur les nanogels réticulés

Comme le montrent les analyses RMN dans la publication, la réticulation des nanogels même avec un ratio [SH]/[=] de 2, ne permet pas la conversion de l'ensemble des doubles liaisons. La suite de notre démarche a donc consisté à tester un autre bisthiol susceptible de convertir l'intégralité des doubles liaisons restantes après le greffage du copolymère.

Ce dernier se doit de présenter le critère prérequis, celui des petites molécules afin de favoriser les réactions intra-particules, c'est-à-dire entre les chaines de polysaccharide d'une même particule. C'est la raison pour laquelle le PEG-bisthiol régulièrement utilisé à cet effet notamment lors de l'élaboration de gels chimiquement réticulés n'est pas approprié dans notre cas : il présente des masses molaires trop élevées (M_n comprises entre 800 et 6000 g/mol). Suivant ce prérequis, nous avons identifié le 3,6-dioxa-1,8 octane-dithiol (DODT)

(Figure 3.13). Cette molécule a déjà été utilisée pour la réticulation de biomatériaux [39] et s'avère être très réactive.

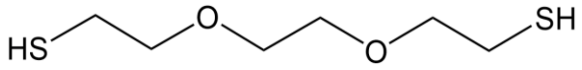

Figure 3.13 *Structure chimique du 3,6 Dioxa-1,8 octane-dithiol (DODT).*

L'analyse RMN (Figure 3.14-A) confirme cette particularité et révèle la réticulation complète des nanogels, pour un ratio [SH]/[=] de 1, avec la disparition des signaux correspondant aux protons de la double liaison à 5,9 ppm (cf. signal b encadré). Cette disparition est associée d'une part à l'apparition à 1,6 ppm des signaux des protons CH_2-CH_2-CH_2-S (c', b') et d'autre part à l'apparition entre 2,6 et 3 ppm des signaux liés au DODT. Par ailleurs, l'analyse FTIR révèle la présence des signaux à 920 et 1250 cm^{-1} qui peut être attribuée aux liaisons C-CH et O-CH du DODT et à la réticulation entre les groupements SH présents sur le DODT et les groupements pentenoate (Figure 3.14-B).

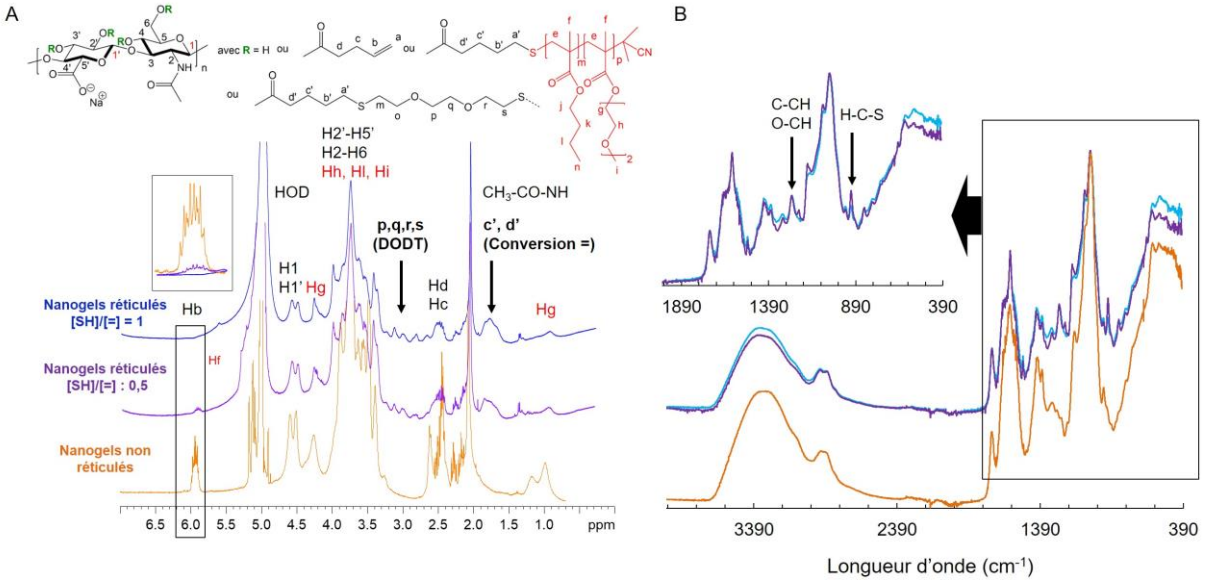

Figure 3.14 *A) Superposition des spectres RMN ^{1}H des nanogels avant et après réticulation B) Superposition des spectres FTIR dans le but de comparer les spectres des nanogels réticulés à 0,5 (spectre violet) et 1 équivalent (spectre bleu) en thiol.*

Cependant, cette forte réactivité semble entraîner des réactions inter-particulaires. L'observation en DLS des nanogels réticulés en solution, à 15°C et 40°C, met en évidence l'hétérogénéité de l'échantillon avec des PdI de ~ 0,250 et ~0,320 pour des ratios [SH]/[=] de 0,5 et 1, respectivement, ainsi que la présence de très grosses particules (Figure 3.15). La

distribution en taille des nanogels résultant de cette formulation est bimodale avec un pic important d'agrégation (3% de l'intensité mesurée).

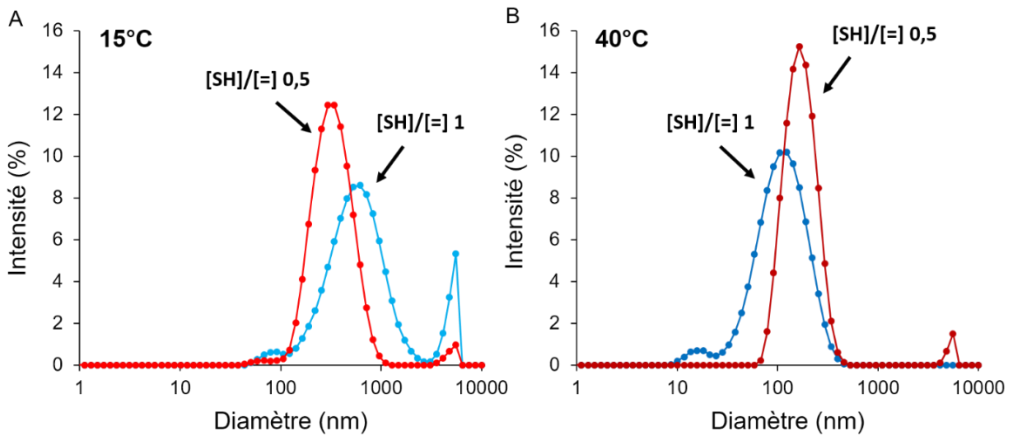

Figure 3.15 *Evolution du diamètre hydrodynamique par DLS des dérivés nanogels en solution réticulés avec un ratio en DODT de [SH]/[=] de 0,5 (rouge) ou 1 (bleu) ([AH-copolymère] = 0,5 g/L, PBS) A) en dessous de la CAT, à 15°C B) au-dessus de la CAT, 40°C.*

Une optimisation de la réticulation par le DODT est donc nécessaire. Une dilution du milieu réactionnel favoriserait un meilleur contrôle des réactions inter-particules non désirées afin de conserver une réticulation totale pour un mélange équimolaire.

Nous supposons que cela est également nécessaire lors de la réticulation avec le DTT. Une étape systématique de filtration met en avant le besoin de compléter ce travail par une étude de l'influence de la concentration sur la réticulation. Nous pouvons présumer que pour de plus faibles concentrations, toujours au-dessus de la CAC, comme par exemple : 0,01 et 0,005 g/L, la réticulation intra-chaînes pourrait être optimisée

Perspectives/autre intérêt de la réticulation

La réticulation offre également un second avantage, celui de retarder le relargage des molécules encapsulées. Il est rapporté dans la littérature, notamment par Chen et al. que la variation du temps de dégradation des nanogels dépendait de la nature chimique de l'agent réticulant et de la densité de réticulation [40]. Ainsi, une étude complémentaire portant sur la dégradation par hydrolyse enzymatique (hyaluronidase) des nanogels réticulés pourrait être envisagée. L'étude comparative de la cinétique de dégradation des dérivés de HA et d'Hep par hydrolyse enzymatique avant et après réticulation nous renseignerait à la fois sur l'efficacité de la réticulation mais également sur la possibilité de contrôler la dégradation de nos systèmes afin d'optimiser le relargage des principes actifs.

II.2.6 Quantification de la disulfo-cyanine7 amine greffée sur les produits

Afin de pouvoir visualiser les nanogels une fois injectés dans les souris par un système non invasif d'imagerie de fluorescence proche de l'infrarouge, une molécule fluorescente, la disulfo-cyanine7, a été couplée aux dérivés Hep- et HA-poly(DEGMA-co-BMA) réticulés et non réticulés. Pour cela un agent de couplage, le 4-(4,6-dimethoxy-1,3,5-triazin-2-yl)-4-methylmorpholinium chloride (DMTMM) a permis de greffer la molécule fluorescente *via* les groupements carboxyliques présents sur le squelette des polysaccharides.

Le fluorophore permet le moment venu (en fonction du temps de circulation fixée après administration) de quantifier dans les organes la présence de nos systèmes et ainsi de déterminer leur biodistribution. Il s'avère nécessaire de connaître le taux de greffage du fluorophore à la surface de chaque système injecté. En effet, la quantification de la fluorescence dans les organes doit être normalisée par rapport à la quantité de dérivé Hep- ou HA-poly(DEGMA-co-BMA) administrée. La figure 3.16 présente à titre d'exemple, la détermination de la concentration en fluorophore par spectroscopie UV-Vis pour un lot de nanogels destinés aux études *in vivo*. Une concentration similaire en fluorophore a pu être mesurée pour les différents nanogels.

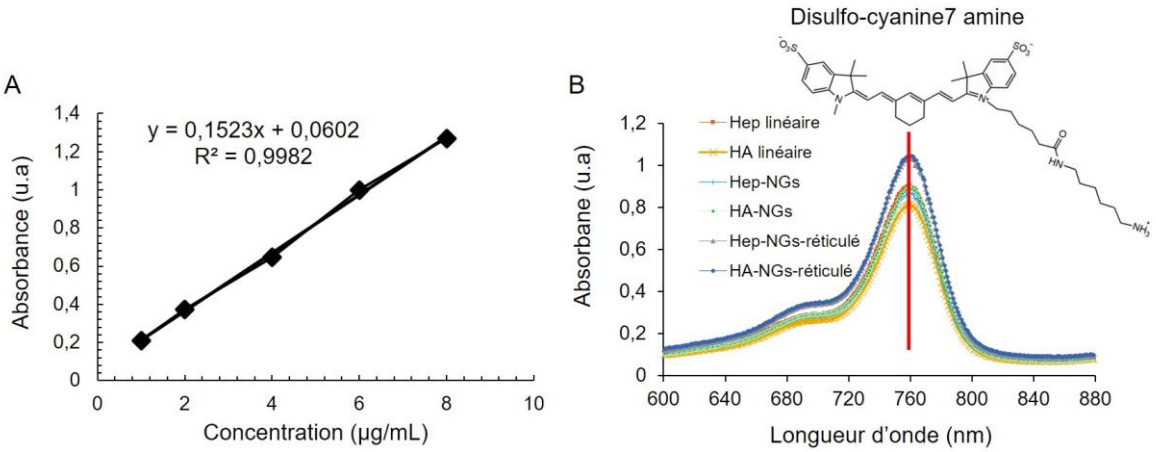

C

Produit	[Cya7] µg/mL
HA linéaire	15,0 (± 0,21)
HA-copolymère	16,5 (± 1,48)
HA-copolymère-réticulé	16,8 (± 0,21)
Hep linéaire	16,5 (± 0,42)
Hep-copolymère	15,9 (±0,64)
Hep-copolymère-réticulé	19,2 (±0,42)

Figure 3.16 *Quantification de la disulfo-cyanine7 amine (A) courbe étalon obtenue à 760 nm dans un mélange 1/1 eau/DMF (B) Graphe du fluorophore greffé sur l'AH et l'Hep linéaire ainsi que sur leurs dérivés (C) Concentration en fluorophore pour [Cproduit] = 0,5 mg/mL.*

III Conclusion

Les objectifs de ce chapitre étaient premièrement d'élaborer des nanogels thermosensibles capables de s'auto-associer à température ambiante, deuxièmement de conférer à ces systèmes une meilleure stabilité colloïdale par la réticulation des chaînes de polysaccharides en surface et enfin d'évaluer le potentiel *in vivo* de l'héparosan par rapport à l'acide hyaluronique en tant que matrice hydrophile pour l'élaboration de nanovecteurs.

Tout d'abord, il est possible grâce à l'élaboration d'un polymère thermosensible « sur mesure » d'obtenir même pour de faible taux de greffage (2%) du copolymère sur le squelette du polysaccharide, des nanogels capables de s'auto-associer à température ambiante. Une gamme de CAT allant de 20°C à 26°C a été obtenue en fonction du DS. Les nanogels répondent ainsi au premier critère visé.

Cependant, l'étude de la réaction de couplage par chimie thiol-ène radicalaire souligne l'importance d'optimiser plusieurs paramètres expérimentaux afin d'améliorer le taux de greffage. Ce dernier dans les meilleures conditions ne dépasse pas les 10%, ce qui nous a contraint à travailler sur de faibles DS (2%, 4%, 7% majoritairement). Une étude complémentaire dédiée à la détermination en fonction du DS i) du nombre de nanodomaines hydrophobes ainsi que ii) du nombre d'agrégation de chaîne par nanodomaines permettrait d'appréhender le mécanisme d'auto-association et de mieux comprendre la structure interne des nanogels synthétisés [41].

De plus, l'obtention des dérivés polysaccharidiques s'est avérée plus délicate que prévu. Notamment l'étape de purification a nécessité la mise au point d'un nouveau protocole de purification par chromographie ionique en batch à basse température afin d'obtenir des dérivés purs.

La stratégie que nous avons retenue pour l'élaboration des nanogels repose entièrement sur la chimie thiol-ène radicalaire. Ainsi, cette dernière a été réutilisée dans le but de réticuler la surface des nanogels à l'aide d'une molécule bisthiol, afin de leur apporter une meilleure stabilité colloïdale en milieu très dilué. Une étude par diffusion dynamique de la lumière, nous a permis de dégager des tendances sur les propriétés des nanogels en solution en fonction de leur taux de réticulation. Nous montrons qu'après réticulation, les nanogels ne se désassemblent plus et restent stables à des températures inférieures à la CAT. La réticulation a donc permis de figer la structure des nanogels. La caractérisation de ces systèmes pourrait être parachevée par une étude de diffusion des neutrons aux petits angles

(SANS) afin de mettre en évidence leur morphologie précise en fonction de la température et de leur composition avant et après réticulation.

Nous montrons *via* la caractérisation par de nombreuses techniques (DLS, MET, MEB, Nanosight, UV/Vis) qu'il est possible d'obtenir, de manière reproductible, un comportement en solution et une morphologie similaire pour des dérivés HA et Hep possédant le même DS et le même taux de réticulation. Cette observation nous a permis de pousser notre investigation à la comparaison de ces deux systèmes *in vivo*, après injection par voie intraveineuse dans des souris porteuses de tumeurs, afin de répondre à la question posée : l'héparosan pourrait-il remplacer l'acide hyaluronique en tant que matrice de nanovecteur pour la délivrance de principes actifs en thérapie anticancéreuse ?

Bien que préliminaires, les observations faites *in vivo* sont très encourageantes. Elles suggèrent une absorption hépatique plus faible et une accumulation tumorale significativement plus élevée pour les nanogels à base de Hep et ainsi apporte une preuve supplémentaire du ciblage spécifique à la tumeur basé sur l'effet EPR. Fait important, ces expériences appuient les résultats obtenus précédemment par Garcia et al. [42] et confirment le comportement *in vivo* similaire des polysaccharides seuls. Elles indiquent que la biodistribution des nanogels est principalement déterminée par la nature du polysaccharide formant la coquille.

A ce jour et à notre connaissance, aucun système combinant l'utilisation de l'héparosan et un copolymère thermosensible n'a été étudié. Plus généralement, l'héparosan a fait l'objet de quelques travaux pour son utilisation dans la vectorisation de PA. Par ailleurs, de rares d'études comparent les propriétés des matrices de polysaccharides entre elles dans ce domaine. Ces expériences ouvrent ainsi la voie à un sujet de recherche à part entière portant sur la comparaison de différentes matrices polysaccharidiques entre elles. Notamment à la suite de ce travail, il serait intéressant d'observer le comportement *in vivo* de nanogels possédant un mélange de polysaccharides : HA et Hep et de les comparer à nos systèmes. Afin de mieux comprendre leur devenir *in vivo* plusieurs lignées de cellules cancéreuses pourront être testées. Enfin, cette investigation pourrait être complétée par une étude sur le potentiel d'encapsulation et de relargage de ces systèmes d'une molécule modèle d'intérêt telle que le paclitaxel (PTX) (un des PA les plus efficaces pour une grande variété de tumeurs). Une comparaison pourrait être réalisée entre les systèmes non réticulés et réticulés. Il est envisageable, comme observé dans la littérature (chapitre I) que la densité de réticulation soit susceptible d'influencer le taux de relargage de la molécule [43].

IV Références

1. Shukla, S.K.; Shukla, S.; Govender, P.P.; & Giri, N.G. Biodegrable polymeric nanostructure in therapeutic applications: opportunities and challenges. *RCS advances,* **2016**, 6, 94325-9435.
2. El-Say, K.M.; & El-Sawy, H.S. Polymeric nanoparticles: promising platform for drug delivery. *International Journal of Pharmaceutics*, **2017**, 528, 675-691.
3. Neamtu, I.; Rusu, A.G.; Diaconu, A.; Nita, L.E.; & Chiriac, A.P. Basic concepts and recent advances in nanogels as carriers for medical applications. *Drug Delivery*, **2017**, 24, 539-557. Debele, T.A.; Mekuria, S.L.; & Tsai, H.C. Synthesis and characterization of redox-sensitive heparin-β-Sitosterol micelles: their Application as carriers for the pharmaceutical agent, doxorubicin, and investigation of their antimetastatic activities in vitro. *Materials Science and Engineering: C*, **2017**, 75, 1326-1338.
4. Freudenberg, U.; Liang, Y.; Kiick, K.L.; & Werner, C. Glycosaminoglycan-based biohybrid hydrogels: a sweet and smart choice for multifunctional biomaterials. *Advanced Materials,* **2016**, 28, 8861-8891.
5. Cui, J.; Richardson, J.J.; Bjornmalm, M.; Faria, M.; & Caruso, F. Nanoengineered templated polymer particles: navigating the biological realm. *Accounts of Chemical Research*, **2016**, 49, 1139-1148.
6. Karlsson, E.; Ryden, L.; & Brewer, J. Protein purification: principles, high resolution methods, and applications. Ion exchange chromatography. Second edition. *New York: Wiley*, **1998**.
7. Hardin, A. M.; Harinarayan, C.; Malmquist, G.; Axén, A.; & Van Reis, R. Ion exchange chromatography of monoclonal antibodies: effect of resin ligand density on dynamic binding capacity. *Journal of Chromatography A*, **2009**, 20, 4366–4371.
8. Stahlberg, J. Retention models for ions in chromatography. *Journal of Chromatography A*, **1999**, 1, 3-55.
9. Helfferich, F. Ion Exchange. *McGraw-Hill Book Company*, *New York*, **1962**.
10. Willcock, H.; & O'Reilly, R.K. End group removal and modification of RAFT polymers. *Polymer Chemistry,* **2010**, 1, 149–157.
11. Jagadeeswara Reddy, K.; & Karunakaran, K.T. Purification and characterization of hyaluronic acid procedure by streptococcus zooepidemicus. Journal of bioscience and biotechnology, **2013**, 2, 173-179.
12. Snavely, D. L.; & Dubsky, J. Near-IR spectra of polyethylene, polyethylene glycol and polyvinylethyl ether. *Polymer Chemistry*, **1996**, 34, 2575–2579.

13. Rangaswamy, V.; & Jain, D. An efficient process for production and purification of hyaluronic acid from Streptococcus *equi* subsp. *Zooepidemicus. Biotechnology letters*, **2008**, 30, 493-496.
14. Duan, X.J.; Yang, L.; Zhang, X.; & Tan, W.S. Effect of oxygen and shear stress on molecular weight of hyaluronic acid produced by streptococcus zooepidemicus. *Journal of microbiology biotechnology*, **2008**,18, 718-724.
15. Frazier, S.B.; Roodhouse, K.A.; Hourcade, D.E.; & Zhang, L. The quantification of glycosaminoglycans: a comparison of HPLC, carbazole, and alcian blue methods. *Open Glycoscience*, **2008**, 1, 31–39.
16. Bitter, T.; & Muir, H.M.A. Modified uronic acid carbazole reaction. *Analytical Biochemistry*, **1962**, 4, 330–334.
17. Plaetzer, M.; Ozegowski, J.H.; & Neubert, R.H.; Quantification of hyaluronan in pharmaceutical formulations using high performance capillary electrophoresis and the modified uronic acid carbazole reaction. *Journal of Pharmaceutical and Biomedical Analysis*, **1999**, 21, 491-496.
18. Wang, X.; Gu, X.; Wang, H.; Sun, Y.; Wu, H.; & Mao, S. Synthesis, characterization and liver targeting evaluation of self-assembled hyaluronic acid nanoparticles functionalized with glycyrrhetinic acid. *European Journal of Pharmaceutical Sciences*, **2017**, 96, 255–262.
19. Hoyle, C.E.; & Bowman, C.N. Thiol–ene click chemistry. *Angewandte Chemie International Edition*, **2010**, 49, 1540-1573.
20. Yang, T.; Malkoch, M.; & Hult, A. Sequential Interpenetrating Poly(ethylene Glycol) Hydrogels Prepared by UV-Initiated Thiol-Ene Coupling Chemistry. *Journal of Polymer Science Part A: Polymer Chemistry*, **2013**, 51, 363-371.
21. Shih, H.; & Lin, C.C. Cross-linking and degradation of step-growth hydrogels formed by thiol-ene photoclick chemistry. *Biomacromolecules*, **2012**, 13, 2003-2012.
22. Shih, H.; & Lin, C.C.; Visible-light-mediated thiol-ene hydrogelation using eosin-Y as the only photoinitiator. *Macromolecular Rapid Communications,* **2013,** 34, 269-273.
23. Toepke, M.W.; Impellitteri, N.A.; Theisen, J.M.; & Murphy, W.L. Characterization of thiol-ene crosslinked PEG hydrogels. *Macromolecular Materials and Engineering,* **2013**, 298, 699−703.
24. Hu, J.; Hou, Y.; Park, H.; Choi, B.; Hou, S.; Chung, A.; & Lee, M. Visible light crosslinkable chitosan hydrogels for tissue engineering. *Acta Biomaterialia,* **2012**, 8, 1730-1738.
25. Costa, P.; Gautrot, J.E.; & Connelly, J.T. Directing cell migration using micropatterned and dynamically adhesive polymer brushes. *Acta Biomaterialia*, **2014**, 10, 2415-2422.
26. Boyd, D.A. Sulfur and its role in modern materials science. *Angewandte Chemie International Edition*, **2016**, 55, 15486-15502.

27. Colak, B.; Da Silva, J.C.S.; Soares, T.A.; & Gautrot. J.E. Impact of the molecular environment on thiol–Ene coupling for biofunctionalization and conjugation. *Bioconjugate Chemistry*, **2016**, 27, 2111-2123.
28. Koo, S.P.S.; Stamenović, M.M.; Arun Prasath, R. Inglis, A.J.; Du Prez, F.E.; Barner-Kowollik, C.; Van Camp, W.; & Junkers, T. Limitations of radical thiol-ene reactions for polymer-polymer conjugation. *Journal of Polymer Science Part A: Polymer Chemistry*, **2010**, 48, 1699-1713.
29. Derboven, P.; D'hooge, D.R.; Stamenovic, M.M.; Espeel, P.; Marin, G.B.; Du Prez, F.E.; & Reyniers, M.F. Kinetic Modeling of Radical Thiol-Ene Chemistry for macromolecular design: importance of side reactions and diffusional limitations. *Macromolecules*, **2013**, 46, 1732-1742.
30. Cao, Z.; Liu, W.; Gao, P.; Yao, K.; Li, H.; & Wang, G. Toward an understanding of thermoresponsive transition behaviour of hydrophobically modified *N*-isopropylacrylamide copolymer solution. *Polymer*, **2005**, 46, 5268-5277.
31. Burns, J.A.; Butler, J.C.; Moran, J.; & Whitesides, G.M. Selective reduction of disulfides by tris (2-Carboxyethyl) phosphine. *The Journal of Organic Chemistry*, **1991**, 56, 2648-2650.
32. Chen, J.; Wan, Q.; Yuan, Y.; Zhu, J.; & Danishefsky, S.J. Native chemical ligation at valine: A contribution to peptide and glycopeptide synthesis. *Angewandte Chemie International Edition*, **2008**, 47, 8521-8524.
33. Thompson, R.E.; Chan, B.; Radom, L.; Jolliffe, K.A.; & Payne, R.J. Chemoselective peptide ligation-desulfurization at aspartate. *Angewandte Chemie International Edition*, **2013**, 52, 9723-9727.
34. Wang, Z.; Rejtar, T.; Zhou, Z.S.; & Karger, B.L. Desulfurization of cysteine-containing peptides resulting from sample preparation for protein characterization by mass spectrometry: desulfurization of cysteine-containing peptides. *Rapid Communications in Mass Spectrometry*, **2010**, 24, 267–75.
35. Li, G.Z.; Randev, R.K.; Soeriyadi, A.H.; Rees, G.; Boyer, C.; Tong, Z.; Davis, T.P.; Remzi Becer, C.; & Haddleton, D.M. Investigation into thiol-(meth)acrylate michael addition reactions using amine and phosphine catalysts. *Polymer Chemistry*, **2010**, 1, 1196.
36. Kolb, H.C.; Finn, M.G.; Sharpless, K.B. Click chemistry: diverse chemical function from a few good reactions. *Angewandte Chemie International Edition*, **2001**, 40, 2004–2021.
37. Boyer, C.; Bulmus, V.; & Davis, T. P. Efficient usage of thiocarbonates for both the production and the biofunctionalization of the polymers. *Macromolecular Rapid Communications*, **2009**, 30, 493–497.

38. Yoon, J.A., Kowalewski, T.; & Matyjaszewski, K. Comparison of thermoresponsive deswelling kinetics of poly(oligo(ethylene oxide) methacrylate)-based thermoresponsive hydrogels prepared by “graft-from” ATRP. *Macromolecules*, **2011**, 44, 2261-2268.
39. Cash, J.J.; Kubo, T.; Bapat, A.P.; & Sumerlin B.S. Room-temperature self-healing polymers based on dynamic-covalent boronic esters. *Macromolecules*, **2015**, 48, 2098-2106.
40. Chen, Y.; Van Steenbergen, M.J.; Li, D.; Van de Dikkenberg, J.B.; Lammers, T.; Van Nostrum, C.F.; Metselaar, J.M.; Hennink, W.E. Polymeric nanogels with tailorable degradation behavior. *Macromolecular Bioscience Journal*, **2016**, 16, 1122-1137.
41. Akiyama, E.; Morimoto, N.; Kujawa, P.; Ozawa, Y.; Winnik, F.M.; & Akiyoshi, K. Self-assembled nanogels of cholesteryl-modified polysaccharides: effect of the polysaccharide structure on their association characteristics in the dilute and semidilute regimes. *Biomacromolecules*, **2007**, 8, 2366–2373.
42. Garcia, F.; Rippe, M.; Companhoni, M.; Stefanello, T.; Louage, B.; Van Herck, S.; Sancey, L.; Coll, J.L.; De Geest, B.; & Nakamuea, C.V. Hyauronic acid-based nanogels with tunable stability using ketone-hydrazide cross-linking for anticancer therapy. *ACS Applied Materials & Interfaces* (publication soumise)
43. Ryu, J.H.; Chacko, R.T.; Jiwpanich, S.; Bickertin, S.; Babu, R.P.; & Thayumanavan, S. Self-cross-linked polymer nanogels: a versatile nanoscopic drug delivery platform. *Journal of the American Chemical Society*, **2010**, 132, 17227-17235.

Chapitre 4 – Design of magnetic nanobeads based on hyaluronic acid

I Introduction

Different hybrid nanomaterials containing inorganic nanoparticles such as gold, iron oxide, silver, quantum dots, carbon nanotubes are tested for the treatment, diagnosis and detection of many diseases [1-3]. Iron oxide nanoparticles (IONPs) are one of the most investigated nanoparticles for various biomedical applications such magnetic resonance imaging (MRI), targeted drug delivery (magnetic guidance), hyperthermia (localized heating), or stem cell tracking. Despite clear advantages, very few types of iron oxide nanoparticles systems have been approved for clinical use by the Food and Drug Administration [4-5].

In order to avoid the aggregation for clinical application, magnetic nanoparticles should have superparamagnetic properties which can be obtained only for small nanoparticles (<20 nm) [6-7] and decorated with biocompatible ligand to ensure dispersion in the biological fluid. It has been demonstrated that the intensity of the magnetic response becomes smaller with the reduction of SPIONs size. To improve magnetic response without removing superparamagnetic properties, ensure biocompatibility, colloidal dispersion and stabilization in aqueous media as well as prolong the blood circulation time, the IONPs have been encapsulated in the polymer matrix through *in situ* encapsulation during the IONP formation or post-synthesis encapsulation by dispersing the IONPs in a solution containing the polymer [8].

Among all the functionalizing compounds the amphiphilic polymers, capable to self-assembly into nanogels in aqueous environment, have significant advantages as platform for simultaneous drug and IONPs encapsulation. A variety of amphiphilic synthetic block polymers predominate in the experiments for incorporation of magnetic nanoparticles into polymer matrix. The IONPs are first stabilized with a primary surfactant (such as oleic acid), followed attachment of PEG derivatives (amphiphilic block copolymer, *i.e.* PEG-PCL), as a secondary surfactant, to form nanoparticles with a hydrophobic core and hydrophilic shell [9]. Particularly, a facile and highly efficient method is to use thermoresponsive nanogels which self-assemble by a simple increase of temperature. To this end, several systems have been described for transferring hydrophobic magnetic nanoparticles from an organic to aqueous solution by wrapping a thermo-responsive polymer such as poly(N-isopropylacrylamide) (PNIPAM) [10-13], a pH- and thermo-responsive polymer based on PNIPAM derivatives [14] or olygoethylene-gycol derivatives (poly(MEO_2-MA-co-OEGMA-co-MAA) [15].

Taking into account the beneficial characteristics of polysaccharides (*i.e.* nontoxicity, biodegradable, etc.), alginate [16], chitosan [17-18], dextran [19-20], heparin [21] and recently HA [22], have been investigated for modification of magnetic nanoparticles for *in vivo* applications [23]. However, unlike synthetic polymer systems, the main studied approaches were limited to the coating of HA onto the surface of IONPs by covalent coupling (*i.e.* EDC/NHS coupling) [24-29] and very few examples of IONPs physically entrapped *via* hydrophobic or electrostatic interactions have been developed.

The most beneficial way to effectively increase the magnetic force acting on a nanocarrier in a stable suspension exposed to a magnetic-field gradient, while maintaining the superparamagnetic state, is to increase its volume. This could be achieved by dense packing of superparamagnetic nanoparticles. The nanoparticle assemblies inside the nanobeads show great potential for applications requiring high mobility in magnetic field gradients and high sensitivity at low doses [30-31].

Table 4.1 presents HA-based nanobeads obtained by physical encapsulation of IONPs. Only few examples of IONPs loaded in amphiphilic-HA have been developed and, to the best of our knowledge, none from thermoresponsive-HA derivatives [32-36]. The obtained structures show mainly heterogenous and not well-defined nano-structures, often limited for MRI applications without investigation their potential for magnetic guidance to the target.

The goal of this work was to study the assembly of IONPs in our thermoresponsive nanogels (HA-g-poly(DEGMA-co-BMA) previously described in Chapter 3. To develop magnetic polysaccharide nanocarriers two different strategies were investigated and compared. These systems were fully characterized in terms of size (DLS), composition (FTIR) and morphology (SEM, TEM). We will discuss the chemistry and design considerations associated with the synthesis of SPIONs and their incorporation into nanogel formulations. Finally, the magnetic properties of these systems will be compared to those of single IONPs.

Table 4.1 *Examples of HA-based magnetic nanobeads. Size distribution obtained by DLS analysis.*

Components Main characteristics		Encapsulation method	Application	Morphology	Ref
Hydrophobic block	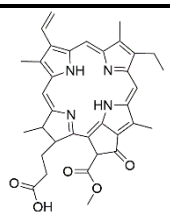 Pheophorbide	Emulsion by Sonication Hydrophobic and electrostatic interaction with acetyl group with nanocluster	MRI and photodynamic/ hyperthermia therapy	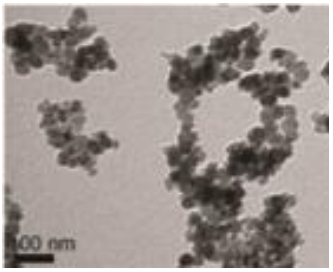	[32]
HA (kg/mol)	5.8				
Nanobead Size (nm)	108-222				
Hydrophobic block	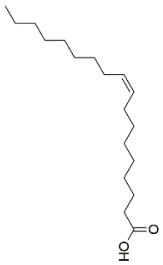 Oleic acid	Micro-emulsion under ultrasonication process Hydrophobic Interaction with nanocluster	MRI	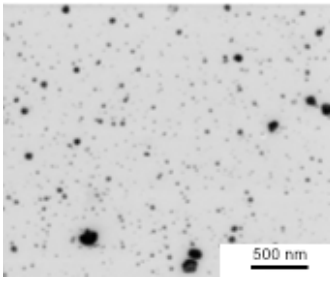	[33]
HA (kg/mol)	15				
Nanobead Size (nm)	87-108				
Hydrophobic block	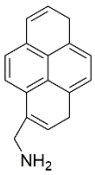 pyrenyl	Nanoemulsion under ultrasonication process Hydrophobic interaction With nanocluster	MRI	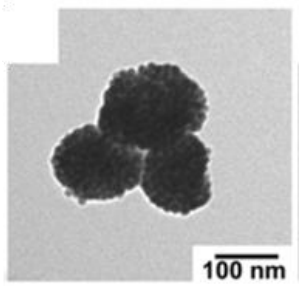	[34] [35]
HA (kg/mol)	1000				
Nanobead Size (nm)	72-137				
Hydrophobic bloc	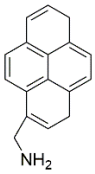 pyrenyl	Solvent exchange (dialysis method) Hydrophobic interaction	MRI	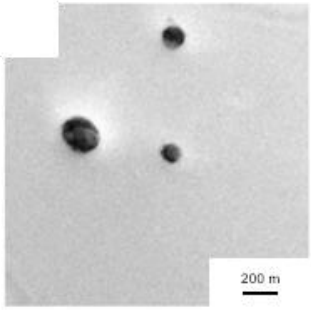	[36]
HA (kg/mol)	130				
Nanobead Size (nm)	393				

Components Main characteristics		Encapsulation method	Application	Morphology	Ref
Moiety	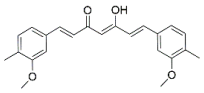 Curcumin	Layer by layer with poly(vinylpyrroi done) - Curcumin Electrostatic interaction	MRI and drug targeting	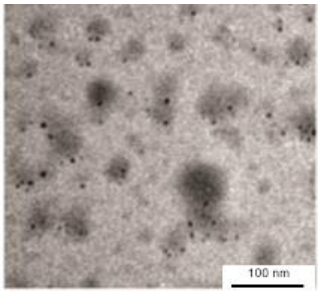	[37]
HA (kg/mol)	-				
Nanobead Size	99-131				
Moiety	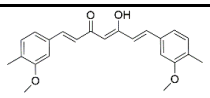 Curcumin	Layer by layer with curcumin-chitosan Electrostatic interaction	MRI	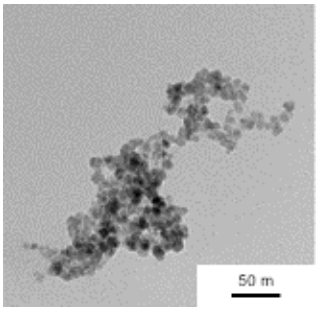	[38]
HA (kg/mol)	-				
Nanobead Size (nm)	100 nm				
Moiety	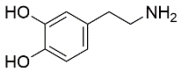 Dopamine (DPA)	Electrostatic interaction	MRI	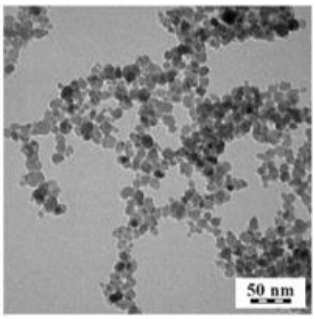	[39]
HA (kg/mol)	300				
Nanobead Size (nm)	100 – 1000 function of DPA/HA ratio				
Moiety	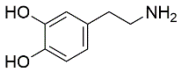 Dopamine (DPA)	Electrostatic interaction	MRI	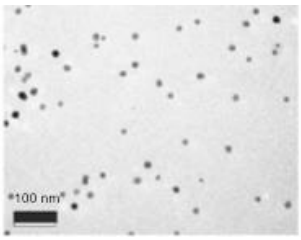	[40]
HA (kg/mol)	17				
Nanobead Size (nm)	45-400				

II Synthesis of hydrophobic iron oxide nanoparticles (IONPs)

To date, a variety of methods such as co-precipitation, thermal decomposition, hydrothermal and solvothermal synthesis, sol–gel synthesis, microemulsion, ultrasound irradiation and biological synthesis have been applied to produce magnetic IONPs [41-42]. In these different methods, the efforts have been put on the control of the size, shape, morphology and magnetic properties of fabricated nanoparticles. These are crucial parameters for different applications.

In this work, monodisperse magnetic nanoparticles were obtained through the thermal decomposition of iron III acetylacetonate ($Fe(acac)_3$) in benzyl ether at 300°C in the presence of oleylamine and oleic acid [43-45]. Thermal decomposition of $Fe(acac)_3$ in high boiling point solvents containing stabilizing surfactants leads to the formation of Fe_3O_4 nanocrystals coated with oleic acid/oleylamine (Figure 4.1-A). Nanocrystals are formed by nucleation, the process whereby nuclei (seeds) act as templates and further crystal growth. The mechanism involves the decomposition of $Fe(acac)_3$ forming an intermediate metal-complexes-metal oleates (oleic acid (OA) with its carboxylic group bound selectively to crystal facets) followed by the particle growth which takes place mainly at the boiling point of the mixture. Stabilizers play an important role in the final size and dispersity of the particles since they form a dynamic layer around the nuclei that actively controls the growth process of the IONPs core after nucleation [46-48]. The key of the success to prepare monodisperse nanoparticles, with an acceptable crystallinity quality and narrow polydispersity, is a fast nucleation and growth process which can be achieved by separation of burst nucleation from particle growth [49-51]. Thus, the mixture was first heated up to 200°C (nucleation) and kept at this temperature for some time before heating to reflux at 300°C in benzyl ether (growth).

The size and shape of oleic acid-coated iron oxide nanoparticles (OA-IONPs) were determined using transmission electron microscopy (TEM). TEM images show monodisperse nanocrystals with a narrow size around 7.8 ± 0.8 nm (Figure 4.1-B-C). Dynamic light scattering (DLS) of IONPs in chloroform confirmed the same order of IONPs size ~ 10 nm. Due to the long hydrophobic tail, colloidal oleic acid coated-IONPs are highly soluble and stable in organic solvents, such a hexane, toluene, tetrahydrofuran or chloroform, but insoluble in water.

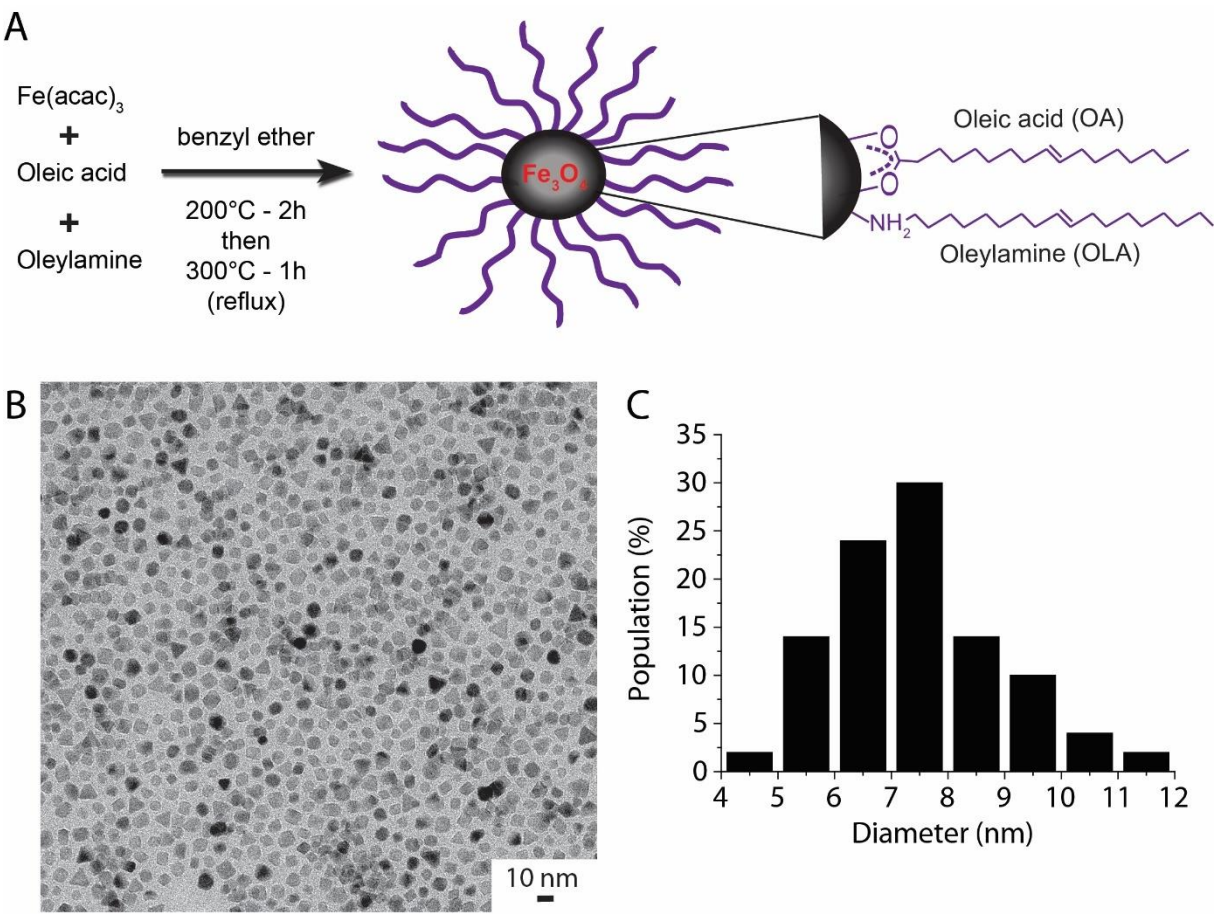

Figure 4.1 *A) Scheme of a colloidal nanoparticle consisting of oleic acid/oleylamine-stabilized Fe_3O_4 (linkage with iron oxide nanoparticle) B); TEM image of iron oxide nanoparticles stabilized with an oleic/oleylamine mixture and C) Size distribution histogram determined from the TEM image.*

Different shapes of oleic acid-coated nanoparticles such as triangular, square and diamond were observed. As it has been previously reported, the kinetics of growth rate of facets of the nuclei plays a critical role. Zhang et al. [50] demonstrated that the variation of heating conditions of the reactional mixture may induce the formation of different morphologies. A low heating rate (1.3 °C/min) mainly induces the formation of pyramidal (3D prism/triangular geometry) Fe_3O_4 nanocrystals. At a higher heating rate, 6.3 °C/min and 10°C/min, the cubic and truncated octahedral nanocrystals were obtained, respectively. In our case, the heating rate applied for the growth step was 4.5 °C/min, which could result in different morphologies of the synthesized nanocrystals. Moreover, a small variation of the heating rate during experiment could also influence the final morphology of our NPs.

Figure 4.2 presents the FTIR spectra of oleylamine, oleic acid, and OA-IONPs respectively. Three distinct zones stand out from the IONPs spectrum: alkyl chains (3000 - 2800 cm^{-1}), COO^- groups of oleic acid (1800 - 900 cm^{-1}) and Fe-O links of iron oxide (800 - 400 cm^{-1}). Comparing the three spectra, it can be seen that the two bands at 2922 cm^{-1} and 2849 cm^{-1} are characteristic for oleic and oleylamine carbon-hydrogen stretching in alkyl chains v(C-H). The intensities of the C=O at 1730 cm^{-1} and of C-O stretching at 1265 cm^{-1} and 962 cm^{-1} are significantly reduced in the IONPs, and two new peaks centred at 1564 cm^{-1} and 1400 cm^{-1} from the symmetric and asymmetric stretching of COO^-. This result is consistent with the formation of iron carboxylate bonds. It is well reported that the C=O peak shifts when the molecule is attached to a ferrite surface [51-52]. Finally, we could observe the Fe-O bonds between 800 and 400 cm^{-1}. Interestingly, magnetite (Fe_3O_4) and maghemite (Fe_2O_3) present two different infra-red signatures in this part. The spectrum of a magnetite sample presents a single band around 580-590 cm^{-1} while the spectrum of a maghemite sample presents several close bands between 400 and 800 cm^{-1} whose resolution depends on the structural order [51, 53-54]. In our case, a broad band with a maximum at 577 cm^{-1} and a shoulder towards 700 cm^{-1} indicates an oxidation of the magnetite which is in agreement with crystallography studies presented in supporting information. It has been reported that the magnetite oxidizes easily to maghemite (γ-Fe_2O_3). As Fe_3O_4 and γ-Fe_2O_3 crystal structures are very similar, they cannot be distinguished from standard techniques. The combination of several techniques is necessary to quantitatively differentiate magnetite from maghemite like deep analysis by X-ray absorption spectroscopy (XAS) and X-ray magnetic circular dichroism (XMCD) [55-56].

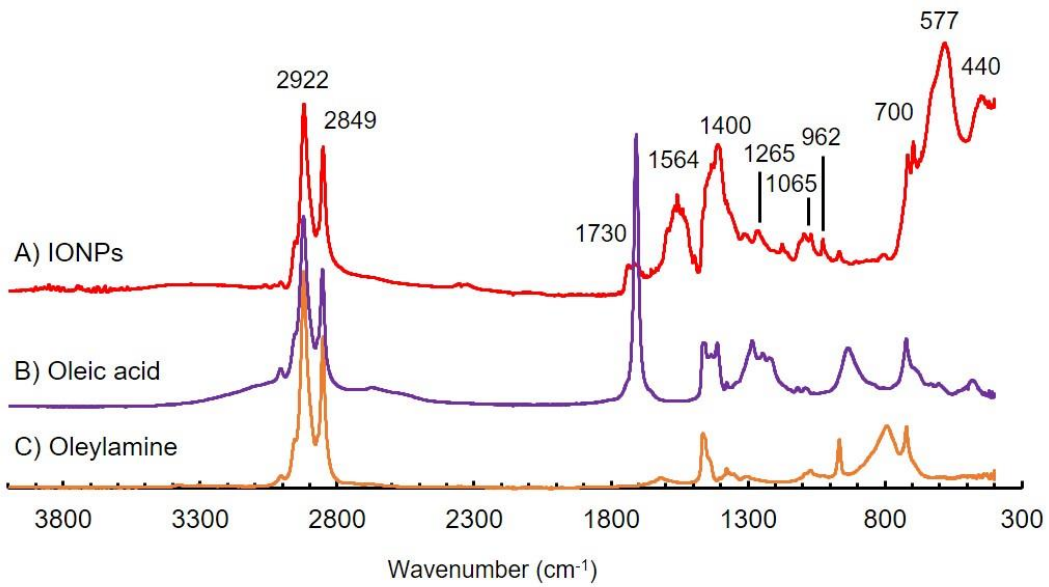

Figure 4.2 *Infrared spectra of synthesized oleic acid-Fe_3O_4 nanoparticles (A), oleic acid (B), and oleylamine (C).*

To study magnetic properties, the hydrophobic IONPs were dispersed in PDMS to ensure immobilization and separation of individual NPs in the matrix.

The zero field-cooled (ZFC) and field cooled (FC) curves were measured in a magnetic field of 100 Oe in the temperature range of 5-300 K. The ZFC curve of IONPs shows the blocking temperature (T_B) at 30 K (data not shown). Such behavior is characteristic of superparamagnetism typically observed in small ferromagnetic and ferrimagnetic nanoparticles. Below T_B, the IONPs exhibit ferrimagnetic properties. When the temperature is above T_B, the thermal energy overcomes the anisotropy barrier and randomizes the magnetic moment, leading to superparamagnetic behavior of nanoparticles.

Figure 4.3 shows the hysteresis loops of IONPs at 5 and 300 K. At 5 K, the hysteresis loop indicates ferromagnetic behavior with a coercivity of 200 Oe and a remanence of 4.5 emu g^{-1}. In the same figure, in contrast to the hysteresis observed at 5 K, the response of nanoparticles to an external field at 300 K also follows a sigmoidal curve but shows no hysteresis. Only a negligible value (less than 25 Oe) is observable, that is attributed to the remanent field of the VSM coils.

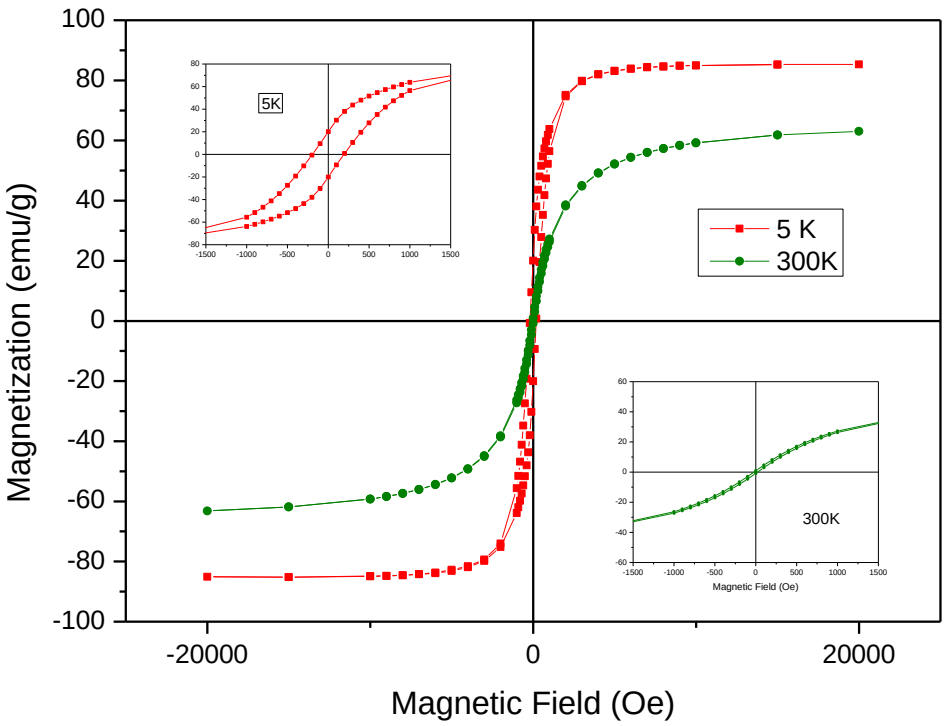

Figure 4.3 *Hysteresis loops and their zooms of IONPs at 5 K (red) and 300 K (green).*

When magnetization of NPs is equal to zero in the absence of an external field, such NPs are referred to as superparamagnetic. Superparamagnetism is important in applications such as drug delivery or MRI, where NPs exhibit no magnetic properties upon removal of the external magnetic field and therefore no attraction for each other, preventing aggregation [6].

The saturation magnetization of IONPs at 5 and 300 K are 85 and 63 emu.g^{-1}, respectively. Magnetization loops show that there is a reduction of the saturation magnetization (M_s) values of IONPS. It should be noted that besides the iron oxide core, the coating layer also contributes to the mass of the sample. Consequently, the saturation magnetization might be influenced by the amount of OA on the surface of IONPs. Thus, the saturation magnetization was calculated by subtracting the mass contribution of non-magnetic substance estimated to be 32% through thermogravimetric measurement (Figure 4.4). The thermogravimetry analysis (TGA) shows the first loss of weight related to the dehydration of the sample. At 200-450°C decomposition of organic coating ligands present of the surface of the IONPs occurs which results in the next mass loss, and finally the percentage of inorganic residue (Fe_3O_4) was calculated at 700°C were the TG curve is stabilized.

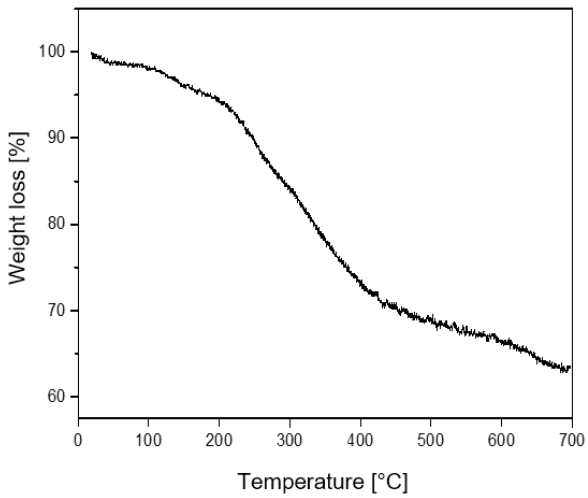

Figure 4.4 *TGA curves of IONPs under N_2 atmosphere.*

In conclusion, using thermal decomposition method, we prepared small (~10 nm) monodispersed superparamagnetic IONPs. They were characterized by TEM, DLS, FTIR, while superparamagnetic properties were confirmed by SQUID measurements. These oleic acid coated IONPs are soluble only in non-polar solvents. To obtain water soluble magnetic IONPs as well as expand their biomedical application, in the next part of this chapter, we propose to integrate superparamagnetic NPs into biocompatible, biodegradable HA matrix.

III Design of magnetic nanobeads based on hyaluronic acid

Self-assembly is the process of specific association of molecules through non-covalent interactions leading to the formation of organised structures. In the case of thermo-responsive HA-g-poly(DEGMA-co-BMA), the self-assembly can be triggered by the collapsing the hydrophobic domains above its CAT as presented in Chapter 3. To build-up the magnetic nanobeads, in this part, we propose the incorporation of oleic acid stabilized IONPs (OA-IOPNs) in the self-assembled structure of our modified HA. The OA-IONPs, pre-dissolved in organic solvent, can be mixed with an aqueous solution of thermoresponsive macromolecules. The HA-g-poly(DEGMA-co-BMA) is expected to self-associate above its CAT enclosing IONPs in its hydrophobic domains [57].

In the following, we present two different formulation strategies for encapsulation of IONPs including *in situ* enclosing owing formation of HA nanogels and IONPs clustering followed by coating with grafted polysaccharide to obtain core/shell structure. In the first case, IONPs were added in an aqueous solution of HA-g-poly(DEGMA-co-BMA) and encapsulated in nanogels by a fast increase of the temperature above the CAT (T>24°C), in a one step process. In the second case, clusters of IONPs were first formed by solvent destabilization approach, and next HA-g-poly(DEGMA-co-BMA) was added to enwrap the preformed clusters by a polymeric layer in aqueous solution.

III.1 Preparation of HA-g-copolymer/IONPs nanogels by *in-situ* encapsulation

To prepare the IONP-loaded nanogels (HA-g-copolymer/IONPs), oleic acid-coated IONPs were suspended in chloroform and added drop by drop (volume = 60 µL, C = 0.5 g/L) to 2 mL of an aqueous solution of HA-g-copolymer ($DS_{copolymer}$ = 2%, TAC = 24°C, CAC = 0.02 mg/mL, Cp = 0.5 g/L in PBS) at a temperature between 5 and 24°C under vortex agitation (T<CAT). Then the temperature of the mixture was increased to 40°C to allow self-association of HA-g-copolymer and enclosing the IONPs into hydrophobic nanodomains. The reaction media was kept under N_2 at 40°C for 1 h to evaporate chloroform (Figure 4.5).

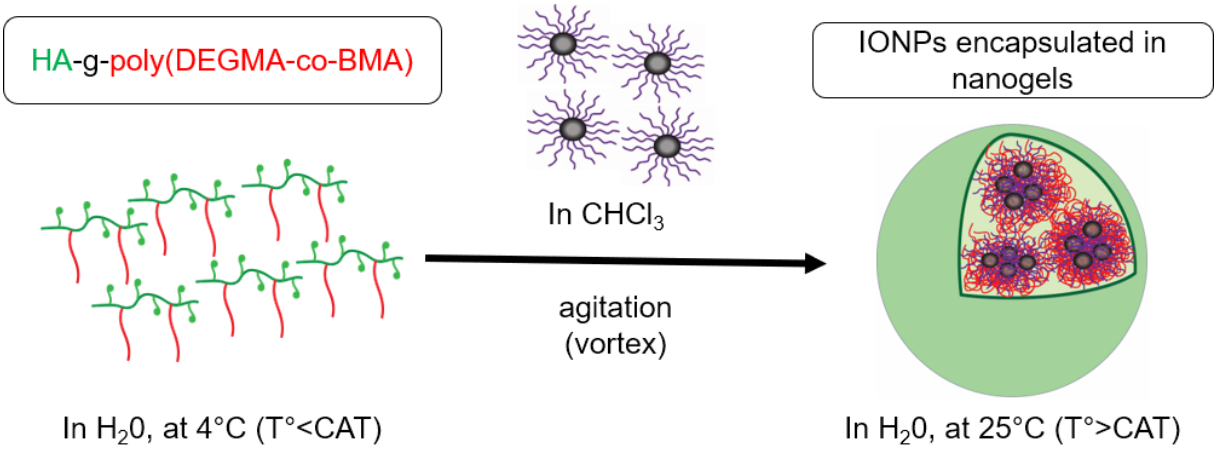

Figure 4.5 *Formation of the magnetic thermosensitive nanogels based on hyaluronic acid (HA-g-copolymer/IONPs).*

As the self-assemblies of HA-g-copolymer are more stable when crosslinked (as presented in Chapter 3), we have also frozen the hybrid structure using dithiothreitol (DTT) crosslinker to covalently bind HA chains through radical thiol-ene chemistry. To this aim, we used the ratio of [SH]/[=] : 2/1 which showed earlier good colloidal stability of nanogels. Subsequently to the evaporation of chloroform at 40°C, nanogels were crosslinked by reaction of the remaining pentenoate groups with a bis-thiol crosslinker, under UV irradiation. After shell-crosslinking, the nanogels were dialysed for 32h to remove salts and un-reacted residues. The crosslinked nanogels were recovered by freeze-drying for storage. The obtained structures without freeze drying were also observed by simple drying of suspension drop on the carbon-coated copper grid and gave similar images as after freeze-drying (data not shown).

The size and shape of the HA-g-copolymer/IONPs system is presented in Figure 4.6-A. As a control, we present the structures obtained from i) copolymer in the absence of hyaluronic acid (Figure 4.6-B), and ii) crosslinked nanogels in the absence of IONPs (Figure 4.5-C). The formed structures were re-dispersed in water and dried on carbon coated copper grids before TEM imaging.

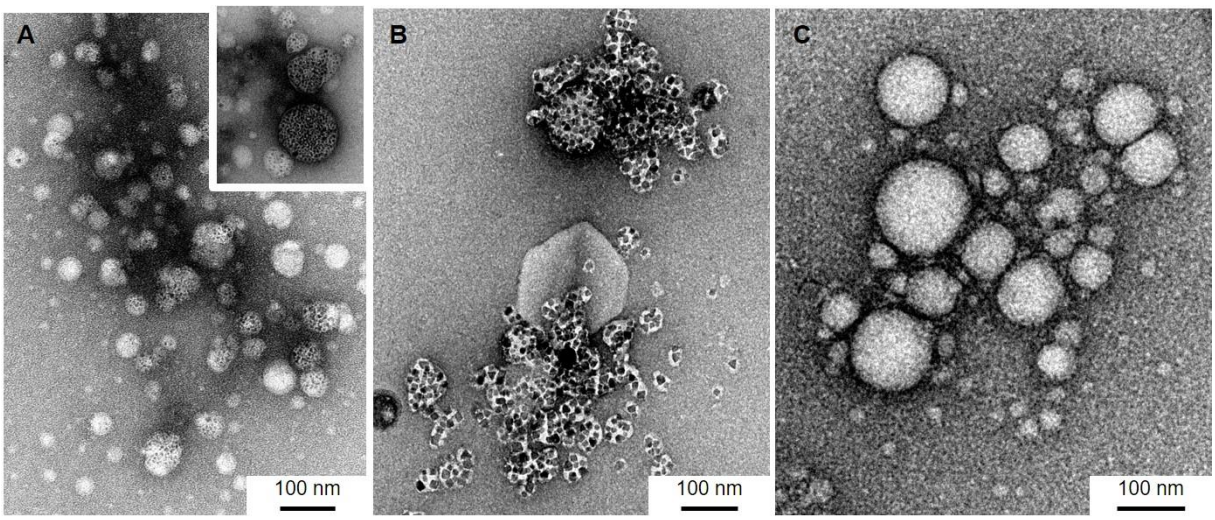

Figure 4.6 *TEM images of negatively stained A) HA-g-copolymer/IONPs nanogels, B) IONPs (C = 0.15 g/L) coprecipitated with thermoresponsive copolymer (C = 0.18 g/L) and C) un-loaded crosslinked nanogels at 0.5 g/L.*

Figure 4.6-A shows the spherical shape of the nanogel with a diameter of ~60 nm with IONPs dispersed randomly into the polymer matrix, the nanogels without IONPs and nanogels filled partially with IONPs. This random dispersion of IONPs could be the result of a vigorous shaking by vortex in which different sizes of IONPs droplets in chloroform could be formed and enclosed randomly in hydrophobic domains. When a dispersion of IONPs in chloroform (0.15 g/L) was added to a copolymer (without HA) in water (0.18 g/L), the strong aggregation was observed. IONPs were stacked in copolymer aggregates which precipitated from water by un-controllable manner (Figure 4.6-B). Finally, Figure 4.6-C highlights the spherical shape of the crosslinked-nanogel with a size distribution from 30 to 100 nm obtained by self-assembly of thermoresponsive HA derivative without the presence of inorganic NPs.

The presence of loaded nanogels dispersible in water confirms that the hydrophilicity of HA helps in the formation of individual magnetic nanogels in aqueous solution. This assembly is the result of combination of the HA properties and those of the thermo-responsive copolymer. The poly(DEGMA-co-BMA) copolymer chains act as reservoirs while HA plays the critical role of colloidal stabilizer in aqueous solution.

In order to better understand the formation of HA-g-copolymer/IONPs nanogels, we investigated the nanogels synthesized by addition of different concentrations of IONPS in chloroform (30 µL/mL) 0.3, 0.5, and 1.0 g/L. The Figure 4.7 represents the DLS size distribution of nanogels in “intensity” and in “number”. As large particles scatter much more light than small particles (the intensity of scattering of a particle is proportional to the sixth power of its diameter from Rayleigh’s approximation), the size distribution in intensity highlights the presence of larger particles, while the size distribution in number takes into account the contribution of each population by determining the number of each size particles.

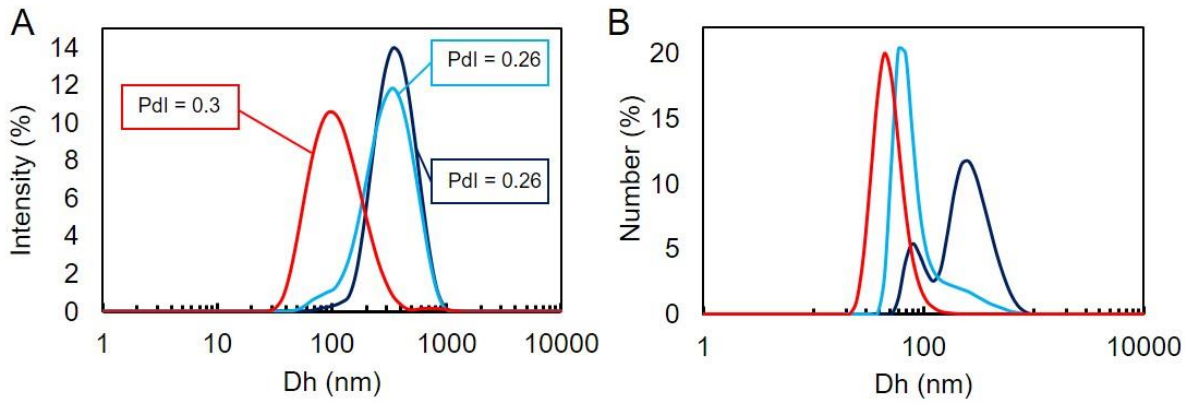

Figure 4.7 *DLS size distributions of IONPs-loaded nanogels containing 0.5 g/L of HA-g-copolymer and different concentration of SPIONs: 0.3 g/L, 0.5 g/L and 1.0 g/L A) D_h in intensity and B) D_h in number.*

The measurements performed at 40°C (T>CAT) in PBS revealed a broad intensity peak with a size-average around 100 nm for 0.3 g/L of IONPs, while for higher amount of IONPs (0.5 and 1 g/L), a bimodal distribution, with one population at 70-80 nm and another at 450 nm. The distribution in number that show the contribution of each population, confirms this trend and a bimodal distribution was observed for the highest concentration of IONPs. SEM and TEM observations of nanogels with IONPs (c = 0.5 g/L) also showed larger HA-g-copolymer/IONPs nanogels (>60 nm) with a size distribution from 100 to 200 nm and larger polydispersity (Figure 4.8-A-B). In the TEM images, the nanogels appeared to be much smaller than in DLS likely due to shrinkage during the drying process.

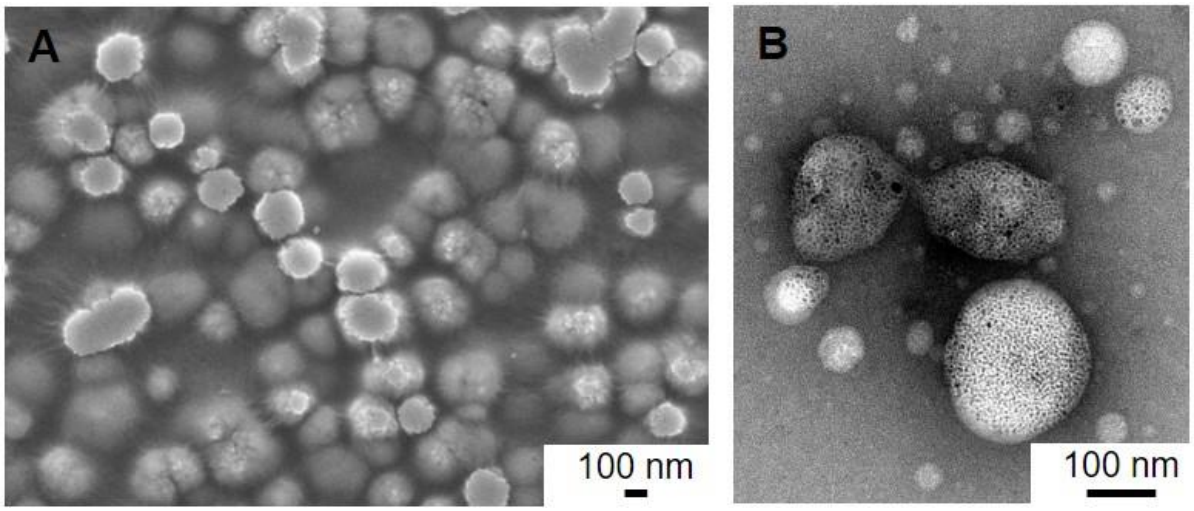

Figure 4.8 *Images of SPION-loaded nanogels containing 0,5 g/L of HA-g-copolymer and 1 g/L of SPIONs in water by SEM (A) and TEM (B).*

From Figure 4.8-B, we observed that higher concentration of IONPs does not eliminate the presence of unloaded nanogels. Similar difficulties with encapsulation of IONPs have already been encountered in other reports. Talelli et al. [57] encapsulated IONPs in thermoresponsive mPEG-b-p(HPMAm-Lac_2) block copolymer micelles (D_h = 200-300 nm) formed *via* a similar mechanism based on “rapid heating” using different concentrations of IONPs from 1 to 20 mg/mL. They observed that the presence of unloaded nano-assemblies was related to the high concentration of polymer used for formulation of nanogels. Thus, in our case, it seems that the IONPs/polymer ratio needs to be further adjusted. Interestingly, thermoresponsive mPEG-b-p(HPMAm-Lac_2) block copolymer nano-assemblies present similar spherical arrangement (shape and morphology) and distribution of IONPs into nanogels.

The heterogeneous dispersion of IONPs in a nanogel matrix could also result from the use of the magnetic stirrer during crosslinking step. In order to avoid the problem of magnetite aggregation on the magnetic stirrer, others techniques such as mechanical stirring have been tried. Unfortunately, in the latter cases, large variations in nanogel size were noted.

The comparison of the FTIR spectrum of hybrid nanogels with that of HA-g-copolymer and OA-IONPs is presented in Figure 4.9 Apart from many characteristic bands of HA-g-copolymer (characterized in Chapter 3), the FTIR of crosslinked HA-g-copolymer/IONPs nanogels shows a moderate peak around 2900 cm^{-1} which could be attributed to carbon-hydrogen stretching v(C-H) in alkyl chains of OA present on inorganic NPs (two bands at 2922 and 2849 cm^{-1} characteristics of oleic and oleylamine).

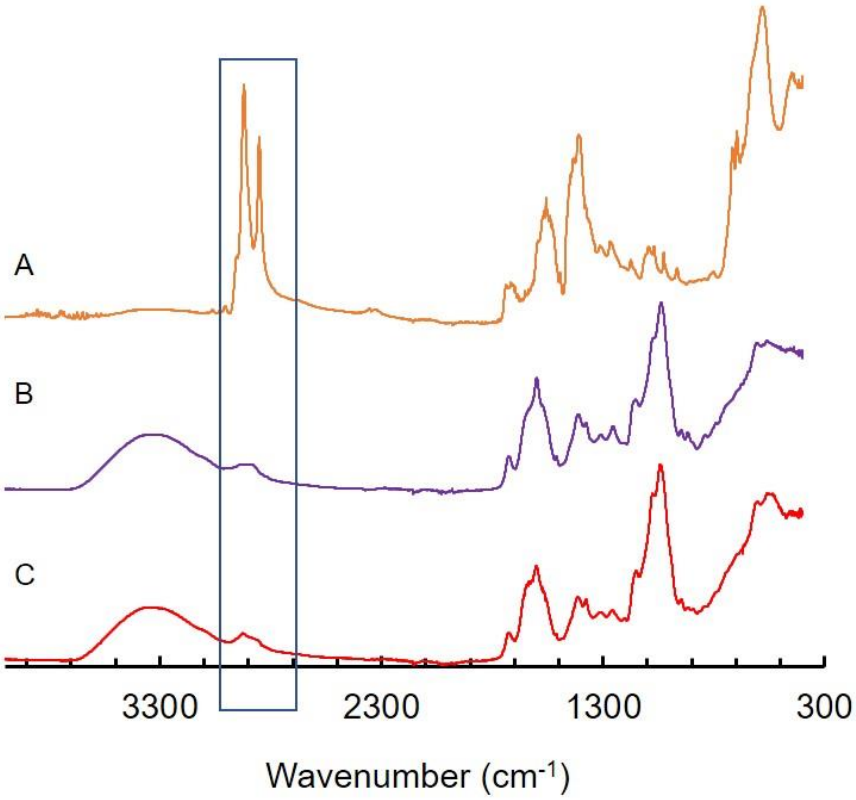

Figure 4.9 *FTIR spectra of A) OA-IONPs, B) Crosslinked HA-g-copolymer nanogels, C) Crosslinked HA-g-copolymer/IONPs nanogels after freeze-drying.*

In conclusion, the IONPs were encapsulated into the hydrophobic domains of the HA-g-copolymer by simple increasing the temperature above the CAT. The transfer of SPIONs from chloroform to the water-soluble nanogels was possible using HA-g-copolymer. HA-g-copolymer/IONPs nanogels could be freeze-dried and stored easily. Unfortunately, we observed non-homogeneous encapsulation of IONPs.

III.2 Core/shell nanobeads

The incorporation of IONPs in HA nanogels by *in situ* encapsulation presented in the previous section (III.1) resulted in hybrid HA nanogels. Unfortunately, we observed non-homogenous dispersion of nanoparticles in polymer matrix, and low density of magnetic nanocrystals in polymer matrix. In the next part, we propose to increase the amount of magnetic nanoparticles in relation to the non-magnetic material (polymer) by the fabrication of IONP clusters with a high content of NPs followed by deposition of HA-g-poly(DEGMA-co-BMA).

For last two decades, different methods for preparation of clusters of colloidal nanoparticles have been investigated. In the emulsion based colloidal assembly, the nanoparticles are assembled spontaneously into colloidal clusters during evaporation of emulsion phase. Various parameters influencing the clusters formation were tested such as emulsion composition (IONPs, polymer, surfactant molecule) or packing characteristics (temperature, time shearing) [58-61]. IONPs dissolved in non-polar solvent form droplets in the polar phase under sonication. As the emulsion interface deform and drops shrinks, the colloidal hard particles come into contact with neighbouring particles and form packed structures [62]. The emulsion droplets are fabricated in the presence of surfactant molecules like sodium dodecyl sulfate (SDS) or dodecyltrimethylammonium bromide (DTAB) [60,63-64] or amphiphilic polymers which stabilize the structure after solvent evaporation. The clustering of SPIONs was also achieved by solvent exchange using increasing solvent polarity [65]. Similarly, in the group of Pellegrino, the concentrated magnetic beads were fabricated by the solvent destabilization [66]. The addition of acetonitrile (ACN) to hydrophobic magnetic NPs dissolved in tetrahydrofuran (THF) resulted in the formation of colloidal ordered assemblies. Further, the alkyl polymaleic anhydride polymer was condensed on the hydrophobic core. After redispersion in water, the hydrolysis of anhydride groups of coating polymer resulted in negatively charged groups making the magnetic nanobeads soluble in aqueous solution.

III.2.1 Preparation of magnetic clusters coated with HA-g-poly(DEGMA-co-BMA)

Figure 4.10 presents the strategy used to elaborate HA-g-copolymer-coated clusters. The OA-IONPs were dissolved in THF solvent (1 mg/mL) and sonicated to ensure good dispersion of individual nanoparticles. Then, acetonitrile (v = 200 µL) was added dropwise (250 µL/min) under sonication, resulting in aggregation of the hydrophobic nanoparticles into nanoclusters. Finally, the clusters were wrapped by polymer chains, the 1 mL of cold aqueous solution of HA-g-copolymer (0.5 g/L) was added to the cluster suspension and heated up to 40°C under agitation for 30 min.

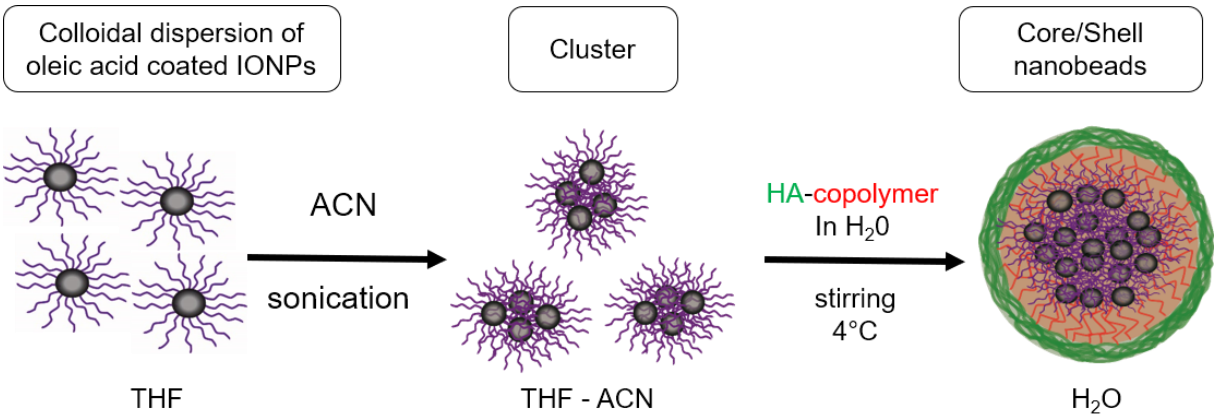

Figure 4.10 *Description of the successive steps in the formation of magnetic nanoclusters coated with HA-g-poly(DEGMA-co-BMA).*

The polysaccharide shell was crosslinked using radical thiol-ene chemistry by reaction of the remaining pentenoate groups on HA chain with dithiothreitol (DTT) as a bis-thiol crosslinker, using UV irradiation for 15 min at 20 mW/cm^2, in water under relatively dilute condition ($C_{polymer}$ = 0.5 g/mol) and N_2 atmosphere. The permanent NdFeB magnet (0.3T) was used to collect IONPs loaded nanobeads from the reaction medium (Figure 4.11-A-B). After removal of supernatant, the magnetic nanobeads were easily redispersed in water that indicated the presence of hydrophilic shell around magnetic clusters (Figure 4.11-C).

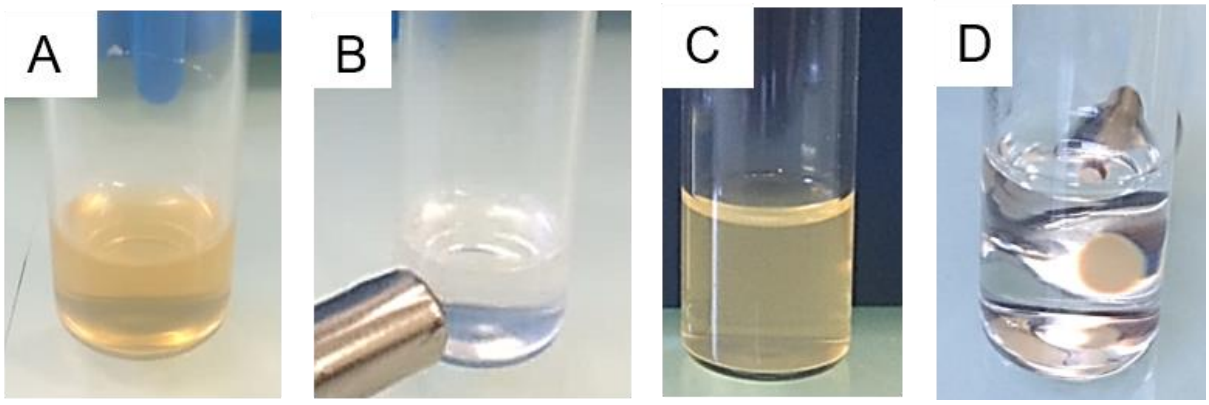

Figure 4.11 *The nanobead suspension directly after polymer assembly (A), after separation from solvents (6 h) (B), re-dispersed in water (C) and attracted by magnet from water after 1 night (D).*

The SEM and TEM images showed individual spherical nanogels ~200 nm with slight presence of agglomerates composed of interconnected clusters (Figure 4.12-A, C). The latter might be formed during cluster coating with HA-g-copolymer. These agglomerates could be easily removed by purification with magnet, resulting in a homogenous dispersion of nanobeads (size between 150 and 200 nm) (Figure 4.12-D-F). The nanogels presented in

Figure 4.12-B and 4.12-E showed the presence of IONPs concentrated in the center and at lower density in the polymer shell.

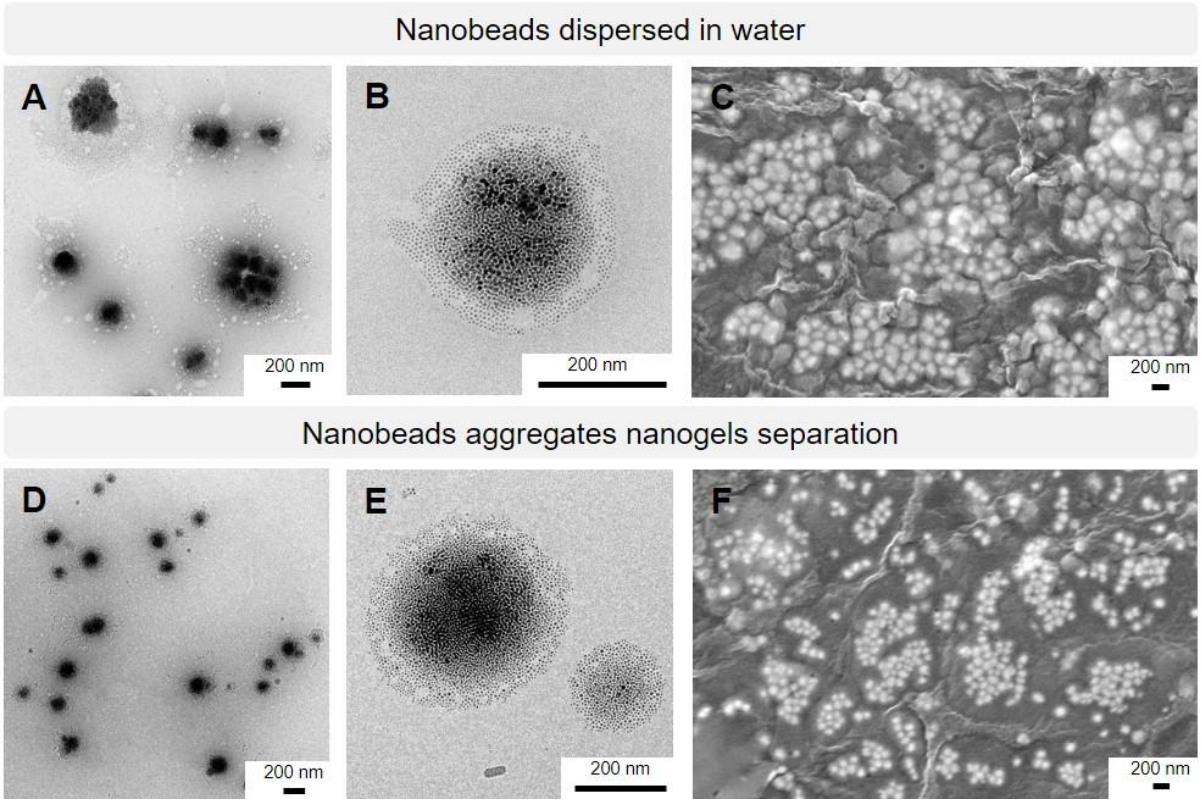

Figure 4.12 *TEM images of magnetic nanobeads at low magnification A) and D), high magnification B) and E) and SEM images C) and F) of magnetic nanobeads after re-dispersion in water (A-C) and after magnetic separation from big agglomerates (D-F), after 30 min in contact with a magnet.*

The size of NPs presented in Figure 4.12 D-F were also analysed by DLS in water showing the diameter of around 200 nm (Figure 4.13), which is in agreement with TEM images.

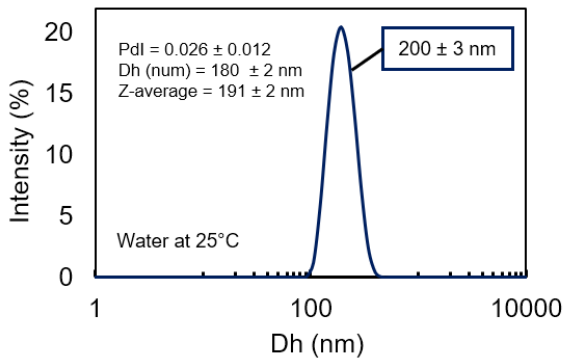

Figure 4.13 *DLS size distributions of nanobeads in water after magnetic separation from big agglomerates (25°).*

To confirm the role of HA-g-copolymer in the formation of well-dispersed magnetic nanobeads, the control experiments were performed. The formation of different structures was observed when clusters were: i) without polysaccharide coating, ii) mixed with hyaluronic acid without grafted copolymer, and iii) mixed with pure poly(DEGMA-co-BMA). The IONPs dispersed in THF and sonicated with ACN without further HA-g-copolymer coating are shown in Figure 4.14-A-B. Upon drying, they were dispersed on carbon-coated copper grid by uncontrollable manner, regardless of whether made with 200 µL or 800 µL of ACN. The coating of clusters with unmodified HA (without grafted copolymer) resulted in a mixture of individual nanoparticles and clusters dispersed in a polymer (Figure 4.14-C), while addition of aqueous solution of pure copolymer (poly(DEGMA-co-BMA) resulted in the precipitation (like a glue) of IONPs in the copolymer matrix after heating (data not shown). To prepare the latter, the copolymer was first dissolved in water at 4°C and then, after addition to the clusters suspension under agitation, heated up to 40°C.

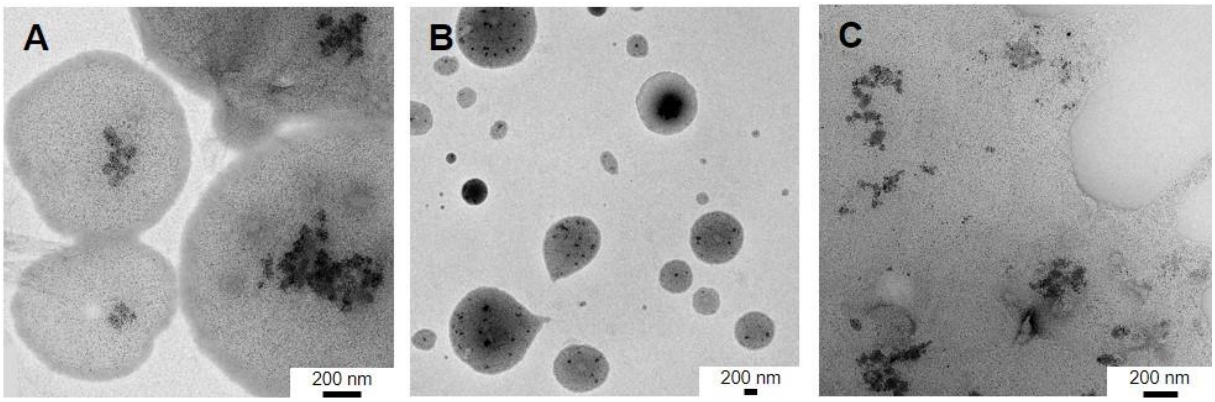

Figure 4.14 TEM images of IONPs clusters obtained from 200 µL of IONPS (1g /L) in THF destabilized by 200 µL (A), and 800 µL (B) of ACN, and clusters obtained by destabilization with 200 µL of ACN and mixed with HA-pentenoate solution (0.5 g/L).

In all three cases, we did not obtain nanobeads, we observed the precipitation and dispersion of particles in the polymer matrix. Thus, the coating with HA grafted with hydrophobic copolymer was necessary to stabilize the compact structure of magnetic cluster. The hydrophilic nature of HA allows dispersion in aqueous solutions, while grafted copolymer helps the deposition of this amphiphilic HA on the hydrophobic cluster.

Cross-linking

Although in the first experiments, we performed cross-linking (described above), we also tested the fabrication of magnetic nanobeads without cross-linking step. The cross-linking step required magnetic agitation for homogenous UV irradiation of nanobeads which risked in the attraction of magnetic structures to the magnetic stirrer and sample loss. Figure 4.15 presents TEM images of cross-linked and un cross-linked nanobeads after purification with magnet. While the cross-linking improved the stability of hybrid nanogels obtained by *in situ* encapsulation, in this case, the crosslinked and un-crosslinked nanobeads showed similar morphology and stability in aqueous solution even after 1 month of storage in H_2O (checked by DLS). Our hypothesis is that grafted HA-copolymer strongly interacts with hydrophobic clusters resulting in stable coating without cross-linking.

In addition, the size distribution of un-crosslinked and crosslinked nanobeads obtained at volume THF/ACN ratio of 1/1 (200 µL / 200 µL) was analyzed by DLS in water and PBS, at 25°C (Table 4.2) In PBS, similar sizes ~214 nm and 235 nm for crosslinked and un-crosslinked nanobeads were observed, while in H_2O the diameter increased to ~280-290 nm for both cases, the swelling property of nanogels is affecting by the concentration of salt. The negative charge on HA surface helps in electrostatic repulsion and prevents aggregation. Thus, the addition of salt results in ionic shielding and a deswelling is observed.

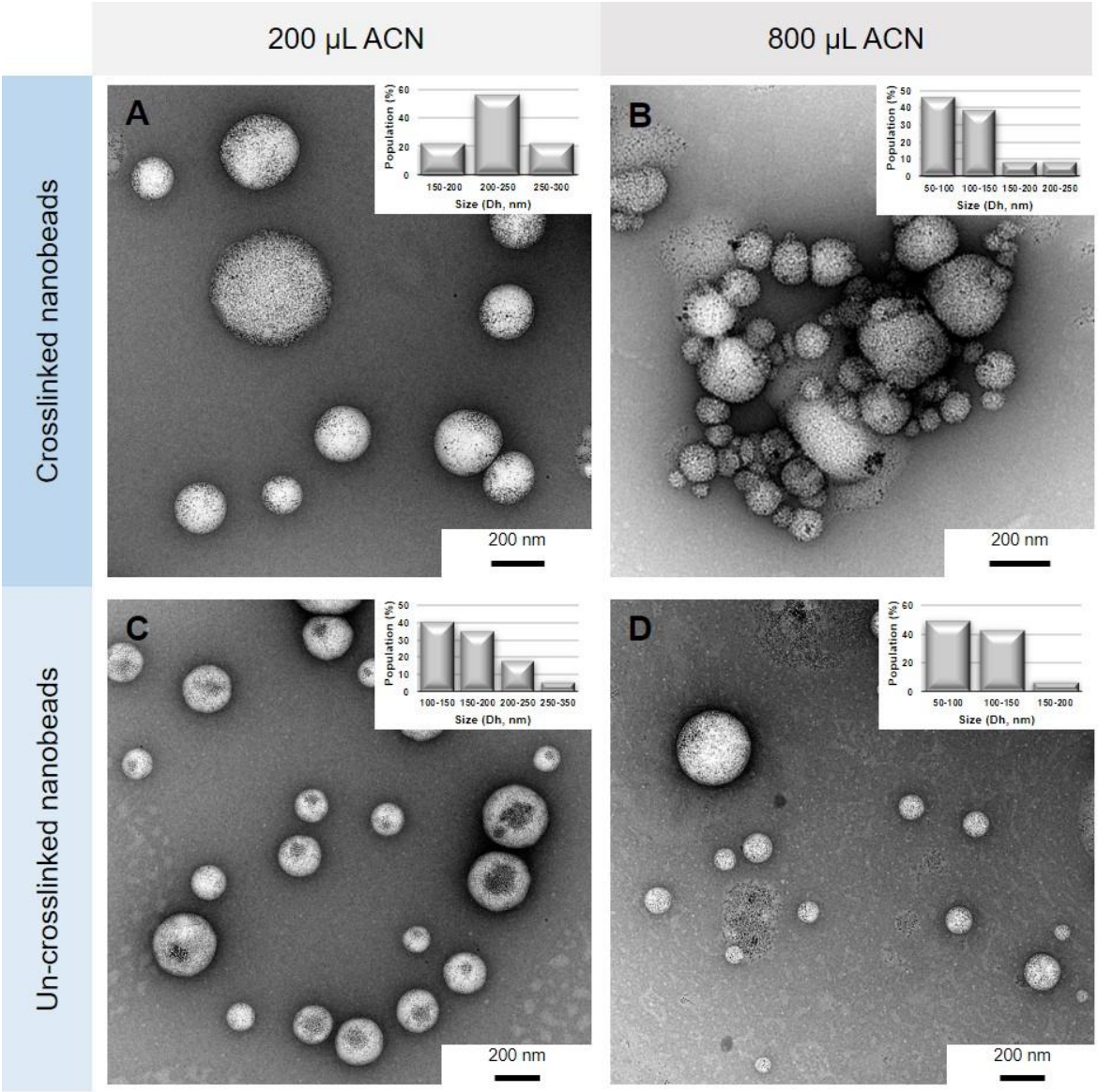

Figure 4.15 *TEM images of negatively stained crosslinked HA-g-copolymer coated SPION clusters made with THF/ACN ratio of A) 200 µL / 200 µL and TEM images of un-crosslinked HA-g-copolymer coated SPIONs clusters made with THF/ACN ratio of C) 200 µL / 200 µL and D) 200 µL / 800 µL HA-g-copolymer.*

Table 4.2 *Size distribution of un-crosslinked and crosslinked nanobeads in suspension made from THF/ACN ratio 1:1. Dynamic light scattering (DLS) analysis of nanobeads in water and PBS media was performed at 25°C.*

	D_h (nm)	
Media	**H_20**	**PBS**
Un-crosslinked	280 ± 1.4	235 ± 3.0
Crosslinked	293 ± 5.0	214 ± 2.0

Destabilizing solvent

We tested water and ACN as destabilizing polar solvents for the formation of the magnetic clusters. After slow addition (250 µL/min) of water (200 µL) to the IONPs in THF (200 µL) under sonication we observed precipitation. Contrary, when the same amount of ACN was added to the nanoparticles in THF, we observed slightly cloudy solution without precipitation. Two different quantities of ACN were added (200 µL and 800 µL) to the 200 µL of IONPs in THF (1 mg/mL) resulting in volume ratio THF/ACN of 1:1 and 1:4, respectively. After ultrasonication, addition of HA derivative and purification step, the image of un-crosslinked and crosslinked nanobeads obtain for two different ratios are presented in Figure 4.15. As a control, the clusters of IONPs without coating are shown in Figure 4.14-A-B.

At THF/ACN 1:4, we obtained higher variation of diameter from 50 to 250 nm, with higher number of small nanobeads with a size below 100 nm, while at 1:1 ratio, we formed more homogenous structures in the range of 200-250 nm for crosslinked and 100-200 nm for un-crosslinked nanobeads. The presence of smaller nanobeads in the sample prepared at THF/ACN 1:4 can be explained by dominant attractive forces due to hydrophobic interactions between IONPs. With the progressive addition of a polar solvent such as ACN into IONPs solutions in THF, NPs attract each other and compress to expel solvent molecules and minimized free energy of the surface [67]. Thus, the droplets could be made smaller during sonication. However, this step of ACN addition and later sonication to evaporate THF is very delicate. Difficulties related to the sonication of very small volume and control of the balance between the maximum of THF evaporation (to obtain small nanoclusters) and avoiding the precipitation (we observed that the complete THF evaporation led to sudden precipitation of clusters) resulted in slightly heterogeneous nanobeads. Chen at al. also demonstrated the incorporation of IONPs nanoparticles in polymer nanogel using ultrasonication [12]. The PNIPAM-co-AA was dissolved in water and mixed with IONPs dispersed in isomeropyl myristate as an oily phase. The authors explain that ultrasonication might trigger the dehydration of the nanogels and induce transformation into the small nanostructure enclosing inorganic nanoparticles or hydrophobic drug. The formation of nanoclusters was reported also by Biggal at al. [66,67]. Here, the authors used THF/CAN ratio v/v 1:4 and coated the formed clusters with synthetic alkyl polymaleic anhydride.

Different structures of magnetic nanobeads

From TEM images of magnetic nanobeads, we observed that two types of structures were formed: core/shell hybrid nanobeads and structures with IONPs homogeneously dispersed in the polymer matrix.

The core/shell nanobeads composed of IONPs nanoclusters surrounded by the polymer shell were found when the IONPs in THF/ACN mixture were sonicated at 65°C for 30 min to evaporate nonpolar solvent. The removal of THF induced a clustering of inorganic nanoparticles. Figure 4.16-A-B, E shows the TEM images of the resulting nanobeads (after polymer deposition and cross-linking) with a spherical morphology, dark contrasted iron oxide nanocrystals in the core and light-contrasted layer of polymer as the shell. The core/shell structure was also confirmed by cryo-TEM (Figure 4.16-C) and SEM (Figure 4.16-D). Meanwhile, some individual nanocrystals of IONPs could be also found in the polymer shell (Figure 4.16-B). As the HA-g-copolymer is insoluble in ACN, after addition of HA derivative in water to the suspension of nanoclusters in ACN, we forced the amphiphilic polymer to assemble on the hydrophobic cluster. The presence of individual nanocrystals in a polymer shell may be explained by the interactions between the hydrophobic copolymer present on HA and non-clustered NPs present in the suspension, or by diffusion from the cluster surface in to the polymer shell forming complexed gel network. Apart from individual nanoclusters coated with a polymer shell, we also observed the simultaneous coating of higher number of clusters leading usually to the bigger nanobeads (Figure 4.16-E). However, they could be easily removed from the nanobead suspension using a permanent magnet, as described earlier. Furthermore, we found that clustering of the IONPs could also induce the formation of colloidal ordered assemblies, the structures in which the inorganic nanoparticles are organized (Figure 4.16-B-C, E), similarly as Bigall et al. [66-67]. When the sonication of IONPs in THF/ACN mixture was stopped after 10min at RT (without THF evaporation), we obtained the nanobeads with homogeneously dispersed IONPs in polymer matrix (Figure 4.16-F), The hydrophobic nanocrystals likely interact with hydrophobic chains on HA and form a complex polymer network.

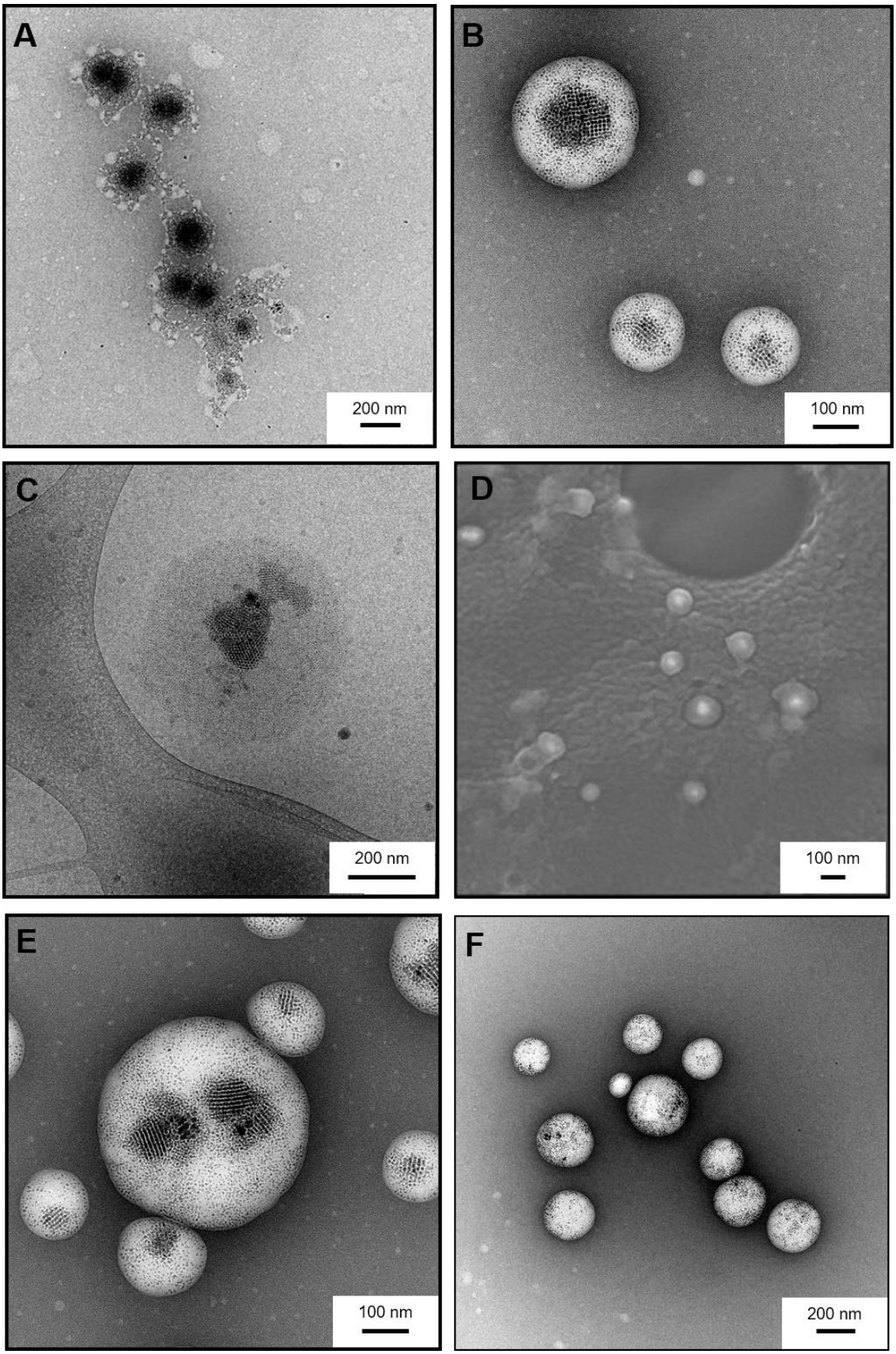

Figure 4.16 *TEM (A-B and E-F - negative staining), cryo-TEM (C) and SEM (D) images of core/shell (A-E) cross-linked nanogels and nanogels with dispersed IONPs (F).*

Quantitative analysis of encapsulated magnetic NPs

To give insight into the quantity of inorganic magnetic nanoparticles in nanogels and core/shell nanobeads, thermogravimetric (TGA) measurements were performed.

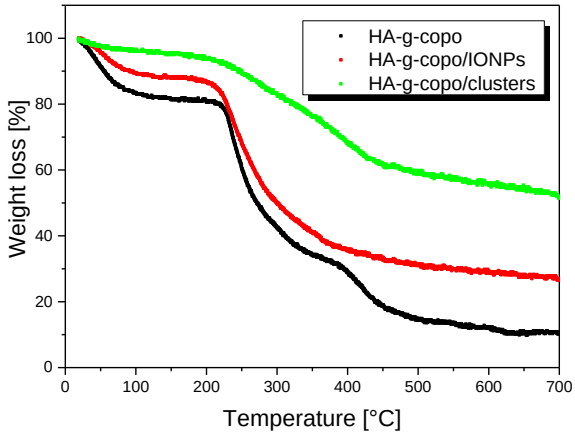

Figure 4.17 *TGA curves of pure HA-g-poly(DEGMA-co-BMA) indicated as HA-g-copo curve (black), HA-g-poly(DEGMA-co-BMA) nanogels with incorporated IONPs as HA-g-copo/IONPs curve (red) and HA-g-poly(DEGMA-co-BMA) coated nanoclusters of IONPs as HA-g-copo/clusters (green) line, under* N_2 *atmosphere, all samples were freeze dried before analysis.*

The curve of pure HA-g-copo exhibits three weight losses from 40 to 700°C to attain total weight loss of 90 %. The first loss occurs in the 40-120 °C temperature range from water evaporation. Similar losses were observed for nanogels and coated clusters. Next weight losses observed for HA-copo sample were recorded at approximately 220-400°C, attributed to the decomposition of HA, followed by next weight loss at 400 °C due to the DEGMA-co-BMA copolymer grafted on HA chains. Heating to 700°C resulted in a final weight of 10% residual weight. Similar steps of weight loss for the HA/PEO were observed [69], with confirmation of the resistivity of this polymer for complete decomposition of HA [70]. The weight losses which begins at 200°C for both HA-g-(DEGMA-co-BMA)/IONPs nanogels and HA-g-(DEGMA-co-BMA) coated magnetic clusters can be related to the decomposition of HA-g-copolymer as well as oleic acid present on the surface of IONPs. At 450°C the sample weight begins to stabilize. From the weight residues at 700°C, quantity of magnetic nanoparticles in these two different hybrids nanocomposites can be calculated. The percentage of magnetic nanoparticles in hybrid samples was calculated after normalization of samples weights at 200°C (after water evaporation) (Figure SI.4.2) and subtraction of the residue of non-decomposed polysaccharide at 700°C. Finally, we could conclude that the percentage of magnetic material, thus the content of IONPs in the nanogels prepared by *in-situ* encapsulation is equal to 18%, while in the case of HA coated nanoclusters 44%. Thus, we confirm that using clustering of IONPs followed by

coating with HA-g-copolymer we could increase the amount of magnetic nanoparticles in the polymer nanobeads.

III.2.2 Magnetic attraction

To demonstrate the possibility of guiding/trapping the magnetic nanogels using external magnetic field, we used a flat thermomagnetically micro-patterned hard magnetic film with an Mr (remanent magnetization) of 1.2 T and magnetic field gradients up to 10^6 T/m [71]. First, the nanogels were loaded with IONPs together and di-strylbenzene derivative (DSB). DSB is a hydrophobic fluorescent dye used as a model of drug as described earlier [72-73]. This fluorescent molecule is soluble in apolar solvents and precipitating in aqueous solutions. The loading was achieved by adding concentrated solution of DSB (0.5 mg/mL) in THF to a solution of dispersed IONPs in THF. Then, ACN was added under sonication to have THF/ACN ratio v/v: 1/1. After cooling to 4°C, an aqueous solution of HA-copolymer was added to the mixture. The low temperature ensured the solubility of thermoresponsive HA-g-copolymer and good dispersion in the mixture followed by a slow heating up to RT resulting in assembly of polymer on hydrophobic core. The prepared fluorescent magnetic nanobeads were placed close to a permanent magnet for 4 h for purification, and next for 30 min to remove agglomerates. The fluorescence microscopy images show a size of 250 nm (DLS) when 25 µg of DSB (Figure 4.18-A) was used for encapsulation and larger nanobeads when higher amount of DSB was used (Figure 4.18-B).

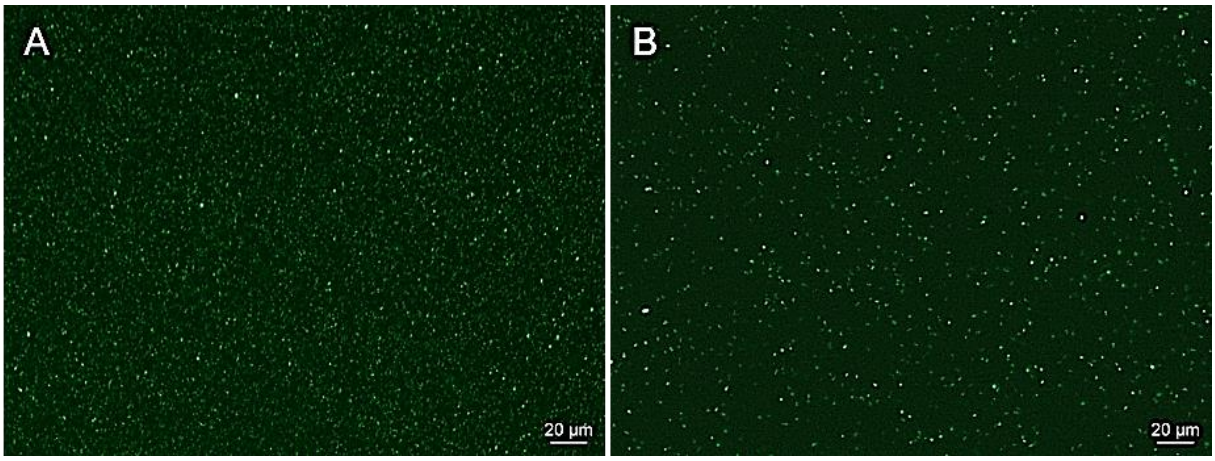

Figure 4.18 *Representative fluorescence microscopy images of nanogels re-suspended in water filled with 25 µg (A) and 50 µg (B) of DSB.*

To observe the response of nanogels to the magnetic field pattern produced by micro-magnet arrays the suspension of fluorescent magnetic nanogels was dropped onto the thermomagnetically patterned film and images were taken with an interval of 2 frames/s. Figure 4.19 presents the images within 30 s of interaction with magnetic arrays with square and line patterns. Nanobeads initially dispersed in the solution are positioned on the tops of the micromagnets, creating patterns that reflects the geometry of the underlying magnetic structure. The particles dispersed in the solution move towards the highest magnetic field gradients which are located at the interfaces between the magnetic zones with a positive and negative stray field. In the case of magnetic stripes, the particle will eventually agglomerate between the stripes and fluorescent lines are observed. In the case of magnetic chessboards, the particles will agglomerate between the squares and some fluorescent lines will appear. After 30 s, the fluorescence intensity of magnetic pattern is practically stable indicating that all magnetic nanogels are attracted. A few nanogels observed in the space between the micromagnets is related to the fact that the surface of micro-patterned hard magnetic films is not perfectly homogenous and shows some defects leading to the presence of local variation of the magnetic field gradient peaks.

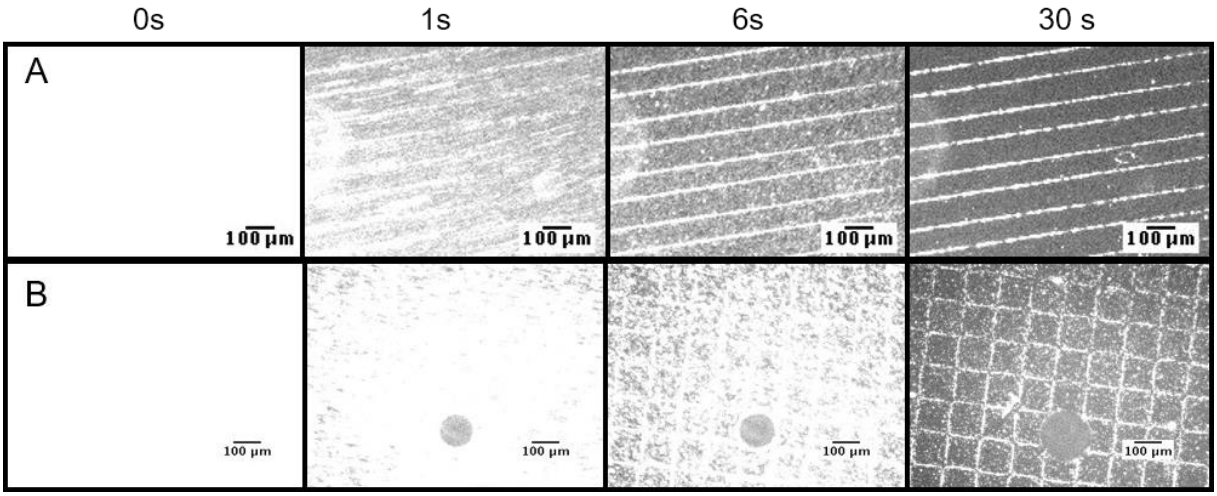

Figure 4.19 *Fluorescence images of the nanobeads trapped by micro-magnets after 0, 1, 6, and 30s. The magnetic lines (A) represents attracted nanobeads with 25 µg of DSB, while squares (B) represents attracted nanobeads with 50 µg of DSB used for encapsulation.*

The ordered position of the nanobeads under magnetic field proved the magnetic nature of our nanobeads. The 10 nm superparamagnetic iron oxide nanoparticles concentrated in core/shell structure allow to rapid response (within seconds) to the patterned magnetic field. This simple experiment demonstrates the possibility to accurately position/align nanobeads using arrays of permanent micromagnet. The study of magnetic attraction and controlled positioning can be further enlarged to attraction and guiding the magnetic nanogels towards desired organ in the body using external magnetic field for application such as MRI, hyperthermia treatment or targeted drug release.

Squid magnetic susceptibility measurements confirmed that IONPs preserved the superparamagnetic properties after clustering and HA-copolymer assembly since no hysteresis loop is observed (Figure 4.20). Small coercivity of 25 Oe is close to the resolution measurements. However, the saturation magnetization (Ms) of 6 emu/g at 300 K is low comparing to the Ms of individual NPs. Similar Ms has been also observed for Wang et al [24]. This result could be attributed to two possible reasons. One is that the HA-g-poly(DEGMA-co-BMA) coated nanoclusters of IONPs contain only about 44% of magnetic IONPs which reduces the relative mass ratio of the magnetic component and thus decrease the value of Ms per gram of HA-g-poly(DEGMA-co-BMA) coated nanoclusters of IONPs. Another is that the polymer coating may adversely affect the magnetic property. The surface property changes are known to influence magnetic properties.

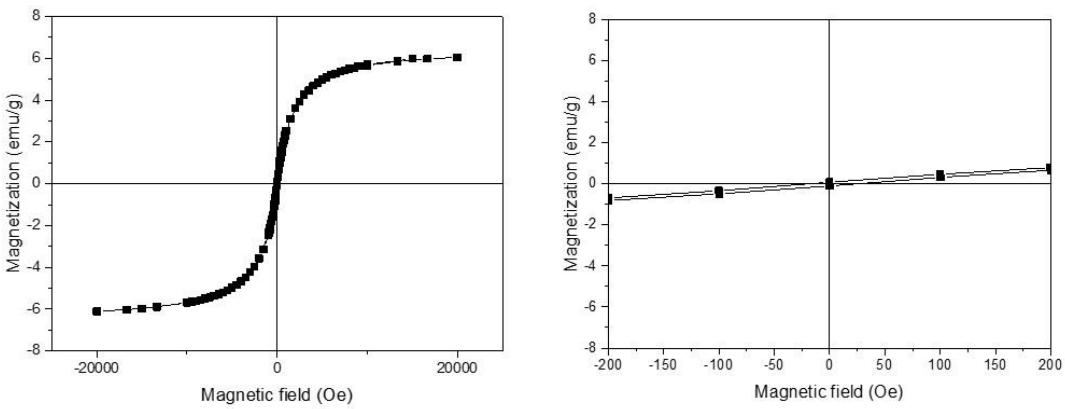

Figure 4.20 *Hysteresis loop and it zoom of self-assembly HA-g-copolymer/IONPs coated clusters at 300K.*

IV Conclusion

In this chapter, we demonstrated the possibility of incorporation of inorganic nanoparticles into the HA based nanogels.

As an example of inorganic NPs, we selected superparamagnetic iron oxide nanoparticles, as they can introduce interesting magnetic properties to HA nanogels. To synthesize the small IONPs (8 nm), thermal decomposition method in an organic solution was used, the NPs were characterized using TEM, DLS, IR, TGA, as well as their superparamagnetic properties were confirmed by SQUID-VSM measurements.

To build-up the hybrid HA nanobeads, two different formulation strategies were studied including *in situ* enclosing within HA nanogels and SPIONs clustering followed by coating with (DEGMA-co-BMA) grafted on HA polysaccharide. In the first case, the IONPs were encapsulated in the hydrophobic domains of the HA-g-copolymer during self-assembly process, while in the second strategy, we first formed magnetic cluster and later coated with amphiphilic HA-g-copolymer. Both strategies resulted in nanoscale beads, easily dispersible in water. The distribution of inorganic particles in polymer matrix differed. Electron microscopy analysis revealed the formation of two different structures: nanogels with individual IONPs dispersed in polymer matrix, and core/shell nanobeads, in first, and second strategy, respectively. Different parameters were varied to increase the efficiency of encapsulation of inorganic nanoparticles.

The TGA comparison of both structures showed the presence of inorganic matter of 18% in nanogels, while the clustering if IONPs allowed to increase the inorganic material in relation to non-magnetic polymer to 40%. The core/shell nanobeads were attracted within seconds to the patterned magnetic films. The SQUID-VSM analysis showed that IONPs maintain the superparamagnetism after incorporation.

The increased content of SPIONs can offer good response to magnetic field used in magnetic guidance to the desired region, can improve the heating power hyperthermia treatment and change the contrast effect in MRI.

V Experimental section

Materials

Hyaluronic acid samples (M_w = 20 kg/mol) were purchased from Lifecore (USA), Iron III acetylacetonate ($Fe(acac)_3$), 1,2-tetradecanediol, oleic acid, oleylamine, 1,4-dithiothreitol (DTT), benzyl ether, chloroform, tetrahydrofuran, phosphate buffer saline (PBS, pH 7.4), tris-(2-carboxyethyl) phosphine hydrochloride (TCEP), were purchased from Sigma-Aldrich-Fluka (France). 2-Hydroxy-1-[4-(2-hydroxy-ethoxy) phenyl]-2-methyl-1-propanone (Irgacure 2959) was kindly provided by Ciba Speciality Chemicals (Basel, Switzerland). Uranyless™ negative stain was purchased from Delta Microscopies. All chemicals, were used without any further purification. The water used in all experiments was purified by a Elga Purelab purification system, with a resistivity of 18.2 MΩ cm.

Synthesis of iron oxide nanoparticles

The reaction of synthesis of iron oxide nanoparticles was performed in a 3-neck flask (100 mL) under the nitrogen atmosphere to minimized oxidation of magnetite (Fe_3O_4) to maghemite (γ-Fe_2O_3). All the reactants were used in the synthesis without further purification as follows: Iron III acetylacetonate ($Fe(acac)_3$) (2 mmol, M_w = 353,17 g/mol, m = 709 mg), 1,2-tetradecanediol (10 mmol, M_w = 230.39 g/mol, m = 2,56g), oleic acid (6 mmol, M_w = 282.46, v=1.90 mL) and oleylamine (6 mmol, M_w = 267.49 g/mol, v = 1.97 mL) and benzyl ether (10 mL) were mixed and degassed at room temperature for 30 min under a constant flow of N_2 and vigorous stirring. After that, the flask was sealed and the solution was first heated up at 3°C/min and kept at 200°C for 2 h. After the addition of a reflux column, a second heating rate follow of 4.5°C/min to reach the reflux temperature (300°C) and kept at this temperature for 1 h. The resultant black-colored mixture was cooled to room temperature by removing the heat source. Ethanol (about 10 mL, 3 times) was added to the mixture, to precipitate the particles an separate *via* permanent magnet.

Synthesis of HA-g-copolymer/IONPs nanogels

HAp-g-poly(DEGMA-co-BMA) (with $DS_{copolymer}$ 0.02, $DS_{pentanoate}$ 0.48) was dissolved at in 2mL of PBS (pH 7.4) at 4°C to obtain concentration 0.5 g/L. The IONPs in chloroform (16 g/L) were added drop by drop to the HAp-g-poly(DEGMA-co-BMA) solution at RT under vortex. After complete addition the flask was put in a water bath, the temperature was increased up to 40°C and the solution was bubbled under nitrogen for 15 min without stirring.

Synthesis of core/shell nanobeads

Oleic acid coated IONPs were dissolved in 200 µL of tetrahydrofuran (1 mg/mL). 200 or 800 µL destabilizing solvent (ACN) was added to the suspension at a rate of 250 µL/min and sonicated for 30 min at 65°C. Then the nanoclusters suspension was place in an ice bath at 4°C. 1 mL of cold aqueous solution of HA-g- poly(DEGMA-co-BMA) (0.5 g/L) was slowly added to the nanoclusters in ACN and agitated for 15 min at 40°C. The nanobeads were crosslinked according the same procedure as magnetic nanogels and purified using permanent magnet.

Cross-linking HA-g-copolymer/IONPs nanogels

Next, a solution of DTT in PBS (2.5 g/L) was added to nanogels in order to reach the ratio [SH]/[=] : 1/1 followed by 5 min of vortexing. The flask was kept for 30 min at 40°C without stirrer under N_2. Finally, 200 µL of an aqueous solution of Irgacure 2959 (10 mg/mL) was added to the nanogels suspension to obtain a final photoiniator concentration of 10% (w/v). The mixture was exposed to UV light (λ = 365 nm) with an intensity of 20 mW/cm^2 for 15 min under stirring and nitrogen atmosphere at 40°C. The nanogels suspension was transferred into a dialysis bag (MWCO = 6-8 kg/mol), dialyzed against milli-Q water or purified by magnet separation and recovered by freeze-drying.

Magnet separation

Nanobeads were separated from the solvent and residues using permanent NdFeB(0.3T) magnet. Nanobeads could be easily re-dispersed in Milli-Q water. Finally, a second purification step through an external magnetic field for 30 min is applied to separate aggregates from homogenous dispersed nanobeads. After this last separation, the supernatant with small nanobeads was kept for further characterization and the pellet was removed.

TEM, cryo-TEM and, electron diffraction characterization

200-mesh TEM grids coated with a thin film of amorphous carbon were submitted to a glow discharge treatment (Pelco easiGlow) to make the surface of the carbon film hydrophilic. Droplets (4 µL) of dilute particle suspensions were deposited on the grid and, after a few minutes, the liquid in excess was blotted with filter paper. Prior to complete drying, droplets of Uranyless™ (neutral contrasting agent, Delta Microscopies) were deposited. After a few minutes, the stain in excess was blotted out and the remaining liquid film allowed to dry. Images of the specimens were recorded with a TVIPS TemCam F216 digital camera, using a Philips CM200 (FEI) microscope operating at 200 kV. Unstained specimens of pure magnetite

nanoparticles were prepared as well by air-drying of dilutes suspensions on the glow-discharged carbon film.

For these specimens, selected-area electron diffraction patterns were recorded on groups of nanoparticles and the diffraction rings were calibrated using those from gold particles. The particle size was measured from the TEM images using the ImageJ software. Statistical size distribution result evaluated from approximatively 200 particles.

For cryo-TEM imaging, thin liquid films of the suspensions were formed on NetMesh lacy carbon films (Pelco) and quench-frozen in liquid ethane using a Leica EM-GP workstation. The specimens were mounted on a precooled Gatan 626 specimen holder, transferred in the microscope and observed at low temperature (-176°C). All specimens were observed with Philips CM200 'Cryo' (FEI) microscope operating at 200 kV. Images were recorded with a TVIPS TemCam F216 digital camera (2040 × 2040 pixels).

SEM characterization

Drops of un-crosslinked and crosslinked nanogels solutions (0.5 mg/mL) in ultrapure water at both 5 and 40°C were deposited onto mica-coated copper stubs (also precooled/heated at 5 or 40°C, respectively) and allowed to air drying at 4 or 40°C. The samples were then coated by approximately 2 nm of sputtered Au-Pd and observed in secondary electron imaging mode with a ZEISS Ultra 55 FEG-SEM (Grenoble INP - CMTC). Images were acquired at low voltage of 3 kV using an in-lens detector.

Optical and fluorescence imaging

The observations of fluorescent samples were performed using an inverted Axio Vert A1 microscope (Zeiss) driven by Zen software.

DLS characterization

The size distribution and the polydispersity in solution was assessed using a Zetasizer NanoZS Malvern Instruments apparatus equipped with a HeNe laser at 173° and a temperature controller.

FTIR characterization

Fourier transform infrared spectroscopy (FTIR) measurements were done on a RX1 spectrometer (Perkin Elmer, UK) with horizontal ATR accessory. For each sample, 32 scans were recorded between 4000 and 400 cm-1 with a resolution of 2 cm-1 using the Spectrum Software V 5.0.0.

Thermogravimetric Analysis (TGA)

The mass of iron oxide nanoparticles content encapsulated inside HA-g-polymer structures was determinate by thermogravimetric analysis using a TGA 92, Setaram Instruments. The samples were analyzed under nitrogen (1 bar) and at a heating rate of 5°C/min from room temperature (25 °C) to 800 °C.

SQUID-VSM

The magnetic properties of the sample were evaluated using superconducting quantum interference device (SQUID) VSM Quantum Design. The individual IONPs were dispersed in PDMS, while the magnetic nanogels were freeze dried and placed in the holder. Magnetization loops were measured at 5 K and at 300K and the results were corrected by subtracting the diamagnetic contribution of holders. The saturation magnetization at the maximum field was normalized to the gram of IONPs. Temperature dependent zero-field cooling and field cooling magnetization measurements were performed by cooling the sample to 5 K under a zero or a 100 Oe magnetic field, respectively. Then, the magnetization was measured while the samples were heated to 300K under a 100 Oe field.

Loading of DSB into magnetic nanogels

25 and 50 µL of a DSB dissolved in THF (0.5 mg/mL) were added to a 200 µL of IONPs in THF (1 mg/mL), giving solution A and B, respectively. The mixtures were sonicated for 30 min. 225 and 250 µL of ACN was added to sample (A) and sample (B), respectively. Finally, the samples were cooled in an ice glace before adding 1 mL of HA-g-poly(DEGMA-co-BMA) in H_2O (0.5 mg/mL). After 30 min of agitation the samples were placed close to permanent magnet to purify and collect nanogels loaded with magnetic nanoparticles and DSB. After 6h of separation the supernatant with unloaded DSB was removed and replaced with 1mL of water. This step was repeated twice to remove unloaded DSB.

Micro-patterned hard magnetic films

The 5 µm thick hard-magnetic neodymium iron boron (NdFeB) films deposited on 100 mm Si wafers were first magnetised out of plane in 8 T and than partially irradiated with a KrF (248 nm) pulsed excimer laser during 20 ns [74]. During irradiation, a chessboard mask consisting of pattern with individual features of size 100 × 100 μm^2 or a stripe mask consisting of patterns with individual feature sizes of 3 mm × 100 µm was placed in front of the film and an external magnetic field was applied opposite to the initial magnetization direction. As a result, the magnetic regions not masked were heated up by the laser and the magnetization direction was reversed. The resultant structure consists of either an chessboard type or a stripe

type array of oppositely magnetized micro-magnets. A drop of 20 µL of nanogel solution was dropped onto glass coverslip and flattened with micro-patterned magnetic surface. The precise patterns were imaged using inverted fluorescence optical microscopy (Olympus CKX41).

VI Supplementary information

VI.1 OA-IONP crystal structure and morphology of magnetite nanocrystals

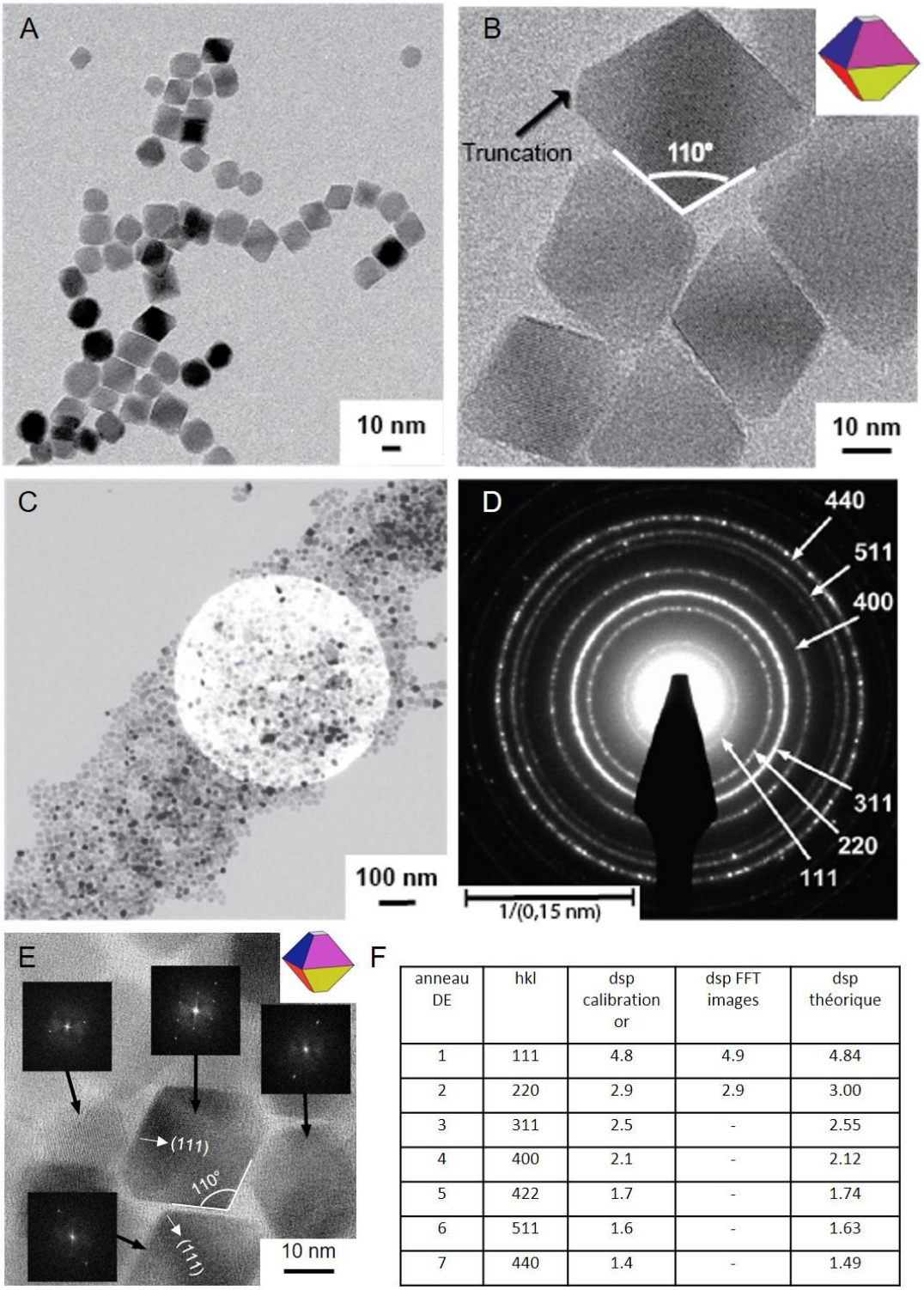

anneau DE	hkl	dsp calibration or	dsp FFT images	dsp théorique
1	111	4.8	4.9	4.84
2	220	2.9	2.9	3.00
3	311	2.5	-	2.55
4	400	2.1	-	2.12
5	422	1.7	-	1.74
6	511	1.6	-	1.63
7	440	1.4	-	1.49

Figure SI.4.1 *A-C) TEM images of oleic acid-coated IONPs at different magnifications; D) Electron diffraction pattern recorded form the area selected in C and indexation of diffraction rings. E) high resolution lattice images of selected particles with calculated power spectra. F) Summary of the lattice spacings in relation i^{th} electron diffraction rings.*

In Figure SI.4.1-A. the IONP sample with a size around 16 nm contains truncated octahedral NCs. In Figure SI.4.1-B, we can see the facets of each nanocrystal and from this image it is possible to measure, in projection, the angle between facets and deduce the lattice plane and the corresponding type of crystallographic plane (Figure SI.4.1-E) which were summarized in Figure SI.4.1-F. This analysis revealed an angle of 110° associated with {111} planes which typically characterize an octahedral structure (eight {111} planes). Yang et al. explained this phenomenon: the crystal shape is determined by the ratio (R) of growth rate in [100] direction to that of [111] direction. Thus, a faster growth along the [100] direction promotes the formation of octahedral nanoparticles, while a faster growth along a [111] direction generates cubic particles. [75] It is worth noting that the octahedral also called "spherical like" shaped octahedron Fe3O4 nanocrystals is the most frequently reported shape. [76] The electron diffraction pattern in Figure SI.4.1-D from a group of randomly oriented IONP particles shown in Figure SI.4.1-C revealed a clear set of diffraction rings, indicating the highly crystalline nature of the 16-nm iron oxide nanocrystals and was in good agreement with those from standard magnetite. [77] This observation should however be nuanced as the control of the degree of oxidation of iron during the synthesis by thermal decomposition is difficult. The high resolution TEM images (Figure SI.4.1-E) shows the lattice fringes corresponding to different crystallographic planes in few particles. Figure SI.4.1-F presents a Table summarizing the indexing of the diffraction rings and lattice planes, in comparison with the theoretical values calculated from the magnetite unit cell.

VI.2 Quantity of encapsulated magnetic nanoparticles

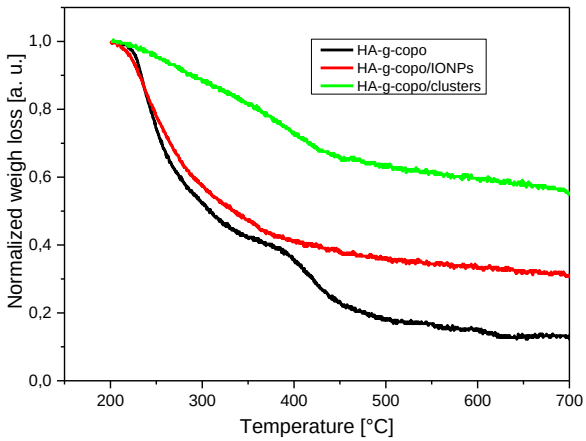

Figure SI.4.2 *TGA curves of pure HA-g-poly(DEGMA-co-BMA) indicated as HA-g-copo curve (black), HA-g-poly(DEGMA-co-BMA) nanogels with incorporated IONPs as HA-g-copo/IONPs curve (red) and HA-g-poly(DEGMA-co-BMA) coated nanoclusters of IONPs as HA-g-copo/clusters (green) line, under N_2 atmosphere, all samples were freeze dried before analysis, with respect to normalized weight vs. temperature.*

VII References

1. Lammers, T.; Aime, S.; Hennink, W.E.; Storm, G.; & Kiessling, F. Theranostic nanomedicine. *Accounts of Chemical Research*, **2011**, 44, 1029-1038.
2. Fan, Z.; Fu, P.P.; Yu, H.; & Ray, P.C. Theranostic nanomedicine for cancer detection and treatment. *Journal of Food and Drug Analysis*, **2014**, 22, 3-17.
3. Kunjachan, S.; Ehling, J.; Storm, G.; Kiessling, F.; & Lammers, T. Noninvasive imaging of nanomedicines and nanotheranostics: principles, progress, and prospects. *Chemical Reviews*, **2015**, 115, 10907-10937.
4. Anselmo, A.C.; & Mitragotri, S. A review of clinical translation of inorganic nanoparticles. *The AAPS Journal*, **2015**, 17, 1041-1054.
5. Hola, K.; Markova, Z.; Zoppellaro, G.; Tucek, J.; & Zboril, R. Tailored functionalization of iron oxide nanoparticles for MRI, drug delivery, magnetic separation and immobilization of biosubstances. *Biotechnology Advances*, **2015**, 33, 1162-1176.
6. Mahmoudi, M.; Sant, S.; Wang, B.; Laurent, S.; & Sen, T.; Superparamagnetic iron oxide nanoparticles (SPIONs): Development, surface modification and application in chemotherapy. Advanced Drug Delivery Reviews, **2011**, 24-46.
7. Wilczewska, A.Z.; Niemirowicz, K.; Markiewicz, K.H.; & Car, H. Nanoparticles as drug delivery systems. *Pharmacology Reports*, **2012**, 64, 1020-1037.
8. Cheng, Z.; Liu, S.; Gao, H.; Tremel, W.; Ding, N.; Liu, R.; Beines, P. W.; Knoll, W. A facile approach for transferring hydrophobic magnetic nanoparticles into water-soluble particles. *Macromolecular Chemistry and Physics*, **2008**, 209, 1145-1151.
9. Glover, A.L.; Bennett, J.B.; Pritchett, J.S.; Nikles, S.M.; Nikles, D.E.; Nikles, J.A.; & Brazel. C.S. Magnetic heating of iron oxide nanoparticles and magnetic micelles for cancer therapy. *IEEE Transactions on Magnetics*, **2013**, 49, 231-235.
10. Cheng, Z.; Liu, S.; Gao, H.; Tremel, W.; Ding, N.; Liu, R.; Beines, P.W.; & Knoll, W. A facile approach for transferring hydrophobic magnetic nanoparticles into water-soluble particles. *Macromolecular Chemistry and Physics*, **2008**, 209, 1145-1151.
11. Deka, S.R.; Quarta, A.; Di Corato, R.; Riedinger, A.; Cingolani, R.; & Pellegrino, T. Magnetic nanobeads decorated by thermo-responsive PNIPAM shell as medical platforms for the efficient delivery of doxorubicin to tumour cells. *Nanoscale*, **2011**, 3, 619-629.
12. Chen, H.; Zhu, H.; Zhao, Y.; Wang, Q.; Wan, J.; Yang, Y.; Xu, H.; & Yang, X. Highly compressed assembly of deformable nanogels into nanoscale suprastructures and their application in nanomedicine. *ACS NANO*, **2011**, 5, 2671-2680.
13. Singh, V.; Zhu, J.; Nand, A.; Cheng, Z.; & Mo, Y. Retracted article: 3D small molecule microarray with enhanced sensitivity and immobilization capacity monitored by surface plasmon resonance imaging. *RSC Advances*, **2014**, 6, 115345-115345.

14. Paquet, C.; De Haan, H.W.; Leek, D.M.; Lin, H.Y.; Xiang, Bo.; Tian, G.; Kell, A.; & Simard, B. Clusters of superparamagnetic iron oxide nanoparticles encapsulated in a hydrogel: a particle architecture generating a synergistic enhancement of the T_2 relaxation. *ACS NANO*, **2011**, 5, 3104-3112.
15. Cazares-Cortes, E.; Espinosa, A.; Guigner, J.M.; Michel, A.; Griffete, N.; Wilhelm, C.; & Ménager, C. Doxorubicin intracellular remote release from biocompatible oligo(ethylene glycol) methyl ether methacrylate-based magnetic nanogels triggered by magnetic hyperthermia. *ACS Applied Materials & Interfaces*, **2017**, 9, 25775-25788.
16. Ma, H.L.; Qi, X.R.; Maitani, Y.; & Nagai, T. Preparation and characterization of superparamagnetic iron oxide nanoparticles stabilized by alginate. *International Journal of Pharmaceutics*, **2007**, 333, 177-186.
17. Zhu, L.; Ma, J.; Jia, N.; Zhao, Y.; & Shen, H. Chitosan-coated magnetic nanoparticles as carriers of 5-fluorouracil: preparation, characterization and cytotoxicity studies. *Colloids and Surfaces B*, **2009**, 68, 1-6.
18. Key, J.; Dhawan, D.; Cooper, C.L.; Knapp, D. W.; Kim, K.; Kwon, I.C.; Choi, K.; Park, K.; Decuzzi, P.; & Leary, J.F. Multicomponent, peptide-targeted glycol chitosan nanoparticles containing ferrimagnetic iron oxide nanocubes for bladder cancer multimodal imaging. *International Journal of Nanomedicine*, **2016**, 11, 4141-4155.
19. Hong, R.Y.; Li, J.H.; Qu, J.M.; Chen, L.L.; & Li, H.Z. Preparation and characterization of magnetite/dextran nanocomposite used as a precursor of magnetic Fluid. *Chemical Engineering Journal*. **2009**, 150, 572−580**.**
20. You, D.G.; Saravanakumar, G.; Son, S.; Han, H.S.; Heo, R.; Kim, K.; Kwon, I.C.; Lee, J.Y.; & Park, J.H. Dextran sulfate-coated superparamagnetic iron oxide nanoparticles as a contrast agent for atherosclerosis imaging. *Carbohydrate Polymers*, **2014**, 101, 1225-1233.
21. Lee, J.H.; Jung, M.J.; Hwang, Y.H.; Lee, Y.J.; Lee, S.; Lee, D.Y.; & Shin, H. Heparin-coated superparamagnetic iron oxide for in vivo MR imaging of human MSCs. *Biomaterials*, **2012**, 33, 4861-4871.
22. Cai, Z.; Zhang, H.; Wei, Y.; & Cong, F. Hyaluronan-inorganic nanohybrid materials for biomedical. *Biomacromolecules*, **2017**, 18, 1677-1696.
23. Swierczewska, M.; Han, H.S.; Kim, K.; Park, J.H.; & Lee, S. Polysaccharide-based nanoparticles for theranostic nanomedicine. *Advanced Drug Delivery Reviews*, **2016**, 99, 70-84.
24. Yang, R.M.; Fu, C.P.; Li, N.N.; Wang, L.; Xu, X.D.; Yang, D.Y.; Fang, J.Z.; Jiang, X.Q.; & Zhang, L.M. Glycosaminoglycan-targeted iron oxide nanoparticles for magnetic resonance imaging of liver carcinoma. *Materials Science & Engineering. C, Materials for Biological Applications*, **2014**, 45, 556-563.

25. Xiong, Z.; Qin, H.; Wan, H.; Huang, G.; Zhang, Z.; Dong, J.; Zhang, L.; Zhang, W.; & Zou, H. Layer-by-Layer assembly of multilayer polysaccharide coated magnetic nanoparticles for the selective enrichment of glycopeptides. *Chemical Communications*, **2013**, 49, 9284-9286.
26. Kamat, M.; El-Boubbou, K.; Zhu, D.C.; Lansdell, T.; Lu, X.; Li, W.; & Huang, X. Hyaluronic acid immobilized magnetic nanoparticles for active targeting and imaging of macrophages. *Bioconjugate Chemistry*, **2010**, 21, 2128-2135.
27. El-Dakdouki, M.H.; Zhu, D.C.; El-Boubbou, K.; Kamat, M.; Chen, J.; Li, W.; & Huang, X. Development of multifunctional hyaluronan-coated nanoparticles for imaging and drug delivery to cancer cells. Biomacromolecules, **2012**, 13, 1144-1151.
28. El-Dakdouki, M.H.; Xia, J.; Zhu, D.C.; Kavunja, H.; Grieshaber, J.; O'Reilly, S.; McCormick, J.J.; & Huang, X. Assessing the *in vivo* efficacy of doxorubicin loaded hyaluronan nanoparticles. *ACS Applied Materials & Interfaces*, **2014**, 6, 697-705.
29. Thomas, R.G.; Moon, M.J.; Lee, H.; Sasikala, A.R.K.; Kim, C.S.; Park, I.K.; & Jeong, Y.Y. Hyaluronic acid conjugated superparamagnetic iron oxide nanoparticle for cancer diagnosis and hyperthermia therapy. *Carbohydrate Polymers*, **2015**, 131, 439-446.
30. Kralj, S.; Potrc, T.; Kocbek, P.; Marchesan, S.; & Makovec, D. Design and fabrication of magnetically responsive nanocarriers for drug delivery. *Current Medicinal Chemistry*, **2017**, 24, 454-469.
31. Bealle, G.; Di Corato, R.; Kolosnjaj-Tabi, J.; Dupuis, V.; Clément, O.; Gazeau, F.; Wilhelm, C.; & Menager, C. Ultra magnetic liposomes for MR imaging, targeting, and hyperthermia. *Langmuir*, **2012**, 28, 11834-11842.
32. Kim, K.S.; Kim, J.; Lee, J.Y.; Matsuda, S.; Hideshima, S.; Mori, Y.; Osaka, T.; & Na, K. Stimuli-responsive magnetic nanoparticles for tumor-targeted bimodal imaging and photodynamic/hyperthermia combination therapy. *Nanoscale*, **2016**, 8 (22), 11625-11634.
33. Šmejkalová, D.; Nešporová, K.; Huerta-Angeles, G.; Syrovátka, J.; Jirák, D.; Gálisová, A.; & Velebný, V. Selective in vitro anticancer effect of superparamagnetic iron oxide nanoparticles loaded in hyaluronan polymeric micelles. *Biomacromolecules*, **2014**, 15, 4012-4020.
34. Lim, E.K.; Kim, H.O.; Jang, E.; Park, J.; Lee, K.; Suh, J.S.; Huh, Y.M.; & Haam, S. Hyaluronan-modified magnetic nanoclusters for detection of CD44-overexpressing breast cancer by MR imaging. *Biomaterials*, **2011**, 32, 7941-7950.
35. Lim, E.K.; & Chung, B.H. Preparation of pyrenyl-based multifunctional nanocomposites for biomedical applications. *Nature Protocols*, **2016**, 11, 236-251.

36. Zhang, Y.; Sun, Y.; Yang, X.; Hilborn, J.; Heerschap, A.; & Ossipov, D.A. Injectable in situ forming hybrid iron oxide-hyaluronic acid hydrogel for magnetic resonance imaging and drug delivery. *Macromolecular Bioscience*, **2014**, 14, 1249-1259.
37. Manju, S.; & Sreenivasan, K. Enhanced drug loading on magnetic nanoparticles by layer-by-layer assembly using drug conjugates: blood compatibility evaluation and targeted drug delivery in cancer cells. *Langmuir*, **2011**, 27, 14489-14496.
38. Lachowicz, D.; Szpa, A.; Malek-Zietek, K.E.; Kepczynski, M.; Muller, R.N.; Laurent, S.; Nowakowska, M.; Zapotoczny, S. Biocompatible and fluorescent superparamagnetic iron oxide nanoparticles with superior magnetic properties coated with charged polysaccharide derivatives. *Colloids surface B: Biointerfaces*, **2017**, 150, 402-407.
39. Babic, M.; Horak, D.; Jendelova, P.; Herynek, V.; Proks, V.; Vanecek, V.; Lesny, P.; & Sykova, E. The use of dopamine-hyaluronate associate-coated maghemite nanoparticles to label cells. *International Journal of Nanomedicine*, **2012**, 1461-1474.
40. Lee, B.Y; Lee, H.; Kim, Y.B.; Kim, J.; Hyeon, T.; Park, H.; Messersmith, P.B.; & Park, T.G. Bioinspired surface immobilization of hyaluronic acid on monodisperse magnetite nanocrystals for targeted cancer imaging. *Advanced Materials*, **2008**, 20, 4154-4157.
41. Kharisov, B.I.; H. Rasika Dias, H.V.; Kharissova, O.V.; Vázquez, A.; Peña, Y.; & Gómez, I. Solubilization, dispersion and stabilization of magnetic nanoparticles in water and non-aqueous solvents: recent trends. *RSC Advances*, **2014**, 4, 45354-45381.
42. Wu, W.; Wu, Z.; Yu, T.; Jiang, C.; & Kim, W.S. Recent progress on magnetic iron oxide nanoparticles: synthesis, surface functional strategies and biomedical applications. *Science and Technology of Advanced Materials*, **2015**, 16, 023501.
43. Sun, S.; Zeng, H.; Robinson, D.B.; Raoux, S.; Rice, P.M.; Wang, S.X.; & Li, G. Monodisperse MFe_2O_4 (M = Fe, Co, Mn) nanoparticles. *Journal of the American Chemical Society*, **2004**,126, 273-279.
44. Palma, S.I.C.J.; Marciello, M.; Carvalho, A.; Veintemillas-Verdaguer, S.; Morales, M.P.; & Roque, A.C.A. Effects of phase transfer ligands on monodisperse iron oxide magnetic nanoparticles. *Journal of Colloid and Interface Science,* **2015**, 437, 147-155.
45. Moya, C.; Batlle, X.; & Labarta, A. The effect of oleic acid on the synthesis of $Fe_{3-x}O_4$ nanoparticles over a wide size range. *Physical Chemistry Chemical Physics,* **2015**, 17, 27373-27379.
46. LaMer V.K.; & Dinegar R.H. Theory, production and mechanism of formation of monodispersed hydrosols. *Journal of the American Chemical Society*, **1950**, 72, 4847-4854.
47. Talapin, D.V.; Rogach, A.L.; Haase, M.; Weller, H. Evolution of an ensemble of nanoparticles in a colloidal solution: theoretical study. *The Journal of Physical Chemistry B*, **2001**, 105, 12278-12285.

48. Harris, R.A.; Shumbula, P.M.; Van der Walt, H. Analysis of the interaction of surfactants oleic acid and oleylamine with iron oxide nanoparticles through molecular mechanics modeling. *Langmuir*, **2015**, 31, 3934-3943.
49. Lassenberger, A., Grünewald, T. A.; Van Oostrum, P.D.J.; Rennhofer, H.; Amenitsch, H.; Zirbs, R.; Lichtenegger, H. C.; & Reimhult, E. Monodisperse iron oxide nanoparticles by thermal decomposition: elucidating particle formation by second-resolved in situ small-angle X-Ray scattering. *Chemistry of Materials*, **2017**, 29, 4511-4522.
50. Zhang L.; Li, Quin.; Liu, S.; Ang, M.; Tade, M. O.; & Gu, H. C. Synthesis of pyramidal, cubical and truncated octahedral magnetite nanocrystals by controlling reaction heating rate. *Advanced Powder Technology*, **2011**, 22, 532-536.
51. Bronstein, L.M.; Huang, X.; Retrum, J.; Schmucker, A.; Pink, M.; Stein, B.D.; & Dragnea, B. Influence of iron oleate complex structure on iron oxide nanoparticle formation. *Chemistry of Materials*,19, **2007**, 3624-3632.
52. Zhang, L.; He, R.; & Gu, H. Oleic acid coating on the monodisperse magnetite nanoparticles. *Applied Surface Science*, **2006**, 253, 2611– 2617.
53. Tartaj, P.; Morales, M.D.; Veintemillas-Verdaguer, S.; Gonzalez-Carre, T.; & Serna, C.J. The preparation of magnetic nanoparticles for applications in biomedicine. *Journal of Physics D Applied Physics*, **2003**, 36, 182–197.
54. Daou, T.J.; Grenèche, J.M.; Pourroy, G.; Buathong, S.; Derory, A.; Ulhaq-Bouillet, C.; Donnio, B.; Guillon, D.; & Begin-Colin, S. Coupling agent effect on magnetic properties of functionalized magnetite-based nanoparticles. *Chemistry of Materials*, **2008**, 20, 5869–5875.
55. Park, J.; An, K.; Hwang, Y.; Park, J.G.; Noh, H.J.; Kim, J.Y.; Park, J.H.; Hwang, N.M.; & Hyeon, T. Ultra-large-scale syntheses of monodisperse nanocrystals. *Nature Materials*, **2004,** 3, 891-895.
56. PAULY, M. (**2010**) Structuration de nanoparticules magnétiques d'oxyde de fer en films et étude de leurs propriétés magnétiques et de magnéto-transport. Thèse de doctorat, université de Strasbourg.
57. Talelli, M.; Rijcken, C.J.F.; Lammers, T.; Seevinck, P.R.; Storm, G.; Van Nostrum, C.F.; & Hennin, W.E. Superparamagnetic iron oxide nanoparticles encapsulated in biodegradable thermosensitive polymeric micelles: toward a targeted nanomedicine suitable for image-guided drug delivery. *Langmuir,* **2009**, 25, 2060-2067.
58. Paquet, C.; Pagé, L.; Kell, A.; & Simard, B. Nanobeads highly loaded with superparamagnetic nanoparticles prepared by emulsification and seeded-emulsion polymerization. *Langmuir*, **2010**, 26, 5388-5396.
59. Paquet, C.; De Haan, H.W.; Leek, M.; Lin, H.U.; Xiang, B.; Tian, G.; Kell, A.; & Simard, B. Clusters of superparamagnetic iron oxide nanoparticles encapsulated in a hydrogel: a

particle architecture generating a synergistic enhancement of the T_2 Relaxation. *ACS Nano*, **2011**, 5, 3104-3112.

60. Isojima, T.; Suh, K.S.; Vander Sande, J.B.; & Alan Hatton, T. Controlled assembly of nanoparticle structures: spherical and toroidal superlattices and nanoparticle-coated polymeric Beads. *Langmuir*, **2009**, 25, 8292-8298.
61. Sánchez-Iglesias, A.; Grzelczak, M.; Altantzis, T.; Goris, B.; Pérez-Juste, J.; Bals, S.; Van Tendeloo, G. ; Donaldson Jr, S.H. ; Chmelka, B.F.; Israelachvili, J.N.; & Liz-Marzán, L.M. Hydrophobic interactions modulate self-assembly of nanoparticles. *ACS Nano*, **2012**, 6, 11059-11065.
62. Yang, S.M.; Kim, S.H.; Lim, J.M.; & Yi, G.R. Synthesis and assembly of structured colloidal particles. *Journal of Materials Chemistry*, **2008**, 18, 2177-2190.
63. Zhuang, J.; Wu, H.; Yang, Y.; & Cao, Y.C. Supercrystalline colloidal particles from artificial atoms. *Journal of the American Chemical Society*, **2007**, 129, 14166-14167.
64. Banhart, F.; Kotakoski, J.; & Krasheninnikov, A.V. Structural defects in graphene. *ACS Nano*, **2011**, 5, 26-41.
65. Meyer, T.A.; Quinto, C.A.; & Bao, G. Control of iron oxide nanoparticle clustering using dual solvent exchange. **2016**, 7, 1700904.
66. Bigall, N.C.; Wilhelm, C.; Beoutis, M-L.; García-Hernandez, M.; Khan, A.A.; Giannini, C.; Sánchez-Ferrer, A.; Mezzenga, R.; Materia, M.E.; Garcia, M.A.; Gazeau, F.; Bittner, A.M.; Manna, L.; & Pellegrino, T. Colloidal ordered assemblies in a polymer shell-a novel type of magnetic nanobeads for theranostic applications. *Chemistry of Materials*, **2013**, 25, 1055-1062.
67. Bigall, N.C.; Dilena, E.; Dorfs, D.; Beoutis, M.L.; Pugliese, G.; Wilhelm, C.; & Gazeau, F. Hollow iron oxide nanoparticles in polymer nanobeads as MRI contrast agents. *The Journal of Physical Chemistry C*, 2015, 119, 6246-6253.
68. Pellegrino, T.; Manna, L.; Kudera, S.; Liedl, T.; Koktysh, D.; Rogach, A.L.; Keller, S.; Rädler, J.; Natile, G.; & Wolfgang J. Parak. Hydrophobic nanocrystals coated with an amphiphilic polymer shell: a general route to water soluble nanocrystals. *Nano Letters*, **2004**, 4, 703-707.
69. Sheu, C.; Shalumon, K.T.; Chen, C.H.; uo, C.Y.; Fong, Y.T.; Chen, J.P. Dual crosslinked hyaluronic acid nanofibrous membranes for prolonged prevention of post-surgical peritoneal adhesion. *Journal of Material Chemistry B*, **2016**, 4, 6680-6693.
70. Chen, S.H.; Chen, C.H.; Shalumon, K.T.; Chen, J.P.; Preparation and characterization of antiadhesion barrier film from hyaluronic acid-grafted electrospun poly(caprolactone) nanofibrous membranes for prevention of flexo tenton postoperative peritendinous adhesion. *International Journal of Nanomedicine*, **2014**, 9, 4079-4092.

71. Zanini, L.F.; Osman, O.; Frenea-Robin, M.; Haddour, N.; Dempsey, N.M.; Reyne, G.; & Dumas-Bouchiat, F. Micromagnet structures for magnetic positioning and aligment. *Journal of Applied Physics*, **2012**, 111, 07B312.
72. Stefanello, T.F.; Szarpak-Jankowska, A.; Appaix, F.; Louage, B.; Hamard, L.; De Geest, B.G.; Van der Sanden, B.; Nakamura, C.V; & Auzély-Velty, R. Thermoresponsive hyaluronic acid nanogels as hydrophobic drug carrier to macrophages. *Acta Biomaterialia,* **2014**, 10, 4750-4758.
73. Maurin, M.; Stephan, O.; Vial, J.C.; Marder, S.R.; & Van der Sanden, B. Deep in vivo two-photon imaging of blood vessels with a new dye encapsulated in pluronic nanomicelles. *Journal of Biomedical Optics*, **2011**, 16, 036001.
74. Dumas-Bouchiat, F.; Zanini, L.F.; Kustov, M.; Dempsey, N.M.; Grechishkin, R.; Hasselbach, K.; Orlianges, J.C.; Champeaux, C.; Catherinot, A.; & Givord, D. Themomagnetically patterned micromagnets. *Applied Physics Letters*, 2010, 96, 102511.
75. Yang, C.; Wu, J.; & Hou, Y. Fe_3O_4 nanostructures: synthesis, growth mechanism, properties and applications. *Chemical Communications*, **2011**, 47, 5130-5141.
76. Shi, R.; Liu, X.; Gao, G.; Yi, R.; Qiu, G. Large-scale synthesis and characterization of monodisperse Fe_3O_4 nanocrystals, *Journal of Alloys Compound*, **2009**, 485, 548-553.
77. Park, J.; An, K.; Hwang, Y.; Park, J. G.; Noh, H. J.; Kim, J. Y.; Park, J. H.; Hwang, N. M.; & Hyeon, T. Ultra-large-scale syntheses of monodisperse nanocrystals. *Nature Materials*, **2004**, 3, 891-895.

Conclusion générale et perspectives

L'objectif de ces travaux de thèse était d'élaborer des nanogels à base de GAGs comme nano-vecteurs pour la vectorisation d'agents anticancéreux hydrophobes.

Notre approche a été de modifier l'acide hyaluronique (HA) et l'héparosan (Hep) propices à la comparaison de leur capacité à s'accumuler dans les tumeurs. En effet, ils ont la particularité de présenter une structure macromoléculaire similaire tout en possédant des propriétés biologiques différentes. Ces polysaccharides d'intérêt ont été modifiés par un copolymère thermosensible capable d'induire par simple élévation de la température, au-dessus d'une température d'agrégation critique (CAT), à la fois leur auto-association en nanogels et l'encapsulation de molécules hydrophobes en leur sein. La « coquille hydrophile » formée par le polysaccharide offre quant à elle la possibilité de contrôler le comportement des nanogels *in vivo* après injection par voie intraveineuse ainsi que leur capacité de ciblage.

La première partie de ce travail a porté sur l'optimisation des propriétés du copolymère thermosensible greffé sur le squelette des polysaccharides. Les monomères ainsi que leur ratio ont été soigneusement sélectionnés afin d'obtenir une CAT des nanogels proche de la température ambiante et des nanovecteurs stables lors les manipulations biologiques à 37 °C.

Une gamme de nanogels a été ainsi élaborée dans une seconde partie à partir des deux polysaccharides sélectionnés et du copolymère thermosensible synthétisé « sur mesure ». La voie de synthèse des dérivés HA-poly(DEGMA-co-BMA) et Hep-poly(DEGMA-co-BMA) a reposé sur la chimie radicalaire thiol-ène permettant le couplage du copolymère fonctionnalisé à l'extrémité par une fonction thiol avec le polysaccharide modifié par des groupements alcène. L'avantage de cette chimie est qu'elle peut être utilisée à usage multiple. Par conséquent, elle permet d'exploiter pleinement les groupements alcène restant afin de modifier la surface des nanogels à partir d'un seul intermédiaire polysaccharidique.

Les nanogels physiquement réticulés sont susceptibles de se désassembler sous l'effet de la dilution ou en raison d'interactions avec des biomolécules présentes dans la circulation sanguine. Ainsi, cette chimie a été mise à profit pour réticuler les chaînes polysaccharidiques formant la couronne hydrophile des nanogels à l'aide d'un dérivé bisthiol, de manière à figer leur structure.

Cette étude a permis de soulever certains enjeux dont la difficulté à atteindre des taux de greffage élevés en chaînes copolymère (DS > 10 %). Pour lever ces verrous, une étude plus poussée des conditions réactionnelles a été effectuée et les outils de caractérisation optimisés.

Les différents nanogels synthétisés ont ensuite été soigneusement caractérisés en termes de taille, de morphologie et de comportement en solution. Le contrôle du procédé de fabrication nous a permis d'obtenir de manière reproductible des nanogels bien définis en termes de taille et comportement en fonction de la température qui, *in fine*, répondent aux attentes d'un nanovecteur. Leurs tailles, inférieures à 200 nm, permettent d'envisager l'acheminement préférentiel des nanogels vers la zone tumorale par effet EPR. Une comparaison entre les nanogels non réticulés et réticulés a permis d'ajuster la densité de réticulation par la variation du rapport molaire thiols/ alcènes. Nous montrons qu'un excès de thiols permet d'améliorer la stabilité colloïdale des nanogels.

Ces objets nécessiteront par la suite des caractérisations complémentaires afin de connaître précisément leur composition (nombre de nanodomaines hydrophobes, nombre d'agrégation). Des analyses plus poussées par diffusion de neutrons permettraient de fournir ces informations. Enfin, leur morphologie pourra être précisée par des techniques d'imagerie comme la cryoTEM ou encore en tomographie.

Enfin, nous nous sommes attachés à évaluer leurs propriétés biologiques en lien avec l'application visée. Nous avons mené des études de biodistribution *in vivo* après administration intraveineuse dans des souris porteuses d'une tumeur provenant de cellules Ehrlich qui expriment le récepteur CD44. Celles-ci ont permis de mettre en avant le potentiel de l'héparosan comme alternative à l'acide hyaluronique. Bien que les nanogels d'héparosan ne soit pas reconnu par le récepteur CD44, ils s'avèrent capables d'atteindre la zone tumorale et et de s'y accumuler de manière significative. Ils sont en outre à peine détectés dans le foie, contrairement aux observations faites pour les nanogels à base d'HA. Notre étude apporte la première analyse du comportement *in vivo* de nanoparticules auto-assemblées à base de Hep, démontrant ainsi des différences significatives par rapport aux nanoparticules auto-assemblées à base de HA.

Ces premiers essais pourront être complétés par des études de biodistribution *in vivo* menées en utilisant des modèles de tumeurs murines montrant différents degrés de ciblage passif par effet EPR. L'étape suivante consisterait à étudier la capacité des nanogels à transporter un agent anti-cancéreux jusqu'à la tumeur. Enfin, une étude du bénéfice

thérapeutique par le suivi de la croissance tumorale chez les souris porteuses en présence de nanogels pourra être effectuée.

Au-delà de l'encapsulation de principes actifs hydrophobes, les nanovecteurs peuvent également servir de matrice pour l'encapsulation de nanoparticules inorganiques. C'est pourquoi, afin d'exploiter de manière optimale la biocompatibilité et la distribution bénéfique de ces nouveaux nanovecteurs, nous avons étudié l'incorporation de nanoparticules d'oxyde de fer aux propriétés superparamagnétiques (SPIONs). Ces derniers sont particulièrement intéressants pour la thérapie anti-cancéreuse. En plus des excellentes propriétés de contraste pour l'imagerie par résonance magnétique nucléaire (IRM), leur réponse à un champ magnétique externe peut être utilisée pour générer un échauffement local des cellules cancéreuses, entraînant leur destruction. Ce phénomène est connu sous le nom d'hyperthermie et de thermoablation.

A cette fin, après l'obtention de SPIONs monodisperses par décomposition thermique, deux stratégies différentes d'encapsulation de SPIONs, ont été abordées : i) l'encapsulation in situ au sein des nanogels et ii) la concentration des SPIONs en clusters suivie par un enrobage avec les dérivés de PS thermosensibles. Dans un premier temps, ces deux systèmes modèles ont été réalisés à partir des dérivés d'acide hyaluronique. Nous avons pu mettre en évidence par microscopie électronique la bonne encapsulation des SPIONS au sein des différents systèmes, leur conférant des propriétés super-paramagnétiques.

Ainsi, sur la base de ces considérations, les nanogels synthétisés représentent une plateforme attrayante pour étudier l'impact des paramètres de conception tels que la réticulation de la coque hydrophile, l'introduction de fonctions supplémentaires en surface, les propriétés biologiques de la matrice hydrophile, l'incorporation de plusieurs PA pour avoir un effet synergique, ainsi que des nanoparticules inorganiques (nanoparticules magnétiques, nanoparticules d'or).

Liste des abréviations récurrentes

BMA	Butyl méthacrylate
CS	Chondroitine sulfate
CAT	Température d'agrégation critique / critical aggregation temperature
DEGMA	Di(éthylène glycol) méthacrylate
DLS	Dynamic light scattering
DS	Degré de substitution / substitution degree
DTT	Dithiothreitol
FTIR	Spectroscopie infrarouge à transformée de Fourier /Fourier transform infraRed
GAGs	Glycosaminoglycanes
HA	Acide hyaluronique
Hep	Heparosan
HP	Heparine
HS	Heparane sulfate
IONPs	Iron oxide nanoparticles
LCST	Lower Critical Solution Temperature
MET (TEM)	Microscopie électronique en transmission / transmission electronic microscopy
MEB (SEM)	Microscopie électronique à balayage / Scanning electron microscopy
Mn	Masse molaire moyenne en nombre / number average molecular mass
Mw	Masse molaire moyenne en masse / mass average molecular mass
NPs	Nanoparticles
PA	Principe actif
PEG	Poly(éthylène glycol)
RAFT	Reversible-addition fragmentation chain tranfer
RMN	Résonnance magnétique nucléaire / Nuclear magnetic resonance (NMR)
SPIONs	Superparamagnetic iron oxyde nanoparticles
TCEP	Tris(2-carboxyethy1)phosphine
Tcp	Température de point de trouble / cloud point temperature
UV/Vis	Ultra-Violet/Visible

Liste des figures

Figure 1.1 A) Diagram of part of an aggrecan aggregate. G1, G2, and G3 are globular, folded regions of the central core protein. Proteoglycan aggrecan showing the noncovalent binding of proteoglycan to HA with the link proteins B) Proteoglycans act as coreceptors for growth factor receptor (GFR) signaling, thus influencing cell signaling and cell behavior. GAGs present as a part of proteoglycans on the cell surface and in ECM, bind to numerous proteins, and modulate their function. Figure from Misra et al. [17] ---------- **page 7**

Figure 1.2 Chemical structures of repeating disaccharides of glycoaminoglycans and Heparosan. ---------- **page 8**

Figure 1.3 Schematic representation of different GAGs-based nanocarriers. ---------- **page 11**

Figure 1.4 Scheme of main HA conjugation mechanism at the reducing end.---------- **page 13**

Figure 1.5 A) Synthetic scheme of core crosslinked HA-b-poly(PDSMA) (CC-HAM) micelles loaded with DOX. A1) Release profiles of DOX from CC-HAMs and HAM in the absence or the presence of GSH. The error bars in the graph represent standard deviations (n=5). A2) Fluorescence intensities of tumors and organs. Asterisks (*) denote statistically significant differences (*p<0,05) calculated by one-way ANOVA test. B) Synthetic scheme of the formation of DOX-loaded crosslinked micelles and their GSH responsive drug release behaviour B1) In vitro release behaviour of DOX from DOX-HA-ss-NPs in the absence or the presence of GSH. The error bars in the graph represent standard deviations (n=3). B2) Quantification of the ex-vivo tumor-targeting characteristics of HA micelles in tumor bearing mice. Error bars in the graph represent the standard deviation for five animals per group. [72-73] ---------- **page 16**

Figure 1.6 A) Illustration of disulfide-crosslinked HA X-NPs based on HA-Lys-LA conjugates for active CD44-targeting DOX delivery. B) In vivo biodistribution of X-NP-DOX and free DOX in MCF-7/ADR human breast bearing nude mice at 10h post intravenous injection (fluorescence images and quantification of DOX accumulated in different organs and tumors) C) TEM images of HA-Lys-LA X-NPs. D)Change of size distribution in response to 10 mM GSH in PBS. [107] ---------- **page 24**

Figure 1.7 HA derivatives modified by cholesteryl derivatives. ---------- **page 26**

Figure 1.8 Synthesis scheme HA-SA-CYS-CHOL (A), HA-SA-CYS-OA (B). Transmission electron micrographs of DTX-loaded HA-SA-CYS-OA (C) and HA-SA-CYS-CHOL (D). In vivo disposition of DIR solution and HA-SA-CYS-CHOL, HA-SA-CYS-OA nanogels at different

study intervals (E). Ex vivo fluorescence images of tissue samples collected 24h post-injection (F). Comparison table between HA-SA-CYS-OA and HA-SA-CYS-CHOL nanogels, the cross indicates the higher result, red cross for disadvantageous result and green cross for advantageous one (G). Adapted from Zhu et al 2017 [119]---------- **page 27**

Figure 1.9 Strategies based on “Grafting from” and “grafting onto” approaches to prepare HA-polymer conjugates. ---------- **page 29**

Figure 1.10 Schematic illustration of self-assembly HA-PHis nanogels and pH-responsive intracellular drug delivery. (A) The DOX-encapsulated micelles based on HA-PHis copolymers are formed in aqueous condition. (A1) (B) Particles of suitable size promote nanocarrier accumulation in tumor tissue by the EPR effect. (C) The micelles are selectively taken up by tumor cells via CD44 receptor-mediated endocytosis and delivered to the lysosomes, triggering the release of DOX into the cytoplasm, improving intracellular drug release and increasing the antitumor efficacy. ---------- **pages 31/32**

Figure 1.11 A) Schematic representation of doxorubicin-loaded pH-responsive hyaluronic acid nanonogels (DOX@PHANs). B) TEM photographs of DOX@PHANs at pH 7.4 and 5.0. Magnification is 6000x or 15000x. ---------- **page 32**

Figure 1.12 A) Synthesis of poly(DEGMA-co-OEGMA) by the RAFT polymerization method. Temperature-responsive behavior of the HA-poly(DEGMA-co-OEGMA) A1) Transmittance plots as a function of temperature with DS respectively 3, 4 and 6 % at a concentration C_p= 5 g/L. A2) Fluorescence microscopy image at 40°C (DS: 3 %) loaded with Nile Red and A3) scanning electron microscopy image (Cp = 2 g/L)**.** B) Formation of hyaluronic acid-based nanogels by temperature-induced self-assembly and their covalent crosslinking by hydrazone bond formation within the hydrophobic domains of the grafted copolymer chains. Morphology of HA-based nanogels crosslinked with an IDH:ketone molar ratio of 0.5 observed at 5 °C by TEM (B1) and by cryo-TEM (B2). (B3) In vivo near-infrared fluorescence (NIRF) images of the time dependent biodistribution of Cy5.5-labeled crosslinked nanogels in breast TS/A-pc and HeLa tumor-bearing mice. The tumor was engrafted subcutaneously on the right flank of the mouse. The fluorescence was measured before injection and at the following time elapse after administration: 30 min, 1h, 2 h 30, 5 h, 24 h, and 48 h. The tumor locations are indicated by the arrows. (B4) Fluorescence intensity ratio of the excised tumor to liver at 24 h (blue) and 48 h (orange) post-injection. The results are expressed as the mean ± SD (n=3). C) Formation of light and thermoresponsive HA-poly(DEGMA-co-CMA) nanogels by temperature increase and disassembly upon light exposure, (C3) shift of the CAT. (C1) Characterisation of HA-poly(DEGMA-co-CMA) nanogels (5% CMA, 0.5 g/L in ultrapure water at 40°C) by Scanning

and transmission electron microscopy. Cellular uptake of HA-poly(DEGMA-co-CMA) nanogels by HeLa cells C2) confocal microscopy images of HeLa cells incubated for 16h with nanogels loaded with a fluorescent dye (di-strybenzene derivative, DSB), cyanine5-labelled nanogels and DSB-loaded cyanine5-labelled nanogels (from left to right). C3) ----------**pages 35/36**

Figure 1.13 A) and B) Schematic representation of doxorubicin stabilized amphiphilic HA and CS polymers. Flow-cytometric analysis of the uptake of (C) HA NPs and (D) CS NPs by HCT116 and MCF-7 cell lines in the presence and absence of 7.5 kg/mol HA (10 mg/mL). Estimation of caspase 3/7 activities in (E) HCT116 and (F) MCF-7 cell lines, treated with drug- or drug-loaded nanoparticles. The baseline caspase 3/7 levels in each cell line are considered as 100%. E) Dose dependent cytotoxicity of DOX and DOX-loaded nanoparticles in (G) HCT116 and (H) MCF-7 cell lines. ---------- **page 38**

Figure 1.14 A) The synthetic route for HP-PTX conjugate. B) The TEM observations (B1) HP-PTX polymer carrier before DOX and CFA absorption, and (B2) drug carrier after DOX and CFA absorption. C) The in vitro release profiles of PTX (C1) and DOX (C2) of HP-based drug carrier. [180] ---------- **page 42**

Figure 1.15 A) Chemical structure of Heparosan-DOX conjugate (HDC). B) TEM image of HDC nanoparticles in PBS (pH 7.4). C) Size distribution and ξ-potential of HDC nanogels. The cytotoxicity of HDC against D) HeLa and E) A549 cells, free DOX with the equivalent amount was used as the control. In vitro cytotoxicity of F) HDC and G) free DOX against HeLa cells within different co-incubation periods. ---------- **page 45**

Figure 1.16 A) Schematic illustration of the formation of self-assembled HD nanogels and intracellular drug delivery. B) In vitro a) fluoreorescent images of HeLa cells and b) COS7-cells co-cultured with DOX-loaded nanogels for 1h. (a1, b1) Red fluorescent showed the DOX has internalized into cells; (a2, b2) blue represented cell nuclei stained by DAPI; In vitro cytotoxicity of DOX-loaded nanogels and DOX against c) HeLa cells and d) COS7 cells. Error bars represent standard deviation of 3 replicates for the test. C) Chemical structure of Heparosan-DOCA conjugate (HD). D) TEM images of a1) HD nanogels b1) DOX-loaded nanogels in PBS solution (1 mg/mL). E) Size distributions of a1) HD nanogels and b1) DOX-loaded nanogels. ----------**page 45**

Figure 2.1 *A)* Illustration du diagramme de phase d'un polymère thermosensible en solution en fonction de la température et de la fraction molaire. B) Monomères thermosensibles présentés dans l'introduction. ---------- --***page 66***

Figure 2.2 Synthèse de la polymérisation de type RAFT du poly(DEGMA-co-BMA). ----------***page 67***

Figure 2.3 Mécanisme de transfert de chaîne par addition-fragmentation réversible lors de la polymérisation de type RAFT. Rôle de l'agent de transfert de chaîne (CTA) avec P_n et P_m, les chaînes de polymères en croissance, K_{tr}, la constante de transfert de chaîne de l'agent RAFT et Z, le groupement qui détermine le taux d'addition-fragmentation. ---------- **page 67**

Figure 2.4 A) Comparaison schématique de polymères synthétisés par polymérisation radicalaire classique et par la méthode RAFT. B) Représentation de la structure d'un agent RAFT, où les groupements R et Z influencent la cinétique de polymérisation, la solubilité de l'agent RAFT et donc le degré de contrôle de la longueur des chaînes. Le choix de l'agent RAFT est crucial pour obtenir des polymères de faible polydispersité et d'architecture contrôlée. Adapté de Moad et al. [18]. ----------**page 68**

Figure 2.5 Réaction de polymérisation RAFT du poly(DEGMA-co-BMA) suivie d'une étape d'aminolyse. ----------**page 68**

Figure 2.6 Suivi cinétique par analyse des spectres RMN ^{1}H (400 MHz, $CDCl_3$, 25°C) au cours de la polymérisation du poly(DEGMA-co-BMA) à t= 0h,1h, 2h, 3h, 4h, 5h, 6h et 7h pour un ratio en monomères DEGMA/BMA de 95/5 soit r~19. ---------- **page 69**

Figure 2.7 Spectres RMN ^{1}H (400 MHz, $CDCl_3$, 25°C) des monomères DEGMA et BMA (après purification) ainsi que du CTA. ---------- **page 70**

Figure 2.8 Evolution de Ln ([M0]/[Mt]) en fonction du temps (min) et de la masse molaire (M_n en g/mol) en fonction du taux de conversion pour la synthèse du poly(DEGMA-co-BMA) avec une masse molaire (M_n théo) visée de A) 16 kg/mol (Tableau 2.2, Entrée 1) et (B) 4 kg/mol (Tableau 2.2, Entrée 5). ----------**page 72**

Figure 2.9 Spectres RMN ^{1}H (400 MHz, $CDCl_3$, 25 ºC) de copolymères poly(DEGMA-co-BMA) possédant des masses molaires comprises entre 5 kg/mol et 16 kg/mol. Détermination de la masse molaire du polymère final à partir des intégrales des pics Hg (poly(DEGMA)) et Hj (poly(BMA)) par rapport au pic Ha (CTA), en utilisant l'équation ci-dessus. ---------- **page 74**

Figure 2.10 A) Tableau récapitulatif des T_{cp} en fonction du milieu aqueux et de la concentration. Graphe récapitulatif de l'intensité lumineuse des solutions du poly(DEGMA-co-BMA) (M_n = 16 kg/mol) en fonction de la concentration B) dans le PBS et C) dans l'eau. ---------- **page 76**

Figure 2.11 Influence de la température sur la transmission optique (T_{cp}) de la lumière à 500 nm du poly(DEGMA-co-BMA) de masse molaire A) 4 kg/mol, B) 8 kg/mol et C) 12 kg/mol, dans le PBS sur la gamme de concentration : 3 g/L, 0,5 g/L, 0,2 g/L et 0,1 g/L avec une rampe de température de 0,1°C/min. ---------- **page 77**

Figure 2.12 Evolution de la température sur la transmission optique (T_{cp}) en fonction de la concentration en solution des copolymères de masse molaire 4, 8, 12, 16 kg/mol, d'après les données extraites de la Figure 2.11. ---------- **page 77**

Figure 2.13 A) Influence de l'agent RAFT en bout de chaîne sur la transition optique (T_{cp}) des copolymères de M_n 4 kg/mol et 16 kg/mol. Comparaison des T_{cp} avant et après aminolyse, à 3 g/L et B) Comparaison de la T_{cp} du poly(DEGMA-co-BMA) après aminolyse pour deux masses molaires : 4 kg/mol et 16 kg/mol dans le PBS à 3 g/L et 0,5 g/L. Transmission optique (T_{cp}) de la lumière mesurée à 500 nm, avec une rampe de température de 1°C/min dans le PBS. ---------- **page 79**

Figure 2.14 Influence de la température sur la (T_{cp}) de la lumière à 500 nm du poly(DEGMA-co-BMA) pour une masse molaire de 16 kg/mol et un ratio en monomères DEGMA/BMA de A) 95/5 B) 99/1 à 3 g/L avec une rampe de température de 1°C/min. ----------**page 79**

Figure 2.15 Evolution du diamètre hydrodynamique par DLS des copolymères en fonction de la masse molaire, en solution A) eau ultrapure, B) PBS au-dessus de la T_{cp} à 37°C, à une concentration de 0,1 g/L. ---------- **page 80**

Figure 3.1 Schéma représentatif de la méthode expérimentale mise au point pour réaliser la purification par chromatographie ionique en batch des dérivés de polysaccharides.

---------- **page 117**

Figure 3.2 Analyse des eaux de lavages A) Spectres UV/Vis du copolymère avant et après aminolyse ainsi que du dérivé HA-pentènoate à 20°C B) Spectres UV/Vis des eaux de lavages (n=10) à 20°C, C) Eaux de lavages à température ambiante (n=7). ---------- **page 118**

Figure 3.4 Schéma réactionnel du dosage des unités glucuronique de HA par le carbazole A) formation du dérivé furfural B) formation du chromophore (λ = 530 nm). ---------- **page 122**

Figure 3.5 Détermination du DS par dosage au carbazole de dérivés HA-poly(DEGMA-co-BMA) synthétisés dans les mêmes conditions réactionnelles. ---------- **page 122**

Figure 3.6 Mécanismes réactionnels proposés pour la chimie thiol-ène suivant une suite cyclique dans le cas A) de la réaction d'addition radicalaire B) de la réaction d'addition de

Michael où (i) représente une étape de propagation et (ii) représente une étape de transfert de chaîne. R_1 et R_2 sont des groupes de substituants, et EWG représente un groupe électroattracteur [26]. ---------- **page 124**

Figure 3.7 Taux de greffage (DS%) obtenus en absence de TCEP lors de la réaction thiolène radicalaire pour deux DS visé 30% (n=6) et 60% (n=2). ---------- **page 127**

Figure 3.8 Spectres RMN ^{1}H des dérivés de HA présentant différents DS en copolymère (4 %, 7 %). ---------- **page 127**

Figure 3.9 Caractérisation des dérivés HA-copolymère en-dessous de la CAT, à 5°C A) en solution par DLS ([HA-copolymère] = 0,5 g/L, PBS) et par analyses microscopiques en B) MEB et C) TEM. Caractérisation des dérivés HA-copolymère au-dessus de la CAT, à 37° D) en solution par DLS ([HA-copolymère] = 0,5 g/L, PBS) et par analyses microscopiques en E) MEB et F) TEM. ---------- **page 129**

Figure 3.10 A) DS fixé à 4% (RMN) B) DLS réalisée à 40°C dans le PBS (0,01 M) C) Diamètre hydrodynamique (Z-ave, int, nb) et PdI déterminés par DLS pour des dispersions de HA-copolymère à 0,5 ou 3 g/L. ---------- **page 130**

Figure 3.11 A) CAT en fonction du $DS_{copolymère}$ (4 % et 7%) et de la concentration des dérivés en solution (3 g/L et 0,5 g/L) B) DLS réalisée à 40°C dans le PBS (0,01 Mol) à 0,5 g/L C) Diamètre hydrodynamique (Z-ave, int, nb) et PdI obtenus par DLS pour une dispersion de HA-copolymère à 0,5 ou 3 g/L. ---------- **page 132**

Figure 3.12 A) CAT des dérivés présentant un $DS_{copolymère}$ de 7% en fonction de la concentration (3g/L et 0,5 g/L) et du milieu (eau ou PBS) B) DLS réalisée à 40°C dans le PBS (0,01 Mol) ou dans l'eau à 0,5 g/L C), diamètre hydrodynamique donné en intensité.

---------- **page 133**

Figure 3.13 Structure chimique du 3,6 Dioxa-1,8 octane-dithiol (DODT). ---------- **page 134**

Figure 3.14 A) Superposition des spectres RMN ^{1}H des nanogels avant et après réticulation B) Superposition des spectres FTIR dans le but de comparer les spectres des nanogels réticulés à 0,5 (spectre violet) et 1 équivalent (spectre bleu) en thiol. ---------- **page 134**

Figure 3.15 Evolution du diamètre hydrodynamique par DLS des dérivés nanogels en solution réticulés avec un ratio en DODT de [SH]/[=] de 0,5 (rouge) ou 1 (bleu) ([AH-copolymère] = 0,5 g/L, PBS) A) en dessous de la CAT, à 15°C B) au-dessus de la CAT, 40°C. -------- **page 135**

Figure 3.16 Quantification de la disulfo-cyanine7 amine (A) courbe étalon obtenue à 760 nm dans un mélange 1/1 eau/DMF (B) Graphe du fluorophore greffé sur l'AH et l'Hep linéaire ainsi que sur leurs dérivés (C) Concentration en fluorophore pour [Cproduit] = 0,5 mg/mL ---------- **page 136**

Figure 4.1 A) Scheme of a colloidal nanoparticle consisting of oleic acid/oleylamine-stabilized Fe_3O_4 (linkage with iron oxide nanoparticle) B); TEM image of iron oxide nanoparticles stabilized with a oleic/oleylamine mixture and C) size distribution histogram determined from the TEM image. ---------- **page 148**

Figure 4.2 Infrared spectra of synthesized oleic acid-Fe_3O_4 nanoparticles (A), oleic acid (B), and oleylamine (C). ---------- **page 149**

Figure 4.3 Hysteresis loops and their zooms of IONPs at 5 (red) and 300 K (green).

---------- **page 150**

Figure 4.4 TGA curves of IONPs under N_2 atmosphere. ---------- **page 151**

Figure 4.5 Formation of the magnetic thermosensitive nanogels based on hyaluronic acid (HA-g-copolymer/IONPs). ---------- **page 153**

Figure 4.6 TEM images of negatively stained A) HA-g-copolymer/IONPs nanogels, B) IONPs (C = 0.15 g/L) coprecipitated with thermoresponsive copolymer (C = 0.18 g/L) and C) un-loaded crosslinked nanogels at 0.5 g/L. ---------- **page 154**

Figure 4.7 DLS size distributions of IONPs-loaded nanogels containing 0.5 g/L of HA-g-copolymer and different concentration of SPIONs: 0.3 g/L, 0.5 g/L and 1.0 g/L A) D_h in intensity and B) D_h in number. ---------- **page 155**

Figure 4.8 Images of SPION-loaded nanogels containing 0,5 g/L of HA-g-copolymer and 1 g/L of SPIONs in water by SEM (A) and TEM after negative staining (B). ---------- **page 156**

Figure 4.9 FTIR spectra of A) OA-IONPs, B) Crosslinked HA-g-copolymer nanogels, C) Crosslinked HA-g-copolymer/IONPs nanogels after freeze-drying. ---------- **page 157**

Figure 4.10 Description of the successive steps in the formation of magnetic nanoclusters coated with HA-g-poly(DEGMA-co-BMA). ---------- **page 159**

Figure 4.11 The nanobead suspension directly after polymer assembly (A), after separation from solvents (6 h) (B), re-dispersed in water (C) and attracted by magnet from water after 1 night (D). ---------- **page 159**

Figure 4.12 TEM images of magnetic nanobeads at low magnification A) and D), high magnification B) and E) and SEM images C) and F) of magnetic nanobeads after re-dispersion in water (A-C) and after magnetic separation from big agglomerates (D-F), after 30 min in contact with a magnet. ---------- **page 160**

Figure 4.13 DLS size distributions of nanobeads in water after magnetic separation from big agglomerates. ---------- **page 160**

Figure 4.14 TEM images of IONPs clusters obtained from 200 µL of IONPS (1g /L) in THF destabilized by 200 µL (A), and 800 µL (B) of ACN, and clusters obtained by destabilization with 200 µL of ACN and mixed with HA-pentenoate solution (0.5 g/L). ---------- **page 161**

Figure 4.15 TEM images of negatively stained crosslinked HA-g-copolymer coated SPION clusters made with THF/ACN ratio of A) 200 µL / 200 µL and TEM images of un-crosslinked HA-g-copolymer coated SPIONs clusters made with THF/ACN ratio of C) 200 µL / 200 µL and D) 200 µL / 800 µL HA-g-copolymer. ---------- **page 163**

Figure 4.16 TEM (A-B and E-F - negative staining), cryo-TEM (C) and SEM (D) images of core/shell (A-E) cross-linked nanogels and nanogels with dispersed IONPs (F). ---- **page 166**

Figure 4.17 TGA curves of pure HA-g-poly(DEGMA-co-BMA) indicated as HA-g-copo curve (black), HA-g-poly(DEGMA-co-BMA) nanogels with incorporated IONPs as HA-g-copo/IONPs curve (red) and HA-g-poly(DEGMA-co-BMA) coated nanoclusters of IONPs as HA-g-copo/clusters (green) line, under N_2 atmosphere, all samples were freeze dried before analysis. ---------- **page 167**

Figure 4.18 Representative fluorescence microscopy images of nanogels re-suspended in water filled with 25 µg (A) and 50 µg (B) of DSB. ---------- **page 168**

Figure 4.19 Fluorescence images of the nanobeads trapped by micro-magnets after 0, 1, 6, and 30s. The magnetic lines (A) represents attracted nanobeads with 25 µg of DSB, while squares (B) represents attracted nanobeads with 50 µg of DSB used for encapsulation.

---------- **page 169**

Figure 4.20 Hysteresis loop and it zooms of self-assembly HA-g-copolymer/IONPs hydrogel-coated clusters at 5K. ---------- **page 170**

Figure SI.4.1 A-C) TEM images of oleic acid-coated IONPs at different magnifications; D) Electron diffraction pattern recorded form the area selected in C and indexation of diffraction rings. E) high resolution lattice images of selected particles with calculated power spectra. F) Summary of the lattice spacings in relation i^{th} electron diffraction rings. ---------- **page 177**

Figure SI.4.2 TGA curves of pure HA-g-poly(DEGMA-co-BMA) indicated as HA-g-copo curve (black), HA-g-poly(DEGMA-co-BMA) nanogels with incorporated IONPs as HA-g-copo/IONPs curve (red) and HA-g-poly(DEGMA-co-BMA) coated nanoclusters of IONPs as HA-g-copo/clusters (green) line, under N_2 atmosphere, all samples were freeze dried before analysis, with respect to normalized weight vs. temperature. ---------- **page 178**

Liste des tableaux

Table 1.1 HA-b-polymers used for the formation of micelles. Hydrophobic polymer core. ---------- **page 14**

Table 1.2 HA-based polymersomes**.** ---------- **page 17**

Table 1.3 Summary of HA-drug conjugates which demonstrated self-assembly properties. ---------- **page 20**

Table 1.4 Alkylated HA conjugates forming nanogels. ---------- **page 23**

Table 1.5 HA-polymer conjugates forming nanogels**.** ---------- **page 30**

Table 1.6 HA-thermoresponsive polymer conjugates forming nanogels. ---------- **page 33**

Table 1.7 Amphiphilic derivatives of CS leading to the formation of self-assembled NPs. ---------- **page 38**

Tableau 2.1 Récapitulatif des équations/formules permettant de déterminer le ratio des monomères (r), le taux de conversion (ρ), le degré de polymérisation (DP_n), la masse molaire théorique et expérimentales ainsi que la cinétique de croissance des chaînes (ln[M0]/[Mt]) appliquées à l'analyse par spectroscopie RMN ^{1}H. ---------- **page 71**

Tableau 2.2 Récapitulatif des synthèses des poly(DEGMA-co-BMA) par polymérisation RAFT. M_n théo : masse molaire en nombre théorique ; M_n exp : masse molaire en nombre expérimentale : Đ : indice de polydispersité ; Rdt : rendement de la réaction. [a] Analyse RMN ^{1}H dans le $CDCl_3$; [b] analyse SEC-MALLS dans le DMF ---------- **page 73**

Tableau 3.1 Conditions expérimentales de la purification par dialyse. ---------- **page 116**

Tableau 3.2 Comparaison des purifications par dialyse et chromatographie ionique pour les dérivés de HA-copolymère et le HA. ---------- **page 119**

Tableau 3.3 Analyse DLS des propriétés en solution des nanogels AH-copolymère obtenue après purification par chromatographie ionique ou par dialyse. ---------- **page 120**

Tableau 3.4 Nombre de chaîne de copolymère par chaîne de HA en fonction du degré de substitution. ---------- **page 121**

Tableau 3.5 Taux de greffage du copolymère thermosensible sur les chaînes de HA obtenus par dosage au carbazole après purification par chromatographie ionique. ---------- **page 124**

Tableau 3.6 Taux de greffage obtenu en présence et en absence de TCEP lors de la réaction thiol-ène radicalaire. n : nombre de lot de dérivés synthétisés dans les mêmes conditions. ---------- **page 126**

Tableau 3.7 Récapitulatif de l'ensemble des nanogels préparés en fonction de la masse molaire et du DS en copolymère des dérivés HAp-copolymère obtenus après purification par chromatographie ionique. ---------- **page 130**

Tableau 3.8 Récapitulatif des résultats obtenus pour des nanogels élaborés à partir de dérivés de HA obtenus après purification par chromatographie ionique, présentant une masse molaire et un DS en copolymère différent. ---------- **page 132**

Table 4.1 Examples of HA-based magnetic nanobeads found in the literature. Physical encapsulation of IONPs into HA. Size distribution obtained by DLS analysis. Msat : saturation magnetization. ----------**pages 145/146**

Table 4.2 Size distribution of un-crosslinked and crosslinked nanobeads in suspension made from THF/ACN ratio 1:1. Dynamic light scattering (DLS) analysis of nanobeads in water and PBS media was performed at 25 and 40°C. ---------- **page 163**

Résumé

Dans le domaine des systèmes d'administration de principes actifs, les nanovecteurs formés par auto-association en milieu aqueux de polymères biocompatibles amphiphiles sont apparus comme l'un des systèmes transporteurs de principes actifs (PA) hydrophobes les plus prometteurs. Ces systèmes offrent plusieurs avantages tels qu'une meilleure solubilité du PA hydrophobe dans l'eau, une diminution des effets secondaires et une amélioration de la libération dans les tissus tumoraux grâce à l'effet de perméabilité et de rétention tissulaire (effet EPR). À cet égard, les nanogels sensibles aux stimuli sont des plateformes attrayantes pour l'administration de médicaments en raison de leur capacité à modifier leurs propriétés physiques et/ou chimiques en réponse à un stimulus externe tel que la lumière, l'application d'un champ magnétique, une variation de pH ou de température. Les polymères thermosensibles sont particulièrement intéressants en raison de leur capacité à subir une transition de phase réversible sans avoir besoin de réactifs supplémentaires. Dans ce contexte, nous avons développé et étudié une nouvelle classe de nanogels thermosensibles, biocompatibles et biodégradables à base de glycosaminoglycanes (GAGs) en modifiant le squelette polysaccharidique avec un copolymère thermosensible de méthacrylate de di(éthylène glycol) et de *n*-butylméthacrylate. Celui-ci a été conçu pour obtenir des nanogels stables à température ambiante. La voie de synthèse polyvalente a également permis la réticulation de la couronne afin de figer leur structure. Le choix des GAGs, composant la couronne hydrophile peut être exploité pour contrôler leur comportement biologique. Dans l'objectif d'utiliser ces systèmes en tant que plate-forme polyvalente pour la délivrance de principes actifs et d'autres molécules d'intérêt, nous avons étudié la possibilité d'incorporer des nanoparticules d'oxyde de fer pour des applications de guidage magnétique, d'imagerie et de traitement par hyperthermie. Les synthèses du composant magnétique ainsi que la conception du nanovecteur sont des étapes clés pour réaliser un système de délivrance magnétique capable de réaliser un ciblage efficace.

Abstract

In the field of drug delivery systems, polymeric nanogels obtained by the self-assembly of biocompatible amphiphilic polymers in water have emerged as one of the most promising nanocarriers for various hydrophobic drugs. These systems offer several advantages such as enhanced hydrophobic drug solubility in water, decreased side effects, and improved drug delivery to tumor tissues via the enhanced permeability and retention (EPR) effect. In this regard, stimuli-responsive polymeric nanogels are attractive platforms for drug delivery due to their ability to change their physical and/or chemical properties in response to an external stimulus such as light, magnetic field, pH or temperature. Thermoresponsive polymers are particularly interesting due to their ability to undergo a reversible thermally-induced phase transition without the need of additional reagents. In this context, our aim was to engineer and to study a new class of thermoresponsive, biocompatible and biodegradable nanogels based on glycosaminoglycans (GAGs) through the modification of the polysaccharide backbone with a thermoresponsive copolymer of di(ethylene glycol) methacrylate (DEGMA) and *n*-butylmethacrylate (BMA)). The latter was properly designed to obtain stable nanogels at room temperature. The versatile synthetic route to nanogels also allowed their further shell-crosslinking to capture the nanogel structure at low temperature. The choice of the GAGs forming the hydrophilic shell can be exploited to control their biological behavior. In order to use these systems as a versatile platform for delivery of active ingredients and other molecules of interest, we investigated the possibility of incorporating iron oxide nanoparticles for magnetic guidance, imaging and hyperthermia treatment. The syntheses of the magnetic component as well as the design of the nanocarrier are key steps to achieve a magnetically-responsive nanodelivery system capable of efficient targeting.